

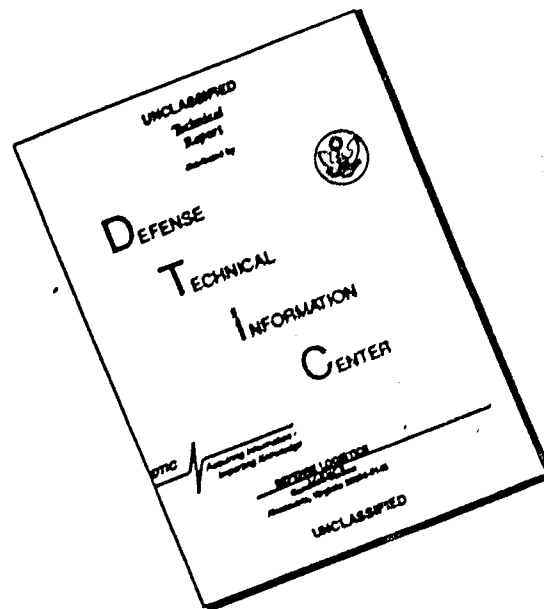
AD A170 806



**INSTITUTE
FOR
AEROSPACE STUDIES**

UNIVERSITY OF TORONTO

DISCLAIMER NOTICE



THIS DOCUMENT IS BEST QUALITY AVAILABLE. THE COPY FURNISHED TO DTIC CONTAINED A SIGNIFICANT NUMBER OF PAGES WHICH DO NOT REPRODUCE LEGIBLY.

REPORT DOCUMENTATION PAGE

1a. REPORT SECURITY CLASSIFICATION Unclassified		1b. RESTRICTIVE MARKINGS													
2a. SECURITY CLASSIFICATION AUTHORITY		3. DISTRIBUTION/AVAILABILITY OF REPORT Approved for public release; distribution unlimited.													
2b. DECLASSIFICATION/DOWNGRADING SCHEDULE															
4. PERFORMING ORGANIZATION REPORT NUMBER(S) UTIAS Technical Note No. 255		5. MONITORING ORGANIZATION REPORT NUMBER(S) AFOSR-TR. 86-0572													
6a. NAME OF PERFORMING ORGANIZATION University of Toronto, Inst. for Aerospace Studies	6b. OFFICE SYMBOL (If applicable)	7a. NAME OF MONITORING ORGANIZATION AFOSR/NA													
6c. ADDRESS (City, State and ZIP Code) 4925 Dufferin St., Downsview, Ontario, Canada, M3H 5T6		7b. ADDRESS (City, State and ZIP Code) Bolling HFB, D													
8a. NAME OF FUNDING/SPONSORING ORGANIZATION Air Force Office of Scientific Research/NA	8b. OFFICE SYMBOL (If applicable) NA	9. PROCUREMENT INSTRUMENT IDENTIFICATION NUMBER AFOSR 82-0096													
8c. ADDRESS (City, State and ZIP Code) Bldg. 410, Bolling Air Force Base, DC 20332, U.S.A.		10. SOURCE OF FUNDING NOS. <table border="1"><tr><td>PROGRAM ELEMENT NO. 61102F</td><td>PROJECT NO. 2307</td><td>TASK NO. A1</td><td>WORK UNIT NO.</td></tr></table>		PROGRAM ELEMENT NO. 61102F	PROJECT NO. 2307	TASK NO. A1	WORK UNIT NO.								
PROGRAM ELEMENT NO. 61102F	PROJECT NO. 2307	TASK NO. A1	WORK UNIT NO.												
11. TITLE (Include Security Classification) Pseudo-Stationary Oblique-Shock-Wave Reflections in a Polyatomic Gas-SF ₆															
12. PERSONAL AUTHOR(S) T. C. J. Hu															
13a. TYPE OF REPORT Interim	13b. TIME COVERED FROM TO	14. DATE OF REPORT (Yr., Mo., Day) January 1985	15. PAGE COUNT 173												
16. SUPPLEMENTARY NOTATION															
17. COSATI CODES <table border="1"><tr><td>FIELD</td><td>GROUP</td><td>SUB. GR.</td></tr><tr><td></td><td></td><td></td></tr><tr><td></td><td></td><td></td></tr><tr><td></td><td></td><td></td></tr></table>		FIELD	GROUP	SUB. GR.										18. SUBJECT TERMS (Continue on reverse if necessary and identify by block number) 1.Pseudo-stationary oblique-shock-wave reflections, 2.Shock-tube flows, 3.Interferometry, 4.Frozen and real-gas effects, 5.Numerical analysis	
FIELD	GROUP	SUB. GR.													
19. ABSTRACT (Continue on reverse if necessary and identify by block number) <p>T I C S W</p> <p>Pseudo-stationary oblique-shock-wave reflections in sulfur hexafluoride were investigated experimentally and numerically. Over 150 experiments were conducted in the UTIAS 10 x 18 cm Hypervelocity Shock Tube in the range of incident shock wave Mach number $1.25 < M_s < 8.0$ and wedge angle $4^\circ < \theta_w < 47^\circ$ with initial pressures P_0 ranging from 4^5 to 267 torr (0.53 to 35.60 kPa) and initial temperatures T_0 near 300 K. The four major types of shock-wave reflection, ie., regular reflection (RR), single-Mach reflection (SMR),</p>															
20. DISTRIBUTION/AVAILABILITY OF ABSTRACT UNCLASSIFIED/UNLIMITED <input checked="" type="checkbox"/> SAME AS RPT. <input type="checkbox"/> DTIC USERS <input type="checkbox"/>		21. ABSTRACT SECURITY CLASSIFICATION Unclassified													
22a. NAME OF RESPONSIBLE INDIVIDUAL R. Wilson		22b. TELEPHONE NUMBER (Include Area Code) (202) 767-4935	22c. OFFICE SYMBOL Unclassified												

complex-Mach reflection (CMR) and double-Mach reflection (DMR), were observed. These were studied with infinite-fringe interferograms using a 23-cm dia field of view Mach-Zehnder interferometer. The isopycnics obtained and the density distributions along the wedge surface are presented for the various reflection processes. Four experimental results in argon, air, carbon dioxide and sulfur hexafluoride with the same wedge angle and similar Mach numbers are compared.

The analytical transition boundaries between the four types of shock-wave reflection were established up to $M_s = 10.0$ for frozen and vibrational equilibrium sulfur hexafluoride. The examination of the relaxation length under the present experimental conditions indicated that a vibrational-equilibrium analysis is required. In general, the equilibrium-gas analytical transition boundaries agree with the experiments. However, RR persists beyond the RR termination boundary determined by the detachment criterion, and several Mach reflections (MR) lie outside their analytically predicted domains. Experiments substantiate that the CMR to DMR transition line approaches the SMR to CMR transition line and merges at a single point on the RR termination line. The analytical results are compared with the experimental data for the reflection angles δ and ω' , and the triple-point trajectory angles χ and χ' , and it is verified that the shock-wave reflection systems were in vibrational equilibrium. It is found that negative values for the angle ω' are possible under certain conditions of Mach reflection. The angle between the two triple-point trajectories ($\chi' - \chi$) is also discussed and the pattern of DMR with $\chi' = 0$ was obtained experimentally. There is little doubt that new criteria for the transition lines are required in order to improve the agreement between analysis and experiment.

The numerical results of the second triple-point system show that for a given incident shock Mach number, the highest pressure is achieved through a DMR instead of a RR. The data show that when the transition of $RR \leftrightarrow DMR$ occurs, no significant pressure change results in the region behind the reflection point P in RR, nor in the region behind the second triple point T'. Numerical simulation of pressure histories as functions of M_s and Θ_w at the $RR \leftrightarrow DMR$ transition boundary is required to substantiate the present analytical and experimental results.

An application of reflections in pseudo-stationary flow to the interaction of spherical blast waves with a planar surface is shown and discussed.

PSEUDO-STATIONARY OBLIQUE-SHOCK-WAVE REFLECTIONS
IN A POLYATOMIC GAS - SULFUR HEXAFLUORIDE

by

T. C. J. Hu

Submitted June, 1984

AIR FORCE OFFICE OF SCIENTIFIC RESEARCH (AFSC)
NOTICE OF TRANSMITTAL TO DTIC
This technical report has been reviewed and is
approved for public release IAW AFR 190-12.
Distribution is unlimited.
MATTHEW J. KERPER
Chief, Technical Information Division

January 1985

UTIAS Technical Note No. 253
CN ISSN 0082-5263

Acknowledgements

I wish to express my gratitude to my supervisor, Professor I. I. Glass for the opportunity to learn from him, and the invaluable guidance and advice given throughout the course of this study. I extend my thanks to Mr. R. L. Deschambault for training me how to operate the shock tube and for his interesting discussions; to Dr. J. J. Gottlieb and Mr. H. Sadek for their help on blast waves from explosions; to Dr. J. H. Lee and Dr. O. Igra for their fruitful discussions; to Mr. M. Shirouzu, especially, for his cooperation and significant assistance on the numerical calculations; to Ms. K. Polack for typing and Mrs. E. Reside for proofreading the manuscript; and to the staff and students of UTIAS for their technical assistance and support. The financial assistance received from the Canadian Natural Sciences and Engineering Research Council, the U.S. Air Force under grant AF-AFUSR 82-0096, and the U.S. Defense Nuclear Agency under DNA Contract 001-83-C-0266 is acknowledged with thanks.

Summary

Pseudo-stationary oblique-shock-wave reflections in sulfur hexafluoride were investigated experimentally and numerically. Over 150 experiments were conducted in the UTIAS 10 x 18 cm Hypervelocity Shock Tube in the range of incident shock wave Mach number $1.25 < M_s < 8.0$ and wedge angle $4^\circ < \theta_w < 47^\circ$ with initial pressures P_0 ranging from 4 to 267 torr (0.53 to 35.60 kPa) and initial temperatures T_0 near 300 K. The four major types of shock-wave reflection, i.e., regular reflection (RR), single-Mach reflection (SMR), complex-Mach reflection (CMR) and double-Mach reflection (DMR), were observed. These were studied with infinite-fringe interferograms using a 23-cm dia field of view Mach-Zehnder interferometer. The isopycnics obtained and the density distributions along the wedge surface are presented for the various reflection processes. Four experimental results in argon, air, carbon dioxide and sulfur hexafluoride with the same wedge angle and similar Mach numbers are compared.

The analytical transition boundaries between the four types of shock-wave reflection were established up to $M_s = 10.0$ for frozen and vibrational equilibrium sulfur hexafluoride. The examination of the relaxation length under the present experimental conditions indicated that a vibrational-equilibrium analysis is required. In general, the equilibrium-gas analytical transition boundaries agree with the experiments. However, RR persists beyond the RR termination boundary determined by the detachment criterion, and several Mach reflections (MR) lie outside their analytically predicted domains. Experiments substantiate that the CMR to DMR transition line approaches the SMR to CMR transition line and merges at a single point on the RR termination line. The analytical results are compared with the experimental data for the reflection angles δ and ω' , and the triple-point trajectory angles χ and χ' , and it is verified that the shock-wave reflection systems were in vibrational equilibrium. It is found that negative values for the angle ω' are possible under certain conditions of Mach reflection. The angle between the two triple-point trajectories ($\chi' - \chi$) is also discussed and the pattern of DMR with $\chi' = 0$ was obtained experimentally. There is little doubt that new criteria for the transition lines are required in order to improve the agreement between analysis and experiment.

The numerical results of the second triple-point system show that for a given incident shock Mach number, the highest pressure is achieved through a DMR instead of a RR. The data show that when the transition of $RR \leftrightarrow DMR$ occurs, no significant pressure change results in the region behind the reflection point P in RR, nor in the region behind the second triple point T'. Numerical simulation of pressure histories as functions of M_s and θ_w at the $RR \leftrightarrow DMR$ transition boundary is required to substantiate the present analytical and experimental results.

An application of reflections in pseudo-stationary flow to the interaction of spherical blast waves with a planar surface is shown and discussed.



iii

By	
Distribution /	
Availability Codes	
Dist	Avail and/or Special
A-1	

Notation

a	speed of sound
Ar	atomic argon
C	explosive charge
CMR	complex-Mach reflection
CO ₂	carbon dioxide
DMR	double-Mach reflection
h	specific enthalpy, Planck constant, height of burst
He	helium
I	incident shock wave
K	kink, degrees Kelvin, Gladstone-Dale constant, Boltzmann constant
L	distance between reflection point and wedge corner, distance between Mach stem and wedge corner, depth of test section
L*	horizontal distance between incident shock and wedge corner
ℓ	horizontal distance between kink and wedge corner
ℓ*	horizontal distance between incident shock and kink
M, M'	Mach stems
M _i	flow Mach number in state (i)
M _s	incident shock wave Mach number
M _{2K}	flow Mach number in region (2) relative to kink
M _{2P}	flow Mach number in region (2) relative to reflection point
M _{2T}	flow Mach number in region (2) relative to triple point
MR	Mach reflection
NR	no reflection
N ₂	molecular nitrogen

O_2	molecular oxygen
P	reflection point
P_i	pressure in state (i)
P_{ij}	ratio of pressure in state (i) to pressure in state (j)
R	universal gas constant
R, R'	reflected shock waves
RR	regular reflection
r	shock radius
S, S'	slipstreams
SF_6	sulfur hexafluoride
SMR	single-Mach reflection
T, T'	triple points
T_i	temperature in state (i)
t	time
U_i	flow velocity in state (i) with respect to pseudo-stationary coordinates
U_{1l}	flow velocity in region 1 relative to laboratory frame
U_{sl}	velocity of incident shock wave relative to laboratory frame
W	explosive charge weight
x	distance from reflection point or Mach stem along wedge surface, x-coordinate in physical plane, ground range
Y_T	height of first triple point
y	y-coordinate in physical plane
Z	compressibility factor
Å	angstrom, $10^{-10}m$
γ	specific heat ratio
Δ	difference between successive values

δ	angle between incident shock wave and reflected shock wave at the triple point
θ_d	displacement angle of boundary layer
θ_i	angle of flow deflection in state (i)
θ_w	actual wedge angle
θ_w'	effective wedge angle ($\theta_w + \chi$)
θ_w''	second confluence angle ($\theta_w + \chi'$)
θ_{2m}	maximum deflection angle from state (1) to state (2)
θ_{2s}	sonic deflection angle from state (1) to state (2)
λ	wavelength of light source
μ	micro
ρ_i	density in state (i)
τ	relaxation time
ϕ_i	incident wave angle for state (i)
ϕ_{1K}	incident wave angle to reflected shock wave from frame attached to kink (upstream side of kink)
ϕ_{1K}^i	incident wave angle to reflected shock wave from frame attached to kink (downstream side of kink)
χ	first triple-point trajectory angle
χ'	second triple-point trajectory angle
ω'	reflection angle

Superscripts

'	secondary, effective
n	normal component

Subscripts

0	initial or referenced value
1 - 5	thermodynamic regions
cal	calculated value
d	according to detachment criterion
i	upstream of a shock wave
j	downstream of a shock wave
K	with respect to the kink
m	according to mechanical equilibrium criterion, maximum
NR	no reflection
P	with respect to the reflection point
s	shock, according to sonic criterion, sonic
T	with respect to the first triple point
w	wedge

TABLE OF CONTENTS

1.0 INTRODUCTION	1
2.0 PSEUDO-STATIONARY OBLIQUE-SHOCK-WAVE REFLECTION	4
2.1 Classification of Types of Reflection	4
2.1.1 Regular Reflection (RR)	5
2.1.2 Mach Reflection (MR)	5
2.1.3 Single-Mach Reflection (SMR)	6
2.1.4 Complex-Mach Reflection (CMR)	6
2.1.5 Double-Mach Reflection (DMR)	7
2.2 Transition Criteria	7
2.2.1 Transition from RR to MR	7
2.2.2 Transition from SMR to CMR	9
2.2.3 Transition from CMR to DMR	10
3.0 EXPERIMENTAL INVESTIGATION	11
3.1 Experimental Instrumentation	11
3.2 Evaluation of Interferograms	13
3.2.1 Regular Reflection	14
3.2.2 Single-Mach Reflection	15
3.2.3 Complex-Mach Reflection	16
3.2.4 Double-Mach Reflection	17
3.2.5 Mach Reflections in Ar, air, CO ₂ and SF ₆	18
4.0 RESULTS AND DISCUSSIONS	21
4.1 Transition Boundaries	21
4.2 Persistence of Regular Reflection	23
4.3 Transition Boundary Between CMR and DMR	24
4.4 Comparison of Analytical and Experimental Results of Physical Quantities in Mach Reflection	26
4.4.1 Angle Between Incident and Reflected Shock Waves δ	27
4.4.2 Angle Between Reflected Shock Wave and Triple-point Trajectory ω'	28
4.4.3 First Triple-Point-Trajectory Angle χ	30
4.4.4 Second Triple-Point-Trajectory Angle χ'	31
4.5 Comparison of Analytical and Experimental Results of Physical Quantities in Regular Reflection	33
4.6 Pressure Behind Second Triple Point	35
4.7 Application of Reflections in Pseudo-Stationary Flow to the Interaction of Spherical Blast Waves with Planar Surface	37
5.0 CONCLUSIONS	39
6.0 REFERENCES	42

TABLES

FIGURES

APPENDIX A: Method of Calculation

APPENDIX B: Thermodynamic Properties of Sulfur Hexafluoride

APPENDIX C: Vibrational Relaxation in Sulfur Hexafluoride

1.0 INTRODUCTION

Shock waves appear when particles in a fluid approach and compress one another with a velocity larger than the local sound speed. The thickness of a shock front is of the order of a few molecular mean free paths. The occurrence of shock waves is found in processes that generate abrupt compression fronts such as explosions, electric discharges and supersonic flight. Shock waves become important in the practical applications of fluid mechanics due to the nearly discontinuous changes in fluid velocity and pressure they create, and the challenging analysis of the nonlinearity of the equations of motion [1].

Current interest in the problem of shock-wave diffraction is orientated to the investigation of the nuclear blast fields around aerospace vehicles and around flush-mounted surface structures for their vulnerability and survivability studies [2]. The valuable accumulated data can be utilized to determine the nonuniform shock loading to be applied in structural analysis for the design of aerospace systems. When a spherical blast wave interacts with a planar surface, the complete range of shock reflections result. Regular reflection (RR) occurs from 0° incidence of the blast wave with the surface, and at higher incidence angle Mach reflection (MR) occurs up to 90° incidence (Fig. 1).

The study of oblique-shock-wave reflection has been carried out for more than a century by many experimentalists and theoreticians. Although the phenomenon of regular reflection and single-Mach reflection (SMR) were first observed by the distinguished physicist, Ernst Mach [3], back in 1878, it was not until the early 1940's that von Neumann [4,5] reinitiated the problem and explored it systematically. Under the supervision of Bleakney [6] at Princeton University, Smith [7] discovered complex-Mach reflection (CMR) in 1945, and White [8] identified double-Mach reflection (DMR) in 1951, while they were investigating experimentally nonstationary oblique-shock-wave reflections. SMR, CMR and DMR, as a group, are called Mach reflection. The four types of reflections are illustrated schematically in Fig. 2.

With these four types of reflection being identified, it became necessary to establish their transition criteria and delineate their regions on a transition map. The simplest laboratory experiment designed for the study of shock-wave diffraction consists of a two-dimensional sharp wedge mounted on the wall of a shock tube. When a planar shock wave collides with a sharp compressive corner in a frozen gas, the type of reflection which occurs as a result of the shock-wave reflection and the deflection of the nonstationary flow behind it depends on the incident shock Mach number M_s and the corner wedge angle α_w . For the case of an imperfect gas where nonequilibrium and equilibrium flows occur, the initial pressure P_0 and the initial temperature T_0 are also important. An analytical transition criterion for the termination of RR in a two-dimensional, pseudo-stationary, inviscid perfect gas flow was suggested by von Neumann [4,5] and is referred to as the "detachment" criterion.

Smith [7] found in his experimental results that RR persisted beyond the limit of detachment criterion and MR did not occur immediately when the theoretical RR limit was exceeded. Bleakney and his students [6,8,9] further studied the disagreement found by Smith [7], but no fruitful

explanation was given. This persistence of RR in the MR region is called the "von Neumann paradox". Henderson and Lozzi [10] investigated the transition problem from RR to MR experimentally, both in a wind tunnel and in a shock tube. They proposed an alternative criterion for non-stationary flow, which is referred to as the "mechanical equilibrium" criterion. Instead of reducing the disagreement between theory and experiment found by Smith [7], the mechanical equilibrium criterion made it even worse [see 11]. Hornung and Kychakoff [12] suggested another criterion called the "sonic" criterion. However, the transition boundaries predicted by the sonic and detachment criteria are almost identical and cannot be resolved experimentally.

When RR terminates, three types of Mach reflection can occur in nonstationary flows, and they are SMR, CMR and DMR. White [8] investigated the reflection patterns of CMR and DMR in addition to SMR, and suggested a termination criterion for SMR. Henderson and Lozzi [10] proposed the criteria for the termination of SMR and CMR. However, their proposal was neither analytically nor experimentally substantiated. The criteria for transition from SMR to CMR and from CMR to DMR, which were initiated by Law and Glass [15], were established by Ben-Dor [11] and Ben-Dor and Glass [13, 14]. An additional criterion between SMR and CMR was later appended by Shirouzu and Glass [16].

When an incident shock wave impinges a convex or a concave wedge instead of a sharp wedge, the flow is truly nonstationary since the wedge angle varies along the wedge and the entire flow process is transient. Ben-Dor [11] and Ben-Dor and Glass [13] hypothesized that in truly nonstationary flows, the transitions from RR to MR and from MR to RR are different. Ben-Dor et al [17] and Itoh et al [18] investigated and confirmed that a hysteresis loop exists in the transition phenomenon of RR and MR in truly nonstationary flows. The existing criteria for the transition of RR and MR, which are for pseudo-stationary flows based on stationary flow analyses, cannot be applied to the truly nonstationary case. The flow is pseudo-stationary if it maintains a constant shock configuration and grows linearly with time from the instant when the incident shock wave encounters the leading edge of the wedge. Jones et al [19] transformed the equations of motion of an unsteady flow into those of a steady flow. Since the shock waves in nonstationary flow are usually curved, the steady state analysis is applicable only in the vicinity of the reflection point for RR and the triple point in MR. Bazhenova et al [20] were the first attempting to map out the transition boundary lines experimentally. However, only small ranges of incident shock wave Mach number and wedge angle were covered. Ben-Dor [11] was the first who provided transition maps for perfect and imperfect monatomic and diatomic gases (Ar and N_2) of all the major types of reflection in the range of $1 < M_s < 10$.

Real gas effects in shock waves due to the excitation of the internal degrees of freedom (vibration, dissociation, electronic excitation and ionization) have been studied by some researchers. Mach reflections in perfect argon and nitrogen, oxygen vibrationally excited air and vibrationally excited carbon dioxide were studied at initial pressures of 12 torr (1.60 kPa) by Gvozdeva et al [21]. They found that while the incident shock velocity increases, the reflection angle decreases, and under certain conditions, becomes negative. Naboko et al [22] investigated the flow parameters behind a moving shock wave in relaxing gases. Their results

revealed that the vibration of carbon dioxide molecules does not get completely excited for $4.5 < M_S < 11$; nitrogen is not vibrationally excited and oxygen molecules are in equilibrium for $3.7 < M_S < 7.5$.

Hornung et al [23] studied the transition to Mach reflection in steady and pseudo-steady flow with and without relaxation for dissociating nitrogen and carbon dioxide. Besides real-gas effects, they explained that the von Neumann paradox is due to the displacement effect of the boundary layer on the wedge surface in pseudo-stationary flow. Ben-Dor [11] and Ben-Dor and Glass [13, 14] analyzed the domains and boundaries of nonstationary oblique-shock-wave reflections in dissociating nitrogen and ionizing argon under equilibrium conditions. They showed that real-gas effects play an important role in the size of the regions and their boundaries, and the analytical imperfect boundary lines are different from the perfect boundary lines depending on the initial thermodynamic state of the gas. A wide range of Mach number and wedge angle were covered in their shock-tube experiments, however they were directed well in the regions instead of to the transition boundaries. From the comparison between their experiments and calculations in the transition-boundary maps, Ben-Dor and Glass erroneously suggested that nitrogen should be considered as an equilibrium gas and correctly treated argon as a frozen gas in the range of their experiments. Ando [24] computed the transition-boundary maps in carbon dioxide, using five different thermodynamic state models from dissociational-vibrational equilibrium to a perfect (frozen) gas. Ando concluded from his experimental results that real-gas effects played no role in the prediction of the transition boundaries, and therefore the transition boundaries are best determined by the perfect (frozen) gas model. Shirouzu and Glass [16] maintained that, although the perfect (frozen) CO_2 transition-boundary map provides very useful information for practical applications, the agreement with Ando's results is accidental and the perfect-gas model is fictitious. In their studies, Shirouzu and Glass showed that CO_2 should be treated as an equilibrium gas. Lee and Glass [25] carried out an analytical and numerical study of pseudo-stationary oblique-shock-wave reflection in air and established the transition boundaries up to Mach number 20 for both perfect and imperfect air. No crossings of transition lines were found, and hence they removed the conjecture of possible triple-Mach reflection. Deschambault [26] investigated the transition boundaries in nitrogen and air for $1.1 < M_S < 10$. He also studied the pressure histories on and above a specially constructed 40° wedge to obtain more insight of the complex flow fields. In the range of Ben-Dor's [11] and Deschambault's [26] experiment, Lee and Glass [25] reported that air and nitrogen are frozen, or nearly frozen, regarding vibrational excitation and dissociation, and Shirouzu and Glass [16] showed that for their range of experiments and initial conditions, the air and nitrogen data conclusively support the frozen gas model at lower Mach numbers ($M_S < 6$) and tend towards equilibrium at higher Mach numbers ($M_S > 6$).

To substantiate the claims made by the previous researchers that real-gas effects do play an important role in nonstationary shock wave systems, an investigation of a polyatomic gas with many internal degrees of freedom becomes ideal. Because polyatomic gas sulphur hexafluoride SF_6 has 15 modes of vibrational degrees of freedom, a low specific heat ratio of 1.093 at room conditions, and the merit of not being toxic with a high index of refraction useful for optical studies, it is thus chosen as the test gas for this study.

The present work is a continuation of the program of studying oblique-shock-wave reflections at the University of Toronto, Institute for Aerospace Studies (UTIAS) by Molder [27], Weynants [28], Law and Glass [15], Ben-Dor [11], Ben-Dor and Glass [13,14,29], Ando [24], Ando and Glass [30], Lee and Glass [25], Shirouzu and Glass [16], Hu and Shirouzu [31], Deschambault [26], and Deschambault and Glass [32]. The objectives of the present work were as follows:

- (1) To predict the domains and transition boundaries of the various types of reflection for frozen and vibrational equilibrium sulfur hexafluoride.
- (2) To investigate the various transition criteria by conducting experiments close to the transition boundaries.
- (3) To study the density distribution of the flow fields using infinite-fringe interferometric technique.
- (4) To clarify the contribution of real-gas effects to the shock wave system by comparing the analytical results with the experimental data.
- (5) To solve the second triple-point system and determine the type of reflection that attains the highest pressure.

In this study, over 150 experiments were performed in the 10 cm x 18 cm UTIAS Hypervelocity Shock Tube in sulphur hexafluoride at initial pressures ranging from 4 to 267 torr (0.53 to 35.60 kPa) and an initial temperature near 300 K in all cases. The incident shock wave Mach number range was $1.25 < M_s < 8$, over a series of sharp steel wedges ranging from 4° to 47° . Dual wavelength laser interferograms as well as shadowgrams were used to record the reflection process and were obtained with a 23-cm diameter field-of-view Mach-Zehnder interferometer. The shock shapes and geometries, density field (isopycnics) and the density distribution along the wedge surface and through the bow shock wave in detached cases were ascertained from the corresponding interferograms. However, from the shadowgrams, only the shock shapes and geometries could be ascertained. The experimental data was then compared with the numerical analyses.

2.0 PSEUDO-STATIONARY OBLIQUE-SHOCK-WAVE REFLECTION

2.1 Classification of Types of Reflection

When a planar incident shock wave encounters a sharp wedge in a shock tube, it moves with constant velocity along the wedge surface. The entire reflection problem can be considered pseudo-stationary in a frame of reference attached to the confluence point of the shock waves. Hence, instead of three independent variables x , y and t , the phenomenon becomes describable in terms of x/t and y/t , and the flow problem is self-similar [19]. The variable x and y may be measured relative to any point moving with constant velocity with respect to the wedge corner. The concepts and definitions correlated to regular reflection, single-Mach reflection, complex-Mach reflection, and double-Mach reflection are stated below [13].

2.1.1 Regular Reflection (RR)

The regular reflection shock-wave configuration as shown in Fig. 3a denotes the state ahead of and behind the incident shock wave I by (0) and (1), respectively, and the state behind the reflected shock wave R by (2). The frame of reference is attached to the two shock confluence point P which is moving parallel to the surface of the wedge with angle θ_w at a constant velocity $U_0 = U_s \operatorname{cosec} \phi_0$ or a Mach number $M_0 = M_s \operatorname{cosec} \phi_0$, where ϕ_0 is the incident angle between the flow U_0 and the incident shock wave I which is given as

$$\phi_0 = 90^\circ - \theta_w \quad (2.5)$$

When the flow U_0 passes through the incident shock wave I, it is deflected towards the wedge surface by an angle θ_1 from its original direction. The flow has a new value U_1 and the thermodynamic properties are changed. This supersonic flow U_1 is redeflected by the reflected shock wave R through an angle $\theta_2 = \theta_1$, so that the flow U_2 is now parallel to the wedge surface, thus satisfying the required boundary condition. With the frame of reference attached to the reflection point P, the flow configuration becomes stationary and the two-shock theory [4,6] may be used to find the flow properties of the regions around the reflection point P. The method of calculations is discussed in Appendix A.

If the flow U_2 behind the reflected shock R is sonic or subsonic, the corner signal can reach the point P and affect the reflected shock R. Consequently, R can be curved near point P (Fig. 3b). Since the velocity with which the point P moves along the wedge surface is very high for a small incidence wave angle ϕ_0 , the flow U_2 is generally supersonic relative to point P. Therefore the corner signal cannot reach P and there will be a region behind R in which the thermodynamic state of the gas is uniform and a portion of the reflected shock R is straight near P (Fig. 3c). The reflected shock R can be attached to, or detached from, the wedge corner, depending on the flow Mach number M_1 behind the incident shock wave and the wedge angle θ_w [11, 15] (Fig. 3d to f).

2.1.2 Mach Reflection (MR)

As the wedge angle θ_w is decreased, the flow behind the incident shock cannot negotiate the wedge surface through just the reflected shock R. An additional shock is necessary to alter the flow so that it can negotiate the wedge surface again by turning subsonically. This additional shock protrudes forward into state (0) at the lower part of the incident shock wave I and is known as the Mach stem M. The resulting irregular reflection configuration is called Mach reflection. It is characterized by a confluence of the three shocks and a fourth discontinuity, across which entropy, density, temperature and flow velocity are discontinuous, but pressure and the flow direction are continuous, and is referred to as the contact surface or slipstream S [33]. The confluence of the four discontinuities is called the first triple point T.

Three types of reflection can occur in nonstationary flows, depending on the flow Mach number behind the reflected shock wave R, namely, single-Mach, complex-Mach, and double-Mach reflections. One major difference between these Mach reflections and regular reflection is that

they all produce a subsonic flow near the wedge surface behind the Mach stem M, while in RR the flow is usually supersonic near the wall behind the reflection point P. Like the regular reflection, the reflected shock R can be attached to or detached from the wedge corner.

2.1.3 Single-Mach Reflection (SMR)

When the flow U_2 behind the reflected shock R is subsonic relative to the triple point T and the reflected shock R is curved over its entire length up to the triple point T, this is identified as a single-Mach reflection (Fig. 4). The frame of reference is attached to the triple point T and it moves along a straight line at an angle χ (first triple-point trajectory) with a constant velocity $U_0 = U_s \operatorname{cosec} \phi_0$, where ϕ_0 is the incident angle between the incident shock wave I and the oncoming flow, and is given as

$$\phi_0 = 90^\circ - \theta'_w \quad (2.2)$$

The angle χ is defined as the angle between the first triple-point trajectory and the wedge surface, and is referred to as the effective wedge angle. They are related by

$$\theta'_w = \theta_w + \chi \quad (2.3)$$

The Mach stem M lies in front of the incident shock wave I and is normal to the wedge surface, but not necessarily straight.

The flow in state (0) can reach the region bounded by the shock waves R and M by passing through two shock waves I and R if it is above T, or only one shock wave M if it is below T. From stability consideration, the gas must be compressed to the same pressure, and must move in the same direction. Consequently, this gives rise to a slipstream S dividing the two regions of equal pressure and flow velocities. The reflected shock wave R, therefore, needs to redeflect the flow so that $\theta_3 = \theta_1 - \theta_2$.

With the frame of reference attached to the triple point T, the flow configuration becomes stationary and the three-shock theory [4,6] may be used to find the flow properties around the triple point T. The method of calculations is discussed in Appendix A.

2.1.4 Complex-Mach Reflection (CMR)

When the flow U_2 behind the reflected shock R is supersonic relative to triple point T, a segment of the reflected shock R near T becomes straight, and the flow behind it is uniform, whereas the rest of R has continuous curvature until it finally terminates at the surface. The resulting Mach reflection configuration is referred to as complex-Mach reflection (Fig. 5) which is similar to single-Mach reflection except that instead of a curved reflected shock over its entire length, here the reflected shock wave R develops a reversal of curvature discontinuously. In some cases, a smooth reversal of curvature takes place. The reversal of curvature happens because of the existence of a band of compression waves behind the reflected shock wave [10,11,21] and as a result, a kink K is formed in the reflected shock wave R. The method of calculations used for SMR applies to CMR.

2.1.5 Double-Mach Reflection (DMR)

When the band of compression waves at the kink K of a complex-Mach reflection converges to form a new shock wave M', the kink becomes the second triple point T' and the flow Mach number M_2' behind the reflected shock wave R, in a frame of reference attached to the second triple point T', exceeds unity. Consequently, two systems of the three-shock interactions exist in the flow, hence this configuration is termed double-Mach reflection (Fig. 6). In the second three-shock interaction system, the flows behind the second triple point T', states (4) and (5), can be obtained from state (1) by passing through either the second reflected shock wave R' or through the reflected shock wave R and the second Mach stem M'. A second slipstream S' is formed at the second triple point T', and the second triple-point trajectory angle χ' is defined as the angle between the wedge surface and the line extending from the wedge corner to the triple point T'. The method of calculations used for SMR applies to the first triple point of DMR. Since an analogy can be made between the first and second triple points, the three-shock theory may also be used to find the flow properties around the second triple point T' [11].

2.2 Transition Criteria

With the existence of the four different types of nonstationary oblique-shock-wave reflection, it becomes necessary to determine the transition criterion for one type of reflection to terminate and another type of reflection to occur. Establishment of the transition criteria requires the understanding of the physics of the flow fields, and it is important in the mapping of the transition boundaries.

2.2.1 Transition from RR to MR

There are three most quoted termination criteria for RR in the literature. von Neumann [4] proposed that the transition from RR to MR takes place when the wedge angle γ_w is lowered to an extent where the flow deflection condition $\gamma_1 + \gamma_2 = 0$ (see Sec. 2.1.1) can no longer be satisfied. This violation occurs when the flow deflection angle γ_1 , through the incident shock wave I exceeds the maximum flow deflection angle γ_{2m} , through the reflected shock R. This criterion is referred to as the detachment criterion, and the term detachment stems from steady flows where the oblique shock wave detaches at this angle. The detachment criterion is sometimes called the von Neumann criterion and has the analytical form

$$\gamma_1 + \gamma_{2m} = 0 \quad (2.4)$$

The criterion can be best illustrated by using the pressure-deflection ($P - \gamma$) shock polars as shown in Fig. 7, where the I and R polars represent the incident and reflected shock waves, respectively. Through an RR, the net deflection angle is zero, hence state (2) is at the point where the R polar intersects the P/P_0 axis, say point A on R_1 (Fig. 7). As the wedge angle γ_w decreases, the deflection angle γ_1 through the incident shock wave I increases, and the R polar moves away from the P/P_0 axis until it is tangent to the P/P_0 axis (point B). Decreasing the wedge angle γ_w any further, the R polar no longer intersects the P/P_0 axis and RR is not possible, and MR occurs. Therefore, the detachment criterion corresponds to the reflected-shock polar R_d where the pressure of state (2) behind the

reflected shock wave jumps from point B (RR state) to point C (MR state). Note that there is a discontinuous pressure jump during transition according to the detachment criterion.

An alternative criterion was proposed by Henderson and Lozzi [10] based on the assumption that the system should remain in mechanical equilibrium during transition. They argued that a system which develops a pressure discontinuity during transition cannot be in mechanical equilibrium. In order to enable the system to remain in mechanical equilibrium, the transition between RR and MR should occur at point D (Fig. 7) where the R polar intersects the I polar (MR state) at the same point where it meets the P/P_0 axis (RR state). Consequently, the mechanical equilibrium criterion is illustrated by the reflected-shock polar R_m , and analytically expressed as

$$\Theta_1 + \Theta_2 = \Theta_3 = 0 \quad (2.5)$$

where Θ_3 is the flow deflection through the Mach stem (Fig. 4)

Consider figure 7 now, according to the mechanical equilibrium criterion, MR will take place for all reflected shock polar R above point U, since the transition criterion described by polar R_m has been exceeded. Yet, according to the detachment criterion, RR will take place for all shock polar R below point B, since the transition criterion described by polar R has not been satisfied. Therefore, RR and MR are theoretically possible for all reflected shock polar R lying between polars R_d and R_m . The dual-solution region in the $(M_s - \Theta_w')$ plane is shown for a perfect gas with specific heat ratio $\gamma = 1.4$ in Fig. 8, and it can be seen that the area of disagreement between these two criteria is very large. However, experimental results showed that the mechanical equilibrium criterion made agreement between experiment and theory worse for nonstationary oblique-shock-wave reflection. The detachment criterion is the limit for the two-shock theory to have solutions. The mechanical equilibrium criterion is the limit for the three-shock theory to have solutions which corresponds to $\chi = 0^\circ$.

Hornung and Kychakoff [12] suggested another criterion in which they argued that in order for a MR to form, a length scale must be available at the reflection point; that is, pressure signals must be communicated to the reflection point. They argued that the transition between RR and MR takes place at the sonic deflection angle Θ_{2s} , the deflection angle at which the flow behind the reflected shock R is just sonic relative to the reflection point P. In the $(P - \Theta)$ shock polar diagram of Fig. 7, the transition occurs when the reflected-shock polar intersects the P/P_0 axis at the sonic point E. Consequently, this criterion is referred to as the sonic criterion and is expressed by the relations

$$\Theta_1 + \Theta_{2s} = 0, \quad M_{2p} = 1 \quad (2.6)$$

where M_{2p} is the flow Mach number in state (2) in a frame of reference fixed to the reflection point P. The sonic criterion is illustrated by the reflected-shock polar R_s . The state behind the reflected shock wave jumps from point E (RR state) to point F (MR state) during transition. However, the sonic criterion results in a transition boundary which is too close to the detachment criterion so that the differences are experimentally unresolvable.

Experimental results of nonstationary oblique shock-wave reflection show that the detachment criterion is the correct one, although it has taken thirty-five years to confirm this. Experiments also show that MR does not occur immediately when the theoretical RR limit is exceeded. This persistence of RR in the MR region has been called the von Neumann paradox. Hornung et al [23], and Shirouzu and Glass [16] discuss this paradox in terms of boundary-layer displacement effects, and Shirouzu and Glass suggests that this can explain it. However, more experimental data is presently being obtained at UTIAS to substantiate these findings [43].

2.2.2 Transition from SMR to CMR

In SMR, the flow behind the reflected shock wave R is subsonic in a frame of reference attached to the triple point T, and it can negotiate the wedge surface subsonically. However, when the incident shock wave Mach number is increased, or in some cases when the wedge angle is raised, the flow Mach number behind the reflected shock wave R is also increased and eventually it exceeds unity. Subsequently, a SMR is no longer sufficient, because there exists again a supersonic flow directed towards the wedge surface. Theoretically, this supersonic flow has to be made either parallel to the wedge surface or subsonic before it reaches the wedge by means of a compression wave or a shock wave, so that it can negotiate the wall subsonically. The flow Mach number M_2 behind the reflected shock wave R appears to be reduced by passing through a compression wave and a CMR is formed. As the flow Mach number M_2 increases, the compression wave gets stronger and finally this compression wave becomes a shock wave and CMR terminates. Henderson and Lozzi [10] were the first to suggest that a band of compression waves must exist in a CMR and can converge to a shock wave. Unfortunately, they put forth neither analytical nor experimental substantiation for their suggestion. Ben-Dor and Glass [13,14] suggested that the transition between SMR and CMR occurs when the flow behind the reflected shock wave R is sonic with respect to the triple point T. Consequently, the criterion for the termination of SMR and the formation of CMR is

$$M_{2T} = 1 \quad (2.7)$$

Recently, Shirouzu and Glass [16] studied the problem of whether a flow is in equilibrium or frozen from a more fundamental assessment through the appropriate relaxation length as related by the angle δ between the incident and reflected waves (see Fig. 9a) rather than by the $(M_s - \phi_w)$ plots. During the course of their studies, they came up with an additional condition for the existence of CMR. They argued using the results of Law and Glass [15] that the kink K moves with a horizontal flow velocity as for state (1). This means that the flow in state (1) moves parallel to the incident shock wave I and downward with the frame of reference attached to the kink K, as shown in Fig. 9a. Since the flow properties upstream on either side of the kink K are the same, the existence of a band of compression wave in CMR implies that $\rho_2 < \rho_1^*$ and $|\phi_{1K} - 90^\circ| < |\phi_{1K} - 90^\circ|$ (or $|\beta| < |\alpha|$) as shown in Fig. 9b. Of the four possible cases illustrated in Fig. 9c, only configurations A and B satisfy the condition $|\beta| < |\alpha|$, and also the angle δ is larger than 90° in both cases. Hence, $\delta > 90^\circ$ is a necessary condition for the existence of a band of compression waves which is required for the formation of CMR. This is only a necessary condition because configuration C also has $\delta > 90^\circ$, although it does not satisfy $|\beta|$

$< |\alpha|$. Consequently, the transition from SMR to CMR takes place when both the former criterion Eq.(2.7) and the new necessary condition are satisfied. The new transition criterion from SMR to CMR can be expressed as

$$M_{2T} > 1 \quad \text{and} \quad \delta > 90^\circ \quad (2.8)$$

Shirouzu and Glass [16] showed that the transition boundaries based on this new transition criterion have improved the agreement with experiments in Ar, N₂, air and CO₂.

2.2.3 Transition from CMR to DMR

Law and Glass [15] proposed that the onset of the second triple point T' in DMR, which resulted from the supersonic flow in state (2) trying to negotiate a compressive wedge when striking the wall, started when the flow U₂ in a laboratory frame of reference was supersonic with respect to the wedge surface. Gvozdeva et al [34] suggested that DMR is formed as a result of the excitation of the internal degrees of freedom, which leads to the increase of the density ratio across the incident shock front. Hence, the flow Mach number M₂ becomes supersonic at lower incident shock wave Mach number and smaller wedge angle for real gases than for perfect gases. According to Semenov et al [35], DMR is formed due to the curling of the primary slipstream S into a vortex. In Mach reflection, the slipstream S can either lie along the wedge surface or curl into a large vortex near the wedge surface and the Mach stem M. However, Bazhenova et al [20] indicated that experiments show that DMR can occur when slipstream S does not curl into the vortex but extends over the wedge surface at large wedge angles. Therefore, the curling of the slipstream S does not establish the onset of DMR as proposed by Semenov et al [35]. Bazhenova et al [20] and Gvozdeva et al [21] used piezo-gauges to measure pressure histories on the wedge surface and found that their results did not agree with the formation criterion of DMR suggested by Law and Glass [15]. They considered that the flow U₂ behind the reflected shock R becomes supersonic with respect to the triple point T as the necessary but not sufficient condition for the existence of DMR. They argued that when CMR takes place, there is a small secondary rise on the wall, and it is more pronounced for DMR with the second confluence.

Ben-Dor and Glass [13,14] suggested that the transition from CMR to DMR occurs when the flow U₂ behind the reflected shock R becomes supersonic in a frame of reference attached to the kink K (Fig. 5). Their transition criterion is expressed analytically as

$$M_{2K} = 1 \quad (2.9)$$

Comparisons between the transition boundaries based on this criterion and experiments in nitrogen [13] and air [26] in the (M_s - q_w) plane show good agreement except at lower M_s and higher q_w near the RR boundary line. In the case of argon [14], the predicted transition line has to be lowered to take into account the DMR that penetrated into the CMR region. However, for CO₂ [16,30], the calculated boundary line fails to include many CMR points that lie in the DMR region, and the boundary line must be shifted upward. These discrepancies can be considered as inappropriate for a transition criterion. The criterion M_{2K} = 1 is only one of the necessary conditions

and the existence of other necessary conditions may improve the agreement.

3.0 EXPERIMENTAL INVESTIGATION

3.1 Experimental Instrumentation

The UTIAS 10 cm x 18 cm Hypervelocity Shock Tube [36] was used to perform the experiments for the present work. Bristow [37] reported on further modifications and improvements. An updated and detailed documentation of the shock tube and other associated facilities as well as their maintenance and operation procedures can be found in Ben-Dor and Whitten [38]. Therefore, only a brief discussion of the facilities relevant to the present study will be given.

Cold-gas runs were used to generate the range of incident shock wave Mach numbers required for the present study. The diaphragm used for these cold-gas driven shock runs consisted of several different thickness layers of Mylar polyester film. Initially, a diaphragm of the calculated thickness to give the required pressure ratio P_{30} across the diaphragm was inserted to separate the driver from the channel. The channel was then evacuated down to a vacuum of 5 to 10 millitorr (0.66 to 1.33 Pa) by the mechanical, roots and diffusion pumps, which were connected in series, and the vacuum level was measured by a Pirani vacuum gauge (Type GP140). Concurrently, the driver section was evacuated by a vacuum pump.

The test gas used for the present work was commercial grade SF_6 with a purity rating exceeding 99.8%. Relatively high initial pressures, 4 to 267 torr (0.53 to 35.60 kPa), were employed in the experiments to meet the triggering threshold of the shock wave velocity measuring pressure transducers, to intensify the density contours for the case of infinite-fringe interferometry, as well as to preserve the reproducibility of shocks. Carbon dioxide and helium were employed as the driver gases to generate incident shock wave Mach numbers M_s in the range $1.25 < M_s < 8.0$ in SF_6 .

The initial pressure P_0 in the channel section was monitored by Wallace & Tiernan type FA 160 dial pressure gauges (0 - 50 torr, 0 - 200 torr, 0 - 400 torr, and 400 - 800 torr). The accuracy of measurement using these gauges was listed below:

Gauge	Overall Error	Absolute Error
W & T 0 - 50	± 0.1 torr (13 Pa)	0.2 torr (26 Pa)
W & T 0 - 200	± 0.5 torr (66 Pa)	1.0 torr (133 Pa)
W & T 0 - 400	± 1.0 torr (133 Pa)	2.0 torr (266 Pa)
W & T 400 - 800	± 1.0 torr (133 Pa)	2.0 torr (266 Pa)

The pressure of the driver gas P_3 admitted into the driver section was monitored by Heise type H17507C dual pressure gauge (0 - 500 psi), calibrated in 0.5 psi (3.45 kPa) intervals. The bursting driver pressure P_3 was interpolated to the nearest 0.25 psi (1.72 kPa) with an estimated overall error of ± 0.25 psi (1.72 kPa), and an absolute error of 0.5 psi (3.45 kPa).

The leak rate of room air into the shock tube was found to be 6.1 torr (0.81 kPa) in a typical day. Since most of the experiments were conducted at relatively high initial pressures, $P_0 > 4$ torr (0.53 kPa), and the period between the admission of the test gas to the bursting of the diaphragm was about 15 minutes. The worst possible increase of the initial pressure due to leakage would be 0.08 torr (10.67 Pa), or no more than 2% of the measured initial pressure.

The initial temperature of the test gas T_0 was measured by a mercury bulb thermometer calibrated in 0.1°C intervals which was embedded in the midsection of the channel. The temperature of the test gas was assumed to reach a thermal equilibrium state in the shock tube within 5 minutes after the admission of the test gas. The initial temperature was interpolated to the nearest 0.05°C with an estimated overall error of $\pm 0.05^\circ\text{C}$, and an absolute error of 0.1°C .

The shock speed was calculated from the measured traverse time interval between several stations in the channel (Fig. 10). Three Hewlett-Packard (Type 3734A) and two Racal (Type SA.45) digital counters were connected to a common, external, 1 MHz oscillator providing all counters a uniform time base with a one microsecond resolution. When the shock wave arrived at station D (5.7 m upstream of the test section), all five counters were simultaneously triggered. Each counter was then stopped in succession as the shock wave travelled past subsequent pressure transducers at stations F, G, H, I and J. Atlantic Research LD - 25 piezoelectric pressure transducer flush mounted in the shock tube were used to detect the arrival of the shock wave. The absolute error in calculating the incident shock wave Mach number is outlined by Ben-Dor and Whitten [38]. For SF_6 , the absolute error is 0.01 at $M_s = 1.25$ while the absolute error is 0.11 at $M_s = 8.0$.

To study the reflection process, a 23-cm dia field of view Mach-Zehnder interferometer was used. Details of the design and operation of this interferometer were given by Hall [39]. A detailed description of the spatial resolution and alignment of the interferometer can be found in Ben-Dor and Whitten [38]. The adjustments for the infinite-fringe interferograms were very difficult in order to obtain just one fringe over the entire no-flow field of view. Fortunately, only a few residual fringes remained far from the wedge surface, and their effects on the quality of the infinite-fringe interferograms were negligible. The shapes of the density contours were initially set almost identical before each run, and all the photographs were taken under that condition. The infinite-fringe interferometric technique not only provides excellent isopycnic contours, it also is a very sensitive method of measuring density values. The shadowgrams taken in the present study used the same equipment with the light path of the lower arm blocked by a cardboard which was placed in front of a mirror.

The interferometric light source used was a giant-pulse ruby laser consisting of a TRG model 104A laser head and power supply, and an integrated TRG model 2113-1 harmonic generator and TRG Pockels Q-switch. It was found experimentally that the Pockels cell shutter opened at a time of 900 microseconds into the flash lamp pumping cycle gave an output pulse width of 30 nanoseconds, which was sufficiently fast to freeze the shock motion during the recording of the interferogram. The pulsed laser provided

a monochromatic light at a wavelength of 6943.0 Å (first harmonic) and 3471.5 Å (second harmonic).

Both the interferograms and shadowgrams were recorded on Kodak Royal-X pan (1250 ASA) 10 cm x 13 cm sheet films. The film was developed in dilution A of HC-110 developer for 9 minutes for the first harmonic interferograms and shadowgrams, and 12 minutes for the second harmonic interferograms. The control of the laser light source operation is shown in Fig. 10. The laser flashlamp capacitor bank was triggered by the shock arrival at station F, correctly delayed by a Tektronic type 555 oscilloscope to get 900 microseconds of energy pumping by the time the Pockels cell shutter opened. The Pockels cell Q-switch was triggered from station I, and delayed suitably in a delay unit to take the interferogram of the shock wave at a desired location with respect to station I.

In the present work, wedges with angle θ_w of 4°, 10°, 20°, 30°, 37°, 40°, 42°, 45° and 47° were used, with a tolerance of ± 10 minutes of arc. The wedges were constructed of mild steel, bolted to the bottom of and mounted flush with the inside shock tube walls at the test section (Fig. 11a). This arrangement was adopted due to the simplicity in design and stability during impact of a strong shock wave. However, it has a drawback of producing a boundary layer interactions at the wedge corner which is not of important in the present work. Gvozdeva et al [40] used the elevated wedge model in Fig. 11b to eliminate the boundary-layer interaction at the corner, but a more serious gasdynamic problem arose. In the case of a detached bow shock at the wedge corner, the flow field beneath the wedge will influence that above, thus disturbing the region of interest. A symmetric wedge (Fig. 11c) would be freed of the above problems, but it occupies a larger volume, consequently generating greater disturbances that could choke the flow and even raise the temperature high enough to cause damage to the window surfaces. An asymmetrical wedge (Fig. 11d) with two wedge angles θ_{w1} and θ_{w2} has the merit of producing two sets of results for each run, however, it has all the disadvantages of both models b and c.

3.2 Evaluation of Interferograms

Using infinite-fringe interferometric technique, very small density changes can be recorded on an interferogram. The density difference $\Delta\rho$ between any two consecutive isopycnics is determined by the relation [30]

$$\Delta\rho = \frac{\lambda}{KL} \quad (3.1)$$

where λ is the wavelength of the light source, K is the Gladstone-Dale constant, and L is the depth of the test section of the shock tube. The values of K for several gases listed in reference [26] is reproduced in Table 1.

By using a light source of shorter wavelength, the density contours become more numerous, and a more sensitive density distribution is achieved. Compare Fig. 12a with Fig. 12b, which were obtained simultaneously in the same experiment. The wavelength of the light source for Fig. 12a is 6943 Å (first harmonic) while the wavelength of the light source for Fig. 12b is 3471.5 Å (second harmonic). Although there are twice as many isopycnics

visible with the second harmonic than with the first harmonic, this technique suffers from the limitations of the optics and photographic emulsions used, hence large losses in intensity and improper exposure of the interferograms. An alternative to achieve more sensitive measurements of the density contours is to increase the initial pressure of the test gas, for a fixed Mach number. There will be larger relative pressure changes, and larger density changes, thus giving rise to more detailed and accurate isopycnics. Deschambault [26] reported a case where a CMR observed at lower initial pressure needed to be reclassified as a DMR when the same experiment was repeated with the initial pressure threefold higher. This method also has its practical limits, as the incident Mach number is governed by the required driver pressure and burning of the window may occur at high Mach numbers and high wedge angles. Experimentalists should be aware of the limitations of the equipment and how the initial conditions can change the state of a real gas and affect the classification of a reflection.

The incident shock wave is regarded as stable if the interferogram shows it to be planar and unstable if it is non-planar. In the present experimental work, a light driver gas such as helium is required to produce $M_s > 5.5$. With a light driver gas driving the heavy SF_6 , buoyancy-driven turbulent mixing would take place between the driver and driven gases. The instability of the contact surface could cause pressure fluctuations and nonplanarities or bulges at the shock front (see Fig. 12c). Any shock wave reflection produced from a non-planar shock front would provide erroneous data, hence, the analysis would only be done for experiments with planar shock waves.

Since it is not possible to analyze and discuss each interferogram obtained in the present study in detail, only several interesting cases will be presented. Table 2 is a record of all the experiments performed including the initial conditions and important measurements of each experiment. In the following sections, examples of attached and detached RR, SMR, CMR and DMR are presented, including their interferometric data.

3.2.1 Regular Reflection

Case 1 : $M_s = 1.82$, $\theta_w = 47^\circ$, $P_0 = 149$ torr (19.87 kPa), $T_0 = 23.1^\circ\text{C}$

An infinite-fringe interferogram of a detached RR is shown in Fig. 13. In the same figure, the evaluation of the density field is also presented. Note how clearly the isopycnics appear in the interferogram. The density contours are enhanced due to the relatively high initial pressure of the test gas used for the experiment. There exists a small uniform supersonic region immediately behind the reflection point and the reflected shock wave is straight just in this region. As one moves away from the reflection point toward the wedge corner, the flow decreases in strength and becomes subsonic. Since the corner signals are able to influence the flow up to the region where it just becomes supersonic, the reflected shock wave in the subsonic region becomes curved throughout the rest of its length and terminates on the bottom wall of the shock tube (detached).

In Fig. 14, the wall-density distribution ρ/ρ_0 plotted against the normalized distance L is shown for this example. For regular reflection, L is defined to be the distance from the reflection point P to the wedge corner (see Fig. 15a). For Mach reflection, L is defined as the distance

from the foot of the Mach stem M to the wedge corner (Fig. 15b). The points on the wall-density distribution plot were measured from the interferograms. The wall-density plot also indicated a small constant region behind the reflection point before the density drops continuously. Near the corner of the wedge surface, the density increases slightly and then drops sharply but continuously behind the corner. The sharp decrease in density is seen in the interferogram as a small region at the corner where the isopycnics converge, which may be caused by the interaction of the shock wave with the boundary layer. If the interaction were stronger, a lambda-shock configuration as shown later in case 4 would occur. Finally, after another drop in density due to the reflected shock, the density in state (1) is reached.

Case 2 : $M_s = 4.57$, $\theta_w = 40^\circ$, $P_0 = 7.5$ torr (1 kPa), $T_0 = 24.2^\circ\text{C}$

An example of an attached RR is shown in the infinite-fringe interferogram of Fig. 16. The corresponding wall-density distribution plot is given in Fig. 17. The incident shock wave Mach number for this case is approximately 2.5 times higher than that in case 1. The flow in region (1) is strong, thus forcing the reflected shock wave close to the wedge surface. The region behind state (2) is uniform, hence the flow behind the reflected shock is subsonic and there is communication of the corner signal everywhere. Note that in the wall-density distribution plot, the density near the reflection point is about the same as the density at the corner, and a density drop in between of less than 10%. A weak disturbance ahead of the reflected shock wave which had been observed previously by Ando [24] in CO_2 and Deschambault [26] in air is also seen. This phenomena occurs at high Mach number and Deschambault [26] tried to explain that the shock bifurcation seen at the wedge corner continues along the window boundary layer, gradually diminishing in strength and interaction.

3.2.2 Single-Mach Reflection

Case 3 : $M_s = 1.54$, $\theta_w = 42^\circ$, $P_0 = 138$ torr (18.40 kPa), $T_0 = 23.9^\circ\text{C}$

A detached SMR infinite-fringe interferogram with the evaluation of the density field is shown in Fig. 18. The well defined and numerous isopycnic lines in the interferogram are the result of using relatively high initial pressure. No uniform region is observed behind the triple point and the reflected shock since the flow is subsonic in state (2). The corner signal can propagate upstream to the triple point and influence the reflected shock wave. As a result, the reflected shock shape is curved throughout its entire length from the triple point to the bottom of the shock tube, where it terminates as a detached shock. The straight slipstream clearly emanates from the triple point and merges with the boundary layer on the wedge surface. The wall-density distribution is plotted in Fig. 19. The density decreases gradually behind the Mach stem and then increases slightly at the corner. As one moves along the bottom wall of the shock wave away from the wedge corner, the density is seen to be dropping again, and the sharp discontinuous drop in density across the reflected shock to state (1) is clearly shown.

Case 4 : $M_S = 2.11$, $\theta_w = 20^\circ$, $P_0 = 29.4$ torr (3.92 kPa), $T_0 = 23.8^\circ\text{C}$

In Fig. 20, an example of an attached SMR is shown. Compare the interferogram of this case to the previous case (Fig. 18). The isopycnics shapes are still clearly shown in the interferogram, but note that in this case there are fewer isopycnics recorded. This is due to the relatively lower initial pressure used and a smaller compressive wedge angle, although the incident Mach number is slightly higher in the present case. Since the triple point trajectory angle χ is larger for smaller wedges and the interferogram was taken when the shock system almost reached the crest of the wedge, the Mach stem is much longer and clearer than in the previous case. The slipstream is seen to be straight from the triple point and then it curls up into a vortex structure near the wedge surface. Also seen clearly in the interferogram is the shock-wave boundary-layer interaction at the corner. The reflected shock wave is curved and attached to the wedge surface at the corner. Another shock which is running ahead of the reflected shock at the wedge corner and this system is referred to as a lambda-shock configuration, which will not be studied in this work. The portion of the reflected shock immediately behind the triple point is fairly straight before it curves downward. It can be expected that this experiment is close to the transition boundary from SMR to CMR since the reflected shock is straight at the triple point and the closeness of the angle δ to 90° .

The wall-density distribution is presented in Fig. 21. The density has an increase as it crosses the slipstream from state (3) to state (2), and it remains steady over a large region. As one approaches the wedge corner, the density increases rapidly and drops suddenly when crossing the stem of the reflected shock. Then the density increases sharply again before it drops discontinuously back to the value of state (1) as one crosses the outer stem of the lambda-shock configuration.

3.2.3 Complex-Mach Reflection

Case 5 : $M_S = 1.72$, $\theta_w = 40^\circ$, $P_0 = 226$ torr (30.13 kPa), $T_0 = 24.9^\circ\text{C}$

An excellent infinite-fringe interferogram of a detached CMR is shown in Fig. 22. The clear and enhanced isopycnics are the result of a high initial pressure and a large wedge angle. Note the shallow kink is situated at the intersection of the straight reflected shock and the curved reflected shock. The flow behind the reflected shock between the triple point and the kink is supersonic relative to the triple point, causing the reflected shock to be straight in that region. Note the spreading of the straight slipstream and its termination at the wedge surface without curling up. The boundary-layer behind the slipstream can also be seen in the interferogram. The isopycnics near the wall on the upstream side of the slipstream slant down to the left, whereas those on the downstream side slant down to the right. The boundary layer profile changes shape between the isopycnics 'f' and 'g' because the highest density occurs right behind the slipstream. The wall-density distribution is plotted in Fig. 23. The density jumps behind the Mach stem and rises up gradually till one passes the slipstream and then it decreases to a minimum slowly. Close to the corner on the wedge surface, the density rises to a maximum and it drops at the vortex. Finally, the

density has a sharp discontinuous drop as one goes through the reflected shock back to state (1).

Case 6 : $M_S = 3.14$, $\theta_w = 10^\circ$, $P_0 = 7.95$ torr (1.06 kPa), $T_0 = 24.3^\circ\text{C}$

An example of an attached CMR along with the evaluation of the density field is presented in Fig. 24a. The number of isopycnics in the first harmonic interferogram is dramatically reduced because of the relatively low initial pressure used. Therefore, the second harmonic interferogram is also being analysed in Fig. 24b, due to the fact that it provides twice as many isopycnics as the first harmonic. There is a smooth reversal of curvature of the reflected shock wave and it is difficult to locate exactly the position of the kink. The slipstream is straight emanating from the triple point and is pushed forward near the wedge surface toward the Mach stem by the higher pressure behind the curved reflected shock. The Mach stem is seen slightly curved in this picture. The bow shock wave terminates at the corner straight and attached, and no lambda shock occurs. The wall-density distribution is shown in Fig. 25. The density jumps behind the Mach stem and has a slight rise across the slipstream before it increases gradually to a fairly constant density region near the wedge corner. The density then increases at the corner and drops sharply as one goes through the reflected bow shock back to state (1).

3.2.4 Double-Mach Reflection

Case 7 : $M_S = 2.18$, $\theta_w = 37^\circ$, $P_0 = 35.2$ torr (4.69 kPa), $T_0 = 23.7^\circ\text{C}$

An infinite-fringe interferogram for the case of an attached DMR is shown in Fig. 26. The sharp kink now becomes the second triple point. The band of compression waves, as indicated by the enhanced isopycnics emanating from the second triple point to the wedge surface interacting with the slipstream, converges and merges with the curved reflected shock forming a minute second Mach shock. The slipstream develops instabilities, forming small ripples before it rolls up at the wedge surface. Since the second Mach shock is weak and not yet fully developed, the second slipstream is not recorded in the interferogram. At the wedge corner, the intense lambda-shock interaction is prominent. In Fig. 27, the corresponding wall-density distribution is presented. After the increase of density across the Mach stem, the density remains steady in state (3) before it jumps rapidly to a maximum density across the slipstream. Then it decreases gradually and remains constant till one moves further down closer to the wedge corner where the density increases almost back to the maximum value again. The strong shock-wave boundary-layer-interaction effect at the corner is also clearly indicated in the wall-density profile. As one crosses the two shocks of the lambda shocks on the wall, the density experiences a sharp decrease reaching a minimum at the wedge corner, and then the density rises slightly and falls sharply back to state (1).

Case 8 : $M_S = 2.59$, $\theta_w = 30^\circ$, $P_0 = 11.2$ torr (1.49 kPa), $T_0 = 24.2^\circ\text{C}$

A good example of attached DMR with the evaluation of the density field is shown in Fig. 28. Although the experiment was performed with relatively low initial pressure, there is sufficient information in the interferogram to study the density field. Two fairly uniform regions are seen behind the straight reflected shock and behind the Mach stem. The straight slipstream

gradually develops turbulence and is pushed forward to curl up toward the Mach stem. A few isopycnics behind the curled up slipstream can be seen clearly converging to form a short second Mach shock which merges with the curved reflected shock at the second triple point. The second slipstream is again too weak to be recorded in the interferogram. Note how sharp and detailed the isopycnics are recorded of the lambda-shock interaction at the wedge corner. The wall-density distribution for this case appears in Fig. 29. The effect of the rolling up of the slipstream and the compression wave is illustrated in the wall-density profile as a sharp density jump after the initial density increase across the Mach stem. The effect of the lambda-shock interaction is more dramatic in this case. As one moves along the wedge surface down to the corner, the density rises to a maximum and then drops sharply as one crosses the inner lambda shock. The density then rises again before it drops sharply back to state (1) as one crosses the outer lambda shock.

3.2.5 Mach Reflections in Ar, air, CO_2 and SF_6

Extensive research of shock wave reflection in various types of gases, such as monatomic argon, diatomic O_2 , N_2 and air, triatomic CO_2 and polyatomic SF_6 , have been carried on at UTIAS for more than a decade. Lee and Glass [25] did some numerical work in showing the effects of the specific heat ratio γ on the transition boundaries and the shock-wave configuration. Their calculations show that the transition boundary shifts downward significantly with decreasing γ , and that a decrease in γ lowers the value of the reflection angle ω' . It became necessary to compare some experiments done in gases with different γ . Four experimental results of MR in four different types of gases with the same wedge angle of $\theta_w = 20^\circ$ and a Mach number of $M_s = 3.4 \pm 0.2$ are gathered for a comparison of their types of reflection, shock shapes, wall-density distribution profiles, the differences in the lambda-shock interaction, and the shape of the slipstream and its effect on the Mach stem. The initial conditions of the four runs are listed below.

Case 9:

Monatomic Ar, $M_s=3.20$, $\theta_w=20.0^\circ$, $P_0=100.0$ torr (13.3 kPa), $T_0=24.7^\circ\text{C}$ [32]
 Diatomic air, $M_s=3.60$, $\theta_w=20.0^\circ$, $P_0=60.0$ torr (8.0 kPa), $T_0=25.1^\circ\text{C}$ [26]
 Triatomic CO_2 , $M_s=3.43$, $\theta_w=20.3^\circ$, $P_0=30.0$ torr (4.0 kPa), $T_0=20.8^\circ\text{C}$ [24]
 Polyatomic SF_6 , $M_s=3.51$, $\theta_w=20.0^\circ$, $P_0=4.6$ torr (0.6 kPa), $T_0=24.0^\circ\text{C}$

The first and second harmonic infinite-fringe interferograms for the run in Ar are shown in Figs. 30(a) and 30(b), respectively. The type of reflection is a detached SMR. Because the reflected bow shock is curved throughout its entire length, the corner signals are able to propagate upstream all the way to the triple point. No significant shock-wave boundary-layer interaction near the corner is observed. The slipstream is seen to extend from the triple point and is laminar. Near the wedge surface, the slipstream is pushed ahead slightly and curls upstream because of the high pressure behind the bow shock. Since the slipstream terminates at the wall well behind the Mach stem, it does not disturb the flow in region (3). Hence, the Mach stem is straight and perpendicular to the wall. The wall-density distribution is plotted in Fig. 31(a) for this run. There is a small density jump across the Mach stem and the density behind the Mach stem is fairly constant along the wall, except for the slight increase and

then gradual fall of the density before crossing the bow shock near the corner into state (1).

The second run is an attached CMR in air as shown in Fig. 30(c). The reflected shock near the triple point is fairly straight and then it curves up with the bow shock terminating at the wall. The kink is not well defined in this run. The bow shock wave in the air run is not as bulged as in the Ar run and a shock-wave boundary-layer interaction at the corner is beginning to occur. The slipstream is still laminar but the curling upstream is more apparent. The gap between the Mach stem and the slipstream has decreased. The Mach stem remains straight and perpendicular to the wedge surface. The wall-density distribution is plotted in Fig. 31(b). The relative density jumps across the Mach stem and across the slipstream are higher in the air run than in the Ar run. The fairly constant density region near the center diminishes and near the corner, the density increases swiftly to a maximum before it drops rapidly to state (1) across the bow shock with a shock-wave boundary-layer interaction.

The third run is an attached CMR in CO_2 with the finite-fringe interferogram shown in Fig. 30(d). The vibrational relaxation behind the incident shock is clearly seen in the picture and the relaxation length is comparatively much shorter than the straight portion of the reflected shock near the triple point and the flow is in equilibrium behind the relaxation zone. The bow shock has moved closer to the wedge. The kink is more distinct here than in the air run. The shock-wave boundary-layer interaction is strong and the lambda-shock configuration is more well defined. The slipstream curls up at the wedge surface in a vortical flow, influencing the flow in region (3) pushing the Mach stem further upstream, thus the Mach stem becomes curved. Because the interferogram was not taken in the infinite-fringe mode, the wall-density profile cannot be obtained directly. Analysis would require the reduction of the finite-fringe interferogram which was not done for the present study.

The first and second harmonic interferograms for the fourth run of an attached DMR in SF_6 are shown in Figs. 30(e) and 30(f), respectively. The reflected shock is seen closer to the wedge surface when compared to the CO_2 run with a visible uniform region (2) behind it. There is a very strong and uniform flow region close to the corner behind the bow shock and the interaction of the boundary-layer with the straight attached bow shock is remarkable here. The outer-most shock of the lambda-shock system slants out further and lies closer to the wall here than in the previous runs of air and CO_2 . The bow shock wave also lies closest to the wedge among all four runs. The curling up effect of the laminar slipstream is the greatest here also. The strong vortical flow of the slipstream is situated very close to the Mach stem. It pushes the Mach stem further upstream with a bulge clearly seen in the interferogram. Figure 31(c) illustrates the wall-density distribution of this run. The first jump of density across the Mach stem and the second jump across the slipstream are much larger than in the air run. Then it increases gradually as one moves toward the wedge corner reaching a uniform region at the corner, with the maximum density occurring there. Finally, there is a very sharp jump across the lambda shocks back to state (1).

Some statements can be made from the observations taken of the four runs in the various gases with the same wedge angle and approximately the

same Mach number. Firstly, the statement of Lee and Glass [25] that the transition boundary lines shift downwards significantly and ω' decreases with decreasing γ are supported by the comparison. The flows in Ar and air are both frozen, the flow in CO_2 is almost in equilibrium, whereas the flow in SF_6 is in equilibrium under the run conditions given above. For frozen Ar, $\gamma = 1.667$; frozen air, $\gamma = 1.400$; nearly equilibrium CO_2 , $1.143 < \gamma < 1.290$ and equilibrium SF_6 , $1.056 < \gamma < 1.093$. Ar has the largest γ and the type of reflection here is SMR. Air has a smaller γ than Ar and the type of reflection becomes a CMR. This implies that the transition line of SMR \leftrightarrow CMR has shifted down in the transition map with decreasing γ as shown in Fig. 31(d). If CO_2 is used, γ is further lowered. However, the type of reflection remains as CMR but is a stronger one than in the air run. In SF_6 , γ is the smallest and the type of reflection is a DMR. This corresponds to the CMR \leftrightarrow DMR transition boundary is lowered as γ is decreased as shown in Fig. 31(e).

Secondly, the claim of Lee and Glass [25] that ω' decreases with decreasing γ is also substantiated here. Listed below are the measured physical quantities for the four runs.

Gas	δ	ω'	χ	(angles are in degrees)
Ar	83.4	40.9	14.3	
Air	99.5	23.1	12.6	
CO_2	110.8	10.5	11.0	
SF_6	127.0	- 5.0	10.4	

The angle δ behaves just the opposite to ω' . Therefore lowering γ will increase δ but decrease ω' . The angle χ is also found to be a decreasing function of γ . The behaviour of these measured angles in different γ gases is similar to increasing Q_w at the same Mach number for a given γ gas.

Thirdly, the wall-density profiles show more drastic changes as γ is lowered. The density jumps across the Mach stem, slipstream, bow shock or lambda shocks at the corner, and the maximum density ratio attained behind the slipstream and at the corner are all increased with decreased γ . Since pressure is directly related to density, the pressure profiles would behave in a similar manner. Therefore the lower the γ of the gas is, the stronger the pressure behind the bow shock will be, and this is evidenced by the shape of the bow shock and where it terminates at the wall.

Fourthly, the strength of the shock-wave boundary-layer interaction is observed to increase with decreasing γ . In the Ar run, only the boundary layer is observed near the corner. However, definite shock-wave boundary-layer interactions at the corner with the attached CMR is observed in the air run. The interaction turns into the lambda-shock configuration in both the CO_2 and SF_6 runs, with the SF_6 run being the stronger one.

Lastly, the curling effect of the slipstream and the curving of the Mach stem are enhanced with increasing γ . The laminar slipstream curls up slightly in the Ar and air runs. It curls into a vortical flow in the CO_2 run and is more pronounced in the SF_6 run. The distance between the Mach stem and the slipstream decreases with lowering γ . The Mach stems are found straight for both the Ar and air runs. The slipstream is getting closer to

the Mach stem in the CO_2 and SF_6 runs and as a result the Mach stem is pushed out and curved with the SF_6 run being the more drastic example.

4.0 RESULTS AND DISCUSSIONS

For the present experimental investigation of pseudo-stationary oblique shock-wave reflections in SF_6 , over 150 experiments were performed in the UTIAS Hypervelocity Shock Tube. A listing of the initial conditions for each experiment performed in this study can be found in Table 2. Since several postulates were raised on transition criteria as described in Sec. 2.2, it is necessary to compare them with experimental results and justify their validity. The transition boundary maps in the $(M_S - \theta_w)$ and the $(M_S - \theta'_w)$ planes for the case of frozen and vibrational equilibrium SF_6 were computed according to the criteria proposed by Ben-Dor and Glass [13] and Shirouzu and Glass [16]. To verify the contribution of real-gas effects and the validity of the transition criteria, experiments were done well inside the transition region. Comparisons of some physical phenomena of shock-wave reflection between experimental and numerical results will be presented and discussed.

4.1 Transition Boundaries

The computation of the transition boundaries in this study uses the equations of state for frozen SF_6 ($\gamma = 4/3$) and vibrational equilibrium SF_6 . The thermodynamic states of SF_6 used in the calculation are considered in more detail in Appendix B. In analyses of gasdynamic phenomena including shock waves, relaxation effects are very important. At room conditions, SF_6 is already partially vibrationally excited. By examining the vibrational relaxation lengths behind the shock waves, analysis shows that the flow states behind the shock fronts under the present experimental initial conditions are in vibrational equilibrium. The vibrational relaxation effect in SF_6 is discussed in Appendix C. It will be seen that relaxation lengths play an important role in the interpretation of the transition boundaries and the regions they enclose.

The experimental results are classified into the four possible types of reflection and are plotted in their transition maps for comparison. The comparisons are twofold: first, to determine whether the experimental results agree with the frozen-gas or the equilibrium-gas analysis; second, to verify the validity of the transition criteria. The transition boundaries for frozen SF_6 in the $(M_S - \theta_w)$ and $(M_S - \theta'_w)$ planes are shown in Figs. 32(a) and 32(b), respectively. In these transition boundary plots, the transition between SMR and CMR is represented by two lines. The dashed line shows the former criterion $M_{2T} = 1$ while the solid line shows the new additional criterion $\delta = 90^\circ$ (see Sec. 2.2.2). Transition from SMR to CMR will occur when both the former and the new additional criteria are satisfied. Note that the two SMR \leftrightarrow CMR lines cross over. The new transition criterion to the left of this cross-over point is the dashed line; whereas to the right of the cross-over point, the solid line is the new transition criterion. In $(M_S - \theta'_w)$ plane, there is an additional boundary line in the SMR region. It corresponds to the state of $M_1 = 1.0$, below which no reflection NR can occur. It can be seen in both figures that there is no agreement between the analytical and experimental results. However, there is definite agreement with the equilibrium SF_6 model as shown in Figs. 33(a) and 33(b).

The comparison of the RR \leftrightarrow MR boundary should be done in the $(M_s - \gamma_w)$ plane since there exists a multi-valued portion near this boundary in the $(M_s - \alpha'_w)$ plane (see Sec. 4.2). It is noted in Fig. 33(a) that several RR points lie in the domain corresponding to MR at $M_s < 2.11$ and $\alpha'_w = 45^\circ$. On the other hand, three of the DMR points lie in the domain of RR, at $M_s = 3.45$ (3 runs) for $\alpha'_w = 42^\circ$, and $M_s = 6.48$ (1 run) and 7.96 (2 runs) for $\alpha'_w = 37^\circ$. Note that the RR \leftrightarrow MR boundary is predicted by the detachment criterion and is the limit for the two-shock theory to have solutions. Therefore, any RR which exists beyond this boundary limited by the two-shock theory is a persistence of RR or is known as the von Neumann paradox. Furthermore, the mechanical equilibrium criterion is the limit for the three-shock theory to have solutions, thus any MR lying above the RR \leftrightarrow MR boundary into RR domain, on the contrary, is not a persistence of MR because it has not exceeded the limit of the three-shock theory for a MR to exist. However, the three DMR points lying in the RR domain are in the transition region and very close to the RR \leftrightarrow MR boundary line. Therefore, they become very sensitive to any conditions affecting their type of reflection. It can be seen that the termination of RR line, according to the detachment criterion, is in general very good for engineering applications, however, improvement is still necessary.

In the $(M_s - \alpha'_w)$ plane, the results for α'_w do not require the measurement of χ . Transition boundaries in the MR region are more accurate in the $(M_s - \alpha'_w)$ plane than in the $(M_s - \gamma_w)$ plane. In Fig. 33(b), there are two SMR points lying in the CMR according to the former criterion $M_{2T} = 1$. But according to the new SMR \leftrightarrow CMR criterion, there is only one CMR data point lying below the transition line, at $M_s = 3.47$ and $\alpha'_w = 19.5^\circ$. Therefore the new criterion for SMR \leftrightarrow CMR transition agrees best with experiment. There are also some discrepancies in the transition boundaries between CMR and DMR. At low Mach numbers and high wedge angles, $M_s < 1.95$ and $\alpha'_w > 42^\circ$, there are several DMR points lying beyond the CMR \leftrightarrow DMR transition line ($M_{2K} = 1.0$) into the CMR region. On the other hand, there is one CMR point just lying above the transition line in the DMR domain, at $M_s = 5.5$ and $\alpha'_w = 17.8^\circ$. Generally, except for low Mach numbers and high wedge angles, the CMR \leftrightarrow DMR transition criterion is reasonable, though not precise.

In some cases, the disagreement between experiments and the transition boundary of CMR and DMR are due to experimental impreciseness through the use of interferograms. An interferogram responds to changes in density whereas a shadowgram responds to the second derivative of the density changes. Thereby, a shock-wave-reflection configuration is much easier to interpret in a shadowgram than in an interferogram, although it is true that an interferogram provides more quantitative information. Consequently, it is advisable to employ shadowgram near the transition region of CMR and DMR to give more precise configurations for the classification of the type of reflection.

As mentioned earlier, the transition of RR \leftrightarrow MR should be compared in the $(M_s - \gamma_w)$ plane, whereas the SMR \leftrightarrow CMR and CMR \leftrightarrow DMR transitions should be compared in the $(M_s - \alpha'_w)$ plane. If an accurate prediction of χ can be found in the future, then the $(M_s - \gamma_w)$ plane could be used throughout for comparison of all transition boundaries. Note that the $(M_s - \alpha'_w)$ plane has another disadvantage, beside the multi-valued portion near the RR \leftrightarrow MR

boundary, that the transition boundary lines being too close together, especially at high Mach numbers, and it becomes difficult to determine if experiment and analysis of the various domains are in good agreement. In Fig. 33(b), former SMR \leftrightarrow CMR transition line approaches the NR line for $M_s > 5$. This means that the flow Mach number M_1 behind the incident shock wave diminishes to nearly unity and the reflected shock occurs as a very weak shock wave. Also in the same figure, it can be seen that the CMR \leftrightarrow DMR and the new additional SMR \leftrightarrow CMR transition lines approach the NR and level off at $M_s > 8$, thus narrowing the domains of SMR and CMR, and any comparison in this range would be difficult.

It is evident from Fig. 32(a) to 33(b) that real-gas effects shift every boundary line downwards in both the $(M_s - \theta_w)$ and the $(M_s - \theta_w')$ planes. The equilibrium boundaries begin to drop from their frozen-gas values even at very low Mach numbers, due to vibrational excitation. The divergence between the frozen and equilibrium boundaries becomes greater with increasing Mach number. At higher Mach numbers, $M_s > 5$, the frozen RR \leftrightarrow MR boundary line levels off so that it is almost independent of the incident shock Mach number. However, the equilibrium RR \leftrightarrow MR transition line strongly depends on the incident shock Mach number due to real-gas effect. Both the SMR \leftrightarrow CMR and the CMR \leftrightarrow DMR transition boundaries drop rapidly with increasing Mach number in the case of equilibrium SF_6 . Thus, for equilibrium SF_6 , the domains of SMR and CMR are diminished while the domains of RR and DMR are enlarged. The behaviour of the boundary lines due to real-gas effects is analogous to the results for gases with lower values of specific heat ratio γ as reported by Lee and Glass [25].

4.2 Persistence of Regular Reflection

Several previous experimental studies (Smith [7], Bleakney and Taub [6], White [8], Kawamura and Saito [41], Henderson and Lozzi [10]) have observed that RR exists beyond the detachment criterion. This is referred to as the persistence of RR or von Neumann paradox and the phenomenon has not been clearly understood or explained. Recently, Shirouzu and Glass [16] analysed the data of Ando and Glass [30] and Matsuo et al [42] in CO_2 and noted the same trend. Experimental results of Deschambault [26] in air show that RR persists not only at low incident shock Mach numbers, but also at extremely high Mach numbers.

Consider a transition map in the $(M_s - \theta_w')$ plane (see Fig. 8). At the RR boundary of the MR domain, χ has a finite value not equal to zero. Thus $\theta_w' = \theta_w + \chi$ has a greater value than θ_w at the boundary. On the contrary, θ_w is equivalent to θ_w in the RR domain. Therefore, the RR \leftrightarrow MR transition boundary corresponds to two different lines, ie. θ_w and $\theta_w + \chi$, in the $(M_s - \theta_w')$ plane. Consequently, a point lying between these two lines in the $(M_s - \theta_w')$ plane corresponds to two physical points, one in RR and the other in MR. In order to avoid this multi-valued portion near the RR \leftrightarrow MR boundary, the transition between RR and MR is best studied in the $(M_s - \theta_w)$ plane. The persistence of RR has also been found in the present study at $\theta_w = 45^\circ$ and low incident shock wave Mach number $M_s = 1.52, 1.66, 2.07$ and 2.11 in Fig. 33(a).

Henderson and Lozzi [10] tried to explain the anomaly as the apparent persistence of the RR system is really due to a DMR system that has not developed sufficiently to be observable as such. However, Ando [24]

disagreed and remarked that the resolution of the interferograms (0.2 mm) would enable the angle χ of the range encountered in his experiments (1.5° to 2.5°) to be clearly seen. Deschambault [26] showed that very small triple-point trajectory angles of less than 1° (far smaller than those of the nascent DMR) were observed. In the present work, the values of χ less than 1° were also observed. For example, the infinite-fringe interferogram in Fig. 34 shows a double-Mach reflection with $\chi = 0.7^\circ$ and part of the first slipstream can be seen clearly as a white line along the wedge surface. Deschambault [26] indicated that persistence in some cases, may only be a limitation of the resolution of the experimental apparatus. He reported one case where the reflection was classified as RR when the incident shock wave was only 60% up the wedge, and a run under similar initial conditions with the incident shock wave 80% past the wedge corner, the reflection was a DMR. It becomes desirable to catch the incident shock wave as far up the wedge as possible to observe fine details of the flow field more clearly.

Hornung et al [23] conducted experiments in dissociating gases and both the pseudo-steady and the steady flow experiments yielded results which indicate that the equilibrium transition conditions apply. They showed that the finite relaxation length was not sufficient enough to resolve the discrepancy between the analytical and experimental transition angle from RR to MR. They then suggested that viscous boundary layer effect could be used to resolve the persistence of RR. Analytically, the boundary layer imposes a negative displacement thickness and causes the displaced wedge to have a larger inclination, although the wedge angle in front of the incident shock wave is still equal to the actual wedge angle θ_w (see Fig. 35). With the displaced wedge being further away, the deflection through the reflected shock necessary to direct the flow parallel to the displaced wall is therefore less than that required in the inviscid flow. The displacement angle θ_d thus formed enables RR to persist to lower wedge angles. In response to the displacement effect, the angle made by the reflected shock with the wedge, ω' should decrease. Hornung et al [23] observed the opposite behaviour of ω' in their results. However, Shirouzu and Glass [16] analysed the previous experiments in CO₂ and air, and obtained results which support the viscous boundary-layer theory. More experiments are required for further analysis of this problem, not only at the transition boundary but around the transition region also to provide information on the behaviour of some reflection quantities such as ω' in RR and χ in MR. At present, an investigation of the problem of persistence of RR due to the viscous boundary-layer effect in air is being done (Wheeler [43]).

4.3 Transition Boundary Between CMR and DMR

In the calculation of the transition boundary between CMR and DMR, the location of the kink K is necessary in order to obtain the flow velocity behind the reflected shock wave R with respect to the kink. An assumption was made by Law and Glass [15] that the kink K has the same horizontal velocity as the flow velocity behind the incident shock wave U_{1g} . As a result, the ratio λ^*/L^* (see Fig. 9a) is equal to the density ratio across the incident shock wave irrespective of the wedge angle, that is

$$\lambda^*/L^* = \rho_0/\rho_1 \quad (4.1)$$

Bazhenova et al [20] investigated the ratio λ^*/L^* experimentally and found that this ratio for a given Mach number decreased and approached zero as the wedge angle increased. Since the ratio λ^*/L^* vanished at the critical wedge angle corresponding to the RR \leftrightarrow MR transition, as a result, it can be concluded on physical grounds that the transition boundaries of SMR \leftrightarrow CMR and CMR \leftrightarrow DMR should merge at the RR boundary [16]. The trend of λ^*/L^* is plotted against wedge angle α_w for three Mach numbers in Fig. 36 using the present experimental results. Note that the ratio λ^*/L^* does approach zero as the wedge angle approaches the critical value at the RR boundary.

Some interesting points are found in the behaviour of the ratio λ^*/L^* . Dashed lines are used to link up data points corresponding to the same Mach number range. All three curves are seen to behave in a similar fashion. At lower wedge angles, the ratio λ^*/L^* increases with α_w and reaches a maximum then decreases with further increase in α_w and eventually drops sharply to zero at very high α_w . It is seen that as M_s increases, the curves shift to the left and the relative maximum value becomes smaller. Refer to Fig. 33(a), with the incident shock wave Mach number fixed at $M_s = 4$, all four different types of reflection will occur in the sequence of SMR, CMR, DMR and RR as the wedge angle is raised. With SMR and RR, λ^* and λ^*/L^* are both zero. If an experimental transition boundary line is drawn between SMR and CMR in Fig. 33(a), SMR will just terminate at $M_s \approx 2.1$ and $\alpha_w = 20^\circ$, $M_s \approx 3.0$ and $\alpha_w = 8^\circ$, and $M_s \approx 4.0$ and $\alpha_w = 2^\circ$. Since the transition from SMR to CMR is smooth, the value of λ^*/L^* will begin at zero and increase gradually to the value corresponding to a CMR. If one extrapolates the curves of $M_s = 3.0$ and $M_s = 4.04$ at the lower wedge angle side, the ratio λ^*/L^* will be zero at $\alpha_w \approx 7^\circ$ and 1.5° , respectively, which agree well with the termination conditions of SMR on the transition map found above. Consider the curve of $M_s = 4.04$, the ratio λ^*/L^* is zero as SMR terminates at $\alpha_w \approx 1.5^\circ$. The value of the ratio increases as the wedge angle is increased, and reaches a maximum at $\alpha_w \approx 20^\circ$. Then it decreases and vanishes at $\alpha_w = 40^\circ$ which corresponds to where the termination of DMR and RR occurs. In general, the pressure in states (4) and (5) behind the reflected shock R' is larger than that in states (2) and (3) behind the reflected shock R (see Fig. 6), as evident from the pressure histories taken by Bertrand [44], Merritt [45] and Deschambault [26]. With the increase in wedge angle, the reflected shock R' becomes more and more normal to the induced flow behind the incident shock I. The pressure in states (4) and (5) become higher and the second triple point T' is pushed further upstream and hence the ratio λ^*/L^* decreases.

Several experiments were conducted at high wedge angle near the RR boundary in the CMR region. Refer to Fig. 33(a) and 33(b), at $\alpha_w = 45^\circ$, $M_s = 1.81$ and 1.91 , DMR is observed in the proposed CMR domain. Two DMR are found penetrating into the CMR regime at $M_s = 1.94$, $\alpha_w = 40^\circ$ and $M_s = 1.93$, $\alpha_w = 42^\circ$. Hence the present results support the postulation that the transition lines meet at a point on the RR boundary. However, the MR transition boundaries computed using the criteria suggested by Ben-Dor and Glass [13] terminate at the RR boundary at two separate points. Further analysis for the prediction of the location of the kink K at higher wedge angle is required to modify the transition line between CMR and DMR as shown approximately using the experimental data by the dot-dash line extending to the triple point P on the RR \leftrightarrow MR boundary lines.

4.4 Comparison of Analytical and Experimental Results of Physical Quantities in Mach Reflection

Analytical results based on the frozen-gas model is distinct from the equilibrium-gas model. By comparing the experimental results with the frozen or equilibrium-gas model for certain flow properties, the validity of each model can be justified. From a practical point of view, the chosen properties should be measured accurately and easily, and it is important that they are fundamental quantities which are not affected by other assumptions used in the computations. The angle δ between the incident and reflected shock waves, and the angle ω' between the reflected shock wave and the wall or the triple-point trajectory path are chosen as the fundamental quantities to serve this purpose (see Fig. 37).

In the present comparison, the experimental values are compared with the analytical results for the same Q'_w , instead of Q_w used in previous comparisons [24,25]. In the three-shock theory, the effective wedge angle Q'_w plays an important role. With a given value of Q_w at a fixed M_s , the directions of the reflected shock wave and the Mach stem are determined together with the flow variables. In this calculation, the Mach stem at the triple point is assumed perpendicular to the wedge surface and a value of χ is predicted. The effective wedge angle Q'_w is related to χ by $Q'_w = Q_w + \chi$. This means that Q'_w is a function of Q_w and the value of χ is affected by the orientation of the Mach stem. The assumption of a perpendicular Mach stem to the wedge surface is satisfied precisely at the foot of the Mach stem to meet the necessary boundary condition that flows on both sides of the Mach stem must be parallel to the wedge surface with an inviscid flow. It is also valid at the triple point if the Mach stem is perfectly straight. However, experimental results show that the Mach stem generally is curved. Shirouzu and Glass [16] tried to take into account the effect of the curved Mach stem in the prediction of χ for several gases, but the discrepancies are not minimized. It is important to recognize that comparison of experimental results and analytical results which include the assumption of a straight Mach stem are no longer accurate if they are based on the same value of Q_w . Therefore, the experimental data should be compared with analysis based on the same value of Q'_w .

Besides the comparison of the fundamental angles δ and ω' , the experimental first triple-point trajectory angle χ and second triple-point trajectory angle χ' are also compared with analysis. In the following, the angles, δ , ω' and χ' , are compared twice with Q_w and Q'_w as the parameter, while the angle χ is compared with Q_w as the parameter for both the frozen and equilibrium-gas models in the range of $1 < M_s < 5.5$.

It is important to note that the physical quantities obtained in the present work are measured from photographs. Consequently, there are errors due to measurement and magnification of the prints. Errors involved in measurements are $\pm 1.5^\circ$ for δ and ω' , and $\pm 1^\circ$ for χ and χ' . A line from the reflection point P or the first triple point T, which is tangent to the reflected shock R, needs to be drawn before the angles δ and ω' can be measured (see Fig. 37). Unless region (2) is supersonic relative to the reflection point P or the first triple point T, or region (2) is fairly uniform, the reflected shock is straight, otherwise the reflected shock R curves continuously till it meets the incident shock wave I. This makes it difficult to locate the tangent line to R, thus causing the error of

measurement in δ and ω' higher. When θ'_w is used as the parameter for comparison, the numerical results are based on the measured θ'_w and are iterated within 0.1° of those values.

Table 3 presents the measured experimental data of δ , ω' , χ and θ''_w ($\theta''_w = \theta'_w + \chi'$). The frozen and equilibrium-gas analytical results at fixed θ'_w are also given. Note that the calculated analytical wedge angle θ_{wcal} is different from the experimental θ'_w , and it can be obtained by $\theta_{wcal} = \theta'_w - \chi_{cal}$, where χ_{cal} is the calculated analytical value of χ . For example, in experiment no. 118, both the experimental and analytical results have the same $\theta'_w = 45.7^\circ$. The experimental value of $\theta_w = 45^\circ$, whereas the equilibrium analysis has $\theta_{wcal} = 45.7^\circ - 1.7^\circ = 44^\circ$, and the frozen analysis has $\theta_{wcal} = 45.7^\circ - 2.9^\circ = 42.8^\circ$.

A numerical comparison of the physical quantities in MR between experimental and analytical results at fixed θ'_w is tabulated in Table 4. Note that the analytical values of χ are different from the experimental ones, and so are the values of θ'_w . For example, in experiment no. 118, both the experimental and analytical data have $\theta_w = 45^\circ$. The experimental $\chi = 0.7^\circ$, $\theta'_w = 45.7^\circ$, whereas the equilibrium analysis has $\chi = 1.5^\circ$, $\theta'_w = 46.5^\circ$ and the frozen analysis has $\chi = 2.2^\circ$ and $\theta'_w = 47.2^\circ$.

4.4.1 Angle Between Incident and Reflected Shock Waves δ

The comparison of δ is essentially equivalent to the comparison of ω' if an experimental result is compared with a calculated result which has the same value of θ'_w since they are related by

$$\delta = 90^\circ + \theta'_w - \omega' \quad (4.2)$$

as shown in Fig. 37. Nevertheless, the comparison of δ has some advantages over ω' , for δ is a monotonic function of θ'_w and θ'_w at fixed M_s , whereas ω' has a minimum point at a certain θ'_w and θ'_w for some part of the Mach number range [25]. Moreover, δ is used as a new criterion for the transition between SMR and CMR, it is necessary to check the agreement between measured and calculated results of δ .

Figure 38 shows the experimental results for θ'_w plotted in the ($M_s - \delta$) plane. The number beside each experimental point indicates the measured value of θ'_w . The line that extends above or below a data point shows the discrepancy of the analytical value from the experimental result. The calculated results are shown in this figure for a vibrational equilibrium gas for each fixed θ'_w in solid lines and are used only as a guide to illustrate the behaviour of δ in relation to M_s . It can be seen that the maximum discrepancy found is less than 2.5° . Thus, the agreement between the experimental results and equilibrium-gas calculations is excellent. The same good agreement is expected in the comparison of the angle ω' since both δ and ω' are fundamental quantities.

The plot in Figure 39 uses θ_w instead of θ'_w for comparison. The numerical results are shown for a vibrational equilibrium gas for each fixed θ_w as a solid line. The experimental results at a fixed wedge angle supposedly should fall on top of the corresponding θ_w analytical line. The agreement is not as good as obtained in Fig. 38. In most cases, the experimental δ is larger than the calculated result at lower θ_w . At

high α_w the numerical lines are closer to one another and $d\delta/d\alpha_w$ is small. Therefore any discrepancy at higher wedge angles is not easily seen in the figure. The disagreement shown in this plot illustrates the additional errors caused by χ when using α_w rather than α'_w .

Figure 40 compares experimental results with the frozen-gas analysis in α'_w . The values of α'_w corresponding to each data point are identical to those numbered in Fig. 38 and are not repeated in this plot. It is seen that the numerical lines are all shifted lower to the right from the vibrational equilibrium case. Thus, for a given Mach number and α'_w , δ will have a smaller value with frozen-gas analysis than with vibrational equilibrium analysis. For example, at $M_s = 5.0$ and $\alpha'_w = 40^\circ$, $\delta = 150^\circ$ with equilibrium-gas analysis, while $\delta = 126.7^\circ$ according to frozen-gas analysis. It is important to realize that because of such significant difference between the frozen and equilibrium-gas calculations, it becomes possible to conclude whether the frozen or equilibrium-gas model agrees best with experiments. A similar trend of the constant α_w numerical lines is seen in Fig. 41. Note that the agreement of the frozen-gas results with the experiments is poor in both α'_w and α_w comparisons. Because of the large disagreement with the frozen-gas model, the discrepancy lines are not drawn here.

Since $\delta > 90^\circ$ is the additional necessary condition beside $M_{2T} > 1$ for the transition from SMR to CMR, it is essential to check the agreement between the measured values of δ and the type of reflection that occurs. A plot of the experimental values of δ with incident shock wave Mach number M_s for the various types of reflections is shown in Fig. 42. There are two SMR points at $\alpha_w = 42^\circ$, $M_s = 1.52$ and 1.54 with $\delta = 90.8^\circ$, and another two SMR points at $\alpha_w = 20^\circ$, $M_s = 2.08$ and 2.11 which have δ of 90.1° and 90.6° , respectively, lie above the $\delta = 90^\circ$ line. Any SMR points in the $\delta > 90^\circ$ region is not counterevidence of the new transition condition since it is only a necessary condition for the transition and not a sufficient condition. On the other hand, all experimental CMR but one at $\alpha_w = 4^\circ$, $M_s = 3.47$ and $\delta = 87^\circ$ lies below the $\delta = 90^\circ$ line. Note that a discrepancy of 3° is considered of the similar magnitude as an error in measurement. This means that the experimental results satisfy the condition $\delta > 90^\circ$ and provide good evidence that this is a necessary condition. It is worth mentioning that the results presented in Fig. 42 do not involve any assumptions or calculations. They illustrate only the experimental relation between the transition from SMR to CMR and the angle δ . Therefore this is a direct comparison between the new necessary condition and the available experimental data.

4.4.2 Angle Between Reflected Shock Wave and Triple-point Trajectory ω'

The angle ω' is sometimes called the reflection angle as shown in Fig. 37 and is given for both RR and MR as

$$\omega' = \phi_1 - \alpha_1 \quad (4.3)$$

where ϕ_1 is the incident flow angle to the reflected shock wave, and α_1 is the flow deflection angle behind the incident shock wave (see Fig. 3a, 4). Gvozdeva et al [21] calculated the reflection angle ω' as a function of the incident shock velocity U_0 , and the angle of incidence ϕ_0 for several gases. They discovered that the increasing of incident shock velocity leads to the

decrease of the reflection angle and its sliding into the negative area under certain conditions. Recently, Lee and Glass [25] studied the variation of ω' and concluded that it is always positive for RK, SMR and CMR. The shift of ω' from a positive to a negative value with higher Mach number occurs only in the DMR domain for imperfect air and gases with low γ .

Figure 43 shows the $(M_S - \omega')$ plot with ρ'_w as the parameter. The measured value of ρ'_w is indicated beside each experimental point and the solid lines are the calculated ρ'_w for equilibrium SF_6 . The discrepancy of analytical value from experimental value is shown by the extended vertical line from the data point. No more than a discrepancy of 3.6° is found in this plot. Thereby showing that the experiments agree very well with the equilibrium-gas results.

A similar plot is given in Fig. 44 with ρ_w used as the comparing parameter. Each solid line corresponds to a fixed experimental wedge angle for an equilibrium gas. In general, the experimental data of high wedge angles lie slightly above the analytical line; whereas for low wedge angles, experimental results lie under the analytical line. The maximum discrepancy obtained by using ρ_w rather than ρ'_w is 11° . It seems from the figure that ω' for high ρ_w agree well with numerical lines. However, numerical lines are so close to one another that $d\omega'/d\rho_w$ is small and the discrepancy is not obvious. It is evident from the figure that ω' is a decreasing function of M_S . At low M_S , the numerical lines are close to vertical which implies that ω' is a very sensitive function of M_S . Thus a small error in M_S may cause a large discrepancy in ω' at low M_S .

As discussed earlier, ρ_w is not an adequate parameter to be used in a comparison until χ can be predicted accurately. A comparison in Fig. 44 should use ω' as the parameter instead of ρ_w [46]. As an interpretation of an experimental point at $M_S = 5.5$ and $\rho_w = 4^\circ$ ($\omega' = 0.0^\circ$), for example, should not be compared with numerical result which has ρ_w of 4° , but with that which has ω' of 0.0° . The discrepancy for the point is not $\Delta\omega' = 11^\circ$, but $\Delta\rho_w \approx 2^\circ$. When comparing the results in this way, it cannot be concluded absolutely that the discrepancy is large at low ρ_w and small at high ρ_w . However, the discrepancy of $\Delta\rho_w \approx 2^\circ$ can be read at low ρ_w , since $d\omega'/d\rho_w$ is large, but becomes difficult at high ρ_w . This is one of the reasons why δ has advantage over ω' in a comparison. The same method of comparison can be applied to δ in Fig. 39.

It is seen in both Figs. 43 and 44 that at higher M_S , ω' shifts into the negative region. The higher the wedge angle is, the sooner is the shift. At low M_S , the value of ω' is smaller for higher ρ_w or ρ'_w . After the shift of ω' into the negative region, the high ρ_w or ρ'_w numerical lines begin to merge and cross over. Hence ω' has a minimum value at certain ρ_w or ρ'_w for some range of M_S . That is, for a given M_S , there exist two values of ρ_w or ρ'_w which have the same value of ω' . Figure 45 and 46 show the $(M_S - \omega')$ plots for a frozen-gas analysis using ρ'_w and ρ_w as parameter, respectively. The experimental ρ'_w values are not marked in Fig. 45 but they are identical to those shown in Fig. 43. Note that the numerical lines in both figures are shifted up and to the right from the equilibrium-gas results. The reflection angle ω' stays always positive and no cross-over of the numerical lines is observed with ρ'_w in Fig. 45. The numerical lines in Fig. 46 all lie in the positive ω' region but merging and crossing over of

the lines is observed with Θ_w as parameter. There are many experimental data in the negative ω' region, however, no frozen-gas analytical line exists in the negative ω' region. Thereby, the frozen-gas analysis gives poor agreement with experiments and the discrepancy lines are therefore not indicated here.

4.4.3 First Triple-Point-Trajectory Angle χ

When applying the three-shock theory to a MR it is necessary to give a value of χ as an initial condition in order that the system of equations be closed. Law and Glass [15] proposed an empirical method for predicting the value of χ based on experimental observations that the Mach stem is straight and normal to the wedge surface, and introduced an additional independent geometrical relation

$$\phi_3 = 90^\circ - \chi \quad (4.4)$$

where ϕ_3 is the incident flow angle to the Mach stem (see Fig. 4). At $\Theta_w = 0^\circ$, χ has its maximum value for a fixed M_s . If M_s is fixed, χ is a decreasing function with Θ_w increasing and approaches zero at the critical wedge angle for the transition from MR to RR. The plot of χ as a function of M_s , with the actual wedge angle Θ_w as a parameter for equilibrium SF_6 is shown in Fig. 47. For a given wedge angle Θ_w , χ is a decreasing function with increasing Mach number M_s , except for high Θ_w at low M_s . With $\Theta_w > 37^\circ$ and $M_s > 2.0$, the value of χ becomes almost constant over the entire region of M_s , implying that χ is a simple function of Θ_w . The experimental points are also plotted in the figure. The agreement between the analytical results and experiments is good in general, with discrepancies of the same order of magnitude as the error in measurement. However, the experimental points of $\Theta_w = 10^\circ, 20^\circ$ and 30° have the same trend as the higher Θ_w results that they level off and become independent of the Mach number M_s . The maximum discrepancy found in χ is 3.4° at $M_s = 3.76$ and $\Theta_w = 20^\circ$. The relation between the angles δ , ω' and χ is given by

$$\delta + \omega' = 90^\circ + \Theta_w + \chi \quad (4.5)$$

For a fixed Θ_w , the following applies

$$\Delta\delta + \Delta\omega' = \Delta\chi \quad (4.6)$$

Consider the experimental point at $M_s = 3.76$ and $\Theta_w = 20^\circ$. The differences between the analytical results from the experimental results are $\Delta\delta = -5.4^\circ$ (Fig. 39), $\Delta\omega' = +2.0^\circ$ (Fig. 44) and $\Delta\chi = -3.4^\circ$ (Fig. 47). This illustrates the point that if a discrepancy exists in χ for a data point, each of the $(M_s - \delta)$ and $(M_s - \omega')$ plots will not display the same discrepancy, but their sum will. In the above example, the $(M_s - \delta)$ plot shows a larger discrepancy in δ than in χ , while the $(M_s - \omega')$ plot shows a smaller discrepancy in ω' than in χ .

Figure 48 shows the experimental data in the $(M_s - \chi)$ plot with Θ_w as the parameter for the frozen-gas analysis. Note that the analytical lines are shifted up from the equilibrium values and χ becomes nearly independent of M_s at high Mach numbers, even for low Θ_w . In all cases, the analysis gives a much larger value than the experimental value. Therefore there is poor agreement between the frozen-gas analysis and the experiments.

As described in Section 4.4, experimentally, the Mach stem at the triple point is not perpendicular to the wedge surface because it has curvature. This discrepancy affects the analytical three-shock theory solutions, especially the value of χ . Besides, the bow shock wave has an effect on the position of the triple point. The reflected shock wave is the result of two processes; one is a reflected shock wave emanating from the triple point and the other is the bow shock wave caused by the flow-deflection process of the flow induced by the incident shock wave over the wedge corner [13]. In the three-shock theory, the interaction of these two processes has not been taken into account. At low Mach numbers or wedge angles, the reflected shock wave from the triple point becomes weaker more rapidly than the bow shock wave. Hence, the position of the entire reflected shock wave is governed by the bow shock wave. In the limit when the bow shock is a Mach wave, the intersection point of the bow shock wave and the incident shock wave is at ρ_{WNR}' [16]. Thus at low M_s and small ρ_w , the intersection point of the extension of the bow shock wave and the incident shock wave is closer to a point where it has ρ_{WNR}' . This results in a smaller value of χ than that is given by the three-shock theory. Therefore a better method for the prediction of χ which takes into account the curvature of the Mach stem and the effects of the bow shock wave is necessary.

4.4.4 Second Triple-Point-Trajectory Angle χ'

The best available analytical method to date for the prediction of χ' was developed by Ben-Dor [11]. He assumed in the analysis that the second triple point T' with respect to the first triple point T , moved with the same horizontal velocity as the induced flow behind the incident shock wave I and deduced an empirical relation based on an approximation for the relative motion of the second triple point as

$$\chi' = 90^\circ - \rho_w - \tan^{-1} \left[\frac{1 - \rho_0/\rho_1}{\cot \phi_0 - \rho_0/\rho_1 \cot(\phi_1 - \phi_0 - \rho_1)} \right] \quad (4.7)$$

This method of predicting χ' is applicable for a DMR as well as for a CMR in which χ' is defined as the kink trajectory angle.

Unlike the angles θ and θ' , the comparison of χ' based on the same value of ρ_w is affected by the calculated wedge angle ρ_{wcal} , since χ' has to be measured from the wedge surface. From Section 4.4.3, it has been described that the present method of predicting χ is not accurate. In order to obtain the same ρ_w' as the experiment, the calculated solution will give values of ρ_{wcal} and χ_{cal} which are different from the measured ρ_w and χ . Consequently, if the value of χ_{cal} is compared with the measured χ' from experiment, effectively, this means that the comparison is done on two different wedge angles. To avoid this ambiguity, the comparison should be done on the second confluence angle ρ_w'' , which is measured from the wedge base instead of the wedge surface and is defined as

$$\rho_w'' = \rho_w + \chi' \quad (4.8)$$

Figure 49 shows the $(M_s - \rho_w'')$ plot with ρ_w' as the parameter for equilibrium-gas analysis. The experimental data ρ_w' are shown with their measured ρ_w' indicated also. As revealed by the solid lines, ρ_w'' is generally a decreasing function with increasing Mach numbers and decreasing ρ_w' ,

except at high Mach numbers and Θ'_W where a slight increase in Θ''_W is observed, and Θ'_W becomes nearly independent at high Mach numbers. Note the large discrepancies of the analytical result from the experimental result at relatively low Mach numbers for a set of fixed wedge angle experiment. The analytical Θ''_W are much larger than the measured value at lower Mach numbers.

The disagreement is due to the assumption that the distance λ^* between the two triple points T and T' remains finite (see Fig. 9a). However, the length λ^* should decrease from a certain CMR value with decreasing M_S and eventually when SMR occurs, $\lambda^* = 0$. That is, experimentally, the second triple point T' approaches and merges with the first triple point T with $\lambda^*/L^* = 0$, $\chi' = \chi$ and $\Theta''_W = \Theta'_W$. This will be discussed later in more detail. The agreement improves significantly as M_S is increased. Thus it can be concluded that the prediction of χ' works well for strong CMR and DMR, and the experiments agree well with the equilibrium-gas results.

Figure 50 shows a $(M_S - \chi')$ plot using Θ'_W for the equilibrium-gas model. It can be seen that χ' is a decreasing function with increasing Mach number and wedge angle. At high wedge angles, $\Theta'_W = 37^\circ, 40^\circ$ and 42° , the values of χ' are shown as predicted by the analysis that they decrease with increasing Mach number and eventually equal to zero.

The discrepancies in this figure can be due to two causes. One is that analytical solution does not meet the requirement that λ^*/L^* approach zero as the Mach number decreases. The other is that even though λ^*/L^* approaches zero is taken into account, and χ' approaches χ , χ' still cannot be predicted accurately since χ itself is not well known.

The $(M_S - \Theta''_W)$ plot using Θ'_W as parameter and the $(M_S - \chi')$ plot using Θ'_W for the frozen-gas model are shown in Fig. 51 and 52, respectively. In both of these figures, the frozen analytical lines are seen to be all shifted up from their equilibrium values. The measured value of Θ'_W for each data point is identical to that given in Fig. 49 and is not repeated in Fig. 51. Since the disagreement between experiments and frozen-gas analysis is large, the discrepancy lines are not drawn in Fig. 51. In the $(M_S - \chi')$ plot of Fig. 52, the frozen gas analytical results are all too much larger than the measured experimental values and the agreement is poor.

The other angle that is worth discussing is the difference between χ' and χ , that is $(\chi' - \chi)$, since it indicates the position of the second triple point relative to the first triple point. A $[M_S - (\chi' - \chi)]$ plot of the experimental results is shown for five wedge angles $\Theta'_W = 42^\circ, 37^\circ, 20^\circ, 10^\circ$ and 4° in Fig. 53. A dashed line is used to approximate the profile of $(\chi' - \chi)$ for each fixed wedge angle. As SMR just terminates (e.g. at $\Theta'_W = 42^\circ$ and $M_S = 1.55$), $(\chi' - \chi) = 0$, and ω' is positive indicating that the two triple points merge as one at the first triple point. When CMR and DMR begin to form, the value of $(\chi' - \chi)$ increases with Mach number M_S . It then reaches a maximum and decreases in value. In the positive region of $(\chi' - \chi)$, ω' is positive as shown in Fig. 54(a). As M_S increases further, $(\chi' - \chi)$ crosses zero and goes into the negative region. In this case of $(\chi' - \chi) = 0$, ω' is zero as shown in Fig. 54b meaning that the second triple point lies at a finite distance away from the first triple point and both have the same trajectory direction. It is seen in Fig. 53 that the higher the wedge angle, the sooner $(\chi' - \chi)$ goes negative. When $(\chi' - \chi)$ goes negative, ω' is also negative and the reflection pattern is illustrated

in Fig. 54c. At higher wedge angle and Mach number, $\chi' = 0$, $(\chi' - \chi) = -\chi$ and ω' is negative as shown in Fig. 54d. Lee and Glass [25] studied this last case analytically for a perfect gas with $\gamma = 1.093$ and reported that $\chi' = 0$ may only be hypothetical and it does not exist in practice. However, in the present study, the experimental results confirmed the equilibrium-gas analysis that the case of $\chi' = 0$ does occur. This means that the second triple point T' attaches to the wedge surface and the reflected shock wave R strikes the wedge surface and is reflected like an RR. A shadowgram of a DMR with $\chi' = 0$ taken at $M_S = 7.96$ and $\Theta_W = 37^\circ$ is shown in Fig. 55. Note the small triangular region bounded by the Mach stem, the reflected shock wave and the wedge surface. The second reflected shock wave is lying low on the wedge surface and terminates at the corner as an attached straight bow shock wave showing that the state behind the second reflected shock wave is supersonic. Consequently, this pattern of DMR is different from the other three patterns shown in Fig. 54(a) to (c). A DMR with $\chi' = 0$ has two confluence points, two reflected shock waves, but only one Mach stem, one slipstream and the region behind the second reflected shock wave is supersonic instead of subsonic. Figure 56 shows an interferogram of a DMR with $\chi' \rightarrow 0$ at $M_S = 4.20$, $\Theta_W = 37^\circ$. The second slipstream is clearly seen in this picture.

The behaviour of χ' relative to χ can be explained by the following physical interpretation. For a given wedge angle, when SMR just terminates, the kink K is at the first triple point T and $(\chi' - \chi) = 0$. With a slight increase in M_S , CMR occurs. Now, δ is slightly larger than 90° , the kink K moves to a finite distance on the reflected shock R away from the first triple point T , and in such circumstances $(\chi' - \chi) > 0$. CMR continues to occur with further increase in M_S , K moves further away from T , the value of δ gets larger and $(\chi' - \chi)$ also increases slightly. At the onset of DMR, the portion of the reflected shock R between T and K has to bend further down, i.e. the angle δ has to increase, to have greater density change across the kink. When the densities $\rho_2' > \rho_2$ as shown in Fig. 9(b) become large enough, DMR occurs. Because the reflected shock R drops (δ increases) and the pressure in regions (4) and (5) pushes the second triple point T' upstream, χ' is getting closer to χ and $(\chi' - \chi)$ decreases. If M_S is increased further, χ' will overlap χ and $(\chi' - \chi) = 0$ again, however, in this circumstance, T and T' are at a distance apart and not merged at a point. At higher M_S , the flow in region (1) is getting stronger and stronger, driving the second reflected shock R' down closer to wedge surface and the pressure in regions (4) and (5) pushing the second triple point T' further upstream, thus making $(\chi' - \chi) < 0$. For certain wedge angles, it is possible to have the flow in region (1) be so strong that it presses T' to the wedge surface and $\chi' = 0$ or $(\chi' - \chi) = -\chi$.

4.5 Comparison of Analytical and Experimental Results of Physical Quantities in Regular Reflection

For regular reflection, there is no need for the prediction of χ , because $\chi = 0$ and $\Theta_W' = \Theta_W$, thus only the comparison of the angles δ and ω' with Θ_W as a parameter for frozen and equilibrium-gas analyses is necessary. In fact, a comparison of δ is essentially equivalent to a comparison of ω' since the two are related by

$$\delta + \omega' = 90^\circ + \Theta_W \quad (4.9)$$

as seen from Fig. 37. Comparisons of both angles are shown here. Table 5 presents the measured and analytical results of δ and ω' in RR.

A plot of $(M_S - \delta)$ plane with the experimental results is shown in Fig. 57. The solid lines are the calculated analytical ϕ_w for equilibrium SF_6 . The dashed line is the transition boundary between RR and MR below which no analytical solution of δ in RR exists. The angle δ is seen as an increasing function with increasing Mach number and wedge angle, apart from the low Mach number range at $\phi_w = 45^\circ$. Except for a bit of scattering of data point at $\phi_w = 40^\circ$ and M_S about 4.1, the agreement between experiment and equilibrium-gas analysis is very good. It is seen that for $\phi_w = 45^\circ$, as the Mach number decreases from $M_S = 2.38$, the experimental δ drop more gradually than the analytical values. There are four RR persistent data points shown in the range of $1.5 < M_S < 1.7$ of the same wedge angle. Note that these persistent RR points exist in the range where no two-shock theory solution can be obtained.

Figure 58 shows a plot of the experimental results in the $(M_S - \omega')$ plane with the ϕ_w equilibrium analytical lines drawn in solid. The dashed line is the transition boundary of RR and MR. On the contrary, here the angle ω' is a decreasing function with increasing Mach number and wedge angle, besides the low Mach number range for $\phi_w = 45^\circ$ where an increase in ω' is observed. The same good agreement is found here between experiments and equilibrium gas analytical results. At higher Mach numbers, the analytical lines of ω' are getting closer and begin to level off. It is expected that with ever increasing Mach number or raising the wedge angle ϕ_w closer to 90° , the values of δ and ω' will approach their limits, and the reflected shock will be seen lying closer and closer to the wedge surface. For $M_S \rightarrow \infty$, the pressure in region (1) becomes so large that it forces the reflected shock R to lie on the surface of the wedge in steady flow as well as nonstationary flow, thus $\omega' \rightarrow 0$. This illustrates the fact that the reflection angle ω' is always positive and can be zero for RR, whereas ω' is positive for all gases and can be zero or even negative for some low γ gases in the case of MR [25].

Consider the transition boundary map for frozen SF_6 in Fig. 32(a). All the experimental RR results lie well inside the MR domain. Therefore no two-shock theory solution for frozen-gas case can be obtained and no agreement between experiments and the frozen-gas analysis is seen.

It can be observed from both Figs. 57 and 58 that the behaviour of the analytical δ and ω' for $\phi_w = 45^\circ$ at $M_S < 1.4$ do not have the same trends as in the high M_S range. Refer to Fig. 3 for the flow system and consider ϕ_w is fixed at 45° (ϕ_0 also). The flow deflection angle ϕ_1 and the flow velocity U_1 in region (1) are both increasing functions of U_S or M_S . If M_S and ϕ_0 are given, ϕ_1 and U_1 can be determined. Now, the reflected shock R needs to be positioned so that the flow U_2 is deflected by an angle $\phi_2 = \phi_1$ across the reflected shock R and is parallel to the wall. At $\phi_w = 45^\circ$ and $M_S < 1.4$, increasing M_S will not be able to set up U_1 large enough to meet the boundary condition if ϕ_0 remains constant. To obtain ϕ_2 , one can either fix ϕ_1 and change U_1 or fix U_1 and change ϕ_1 . However, with M_S and ϕ_0 being given, U_1 is fixed and so the angle ϕ_1 has to be increased. R becomes more normal to U_1 and ϕ_2 can now be achieved. As the value of ϕ_1 increases, physically, R propagates further away from the wedge surface, thus decreases δ and increases ω' .

At $M_S > 2.2$ for the same $\alpha_w = 45^\circ$, U_1 increases at a much faster rate than it does at low M_S . U_1 is getting large and R needs to be more tangent to it. As the wave angle ϕ_1 decreases, R lies closer to the wall and as a result increases δ and decreases ω' .

4.6 Pressure Behind Second Triple Point

Three-shock theory has been used to analyze flows around the vicinity of the first triple point and for the prediction of the transition lines between RR and MR. Ben-Dor [11] was the first to analyze the second triple-point system and set up an analytical formulation using three-shock theory and by applying an analogy with the first triple-point system as shown in Fig. 59. However, no known publication has ever shown any numerical results for the physical quantities at the second triple-point system. It is well-known from the transition maps that the most probable type of Mach reflection which will occur at high M_S when RR terminates is a DMR, since the $RR \leftrightarrow DMR$ boundary is the dominant line, especially for $\gamma < 1.4$, that covers a large range of Mach numbers in the $RR \leftrightarrow MR$ region. It is known from experiments that the flow regions behind the first triple point T are uniform, thus the assumption of two uniform states behind T in the analysis of the first triple-point system is well justified. However, the flow regions behind the second triple point T' are not uniform owing to the fact that the second Mach stem M' is nonuniform (for example, see Figures 26 and 28). In order to analyze the second triple-point system numerically, regions (4) and (5) behind T' have to be assumed as two uniform states. Of course, if a numerical solution of the Euler equations is obtained for the entire flow, such an assumption is not necessary. Since the growth of second Mach stem M' contradicts the assumption of uniform states behind T' , therefore the results can only be applied in the vicinity of the second triple point. A method of calculating the second triple point flow fields is given in Appendix A.

Since RR occurs at higher wedge angles than MR for any given flow Mach number in region (0), after the passage of incident I and reflected R shocks, P_2 acquires a high pressure. In MR the highest pressure would be achieved by a DMR since the flow in region (2) becomes supersonic relative to the second triple point T' and a shock wave (second Mach stem M') is required to turn the flow subsonically. Behind the second triple point T' , the pressures are raised to P_4 and P_5 . Hence, it is only necessary to compare the highest pressure attained by RR and DMR, and determine which type of reflection would give the highest pressure.

The highest pressure in RR occurs behind the reflected bow shock R at point E immediately behind the reflection point P as illustrated in Fig. 60(a). In DMR the highest pressure occurs in region F immediately behind the second Mach stem M' and the primary slipstream S as illustrated in Fig. 60(b). Two-shock theory can be used to calculate pressure P_2 in the vicinity of the reflection point P in RR, thus the highest pressure at E takes the value of P_2 . However, three-shock theory can only be used to calculate pressures around the two triple points and not elsewhere. Due to this limitation, only the pressure behind the second triple point in DMR, shown as point G in Fig. 60(b), can be compared with the highest pressure in RR. Although such comparison is not ideal, it does provide a general trend and an approximation of the highest pressure in these two types of reflection. The maximum pressure in DMR occurs on the wedge surface in

region F as indicated by the numerical results of Glaz et al [63], Booen and Needham [64], and Fry et al [65]. The location of maximum pressure on the wedge surface is also consistent with the experimental density contours from the present work.

To study the behaviour of the pressure behind T' in RR and DMR a series of computational runs at a fixed Mach number of $M_s = 6$ ($M_s = 6$ is chosen arbitrarily as it cuts across the RR+DMR transition boundary line; other M_s can also be used instead) over a wide range of Θ_w was done in perfect Ar to avoid any real-gas effects. The results are plotted in Fig. 61. When $\Theta_w \rightarrow 90^\circ$, P_2 approaches the value given by the relation for a normal shock wave reflection $P_{21} = (\alpha + 2 - P_{01}) / (1 + \alpha P_{01})$ where $\alpha = (\gamma + 1) / (\gamma - 1)$ and P_{01} is the strength of the incident shock I. As Θ_w is decreased from 90° , P_2 decreases and reaches a minimum value before it increases to much higher values near the transition angle. Such behaviour can be explained as follows: since the incident shock Mach number is fixed, the velocity component normal to the incident shock I (with respect to the reflection point P) and the pressure P_1 are constant regardless of Θ_w . As Θ_w is decreased, the flow across the incident shock is deflected to a lesser extent and U_1 gets smaller. To satisfy the boundary condition that the flow behind the reflected shock must be parallel to the wall, i.e. $\Theta_2 = \Theta_1$, the wave angle ϕ_1 increases and causes the flow U_1 to become more normal to the reflected shock. The pressure P_2 depends on U_1^n - the normal component of U_1 to the reflected shock. Decreasing U_1 will reduce U_1^n , whereas increasing the wave angle ϕ_1 will increase the value of U_1^n . With U_1 decreasing and ϕ_1 increasing, a minimum value of U_1^n and P_2 would be obtained.

The highest pressure of P_2 in the RR domain is obtained at the transition angle (point X in Fig. 61). Note that this P_2 is even higher than the head-on collision value. With a slight decrease of Θ_w at the transition angle, DMR begins to form. The pressure P_4 and P_5 behind T' right after transition (point Y in Fig. 61) is slightly higher than P_2 in RR just before transition. However, that is not always the case. The pressure P_2 in RR and P_4 and P_5 at point G in DMR (see Fig. 60) at the transition angles for $4 < M_s < 10$ are presented in Table 6. It is shown that at lower M_s , P_2 in RR is larger than P_4 and P_5 in DMR; at higher M_s , P_4 and P_5 in DMR become greater than P_2 in RR. Once DMR is formed, P_4 and P_5 are decreasing functions of Θ_w , as shown in Fig. 61. It is surprising that the flow problem is non-linear, yet P_4 and P_5 in DMR behave almost linearly with Θ_w . The bow shock which terminates on the shock-tube wall near the wedge corner C moves outward at a very much slower rate than the incident shock I. By assuming that the bow shock wave near the corner C is stationary, the stagnation pressure at the corner C can be computed and the results are also presented in Table 6. Although the stagnation pressure at corner C is high, its effects are localized. However, the pressure P_2 in RR, and the pressures P_4 and P_5 in DMR propagate up the wedge along with the incident shock wave. Therefore, the compressive pressure they exert is not a local effect and becomes of major interest. There is a certain range of pressure in which a required pressure can be obtained with more than one Θ_w at point E in RR or at point G in DMR, e.g., point A and B in the RR domain, and point C in the DMR domain all give the same pressure for three different Θ_w .

The following conclusions can be made. Although at lower M_s the pressures P_4 and P_5 in DMR are lower than P_2 in RR, the highest pressure in region F is higher than P_4 and P_5 at point G as indicated by experimental and numerical results. Therefore, the highest pressure in DMR can be higher

than the highest pressure in RR. At higher M_s , P_4 and P_5 at point G in DMR are already higher than P_2 in RR, thus the highest pressure in region F in DMR is even higher than the highest pressure in RR. It can be stated with confidence that with a strong incident shock wave ($M_s > 5$ for $\gamma = 5/3$) the highest pressure is achievable by a DMR. With weaker incident shock wave ($M_s < 5$ for $\gamma = 5/3$) it can only be surmised that the highest pressure can be attained by a DMR as well. Data from complete numerical simulations will provide better answers. Due to the uncertainty of how good the analysis of the second triple-point system predicts the flow properties behind T' , comparisons of the experimental pressure history of DMR in air [26] with the numerical simulation by Glaz et al [63] and with the numerical results of this work are given by Hu and Shirouzu [31]. From a practical point of view more field testing and shock tube experiments should be directed at studying the transition regime between RR and DMR to verify the numerical results obtained from the computer program developed during the course of this work.

4.7 Application of Reflections in Pseudo-Stationary Flow to the Interaction of Spherical Blast Waves with Planar Surface

With the knowledge of blast wave flows and oblique-shock-wave reflections gained in recent years, it is now possible to trace the path of a spherical blast wave that is detonated in free air on a transition map in the $(M_s - \theta_w)$ plane. It is true that in an explosion, the flow field near the charge is very complicated and very difficult to analyze. But when the blast wave front outruns the fireball and starts to interact with the ground surface, the flow can be reasonably treated as two-dimensional at any instant of time. Hence, the analysis used here for pseudo-stationary flow can be applied to the interaction of a blast wave with a planar surface. It becomes possible to predict the type of reflection, the incident shock Mach number and the corresponding wedge angle that a target at a known distance away from the explosion may encounter. This information is of great value to researchers and experimenters in the field.

The flow field associated with a free-air explosion is shown in Fig. 62. To demonstrate how the study of oblique-shock-wave reflection can be applied to the interaction of a spherical blast wave with a planar surface, a typical charge of TNT detonated in free air off a perfect reflecting planar surface in a standard atmosphere of 760 torr (101.33 kPa) and 288 K is considered. Sadek and Gottlieb [66] obtained an equation to describe the spherical blast-wave front in a surface explosion for a 1 kg TNT. Their results were reduced to the case of a 1 kg TNT height-of-burst (HOB) explosion using Sach's scaling laws with a geometric factor of 2 for a perfect reflecting surface. The scaled equation would then give the shock radius r from the charge C as a function of the shock arrival time t_s . For a given HOB h , the ground range x and the corresponding wedge angle θ_w are related geometrically with the radial distance r in the case of RR. However, in the case of MR, the computation of the ground range x and the corresponding wedge angle θ_w are complicated by the introduction of the first-triple-point trajectory. Since the Mach stem M usually occurs bulged out in real explosions or large-scale field-tests, the ground range x is simply estimated by assuming that the Mach stem M is an arc of a circle with the radius being the distance between zero ground range and the first triple point T , which is shown as r_M in Fig. 62(b). Details of the method of calculating the blast-wave-trajectory path are given in Appendix A. Since

the spherical-blast-wave flow can be treated as two-dimensional at any instant of time, the merging of the two triple points at the RR \leftrightarrow DMR transition boundary applies, and there exists a blast-wave-trajectory path which crosses the point where all three transition lines meet on the transition map.

The computed results of the blast-wave-front trajectory path for various HOB cases are presented graphically in Fig. 63 on the transition map in the ($M_s - \theta_w$) plane. Contours of ground range x and height of the first triple point Y_T are also plotted. Height of burst h and ground range x in the figure are scaled to the weight of the charge W and the ambient pressure P_0 by introducing a non-dimensionalized scaling factor of $(W/W_0 \cdot P_0/P)^{-1/3}$ where W_0 and P_0 are taken as 1 kg and 1 atm, respectively. Height of the first triple point Y_T is also shown as a fraction of the HOB h .

Assume that a charge of 1 kg TNT is detonated at a HOB of 1 m with the ambient pressure being 1 atm. When the blast wave front just hits the planar surface directly under the charge, $x = 0$ m, $\theta_w = 90^\circ$ and $M_s = 4.4$. As the blast wave front propagates outward further, the incident shock wave collides with and is reflected off the planar surface resulting in regular reflection RR, which occurs up to a ground range of $x = 0.82$ m and M_s diminishes to 3.5. When DMR just occurs, the height of the first triple point Y_T is zero at the transition line and DMR continues in the range of $0.82 \text{ m} < x < 1.19 \text{ m}$. At the transition point from DMR to CMR, M_s decreases to 2.9, Y_T increases to 0.022 m, and CMR occurs in the ground range of $1.19 \text{ m} < x < 1.9 \text{ m}$. At the termination of CMR, M_s drops to 2.3, Y_T grows to almost 0.1 m, and SMR begins to form at a ground range $x > 1.9 \text{ m}$.

With a given charge weight W , ambient pressure P , HOB h and ground range x , one can read off from Fig. 63, M_s , θ_w , Y_T and the type of reflection that is going to occur. With M_s and θ_w , the flow properties behind the blast wave front at the ground range x can be predicted using the numerical results presented in tabular and graphical forms by Hu and Shirouzu [31]. These results are essential in predicting the dynamic response of structures in the vicinity of a blast wave. For a different explosive charge and height of burst, a different blast-wave-front path has to be constructed on the transition map in order to predict what type of reflection would occur for a certain ground range. Figure 63 also shows the effect of changing the height of burst and charge weight on the blast wave front trajectory path. The trajectories of 12 different HOB cases are calculated and plotted on the same figure to show the effect of changing the HOB.

There are several interesting points that can be made about Fig. 63. First, increasing the HOB for a given charge will decrease the incident shock wave Mach number M_s of the blast wave as it interacts with the planar surface. Second, let Δx be defined as the difference between the ground ranges when a specific type of reflection begins and terminates. For example, on the scaled line $h = 1.0$ m, x increases from 0 m for $\theta_w = 90^\circ$ to 0.82 m when $\theta_w = 50^\circ$ at the RR \leftrightarrow DMR line and $\Delta x = 0.82$ m. In RR region, Δx increases with HOB. For example, at a scaled h of 0.7 m, $\Delta x = 0.58$ m; at $h = 1.00$ m, $\Delta x = 0.82$ m; at $h = 2.00$ m, $\Delta x = 1.7$ m and at $h = 3.00$ m, $\Delta x = 2.8$ m. However, in both DMR and CMR regions, there is a HOB h which gives an optimum Δx . This is because at small h , Δx increases with HOB. As h becomes large, the domains of both DMR and CMR diminish and so their Δx also

decrease. For instance, in the DMR region, at a scaled h of 0.5 m, $\Delta x = (0.83-0.41) = 0.42$ m; at $h = 0.80$ m, $\Delta x = (1.10-0.67) = 0.43$ m; at $h = 0.9$ m, $\Delta x = (1.15-0.75) = 0.40$ m; at $h = 1.00$ m, $\Delta x = (1.19-0.82) = 0.37$ m and at $n = 1.25$, $\Delta x = (1.28-1.01) = 0.27$ m. Due to the increasing and decreasing behaviour of Δx , a maximum Δx exists in the DMR domain and this also applies to the CMR domain. In the SMR region, Δx is an increasing function of HOB since the SMR domain enlarges at low M_s . Third, theoretically, the interaction of a blast wave front with the ground may result in three possible series of reflections: (1) $RR \rightarrow DMR \rightarrow CMR \rightarrow SMR$, (2) $RR \rightarrow CMR \rightarrow SMR$, or (3) $RR \rightarrow SMR$. However, experiments have shown that the CMR to DMR transition line approaches the SMR to CMR transition line and merges at a single point on the RR termination boundary (see Sec. 4.3) as shown by the dotted line in Fig. 63. Therefore, only two possible series of reflection can occur: (1) $RR \rightarrow DMR \rightarrow CMR \rightarrow SMR$ or (2) $RR \rightarrow SMR$. The second possibility occurs if the incident shock Mach number of the blast wave $M_s < 1.52$ when RR terminates. Fourth, from Fig. 63 it can be seen that owing to the steepness of the $RR \leftrightarrow SMR$ transition line compared to the blast-wave paths in the $(M_s - \theta_w)$ plane, RR cannot reoccur when $M_s > 1$. Lastly, increasing the charge weight W has the same effect as decreasing the HOB, whereas an increase in the ambient pressure P has results similar to increasing the HOB.

The method used in this work to study the interaction of a blast wave with a planar surface for the explosive TNT can be used for other types of explosives in predicting the blast-wave-front-trajectory path on the transition map, and in calculating the corresponding ground range and height of the first triple point for the HOB case. For a spherical flow, the growth of the reflected spherical shock cannot be determined from a two-dimensional analysis. Consequently, the second triple point T' trajectory is indeterminate using this analysis. It would be important to verify these results experimentally in the laboratory or in field tests.

5.0 CONCLUSIONS

An experimental and numerical investigation was made of pseudo-stationary oblique-shock-wave reflections in polyatomic SF_6 gas. The domains and transition boundaries between the various types of reflection (RR, SMR, CMR and DMR) were established in the $(M_s - \theta_w)$ and $(M_s - \theta'_w)$ planes for both frozen and vibrational equilibrium SF_6 . The transition boundaries predicted on the basis of an equilibrium flow agreed well with the experimental results. The new criterion [16] $\delta > 90^\circ$ was verified by the present work that it is an additional necessary condition for the transition from SMR to CMR. However, RR persists beyond the boundary line determined by the detachment criterion. A start has been made to explain the persistence of RR in terms of the induced viscous boundary layer on the wedge surface [16,23]. A continuation of the investigation of the persistence of RR with its boundary-layer-displacement effect is presently under way [43].

Experimental results show that the CMR to DMR transition line approaches the SMR to CMR transition line near the RR termination boundary and they eventually merge at the RR boundary. The fact that the ratio l^*/L^* approaches zero as the wedge angle comes near to the RR termination boundary was also verified in this experimental study. A better analytical method to determine the position of the kink or the second triple point near the RR boundary is required in order to predict accurately the behaviour of the merging of the three transition lines at a single point on the RR

termination line. It is also clear from the present study that improved analytical criteria must be found for the SMR→CMR→DMR transitions in order to have better agreement between analysis and the experimental data. Since it is difficult to distinguish CMR from DMR in an interferogram, a shadowgram is required in the transition region of CMR and DMR to provide additional evidence.

Several infinite-fringe interferograms of the density fields were evaluated and their wall-density distribution were plotted. It has been shown that the use of higher initial pressure enhanced the details and accuracy of the isopycnics significantly. The present experimental results provide invaluable data for computational fluid dynamicists in testing and improving the numerical codes that predict various flow properties in nonstationary oblique shock-wave reflections.

The comparison of experimental results in Ar, air, CO₂ and SF₆ at $\Theta_w = 20^\circ$ and $M_s = 3.4 \pm 0.2$ substantiate the claims of Lee and Glass [25] that the transition boundaries are shifted downwards and the reflection angle ω' decreases with decreasing γ . There are higher density jumps across the Mach stem, slipstream and the bow shock or lambda shocks at the wedge corner for smaller γ . The shock-wave boundary-layer interaction (lambda-shock interaction), rolling up of the slipstream and curving of the Mach stem are all prominent with a lower γ gas, because a stronger shock can be produced by a lower γ gas as given by the strong shock wave limit $\rho/\rho_0 \rightarrow (\gamma+1)/(\gamma-1)$ and the density ratio is large as $\gamma \rightarrow 1$.

The large differences in the analytical physical quantities between frozen and equilibrium SF₆ permit a definitive conclusion regarding which model is valid. Comparisons of the fundamental angles δ and ω' , and Θ_w' ($\Theta_w' = \Theta_w + \chi'$) in Mach reflection using Θ_w as the parameter, and the comparisons of δ and ω' in RR using Θ_w as the parameter, justified the validity of the equilibrium SF₆ analysis. The measured angles δ , ω' , χ and χ' in MR are also compared with the analytical results using Θ_w as the parameter. Nonetheless, the agreement with the equilibrium-gas analysis using Θ_w is secondary to that of using Θ_w' , due to the inadequate prediction of χ , by assuming that the Mach stem is straight and perpendicular to the wedge surface. An improved method of predicting χ which takes into account the Mach-stem curvature and the interaction of the bow shock wave with the reflected shock wave is necessary. It has been verified that the reflection angle ω' is positive in RR and can be positive or negative in MR [25]. The angle between the first and second-triple-point trajectories ($\chi - \chi'$) was discussed and a DMR with $\chi' = 0$ was obtained experimentally.

The second triple-point system was analyzed numerically for argon ($\gamma = 5/3$) at $M_s = 6$ over a large range of Θ_w . When the transition of RR to DMR occurs, the pressure behind the second triple point T' (regions 4 and 5) in DMR is almost equal to the pressure behind the reflection point P (region 2) in RR. Numerical results show that for a given Mach number, the highest pressure is achieved by means of a DMR, and not by a RR. This may be because the flow in region (0) has to experience two or three shock waves before it can reach region (4) or (5). Pressure histories as functions of M_s and Θ_w obtained by numerical simulation at the RR→DMR transition boundary are required to substantiate the present experimental and analytical results.

A typical explosive charge (TNT) detonated at various heights-of-burst above a perfect reflecting planar surface in air was considered. The variations of the incident shock Mach number of the spherical-blast-wave front as it decays and the corresponding wedge angle were plotted on a transition map in the ($M_s - \theta_w$) plane. It shows that all four types of shock-wave reflection can occur in a free air explosion. However, if the height of burst is increased past a certain limit, only two types of shock-wave reflection, RR and SMR, can occur.

The collision of a Mach stem from a spherical explosion with various types of buildings is of practical importance. This is presently being simulated at UTIAS [62] by investigating the collisions of the three types of Mach reflection with a 90° ramp fixed to the wedge surface.

References

1. Glass, I. I., "Shock Waves and Man", University of Toronto Institute for Aerospace Studies, Toronto 1974.
2. Carpenter, H. J., Brode, H. L., "Height of Burst Blast at High Overpressure", 4th Int. Symp. on Military Applications of Blast Simulations, England, 1974.
3. Mach, E., "Über den Verlauf der Funkenwellen in der Ebene und im Raume", Oesterreichische akademie der wissenschaften, Mathematisch-naturwissenschaftliche klasse, sitzungsberichte, abt. II, v. 78, pp. 819-38, 1878.
4. von Neuman, J., "Oblique Reflection of Shocks", Explosives Research Report No.12, Navy Dept., Bureau of Ordinance Re2c, Washington, D.C., 1943.
5. von Neumann, J., "Refraction, Interaction, and Reflection of Shock Waves", NAVORD Report 203-45, Navy Dept., Bureau of Ordinance, Washington, D.C., 1945.
6. Bleakney, W., Taub, A.H., "Interaction of Shock Waves", Rev. Mod. phys., Vol. 21, p. 584, 1949.
7. Smith, L.G., "Photographic Investigation of the Reflection of Plane Shocks in Air", OSRD Report No.6271, or NORC Report No.A2350, 1945.
8. White, D.R., "An Experimental Survey of the Mach Reflection of Shock Waves", Tech. Report II-10, Dept. of Phys., Princeton Univ., 1951.
9. Taub, A. H., "Refraction of Plane Shock Waves", Rev. Mod. Phys., Vol. 21, p.51, 1947.
10. Henderson, L. F., Lozzi, A., "Experiments on Transition of Mach Reflection", J. Fluid Mech., Vol. 68, p. 139, 1975.
11. Ben-Dor, G., "Regions and Transitions of Nonstationary Oblique Shock-Wave Diffractions in Perfect and Imperfect Gases", Univ. of Toronto, UTIAS Report No. 232, 1978.
12. Hornung, H. G., Kychakoff, G., "Transition from Regular to Mach Reflexion of Shock Waves in Relaxing Gases", Proc. 11th International Shock Tube Symp., 1977.
13. Ben-Dor, G., Glass, I. I., "Domains and Boundaries of Non-Stationary Oblique Shock-Wave Reflexions. 1. Diatomic Gas", J. Fluid Mech., Vol. 92, p. 459, 1979.
14. Ben-Dor, G., Glass, I. I., "Domains and Boundaries of Non-Stationary Oblique Shock-Wave Reflexions. 2. Monatomic Gas", J. Fluid Mech., Vol. 96, p. 735, 1980.

15. Law, C. K., Glass, I. I., "Diffraction of Strong Shock Waves by a Sharp Compressive Corner", CASI Trans., Vol. 4, No. 1, 1971.
16. Shirouzu, M., Glass, I. I., "An Assessment of Recent Results on Pseudo-Stationary Oblique-Shock-Wave Reflections", Univ. of Toronto, UTIAS Report No. 264, 1982.
17. Ben-Dor, G., Takayama, K., Kawauchi, T., "The Transition from Regular to Mach Reflexion and from Mach to Regular Reflexion in Truly Non-Stationary Flows", J. Fluid Mech., Vol. 100, p. 147, 1980.
18. Itoh, S., Okazaki, N., Itaya, M., "On the Transition Between Regular and Mach Reflection in Truly Non-Stationary Flows", J. Fluid Mech., Vol. 108, p. 383, 1981.
19. Jones, D. M., Martin, P. M. E., Thornhill, C. K., "A Note on the Pseudo-Stationary Flow Behind a Strong Shock Diffracted or Reflected at a corner", Proc. Roy. Soc. sec. A, Vol. 209, p. 238, 1951.
20. Bazhenova, T. V., Fokeev, V. P., Gvozdeva, L. G., "Regions of Various Forms of Mach Reflection and its Transition to Regular Reflection", Acta Astronautica 3, p. 131, 1976.
21. Gvozdeva, L. G., Bazhenova, T. V., Predvoditeleva, O. A., Fokeev, V. P., "Mach Reflection of Shock Waves in Real Gases", Astronautica Acta, Vol. 14, p. 503, 1969.
22. Naboko, I. M., Bazhenova, T. V., Nemkov, R. G., "Experimental Studies of the Parameters of the Flow Behind a Shock Wave Moving in Relaxing Gas", Astronautica Acta, Vol. 14, p. 497, 1969.
23. Hornung, H. G., Taylor, J. R., "Transition from Regular to Mach Reflection of Shock Waves. Part 1. The Effect of Viscosity in the Pseudosteady Case", J. Fluid Mech., Vol. 123, p. 143, 1982.
24. Ando, S., "Pseudo-Stationary Oblique Shock-Wave Reflection in Carbon Dioxide - Domain and Boundaries", UTIAS Tech. Note No. 231, 1981.
25. Lee, J. H., Glass, I. I., "Domains and Boundaries of Pseudo-Stationary Oblique Shock-Wave Reflections in Air", UTIAS Report No. 262, 1982.
26. Deschambault, R. L., "Nonstationary Oblique-Shock-Wave Reflections in Air", Univ. of Toronto, UTIAS Report No. 270, 1983.
27. Molder, S., "Head-on Interaction of Oblique Shock Waves", Univ. of Toronto, UTIAS Tech. Note No. 38, 1960.
28. Weynants, R. R., "An Experimental Investigation of Shock-Wave Diffraction Over Compressive and Expansive Corners", Univ. of Toronto, UTIAS Tech. Note No. 126, 1968.
29. Ben-Dor, G., Glass, I. I., "Nonstationary Oblique Shock-Wave Reflections: Actual Isopycnics and Numerical Experiments", AIAA J., Vol. 16, p. 1146, 1978.

30. Ando, S., Glass, I. I., "Domains and Boundaries of Pseudostationary Oblique-Shock-Wave Reflections in Carbon Dioxide", 7th Int. Symp. of Military Applications of blast Simulation, 1981.
31. Hu, T. C. J., Shirouzu, M., "Tabular and Graphical Solutions of Regular and Mach Reflections in Pseudo-Stationary Frozen and Vibrational-Equilibrium Flows", Univ. of Toronto, UTIAS Report No. 283, 1985.
32. Deschambault, R. L., Glass, I. I., "An Update on Nonstationary Oblique Shock-Wave Reflections, Actual Isopycnics and Numerical Experiments", J. Fluid Mech., Vol. 131, p. 27, 1983.
33. Courant, R., Friedrichs, K. O., "Supersonic Flow and Shock Waves", Interscience Pub. New York, 1948.
34. Gvozdeva, L. G., Bazhenova, T. V., Predvoditeleva, O. A., Fokeev, V. P., "Pressure and Temperature at the Wedge Surface for Mach Reflection of Strong Shock Waves", Astronautica Acta, Vol. 15, p. 503, 1970.
35. Semenov, A. N., Syschikova, M. P., Berezkina, M. K., "Experimental Investigation of Peculiarities of Mach Reflection", Sov. Phys. Tech. Phys., Vol. 15, p. 795, 1970.
36. Boyer, A. G., "Design, Instrumentation and Performance of the UTIAS 4 in x 7 in Hypervelocity Shock Tube", Univ. of Toronto, UTIAS Report No. 158, 1971.
37. Bristow, M. P. F., "An Experimental Determination of the Polarizability for Singly Ionized Argon", Univ. of Toronto, UTIAS Report No. 158, 1971.
38. Ben-Dor, G., Whitten, B. T., "Interferometric Techniques and Data Evaluation Methods for the UTIAS 10 cm x 18 cm Hypervelocity Shock Tube", Univ. of Toronto, UTIAS Tech. Note No. 208, 1979.
39. Hall, J. G., "The Design and Performance of a 9 inch Plate Mach-Zehnder Interferometer", Univ. of Toronto, UTIAS Report No. 27, 1954.
40. Gvozdeva, L. G., Predvoditeleva, O. A., "Experimental Investigation of Mach Reflection of Shock waves with Velocities of 1000 - 3000 m/sec in Carbon Dioxide Gas, Nitrogen and Air", Soviet Physics, Doklady, Vol. 10, No. 8, 1966.
41. Kawamura, K., Saito, H., "Reflection of Shock Waves - 1 Pseudo-Stationary Case", J. Phys. Soc. Japan, Vol. 11, No. 5, p. 584, 1956.
42. Matsuo, K., Aoki, T., Kondo, N., Harada, T., "An Experimental Study on Shock-Wave Reflections on an Inclined Wall", Preprint of the Symp. on Shock Waves, p. 96, 1981 (in Japanese).
43. Wheeler, J. M., "An Interferometric Investigation of the Regular to Mach Reflection Transition Boundary in Pseudo-Stationary Flow", Univ. of Toronto, UTIAS M.A.Sc. Thesis (to be published).

44. Bertrand, B. P., "Measurement of Pressure in Mach Reflection of Strong Shock Waves in a Shock Tube", BRL Memo. Rep. No. 2196, 1972.
45. Merritt, D. L., "Mach Reflection on a Cone", AIAA J., Vol. 6, p. 1208, 1968.
46. Shirouzu, M., [private communication], 1982.
47. Law, C. K., "Diffraction of Strong Shock Waves by a Sharp Compressive Corner", Univ. of Toronto, UTIAS Tech. Note No. 150, 1970.
48. Frost, L. S., Liebermann, R. W., "Composition and Transport Properties of SF_6 and Their Use in a Simplified Enthalpy Flow Arc Model", IEEE Proc., Vol. 59, p. 474, 1971.
49. Carswell, A. J., Cloutier, G. G., "Supersonic Plasma Streams Seeded with Electronegative Gases", Phys. Fluids, Vol. 7, p. 602, 1964.
50. Emery, A. F., Ashurst, W. T., "Development of a Technique for Testing with Heavy Gases in Explosive-Driven Shock Tubes", SCL-DR-67-49, 1967.
51. Glass, I. I., Hall, J. G., "Handbook of Supersonic Aerodynamics, Sec. 18, Shock Tubes", NAVORD Rep. 1488, Vol. 6, 1959.
52. Frie, W., "Berechnung der Gaszusammensetzung und der Materialfunktionen von SF_6 ", Z. Phys., Vol. 201, p. 269, 1967.
53. O'Connor, C. L., "Thermal Relaxation of Vibrational States in SF_6 ", J. Acous. Soc. A, Vol. 26, p. 361, 1954.
54. Hodgkinson, T. B., North, A. M., "Ultrasonic Relaxation in Gaseous Sulphur Hexafluoride and Tungsten Hexafluoride", J. Chem. Soc. A, p. 885, 1968.
55. Holmes, R., Stott, M. A., "Temperature Dependence of Vibrational Relaxation Times in Cyclopropane, Ethylene and Sulphur Hexafluoride", Brit. J. Appl. Phys., Vol. 1, p. 1331, 1968.
56. Breshears, W. D., Blair, L. S., "Vibrational Relaxation in Polyatomic Molecules: SF_6 ", J. Chem. Phys., Vol. 59, p. 5824, 1973.
57. Camac, M., "CO₂ Relaxation Processes in Shock Waves", Avco-Everett Res. Lab. Res. Rep. No. 194, 1964.
58. Lutz, R. W., Kiefer, J. H., "Structure of the Vibrational Relaxation Zone of Shock Waves in Oxygen", Phy. Fluid, Vol. 9, p. 1638, 1966.
59. Breshears, W. D., Bird, P. F., "Effect of Oxygen Atoms on the Vibrational Relaxation of Nitrogen", J. Chem. Phys., Vol. 48, No. 10, p. 4768, 1968.
60. Wilkins, R. L., "Thermodynamics of SF_6 and its Decomposition and Oxidation Products", Aerospace Rep. No. TR-0158(3240-20)-19, 1968.

61. Herzberg, Gerhard, "Molecular Spectra and Molecular Structure", Vol. 1, D. Van Nostrand Co. Inc., New York, 1960.
62. Li, J. C., Glass, I. I., [private communication], 1983.
63. Glaz, H. M., Colella, P., Glass, I. I., Deschambault, R. L., "An Numerical and Experimental Study of Pseudo-Stationary Oblique Shock-Wave Reflections in Argon and Air", Univ. of Toronto, UTIAS Report No. 285 (to be published).
64. Booen, W. B., Needham, C. E., "Two Dimensional HULL Code simulation of Complex and Double Mach Reflections", AFWL Tech. No. NTE-TN-81-U01 (1980).
65. Fry, M., Titsworth, J., Kuhl, A., Book, D., Boris, J., Picone, M., "Shock Capturing Using Flux-Corrected Transport Algorithms with Adaptive Gridding", 13th International Symposium on Shock Tubes and Waves (1981).
66. Sadek, H. S. I., Gottlieb, J. J., "Initial Decay of Flow Properties of Planar, Cylindrical and Spherical Blast Waves", Univ. of Toronto, UTIAS Tech. Note No. 244, 1983.
67. Mirels, H., "Mach Reflection Flow Fields Associated With Strong Shocks", (paper to be published), 1984.

Table 1 Gladstone-Dale Constants for Several Gases [26]	
Gas	K (m ³ /kg)
air	2.274×10^{-4} ($\lambda = 5896 \text{ \AA}$)
Ar	1.574×10^{-4} ($\lambda = 6943 \text{ \AA}$)
Ar	1.629×10^{-4} ($\lambda = 3472 \text{ \AA}$)
CO ₂	2.266×10^{-4} ($\lambda = 5896 \text{ \AA}$)
H ₂	7.870×10^{-5} ($\lambda = 5896 \text{ \AA}$)
He	2.017×10^{-4} ($\lambda = 5896 \text{ \AA}$)
N ₂	2.376×10^{-4} ($\lambda = 6943 \text{ \AA}$)
N ₂	2.460×10^{-4} ($\lambda = 3472 \text{ \AA}$)
N	3.280×10^{-4} ($\lambda = 6943 \text{ \AA}$)
N	3.310×10^{-4} ($\lambda = 3472 \text{ \AA}$)
SF ₆	1.182×10^{-4} ($\lambda = 5896 \text{ \AA}$)
SO ₂	2.344×10^{-4} ($\lambda = 5896 \text{ \AA}$)

Table 2

Initial Conditions for SF₆ Experiments

EXP	θ_w (deg)	M_s	Type	P_0 (torr)	P_0 (kPa)	P_3 (psi)	P_3 (kPa)	T_0 (°C)	Driver
1	47	1.82	RR	149.00	19.9	49.0	337.8	23.1	CO2
110	45	1.25	RR	267.00	35.6	14.0	96.5	24.3	CO2
111	45	1.43	-	177.80	23.7	14.4	99.3	22.4	CO2
112	45	1.52	RR	130.58	17.4	13.8	95.1	23.0	CO2
113	45	1.64	RR	88.80	11.8	13.6	93.8	23.8	CO2
122	45	1.64	RR	88.80	11.8	13.5	93.1	23.6	CO2
123	45	1.66	RR	144.00	19.2	22.0	151.7	23.7	CO2
118	45	1.81	DMR	101.20	13.5	22.0	151.7	23.9	CO2
117	45	1.91	DMR	78.00	10.4	21.6	148.9	23.3	CO2
120	45	2.07	RR	55.80	7.4	21.3	146.9	25.2	CO2
119	45	2.11	RR	50.50	6.7	20.3	140.0	24.9	CO2
115	45	2.17	RR	44.08	5.9	20.5	141.3	24.1	CO2
114	45	2.25	RR	35.20	4.7	19.6	135.1	23.8	CO2
116	45	2.38	RR	29.00	3.9	19.6	135.1	24.5	CO2
121	45	8.22	-	19.10	2.5	300.0	2068.4	24.6	HE
17	42	1.52	SMR	157.00	20.9	25.0	172.4	23.2	CO2
18	42	1.54	SMR	138.00	18.4	21.5	148.2	23.9	CO2
19	42	1.73	CMR	226.00	30.1	50.2	346.1	24.6	CO2
20	42	1.84	CMR	176.50	23.5	48.7	335.8	25.3	CO2
21	42	1.93	DMR	143.00	19.1	48.5	334.4	25.4	CO2
30	42	2.73	DMR	14.20	1.9	20.0	137.9	24.3	CO2

Table 2 (continued)

Initial Conditions for SF₆ Experiments

EXP	θ_w (deg)	M _s	Type	P ₀ (torr)	P ₀ (kPa)	P ₃ (psi)	P ₃ (kPa)	T ₀ (°C)	Driver
29	42	2.74	-	14.00	1.9	20.0	137.9	24.2	CO2
31	42	2.82	RR	23.85	3.2	35.0	241.3	24.3	CO2
108	42	2.84	DMR	42.90	5.7	63.5	437.8	24.0	CO2
107	42	3.00	DMR	31.97	4.3	64.5	444.7	24.4	CO2
76	42	3.01	DMR	70.90	9.5	64.5	444.7	24.2	CO2
25	42	3.02	RR	70.90	9.5	137.5	948.0	25.8	CO2
28	42	3.10	-	109.00	14.5	145.0	999.7	24.7	CO2
77	42	3.10	-	49.00	6.5	110.0	758.4	23.8	CO2
27	42	3.12	-	78.70	10.5	125.0	861.8	24.8	CO2
106	42	3.14	DMR	25.86	3.4	62.0	427.5	24.0	CO2
74	42	3.14	DMR	50.00	6.7	115.0	792.9	23.2	CO2
24	42	3.16	RR	55.80	7.4	136.0	937.7	25.8	CO2
26	42	3.20	-	56.00	7.5	132.0	910.1	25.8	CO2
105	42	3.21	DMR	23.30	3.1	62.0	427.5	23.9	CO2
23	42	3.21	RR	50.00	6.7	136.0	937.7	25.2	CO2
22	42	3.26	RR	49.00	6.5	136.0	937.7	25.6	CO2
78	42	3.26	DMR	49.00	6.5	136.0	937.7	24.2	CO2
75	42	3.27	DMR	49.00	6.5	135.0	930.8	23.5	CO2
104	42	3.43	DMR	16.73	2.2	63.5	437.8	24.2	CO2
79	42	3.44	-	37.00	4.9	136.5	941.1	22.8	CO2
85	42	3.45	DMR	17.35	2.3	60.5	417.1	23.7	CO2

Table 2(continued)

Initial Conditions for SF₆ Experiments

EXP	θ_w (deg)	M_s	Type	P_0 (torr)	(kPa)	P_3 (psi)	(kPa)	T_0 (°C)	Driver
86	42	3.45	DMR	15.95	2.1	61.5	424.0	23.4	CO2
100	42	3.47	RR	15.95	2.1	61.5	424.0	22.8	CO2
84	42	3.48	DMR	15.95	2.1	62.5	430.9	23.3	CO2
81	42	3.57	DMR	23.87	3.2	105.0	723.9	24.7	CO2
32	42	3.63	RR	11.70	1.6	59.5	410.2	24.5	CO2
83	42	3.64	RR	11.65	1.6	62.5	430.9	26.0	CO2
103	42	3.65	DMR	12.10	1.6	64.5	444.7	23.9	CO2
80	42	3.66	DMR	27.00	3.6	136.5	941.1	22.9	CO2
102	42	3.66	DMR	12.18	1.6	65.5	451.6	22.0	CO2
109	42	3.67	RR	11.65	1.6	63.5	437.8	24.1	CO2
82	42	3.73	RR	10.34	1.4	61.5	424.0	25.4	CO2
16	42	5.63	RR	4.20	0.6	317.5	2189.1	23.6	CO2
101	42	8.23	RR	3.70	0.5	59.5	410.2	24.6	HE
11	40	1.49	SMR	166.80	22.2	25.5	175.8	25.1	CO2
12	40	1.53	SMR	138.00	18.4	23.0	158.6	24.8	CO2
10	40	1.72	CMR	226.00	30.1	49.5	341.3	24.9	CO2
143	40	1.90	CMR	46.18	6.2	12.5	86.2	24.6	CO2
8	40	1.94	DMR	143.00	19.1	49.0	337.8	24.6	CO2
2	40	2.07	DMR	100.00	13.3	47.0	324.1	23.7	CO2
177	40	2.08	DMR	30.05	4.0	14.0	96.5	24.0	CO2
176	40	2.15	DMR	56.20	7.5	27.0	186.2	24.2	CO2

Table 2 (continued)

Initial Conditions for SF₆ Experiments

EXP	θ_w (deg)	M _S	Type	P ₀ (torr)	P ₀ (kPa)	P ₃ (psi)	P ₃ (kPa)	T ₀ (°C)	Driver
148	40	3.77	-	7.12	0.9	45.8	315.8	23.9	CO2
146	40	3.80	DMR	11.43	1.5	44.7	308.2	21.5	AIR
4	40	3.88	-	19.20	2.6	138.5	954.9	23.5	CO2
5	40	3.90	-	27.50	3.7	140.5	968.7	23.8	AIR
147	40	3.99	DMR	16.48	2.2	142.0	979.1	23.2	CO2
145	40	4.07	RR	4.42	0.6	44.0	303.4	24.1	CO2
144	40	4.07	RR	4.89	0.7	47.0	324.1	24.5	CO2
9	40	4.14	RR	12.00	1.6	126.5	872.2	25.3	CO2
3	40	4.15	-	19.15	2.6	172.0	1185.9	23.5	CO2
149	40	4.15	RR	3.98	0.5	45.5	313.7	24.2	CO2
179	40	4.18	RR	12.30	1.6	139.0	958.4	24.8	CO2
6	40	4.21	RR	11.95	1.6	135.5	934.2	23.0	CO2
178	40	4.22	RR	5.60	0.7	69.5	479.2	25.4	CO2
7	40	4.56	RR	7.50	1.0	133.0	917.0	24.2	CO2
14	40	5.35	-	21.39	2.9	138.0	951.5	25.2	HE
15	40	5.74	-	5.00	0.7	188.5	1299.7	25.4	AIR
13	40	6.59	-	14.70	2.0	144.0	992.8	25.2	HE
60	37	1.43	SMR	114.00	15.2	11.8	81.4	24.8	SF6
59	37	1.49	SMR	78.50	10.5	10.5	72.4	23.4	CO2
33	37	1.52	SMR	150.70	20.1	22.0	151.7	24.1	CO2
34	37	1.61	SMR	112.50	15.0	20.5	141.3	24.0	CO2

Table 2 (continued)

Initial Conditions for SF₆ Experiments

EXP	θ_w (deg)	M_s	Type	P_0 (torr)	P_0 (kPa)	P_3 (psi)	P_3 (kPa)	T_0 (°C)	Driver
35	37	1.70	CMR	91.00	12.1	20.6	142.0	23.6	CO ₂
36	37	1.86	CMR	62.45	8.3	20.0	137.9	23.5	CO ₂
37	37	2.07	CMR	42.65	5.7	19.8	136.5	23.3	CO ₂
61	37	2.13	DMR	47.80	6.4	45.0	310.3	24.3	CO ₂
41	37	2.18	DMR	35.20	4.7	19.0	131.0	23.7	CO ₂
63	37	2.23	DMR	50.70	6.8	45.0	310.3	23.4	HE
42	37	2.31	DMR	28.90	3.9	19.3	133.1	24.0	CO ₂
39	37	4.07	-	4.00	0.5	319.0	2199.4	23.3	AIR
67	37	4.14	-	17.60	2.3	177.5	1223.8	24.2	CO ₂
68	37	4.14	-	17.60	2.3	179.0	1234.2	24.2	CO ₂
62	37	4.14	DMR	17.60	2.3	179.0	1234.2	24.9	CO ₂
69	37	4.15	-	17.60	2.3	180.5	1244.5	24.4	CO ₂
70	37	4.18	-	11.95	1.6	132.5	913.6	24.6	CO ₂
59	37	4.18	-	11.95	1.6	132.5	913.6	23.3	CO ₂
64	37	4.20	DMR	11.97	1.6	133.0	917.0	23.7	CO ₂
58	37	4.21	-	11.95	1.6	133.5	920.4	24.2	CO ₂
71	37	4.22	DMR	11.95	1.6	136.0	937.7	24.4	CO ₂
56	37	5.19	DMR	4.19	0.6	285.5	1968.5	23.8	CO ₂
73	37	5.52	DMR	5.42	0.7	364.0	2509.7	23.7	CO ₂
57	37	5.55	DMR	4.18	0.6	277.0	1909.8	23.4	CO ₂
43	37	5.78	DMR	5.00	0.7	182.5	1258.3	24.3	N ₂

Table 2 (continued)

Initial Conditions for SF₆ Experiments

EXP	θ_w (deg)	M _S	Type	P ₀ (torr)	P ₀ (kPa)	P ₃ (psi)	P ₃ (kPa)	T ₀ (°C)	Driver
171	37	5.95	DMR	2.82	0.4	378.0	2606.2	24.1	CO ₂
172	37	6.48	DMR	15.10	2.0	94.0	648.1	24.3	HE
40	37	6.73	-	3.95	0.5	310.5	2140.8	23.4	AIR
66	37	6.76	-	4.18	0.6	316.0	2178.7	25.1	CO ₂
53	37	7.65	-	3.63	0.5	59.0	406.8	23.5	HE
54	37	7.66	DMR	4.17	0.6	288.0	1985.7	23.5	CO ₂
55	37	7.72	DMR	4.17	0.6	281.0	1937.4	22.7	CO ₂
50	37	7.75	-	3.63	0.5	60.8	419.2	22.8	HE
65	37	7.89	DMR	4.21	0.6	306.0	2109.8	24.5	CO ₂
72	37	7.96	DMR	11.05	1.5	184.0	1268.6	23.4	HE
173	37	7.99	DMR	6.36	0.8	92.0	634.3	24.8	HE
174	37	8.11	-	6.36	0.8	94.0	648.1	24.5	HE
52	37	8.34	-	3.00	0.4	59.5	410.2	23.0	HE
51	37	8.45	DMR	3.00	0.4	62.5	430.9	23.0	HE
38	37	8.81	-	3.95	0.5	316.0	2178.7	23.3	AIR
124	30	1.76	SMR	116.70	15.6	22.0	151.7	23.9	CO ₂
126	30	1.81	CMR	101.20	13.5	22.0	151.7	23.6	CO ₂
128	30	1.93	CMR	78.00	10.4	22.4	154.4	23.7	CO ₂
127	30	2.19	CMR	44.10	5.9	21.5	148.2	23.5	CO ₂
125	30	2.30	CMR	23.80	3.2	20.5	141.3	23.8	CO ₂
142	30	2.35	CMR	17.95	2.4	12.5	86.2	22.9	CO ₂
140	30	2.59	DMR	11.17	1.5	12.1	83.4	24.2	CO ₂

Table 2 (continued)

Initial Conditions for SF₆ Experiments

EXP	θ_w (deg)	M_s	Type	P_0 (torr)	P_0 (kPa)	P_3 (psi)	P_3 (kPa)	T_0 (°C)	Driver
141	30	2.72	DMR	8.70	1.2	12.0	82.7	24.4	CO ₂
131	20	2.08	SMR	30.00	4.0	12.5	86.2	23.3	CO ₂
135	20	2.11	SMR	29.40	3.9	12.1	83.4	23.8	CO ₂
129	20	2.13	CMR	50.50	6.7	21.5	148.2	23.2	CO ₂
130	20	2.83	DMR	13.30	1.8	20.6	142.0	23.6	CO ₂
132	20	2.84	DMR	13.30	1.8	20.5	141.3	23.6	CO ₂
133	20	2.97	DMR	10.70	1.4	20.7	142.7	23.8	CO ₂
134	20	3.02	DMR	9.70	1.3	20.2	139.3	23.6	CO ₂
136	20	3.15	DMR	7.90	1.1	20.2	139.3	24.0	CO ₂
137	20	3.51	DMR	4.58	0.6	20.6	142.0	24.0	CO ₂
138	20	3.76	DMR	7.39	1.0	46.5	320.6	23.6	CO ₂
139	20	4.08	DMR	4.82	0.6	47.5	327.5	23.8	CO ₂
175	10	2.60	SMR	11.17	1.5	12.1	83.4	25.1	CO ₂
150	10	2.86	CMR	13.33	1.8	23.0	158.6	23.1	CO ₂
151	10	3.00	CMR	9.70	1.3	21.6	148.9	23.8	CO ₂
153	10	3.14	CMR	7.95	1.1	23.1	159.3	24.3	CO ₂
154	10	3.45	DMR	11.43	1.5	46.5	320.6	23.9	CO ₂
155	10	3.65	DMR	12.08	1.6	63.0	434.4	24.3	CO ₂
152	10	3.73	DMR	10.42	1.4	62.5	430.9	24.2	CO ₂
156	10	4.06	DMR	6.44	0.9	63.0	434.4	24.0	CO ₂
157	10	4.25	DMR	4.95	0.7	64.5	444.7	23.9	CO ₂

Table 2 (continued)

Initial Conditions for SF₆ Experiments

EXP	θ_w (deg)	M_s	Type	P_0 (torr)	P_0 (kPa)	P_3 (psi)	P_3 (kPa)	T_0 (°C)	Driver
158	10	4.43	DMR	10.18	1.4	159.0	1096.3	24.6	CO ₂
169	4	3.37	SMR	13.55	1.8	49.5	341.3	24.1	CO ₂
161	4	3.47	CMR	15.95	2.1	67.5	465.4	23.5	CO ₂
160	4	3.74	CMR	10.40	1.4	64.0	441.3	23.5	CO ₂
159	4	4.05	CMR	5.00	0.7	49.0	337.8	23.2	CO ₂
170	4	4.28	CMR	4.98	0.7	67.5	465.4	24.1	CO ₂
166	4	4.36	CMR	10.15	1.4	151.0	1041.1	24.3	CO ₂
162	4	5.50	CMR	5.42	0.7	388.0	2675.2	23.8	CO ₂
165	4	5.94	-	6.70	0.9	383.0	2640.7	24.1	AIR
164	4	5.94	-	2.78	0.4	386.0	2661.4	25.1	CO ₂
163	4	6.01	-	13.52	1.8	63.5	437.8	24.9	HE
167	4	6.26	-	17.50	2.3	95.5	658.4	24.6	HE
168	4	6.65	-	15.10	2.0	101.0	696.4	23.9	HE

Note : Where data are blank, unstable shock fronts
or no interferograms are obtained.

Table 3

Comparison for MR in SF₆ at fixed ω'_w

Exp	θ_w	M_s	Type	Experiments			Equilibrium Analysis			Frozen Analysis		
				δ	ω'	χ	δ	ω'	χ	δ	ω'	χ
118	45	1.81	DMR	110.6	25.3	0.7	111.2	24.5	1.7	100.7	35.0	2.9
117	45	1.91	DMR	116.5	19.9	0.9	115.8	20.1	1.9	104.7	31.3	3.0
17	42	1.52	SMR	90.8	42.8	1.1	91.1	42.1	2.0	81.9	51.2	4.0
18	42	1.54	SMR	90.8	42.2	1.0	91.7	41.3	2.1	82.4	50.6	4.1
19	42	1.73	CMR	103.3	29.7	1.2	103.4	29.8	2.6	92.8	40.5	4.2
20	42	1.84	CMR	108.0	25.0	1.9	109.6	24.3	2.4	98.3	35.6	4.0
21	42	1.93	DMR	113.0	20.6	1.9	113.6	20.3	2.6	101.5	32.3	4.2
30	42	2.73	DMR	129.1	4.2	1.3	133.5	-0.3	2.9	117.5	15.8	5.0
108	42	2.84	DMR	135.4	-2.0	1.6	135.5	-2.0	2.8	119.4	14.3	4.9
107	42	3.00	DMR	138.7	-4.6	1.6	137.9	-4.3	2.7	121.2	12.9	4.9
76	42	3.01	DMR	138.9	-5.0	1.6	138.1	-4.4	2.7	121.3	12.4	4.9
106	42	3.14	DMR	139.6	-5.8	1.8	139.8	-6.0	2.6	122.6	11.1	4.9
105	42	3.21	DMR	140.2	-6.5	1.7	140.5	-6.8	2.6	123.0	10.6	5.0
85	42	3.45	DMR	140.3	-6.8	1.5	142.8	-9.3	2.5	124.7	8.8	5.1
11	40	1.49	SMR	84.8	46.9	1.7	84.9	46.7	2.9	76.0	55.7	5.3
12	40	1.53	SMR	88.1	43.5	1.6	87.8	43.7	3.0	78.1	53.2	5.4
10	40	1.72	CMR	100.0	32.0	2.0	100.5	31.5	3.1	89.3	42.6	5.1
143	40	1.90	CMR	110.1	22.5	2.6	110.1	22.5	3.0	97.8	34.8	4.8
8	40	1.94	DMR	111.6	21.0	2.6	111.9	20.7	3.1	99.5	33.1	4.9
2	40	2.07	DMR	116.2	16.0	2.7	116.8	15.9	3.1	103.7	29.1	4.9
177	40	2.08	DMR	117.2	15.8	3.0	117.4	15.5	3.0	104.3	28.7	4.8

Table 3 (continued)

Comparison for MR in SF₆ at fixed θ'_w

Experiments				Equilibrium Analysis				Frozen Analysis							
Exp	θ_w	M_s	Type	δ	ω'	X	θ_w''	δ	ω'	X	θ_w''	δ	ω'	X	θ_w''
176	40	2.15	DMR	121.2	13.8	2.7	45.0	119.4	13.3	3.1	46.1	105.9	26.9	5.0	51.1
146	40	3.80	DMR	143.0	-13.5	1.4	40.6	143.9	-12.6	2.8	39.4	123.9	7.5	5.8	43.0
147	40	3.99	DMR	144.8	-13.5	1.3	40.2	145.4	-14.1	2.7	39.2	124.9	6.5	5.8	42.7
60	37	1.43	SMR	77.0	52.5	2.5	-	74.8	54.6	4.7	63.1	65.6	63.9	8.2	68.0
59	37	1.49	SMR	78.6	50.5	2.5	-	79.6	49.9	4.6	60.1	69.7	59.8	7.8	65.3
33	37	1.52	SMR	82.0	47.5	2.5	-	82.2	47.3	4.5	58.5	71.9	57.6	7.7	63.9
34	37	1.61	SMR	88.4	41.2	2.6	-	88.8	40.8	4.4	54.8	78.0	51.6	7.2	60.4
35	37	1.70	CMR	94.3	35.7	3.0	43.3	95.0	35.0	4.1	52.2	83.6	46.4	6.6	57.9
36	37	1.86	CMR	102.8	28.2	3.3	44.1	104.2	26.1	4.0	48.4	91.5	38.9	6.3	54.0
37	37	2.07	CMR	112.0	19.3	3.3	43.5	112.7	17.5	4.0	45.0	98.8	31.6	6.3	50.5
61	37	2.13	DMR	115.5	15.5	4.0	43.5	116.0	15.0	3.7	45.0	101.7	29.3	5.9	50.2
41	37	2.18	DMR	116.4	14.6	4.0	43.0	117.8	13.2	3.7	44.4	103.2	27.8	6.0	49.5
63	37	2.23	DMR	118.9	12.1	4.0	43.1	119.4	11.6	3.7	43.9	104.5	26.5	6.0	49.0
42	37	2.31	DMR	120.0	10.9	4.0	43.0	121.5	9.5	3.7	43.3	106.3	24.7	6.0	48.3
62	37	4.14	DMR	145.0	-15.5	2.6	38.7	142.5	-15.5	3.4	37.4	123.2	6.5	6.4	41.1
64	37	4.20	DMR	145.3	-15.5	2.8	38.6	145.5	-15.7	2.9	37.6	123.6	6.2	6.4	41.1
71	37	4.22	DMR	145.1	-15.4	2.7	38.4	145.6	-15.9	2.9	37.5	123.5	6.2	6.4	41.0
56	37	5.19	DMR	150.0	-18.7	1.3	37.2	149.3	-21.0	2.7	35.8	124.6	3.7	6.8	39.0
73	37	5.52	DMR	151.3	-21.0	3.3	37.8	151.9	-21.7	2.4	37.7	128.2	2.1	6.1	40.7
57	37	5.55	DMR	151.1	-20.2	2.5	37.7	151.5	-22.0	2.5	36.9	127.1	2.3	6.4	39.9
43	37	5.78	DMR	153.8	-24.8	2.1	37.1	152.0	-22.8	2.4	36.6	127.1	2.0	6.5	39.5

Table 3 (continued)

Comparison for MR in SF₆ at fixed θ'_w

Experiments				Equilibrium Analysis				Frozen Analysis							
Exp	θ_w	M_s	Type	δ	ω'	χ	θ''_w	δ	ω'	χ	θ''_w	δ	ω'	χ	θ''_w
171	37	5.95	DMR	153.0	-24.9	1.7	37.1	152.2	-23.5	2.4	36.1	126.8	1.9	6.6	39.1
172	37	6.48	DMR	151.0	-20.1	2.0	38.4	153.7	-24.8	2.3	36.3	128.1	1.0	6.5	39.3
72	37	7.96	DMR	152.5	-23.7	1.8	37.0	156.2	-27.4	2.1	36.2	129.0	-0.3	6.5	38.7
173	37	7.99	DMR	153.7	-23.7	2.0	37.5	156.4	-27.3	2.1	36.5	129.4	-0.4	6.4	38.9
124	30	1.76	SMR	89.0	37.4	6.4	-	89.7	36.7	6.5	48.7	75.9	50.5	10.3	55.5
126	30	1.81	CMR	92.4	33.6	6.5	41.6	92.9	33.6	6.3	47.4	78.7	47.8	10.0	54.1
128	30	1.93	CMR	98.3	29.0	6.5	42.7	98.9	27.5	6.1	44.6	84.0	42.5	9.5	51.2
127	30	2.19	CMR	110.5	16.3	6.7	39.5	110.5	16.2	5.5	40.8	93.5	33.2	8.9	46.8
125	30	2.30	CMR	113.8	14.0	6.7	39.5	113.9	12.8	5.3	39.7	96.6	30.2	8.6	45.7
142	30	2.35	CMR	114.1	12.0	6.6	39.1	115.3	11.2	5.3	39.1	97.6	29.0	8.7	45.0
140	30	2.59	DMR	121.0	5.7	6.2	37.7	121.0	5.2	5.1	37.2	101.7	24.5	8.7	42.8
141	30	2.72	DMR	124.0	2.8	6.5	37.3	124.5	2.1	4.8	36.9	104.5	21.9	8.4	42.2
131	20	2.08	SMR	90.1	31.5	10.8	-	89.8	30.9	9.7	38.9	68.3	52.5	16.5	48.1
135	20	2.11	SMR	90.6	30.3	10.3	-	89.7	30.6	10.0	38.2	67.1	53.2	17.2	47.6
129	20	2.13	CMR	92.8	28.0	10.6	32.7	91.7	28.8	9.6	37.9	69.1	51.4	16.6	47.0
130	20	2.83	DMR	115.0	5.9	10.2	31.2	114.4	5.7	7.3	31.1	88.1	32.0	13.3	38.2
132	20	2.84	DMR	115.8	6.0	10.2	31.3	114.7	5.5	7.2	31.2	88.2	32.0	13.3	38.1
133	20	2.97	DMR	117.4	3.4	10.4	31.0	118.0	2.4	6.8	30.8	91.2	29.2	12.8	37.4
134	20	3.02	DMR	119.0	2.8	10.2	30.9	118.8	1.5	6.8	30.6	91.1	29.0	12.9	37.0
136	20	3.15	DMR	122.2	-2.0	10.2	30.0	121.1	-0.9	6.5	30.0	93.3	26.9	12.6	36.4
137	20	3.51	DMR	127.0	-5.0	10.4	29.4	127.1	-6.7	5.8	29.4	98.5	21.9	11.8	35.2

Table 3 (continued)															
Comparison for MR in SF ₆ at fixed θ'_w															
			Experiments				Equilibrium Analysis				Frozen Analysis				
Exp	θ_w	M_s	Type	δ	ω'	χ	θ''_w	δ	ω'	χ	θ''_w	δ	ω'	χ	θ''_w
138	20	3.76	DMR	128.7	-8.2	10.2	28.4	130.0	-9.8	5.5	28.9	100.3	19.9	11.6	34.4
139	20	4.08	DMR	130.3	-9.1	9.6	27.7	132.4	-12.7	5.3	28.1	100.8	18.8	11.8	33.4
175	10	2.60	SMR	84.9	29.2	13.9	-	84.0	29.9	13.4	29.5	-	-	-	-
150	10	2.86	CMR	93.7	21.0	13.7	25.0	93.3	20.3	11.7	27.0	-	-	-	-
151	10	3.00	CMR	96.6	17.4	13.5	25.1	97.2	16.3	11.1	26.1	-	-	-	-
153	10	3.14	CMR	100.0	13.2	13.1	24.7	99.4	13.7	10.8	25.1	-	-	-	-
154	10	3.46	DMR	107.6	6.5	13.6	24.7	108.6	4.9	9.3	24.2	-	-	-	-
155	10	3.65	DMR	109.5	3.6	12.8	22.9	109.4	3.4	9.2	23.2	-	-	-	-
152	10	3.73	DMR	111.0	2.7	12.4	22.6	109.5	2.9	9.2	22.8	-	-	-	-
156	10	4.06	DMR	115.0	-1.9	12.7	22.5	115.9	-3.1	8.2	22.4	-	-	-	-
157	10	4.25	DMR	116.0	-4.0	12.2	21.2	117.3	-4.9	8.0	21.8	-	-	-	-
158	10	4.43	DMR	120.0	-7.1	12.5	21.6	119.8	-7.3	7.7	21.8	-	-	-	-
169	4	3.37	SMR	85.8	24.8	15.9	-	87.2	22.7	13.3	22.8	-	-	-	-
161	4	3.47	CMR	87.0	22.0	15.5	19.8	87.5	22.0	13.2	22.2	-	-	-	-
160	4	3.74	CMR	90.0	19.0	14.9	19.6	90.4	18.5	12.6	20.9	-	-	-	-
159	4	4.05	CMR	93.6	14.6	14.0	18.5	91.1	16.8	12.4	19.6	-	-	-	-
170	4	4.28	CMR	93.2	14.3	13.5	18.0	93.0	14.5	12.0	18.8	-	-	-	-
166	4	4.36	CMR	96.0	11.6	13.8	18.0	97.7	10.2	11.2	18.8	-	-	-	-
162	4	5.50	CMR	105.6	0.0	12.3	16.3	104.1	2.3	9.9	16.5	-	-	-	-

Note: Where data are blank, no measurements or analytical solutions are obtained.

Table 4

Comparison for MR in SF₆ at fixed θ_w

Exp	θ_w	M_s	Type	Experiments				Equilibrium Analysis				Frozen Analysis			
				δ	w'	X	X'	δ	w'	X	X'	δ	w'	X	X'
118	45	1.81	DMR	110.6	25.3	0.7	2.5	112.4	24.0	1.5	9.0	103.2	33.9	2.2	13.8
117	45	1.91	DMR	116.5	19.9	0.9	2.0	116.8	19.8	1.7	7.5	107.0	30.3	2.4	12.3
17	42	1.52	SMR	90.8	42.8	1.1	-	92.2	41.5	1.7	17.8	85.6	49.1	2.7	22.6
18	42	1.54	SMR	90.8	42.2	1.0	-	93.2	40.6	1.7	17.3	86.4	48.3	2.7	22.2
19	42	1.73	CMR	103.3	29.7	1.2	5.2	105.1	29.0	2.1	11.8	96.5	38.6	3.1	17.1
20	42	1.84	CMR	108.0	25.0	1.9	6.0	110.2	24.0	2.3	9.8	100.8	34.4	3.2	15.1
21	42	1.93	DMR	113.0	20.6	1.9	4.6	114.4	20.0	2.4	8.2	104.3	31.0	3.4	13.6
30	42	2.73	DMR	129.1	4.2	1.3	1.7	134.9	-0.3	2.6	2.5	121.3	14.6	4.0	7.8
108	42	2.84	DMR	135.4	-2.0	1.6	1.4	136.5	-2.0	2.6	2.2	122.7	13.4	4.0	7.4
107	42	3.00	DMR	138.7	-4.6	1.6	0.8	138.8	-4.2	2.5	1.7	124.4	11.7	4.1	7.0
76	42	3.01	DMR	138.9	-5.0	1.6	1.0	138.9	-4.4	2.5	1.7	124.5	11.6	4.1	6.9
106	42	3.14	DMR	139.6	-5.8	1.8	1.2	140.4	-5.9	2.5	1.4	125.7	10.4	4.1	6.6
105	42	3.21	DMR	140.2	-6.5	1.7	1.2	141.2	-6.7	2.5	1.3	126.2	9.9	4.1	6.5
85	42	3.45	DMR	140.3	-6.8	1.5	0.8	143.6	-9.2	2.4	0.9	128.1	8.1	4.2	6.0
11	40	1.49	SMR	84.8	46.9	1.7	-	86.6	45.7	2.4	20.8	80.7	52.9	3.5	25.7
12	40	1.53	SMR	88.1	43.5	1.6	-	89.8	42.6	2.4	19.1	83.3	50.2	3.6	24.1
10	40	1.72	CMR	100.0	32.0	2.0	6.9	102.0	30.8	2.7	13.1	93.4	40.4	3.8	18.7
143	40	1.90	CMR	110.1	22.5	2.6	6.0	110.5	22.4	2.9	9.6	100.6	33.4	4.0	15.3
8	40	1.94	DMR	111.6	21.0	2.6	5.8	112.5	20.5	2.9	8.9	102.3	31.8	4.1	14.6
2	40	2.07	DMR	116.2	16.0	2.7	5.0	117.3	15.7	3.0	7.3	106.3	27.9	4.2	13.0
177	40	2.08	DMR	117.2	15.8	3.0	5.5	117.5	15.5	3.0	7.2	106.5	27.7	4.2	12.9

Table 4 (continued)

Comparison for MR in SF₆ at fixed θ_w

Exp	θ_w	M_s	Type	Experiments				Equilibrium Analysis				Frozen Analysis			
				δ	ω'	χ	χ'	δ	ω'	χ	χ'	δ	ω'	χ	χ'
176	40	2.15	DMR	121.2	13.8	2.7	5.0	119.9	13.1	3.0	6.4	108.5	25.8	4.2	12.1
146	40	3.80	DMR	143.0	-13.5	1.4	0.6	145.0	-12.4	2.6	0.7	128.3	6.4	4.7	6.1
147	40	3.99	DMR	144.8	-13.5	1.3	0.2	146.4	-13.9	2.5	0.5	129.2	5.5	4.7	5.9
60	37	1.43	SMR	77.0	52.5	2.5	-	78.0	52.6	3.6	26.2	73.0	59.0	5.0	30.8
59	37	1.49	SMR	78.6	50.5	2.5	-	82.5	48.1	3.6	23.3	76.8	55.2	5.0	28.4
33	37	1.52	SMR	82.0	47.5	2.5	-	85.0	45.6	3.6	21.8	78.9	53.1	5.0	27.1
34	37	1.61	SMR	88.4	41.2	2.6	-	91.4	39.3	3.7	18.2	84.1	47.9	5.0	23.9
35	37	1.70	CMR	94.3	35.7	3.0	6.3	96.6	34.1	3.7	15.6	88.5	43.6	5.0	21.5
36	37	1.86	CMR	102.8	28.2	3.3	7.1	105.1	25.7	3.8	11.7	95.5	36.7	5.1	17.9
37	37	2.07	CMR	112.0	19.3	3.3	6.5	113.7	17.1	3.8	8.5	102.6	29.7	5.2	14.7
61	37	2.13	DMR	115.5	15.5	4.0	6.5	115.6	15.1	3.8	7.8	104.2	28.1	5.2	14.0
41	37	2.18	DMR	116.4	14.6	4.0	6.0	117.4	13.4	3.8	7.2	105.6	26.6	5.3	13.4
63	37	2.23	DMR	118.9	12.1	4.0	6.1	119.0	11.8	3.8	6.7	106.9	25.3	5.3	12.9
42	37	2.31	DMR	120.0	10.9	4.0	6.0	121.2	9.6	3.7	6.0	108.7	23.6	5.3	12.2
62	37	4.14	DMR	145.0	-15.5	2.6	1.7	145.2	-15.4	2.9	0.7	127.0	9.4	5.4	6.6
64	37	4.20	DMR	145.3	-15.5	2.8	1.6	145.6	-15.7	2.9	0.7	127.3	9.1	5.4	6.5
71	37	4.22	DMR	145.1	-15.4	2.7	1.4	145.7	-15.9	2.9	0.7	127.4	9.1	5.4	6.5
56	37	5.19	DMR	150.0	-18.7	1.3	0.2	150.3	-20.7	2.5	0.0	130.3	2.1	5.4	5.9
73	37	5.52	DMR	151.3	-21.0	3.3	0.8	151.4	-21.9	2.5	-0.1	130.9	1.5	5.4	5.7
57	37	5.55	DMR	151.1	-20.2	2.5	0.7	151.5	-22.0	2.5	-0.1	131.0	1.4	5.4	5.7
43	37	5.78	DMR	153.8	-24.8	2.1	0.1	152.2	-22.8	2.4	-0.2	131.4	1.0	5.4	5.6

Table 4 (continued)

Comparison for MR in SF₆ at fixed θ_w

Experiments				Equilibrium Analysis				Frozen Analysis							
Exp	θ_w	M_s	Type	δ	ω'	X	X'	δ	ω'	X	X'	δ	ω'	X	X'
171	37	5.95	DMR	153.0	-24.9	1.7	0.1	152.6	-23.3	2.4	-0.2	131.7	0.8	5.4	5.6
172	37	6.48	DMR	151.0	-20.1	2.0	1.4	153.9	-24.6	2.3	-0.3	132.4	0.1	5.4	5.4
72	37	7.96	DMR	152.5	-23.7	1.8	0.0	156.4	-27.3	2.1	-0.5	133.6	-1.2	5.4	5.2
173	37	7.99	DMR	153.7	-23.7	2.0	0.5	156.4	-27.3	2.1	-0.5	133.6	-1.2	5.4	5.2
124	30	1.76	SMR	89.0	37.4	6.4	-	89.9	36.6	6.4	18.8	81.6	46.7	8.3	25.7
126	30	1.81	CMR	92.4	33.6	6.5	11.6	92.6	33.7	6.4	17.3	83.8	44.4	8.2	24.4
128	30	1.93	CMR	98.3	29.0	6.5	12.7	98.4	27.8	6.2	14.5	88.4	39.7	8.1	21.7
127	30	2.19	CMR	110.5	16.3	6.7	9.5	108.8	17.0	5.9	10.1	96.7	31.2	7.9	17.5
125	30	2.30	CMR	113.8	14.0	6.7	9.5	112.1	13.7	5.7	9.0	99.3	28.6	7.9	16.3
142	30	2.35	CMR	114.1	12.0	6.6	9.1	113.7	12.0	5.7	8.4	100.6	27.3	7.8	15.7
140	30	2.59	DMR	121.0	5.7	6.2	7.7	119.7	5.7	5.4	6.6	105.2	22.6	7.7	13.8
141	30	2.72	DMR	124.0	2.8	6.5	7.3	122.4	2.9	5.3	5.8	107.2	20.4	7.7	13.0
131	20	2.08	SMR	90.1	31.5	10.8	-	88.0	32.2	10.2	18.8	77.9	45.1	13.0	27.6
135	20	2.11	SMR	90.6	30.3	10.3	-	89.2	30.9	10.1	18.1	78.8	44.1	12.9	27.1
129	20	2.13	CMR	92.8	28.0	10.6	12.7	90.1	30.0	10.0	17.7	79.4	43.4	12.9	26.6
130	20	2.83	DMR	115.0	5.9	10.2	11.2	109.6	8.7	8.3	9.8	93.7	28.1	11.7	18.8
132	20	2.84	DMR	115.8	6.0	10.2	11.3	109.7	8.6	8.3	9.8	93.7	28.0	11.7	18.7
133	20	2.97	DMR	117.4	3.4	10.4	11.0	112.1	5.9	8.0	9.0	95.4	26.2	11.6	17.9
134	20	3.02	DMR	119.0	2.8	10.2	10.9	113.0	4.9	7.9	8.7	96.0	25.6	11.6	17.7
136	20	3.15	DMR	122.2	-2.0	10.2	10.0	115.2	2.5	7.7	8.1	97.5	23.9	11.4	17.0
137	20	3.51	DMR	127.0	-5.0	10.4	9.4	120.2	-3.1	7.2	6.7	100.8	20.3	11.2	15.6

Table 4 (continued)

Comparison for MR in SF₆ at fixed θ_w

Exp	θ_w	M_s	Type	Experiments				Equilibrium Analysis				Frozen Analysis			
				δ	ω'	χ	χ'	δ	ω'	χ	χ'	δ	ω'	χ	χ'
138	20	3.76	DMR	128.7	-8.2	10.2	8.4	123.2	-6.3	6.8	6.0	102.7	18.3	11.0	14.9
139	20	4.08	DMR	130.3	-9.1	9.6	7.7	126.2	-9.8	6.5	5.3	104.6	16.2	10.9	14.2
175	10	2.60	SMR	84.9	29.2	13.9	-	82.8	30.9	13.7	19.5	71.5	46.4	17.9	30.3
150	10	2.86	CMR	93.7	21.0	13.7	15.0	88.5	24.3	12.8	16.7	75.2	42.1	17.3	27.7
151	10	3.00	CMR	96.6	17.4	13.5	15.1	91.1	21.3	12.4	15.6	76.9	40.2	17.1	26.6
153	10	3.14	CMR	100.0	13.2	13.1	14.7	93.5	18.5	12.0	14.6	78.4	38.5	16.8	25.7
154	10	3.46	DMR	107.6	6.5	13.6	14.7	98.1	13.1	11.2	12.8	81.2	35.2	16.4	24.0
155	10	3.65	DMR	109.5	3.6	12.8	12.9	100.6	10.2	10.8	12.0	82.6	33.5	16.2	23.2
152	10	3.73	DMR	111.0	2.7	12.4	12.6	101.5	9.1	10.6	11.7	83.2	32.9	16.1	22.9
156	10	4.06	DMR	115.0	-1.9	12.7	12.5	105.0	5.1	10.1	10.6	85.1	30.7	15.8	21.9
157	10	4.25	DMR	116.0	-4.0	12.2	11.2	106.7	3.0	9.8	10.1	86.0	29.6	15.7	21.4
158	10	4.43	DMR	120.0	-7.1	12.5	11.6	108.3	1.2	9.5	9.6	86.8	28.7	15.5	21.0
169	4	3.37	SMR	85.8	24.8	15.9	-	78.3	30.7	15.0	18.9	67.3	47.5	20.8	31.2
161	4	3.47	CMR	87.0	22.0	15.5	15.8	79.5	29.2	14.8	18.3	68.0	46.6	20.6	30.7
160	4	3.74	CMR	90.0	19.0	14.9	15.6	82.4	25.6	14.1	16.8	69.6	44.6	20.2	29.4
159	4	4.05	CMR	93.6	14.6	14.0	14.5	85.2	22.1	13.4	15.5	71.2	42.7	19.9	28.3
170	4	4.28	CMR	93.2	14.3	13.5	14.0	87.1	19.8	12.9	14.7	72.1	41.5	19.7	27.6
166	4	4.36	CMR	96.0	11.6	13.8	14.0	87.8	19.0	12.8	14.5	72.4	41.2	19.6	27.4
162	4	5.50	CMR	105.6	0.0	12.3	12.3	94.3	10.8	11.2	11.9	75.5	37.4	18.9	25.4

Note: Where data are blank, no measurements or analytical solutions are obtained.

Table 5

Comparison for RR in SF₆

Exp	θ_w	M_s	Experiments		Equilibrium Analysis	
			δ	ω'	δ	ω'
1	47.	1.82	104.3	32.7	103.9	33.1
110	45.	1.25	88.7	46.3	87.9	47.1
112	45.	1.52	91.0	44.0	-	-
113	45.	1.64	93.8	41.2	-	-
122	45.	1.64	93.5	41.5	-	-
123	45.	1.66	94.5	40.2	-	-
120	45.	2.07	98.8	36.2	-	-
119	45.	2.11	100.0	35.0	-	-
115	45.	2.17	102.0	34.0	-	-
114	45.	2.25	103.7	31.3	102.8	32.2
116	45.	2.38	106.6	28.4	106.4	28.6
31	42.	2.82	102.0	30.0	-	-
25	42.	3.02	103.0	29.0	-	-
24	42.	3.16	105.0	27.0	-	-
23	42.	3.21	106.0	25.0	103.1	28.9
22	42.	3.26	106.0	24.2	105.5	26.5
100	42.	3.47	109.4	22.6	109.0	23.0
83	42.	3.64	112.0	21.0	111.0	21.0
109	42.	3.67	111.2	20.8	111.2	20.8
82	42.	3.73	111.2	20.8	111.8	20.2

Table 5 (continued)						
Comparison for RR in SF ₆						
Exp	θ_w	M_s	Experiments		Equilibrium Analysis	
			δ	ω'	δ	ω'
16	42.	5.63	121.0	11.0	119.8	12.2
101	42.	8.23	124.2	7.8	123.0	9.0
145	40.	4.07	104.8	25.2	-	-
144	40.	4.07	107.3	21.8	-	-
9	40.	4.14	105.0	24.8	105.5	24.5
149	40.	4.15	106.4	24.0	105.6	24.4
179	40.	4.18	107.0	23.0	106.3	23.7
6	40.	4.21	106.0	24.0	106.7	23.3
178	40.	4.22	107.0	23.0	106.9	23.1
7	40.	4.56	110.0	20.0	110.3	19.7

Note : Where data are blank, no analytical solutions exist.

Table 6

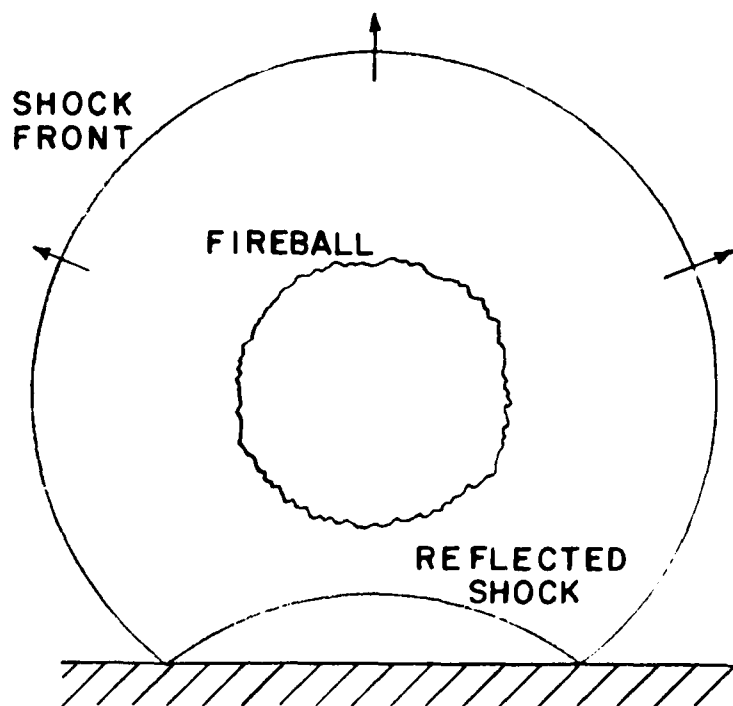
Numerical Results of Pressure
at RR \neq DMR Transition Boundary

for $\gamma = 5/3$ at $P_0 = 15$ torr (2 kPa) , $T_0 = 300$ K

M_∞	Type	Region	Pressure *		$\Delta \%$	Stagnation Pressure at Corner C	
			torr	(kPa)		torr	(kPa)
4	RR	2	1547.1	(206.3)	-5.51	1283.6	(171.1)
	DMR	4,5	1461.9	(194.9)			
5	RR	2	2570.0	(342.6)	-0.43	2595.7	(346.1)
	DMR	4,5	2558.9	(341.2)			
6	RR	2	3831.1	(510.8)	1.82	4311.1	(574.8)
	DMR	4,5	3900.7	(520.1)			
7	RR	2	5328.5	(710.4)	3.03	6401.5	(853.5)
	DMR	4,5	5490.1	(732.0)			
8	RR	2	7058.6	(941.1)	3.80	8850.9	(1180.0)
	DMR	4,5	7326.9	(976.8)			
9	RR	2	9018.6	(1202.4)	4.35	11650.0	(1553.2)
	DMR	4,5	9410.8	(1254.7)			
10	RR	2	11212.1	(1494.8)	4.72	14793.6	(1972.3)
	DMR	4,5	11741.1	(1565.4)			

* Pressures for RR and DMR correspond to point X and point Y in Figure 61, respectively.

a) Regular Reflection



b) Mach Reflection

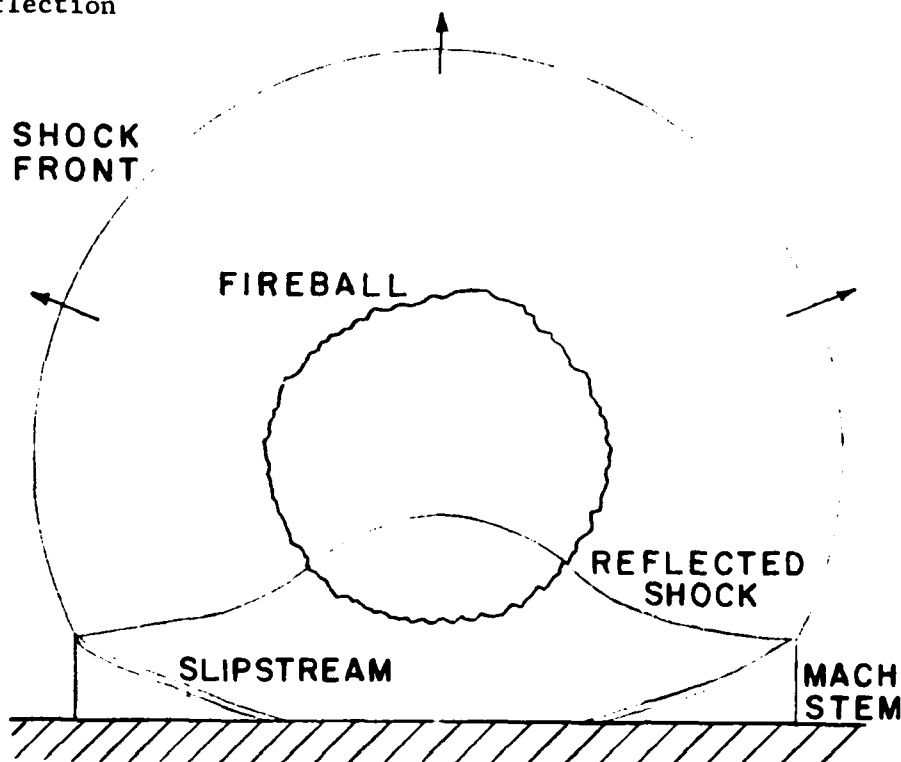
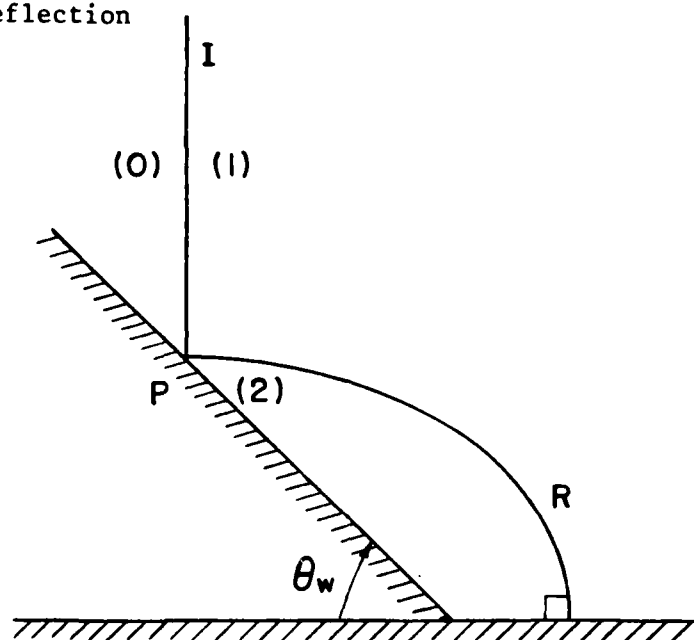


Fig. 1 Interaction of spherical explosion with planar surface.

a) Regular Reflection
(RR)



b) Single-Mach
Reflection (SMR)

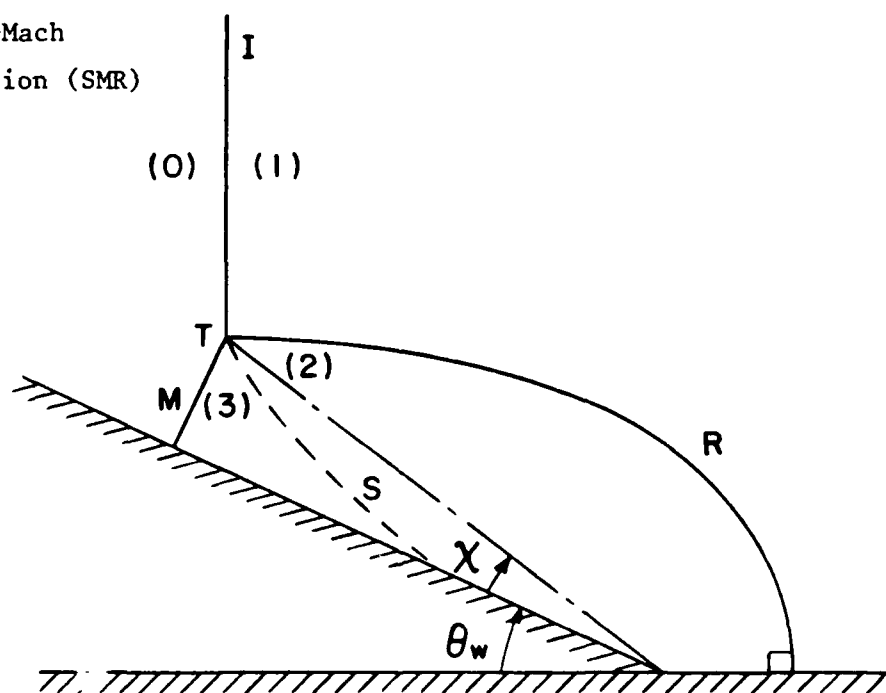
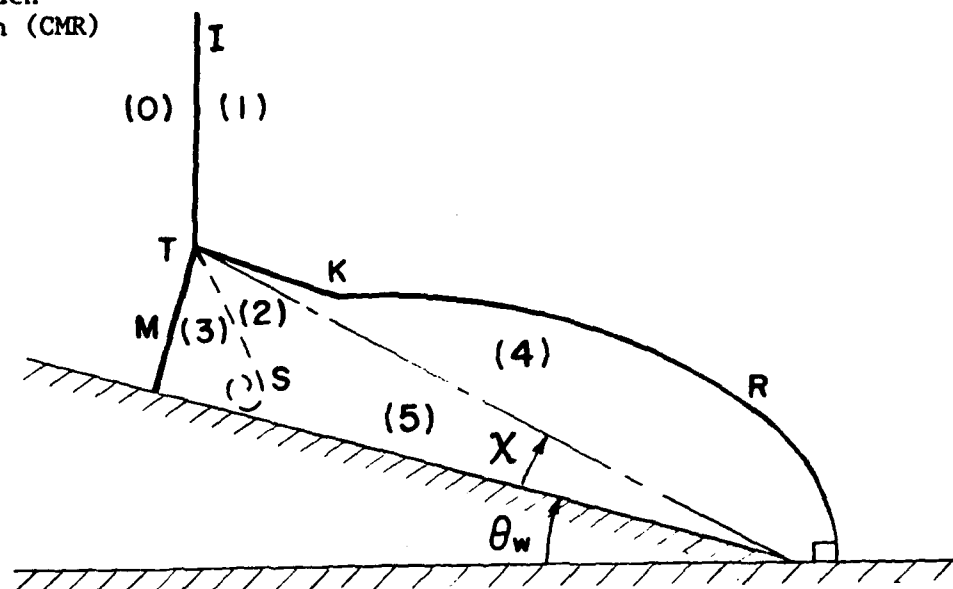


Fig. 2 Schematic diagrams of four types of oblique-shock-wave reflection in pseudo-stationary flows.

c) Complex-Mach
Reflection (CMR)



d) Double-Mach
Reflection (DMR)

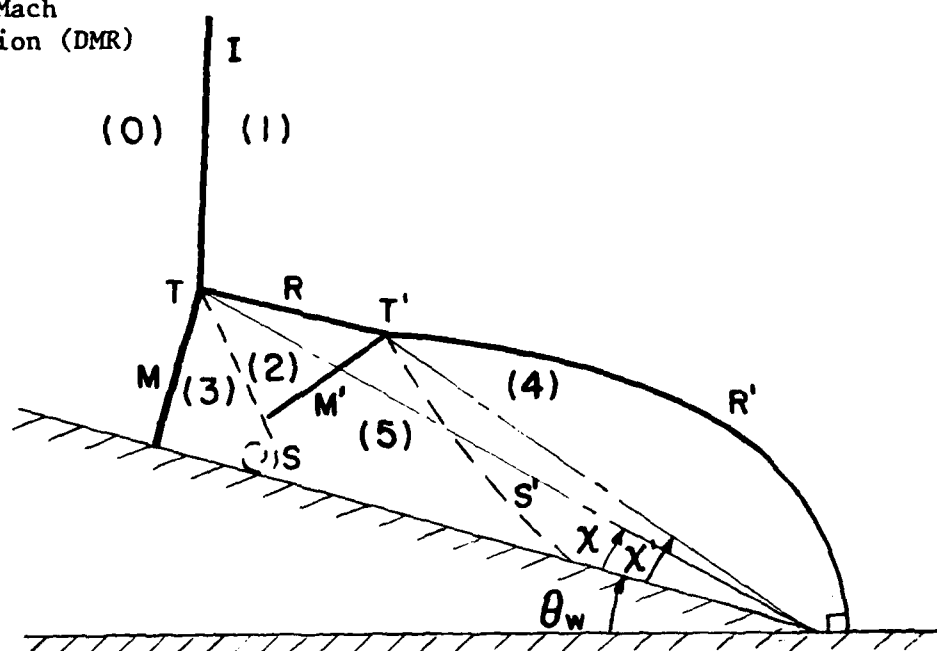


Fig. 2 (continued) Schematic diagrams of four types of oblique-shock-wave reflection in pseudo-stationary flows.

a) Regular Reflection

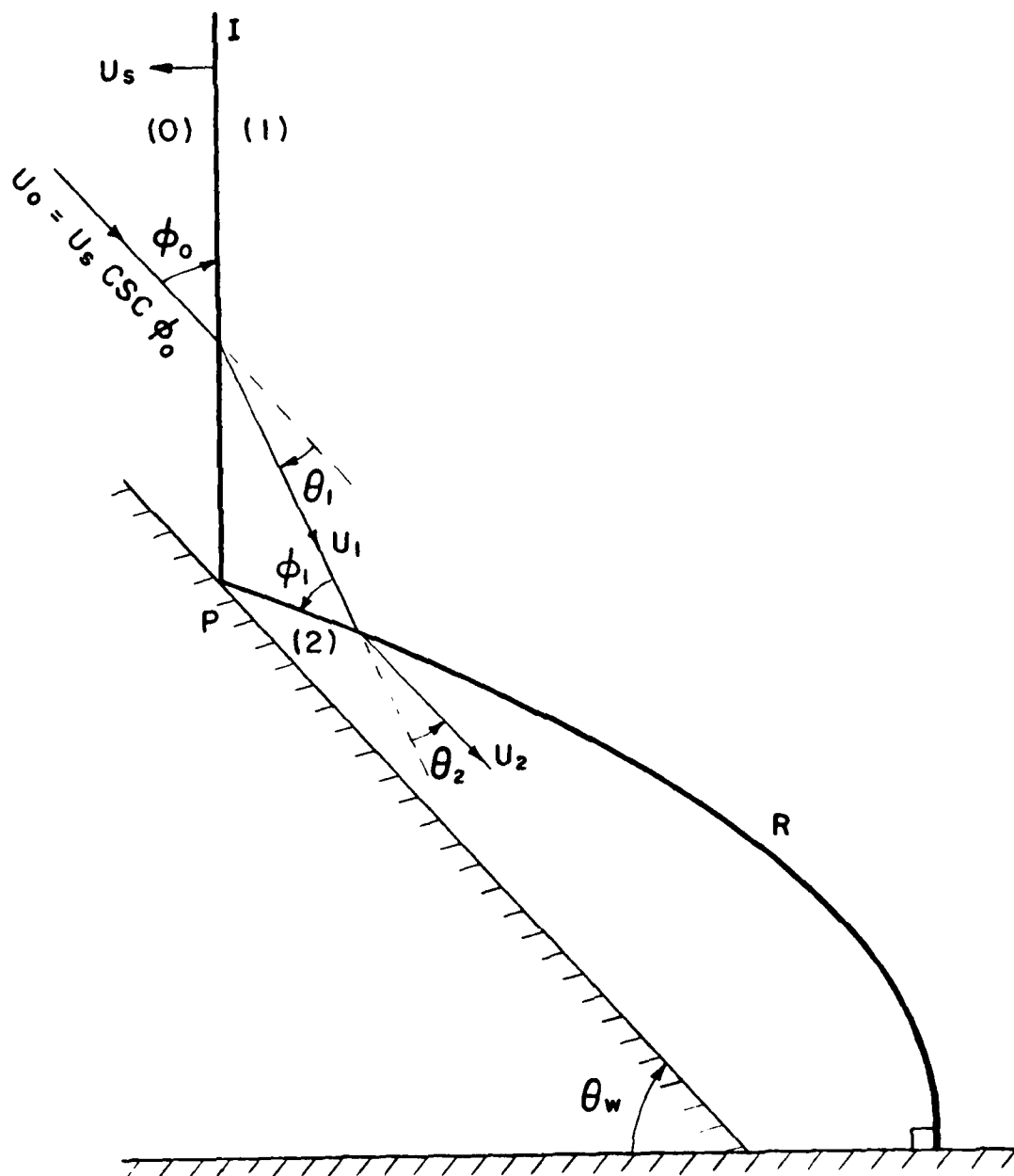
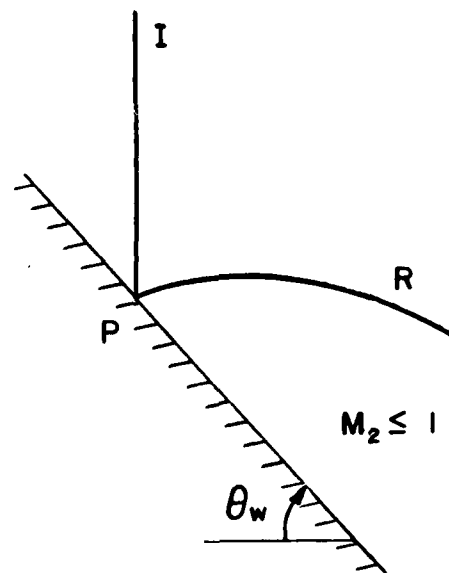


Fig. 3 Schematic diagram of regular reflection.

b) Curved reflected shock R influenced by corner signals.



c) Straight reflected shock R under supersonic conditions.

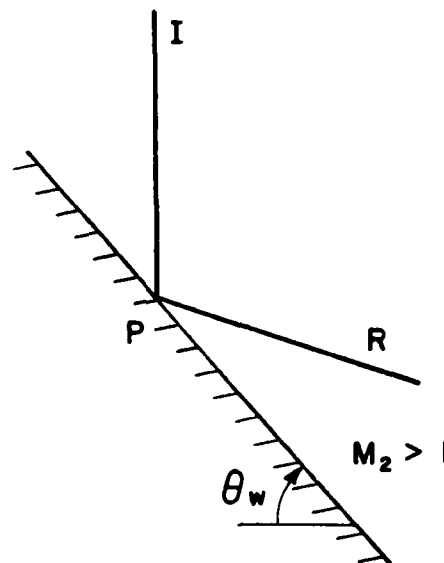
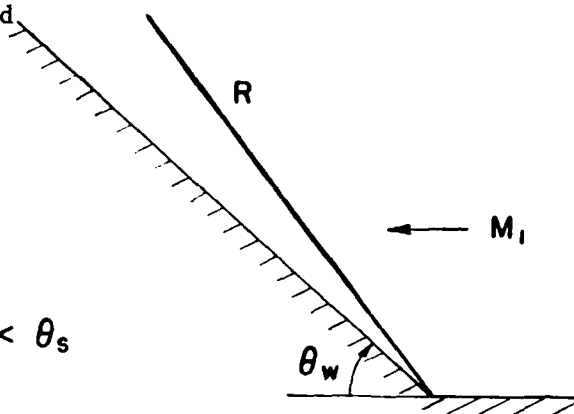


Fig. 3 (continued) Schematic diagram of regular reflection.

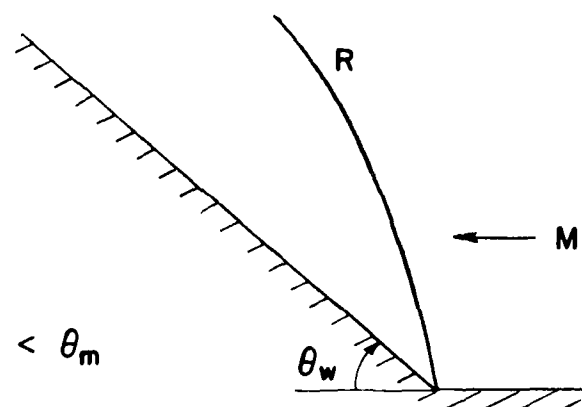
d) Straight and attached bow shock

$$M_1 > 1, 0^\circ < \theta_w < \theta_s$$



e) Curved and attached bow shock

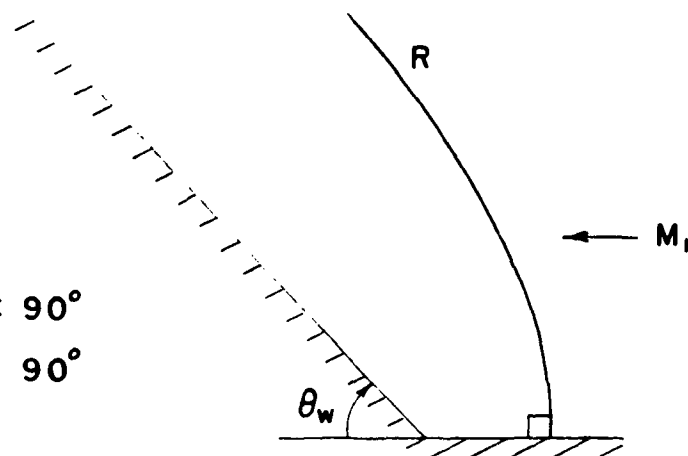
$$M_1 > 1, \theta_s < \theta_w < \theta_m$$



f) Curved and detached bow shock

$$M_1 < 1, 0^\circ < \theta_w < 90^\circ$$

$$M_1 \geq 1, \theta_m < \theta_w < 90^\circ$$



θ_s sonic deflection angle

θ_m maximum deflection angle

Fig. 3 (continued) Schematic diagram of regular reflection.

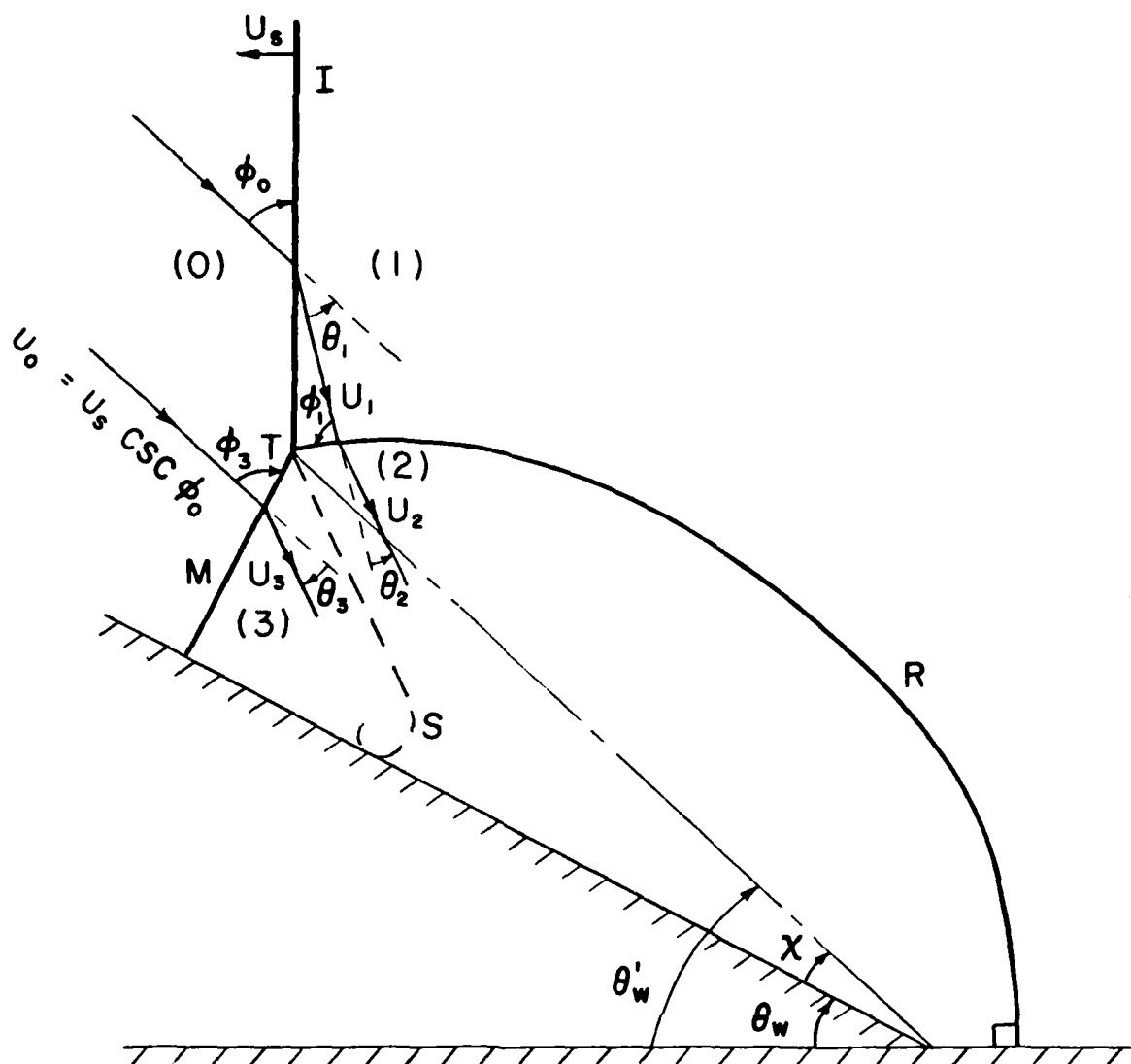


Fig. 4 Schematic diagram of single-Mach reflection.

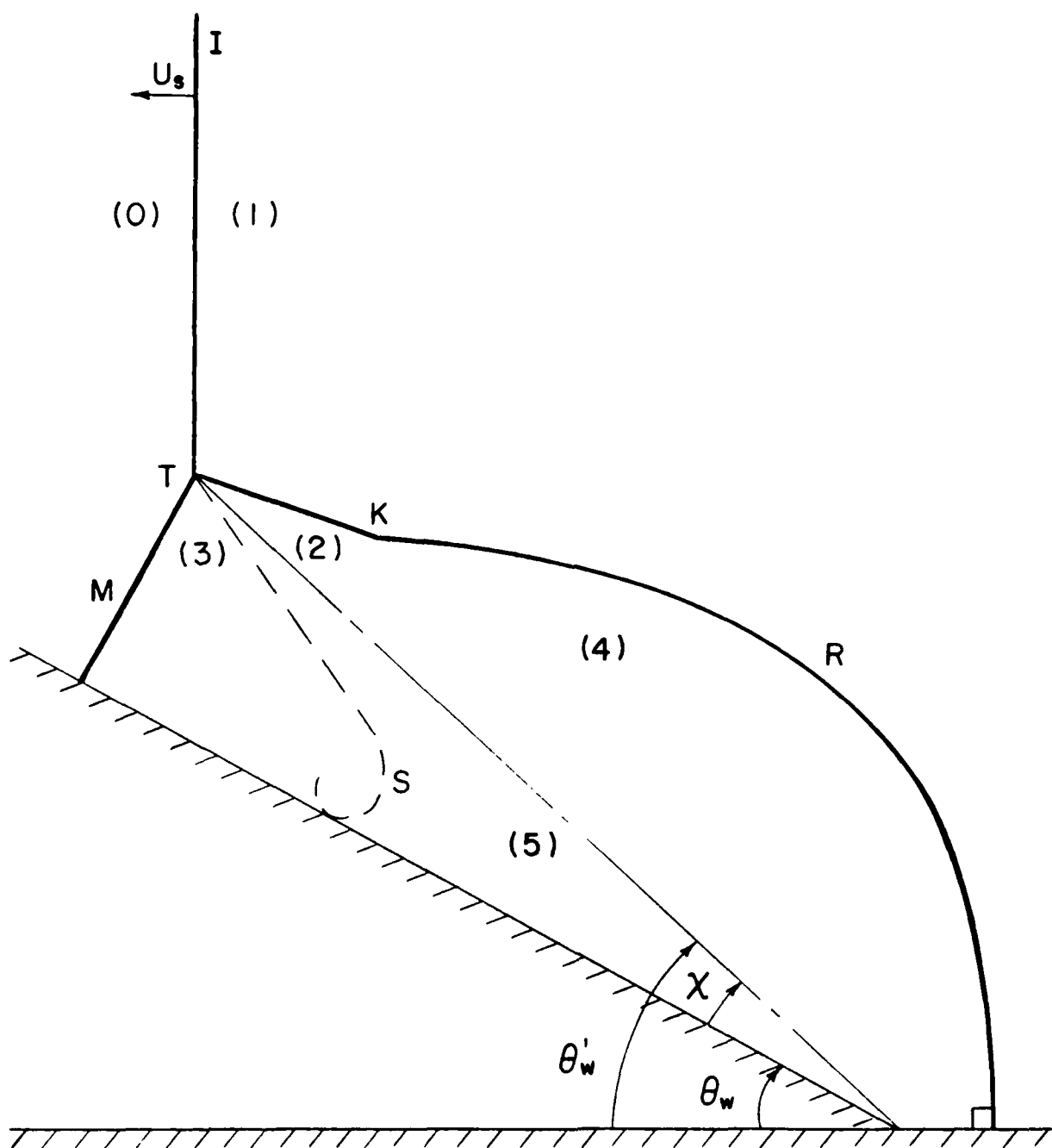


Fig. 5 Schematic diagram of complex-Mach reflection.

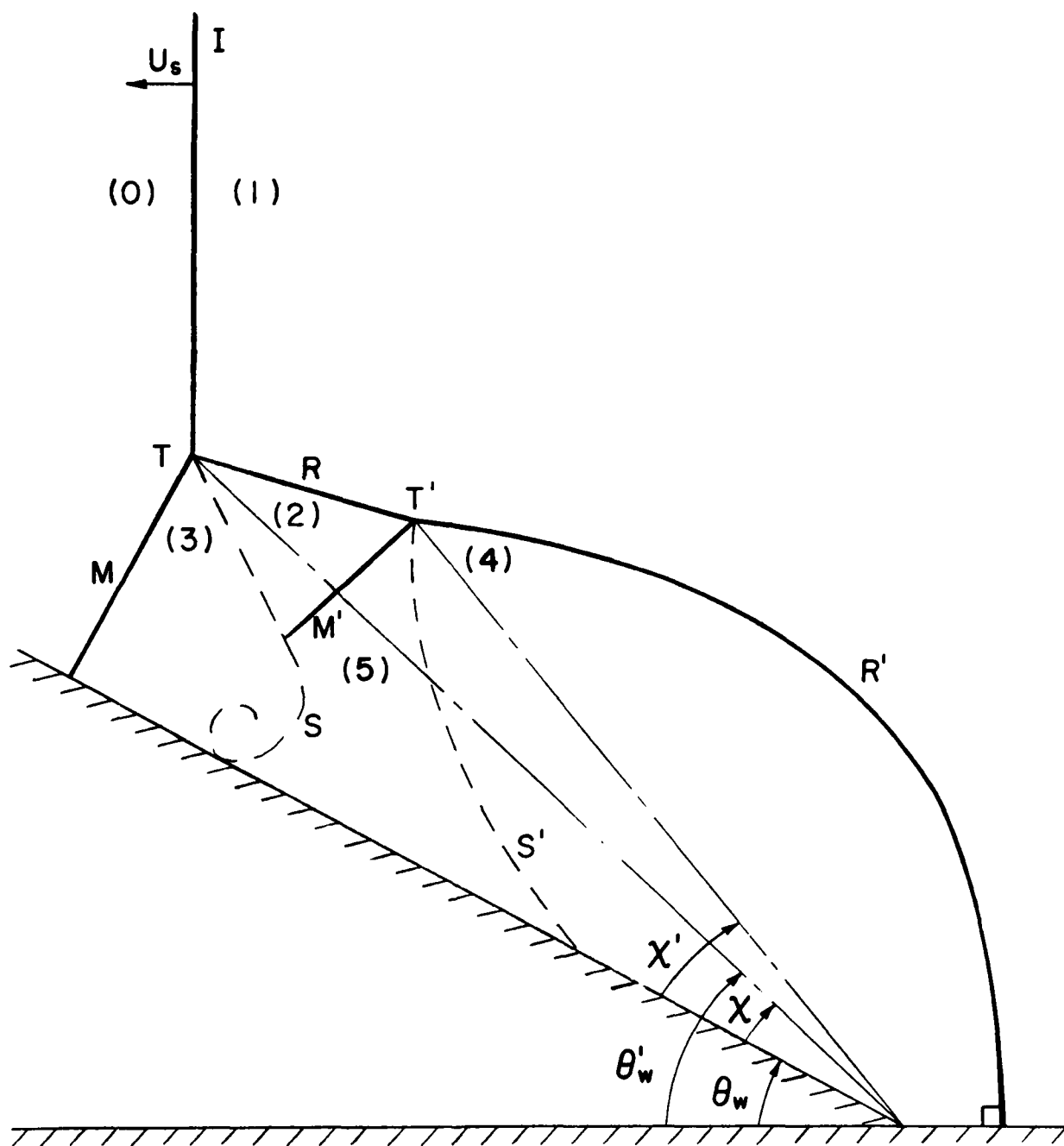


Fig. 6 Schematic diagram of double-Mach reflection.

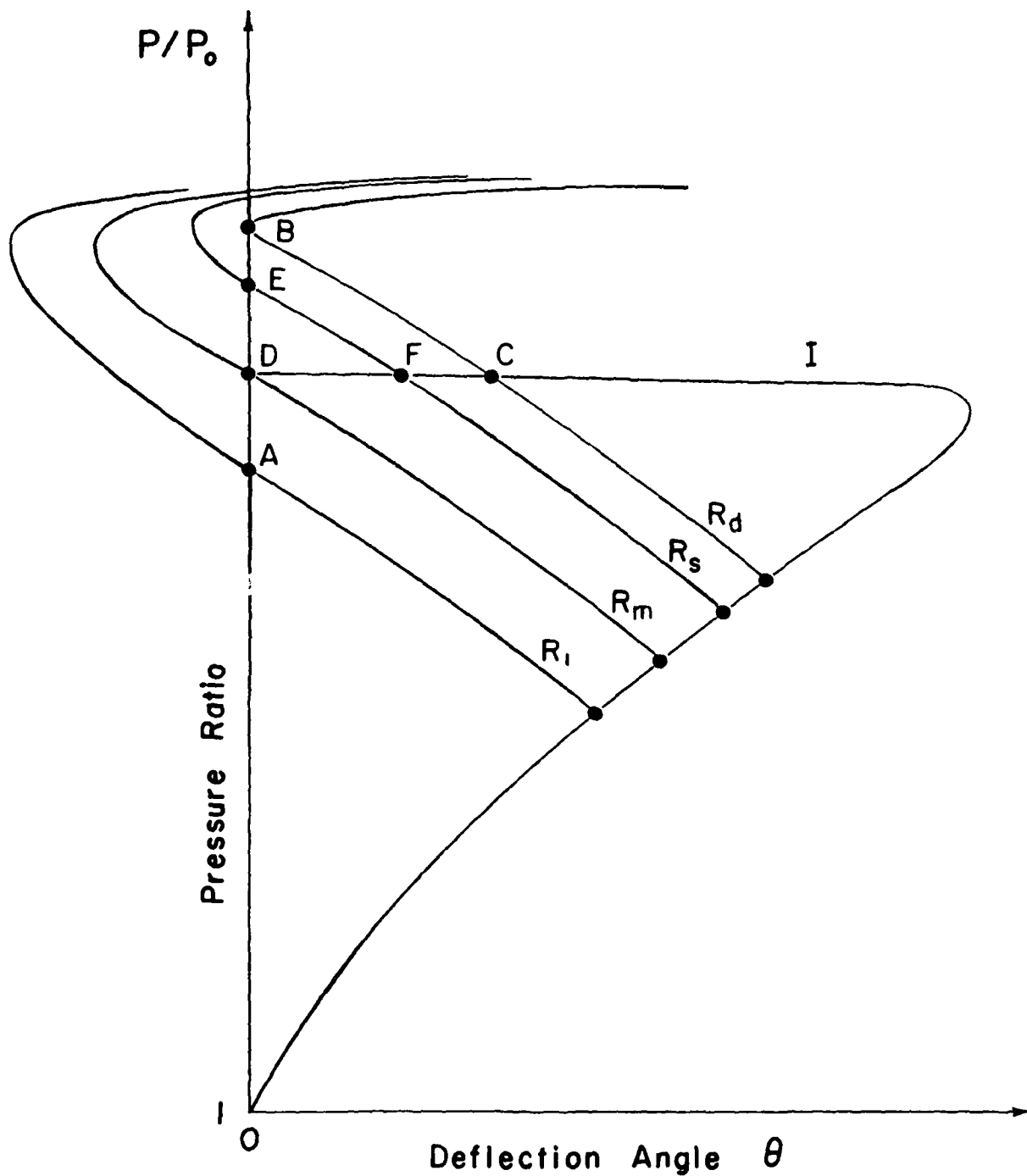


Fig. 7 Shock-polar illustrating three different RR termination criteria.
 I - incident shock wave;
 R_1 - reflected shock wave of RR at A ;
 R_m , R_s , R_d - reflected shock wave at RR termination
 (R_m - mechanical equilibrium criterion at D ,
 R_s - sonic criterion at $E \rightarrow F$,
 R_d - detachment criterion at $B \rightarrow C$).

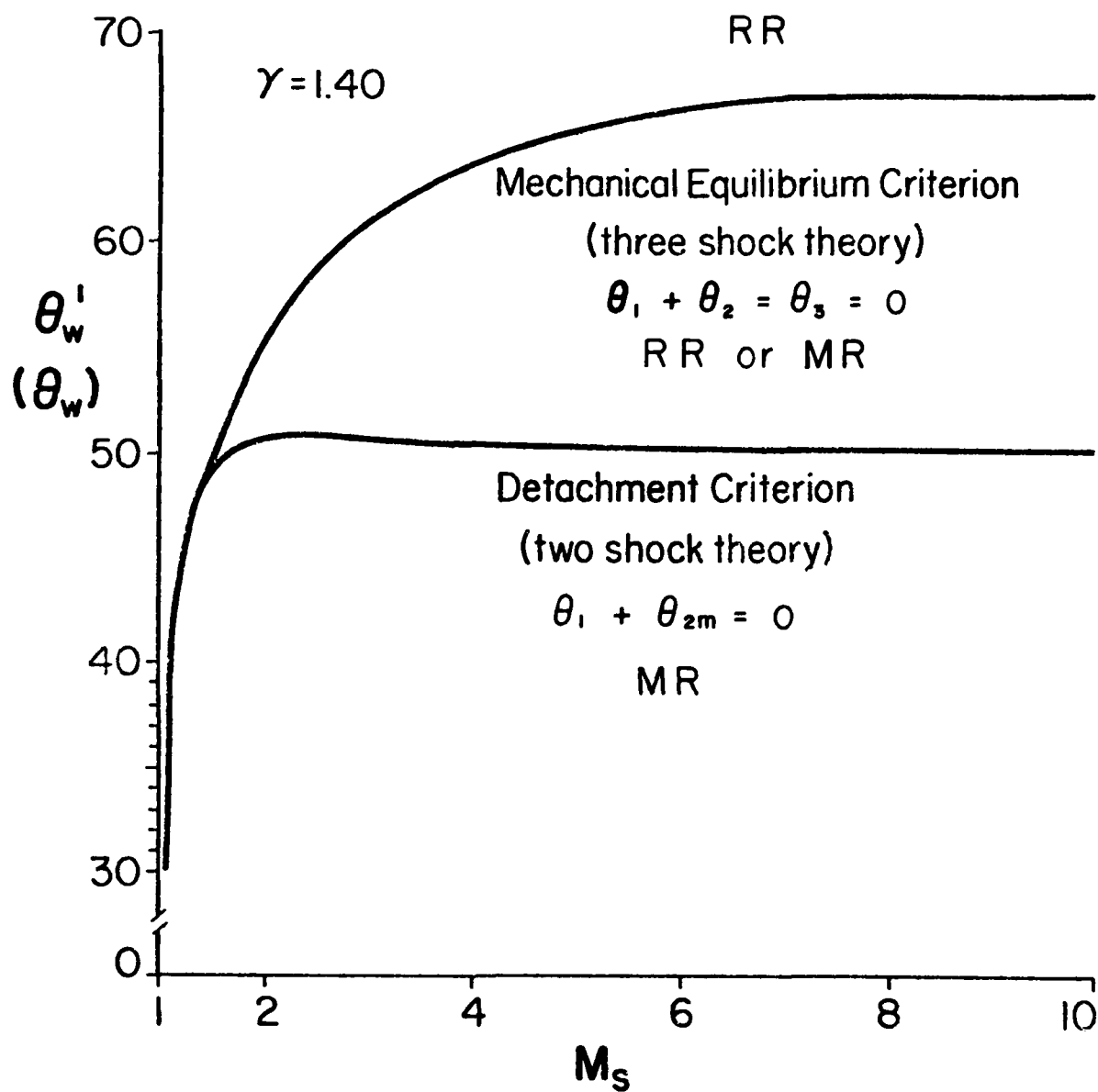


Fig. 8 Detachment and mechanical equilibrium criteria for RR(MR) termination, $\gamma = 1.4$.

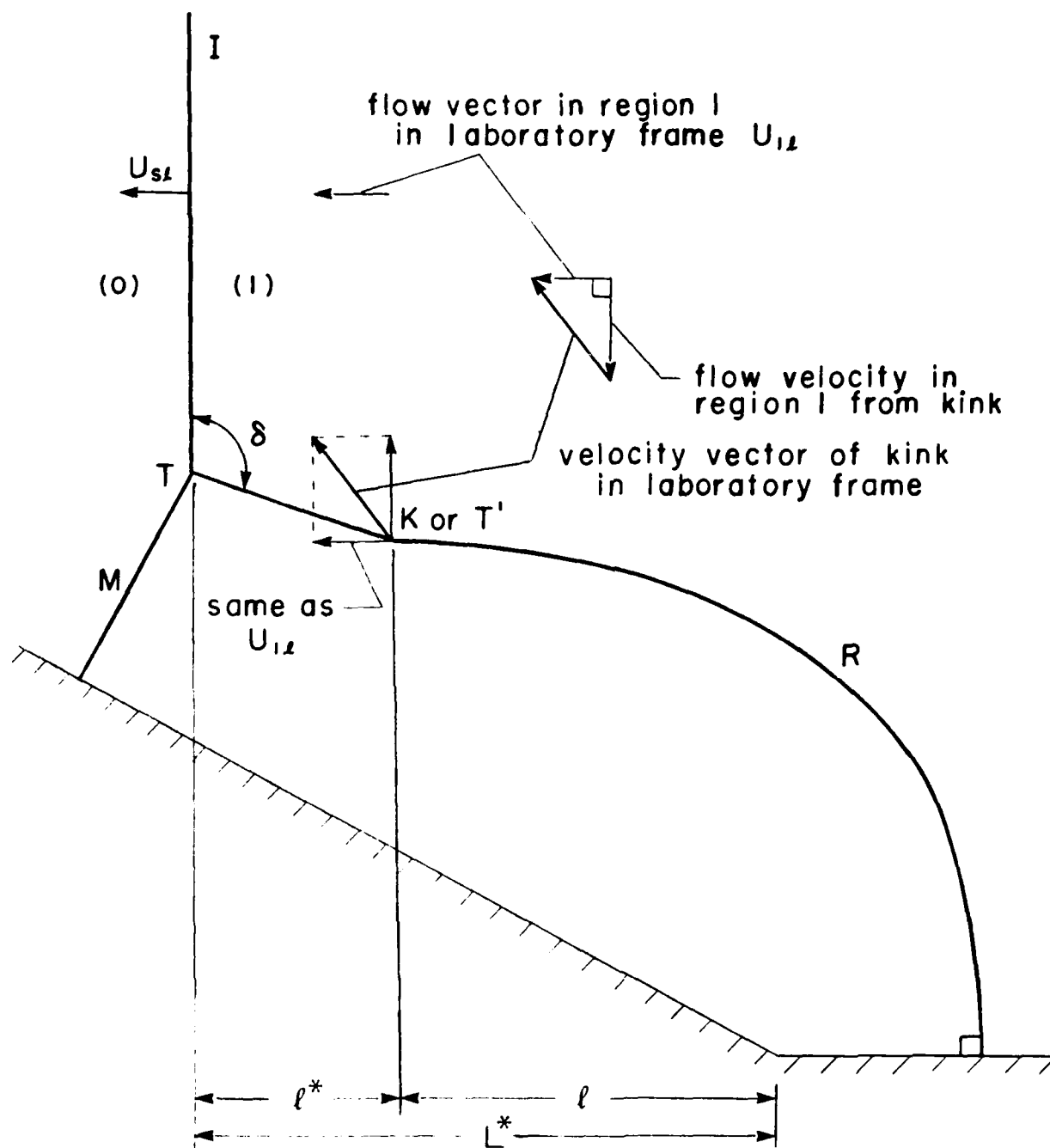


Fig. 9(a) Schematic diagram illustrating assumption of position of K or T' and flow direction in region (1) relative to K.

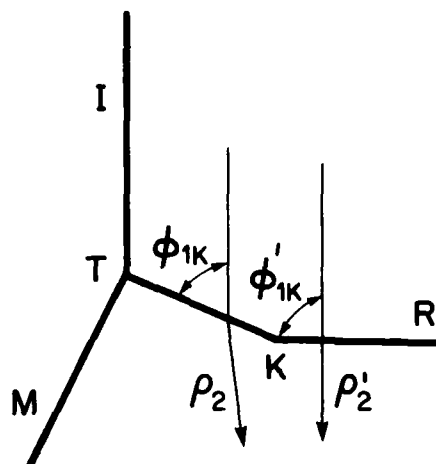


Fig. 9(b) Definitions of ϕ_{1K} , ϕ'_{1K} , ρ_2 and ρ'_2 .

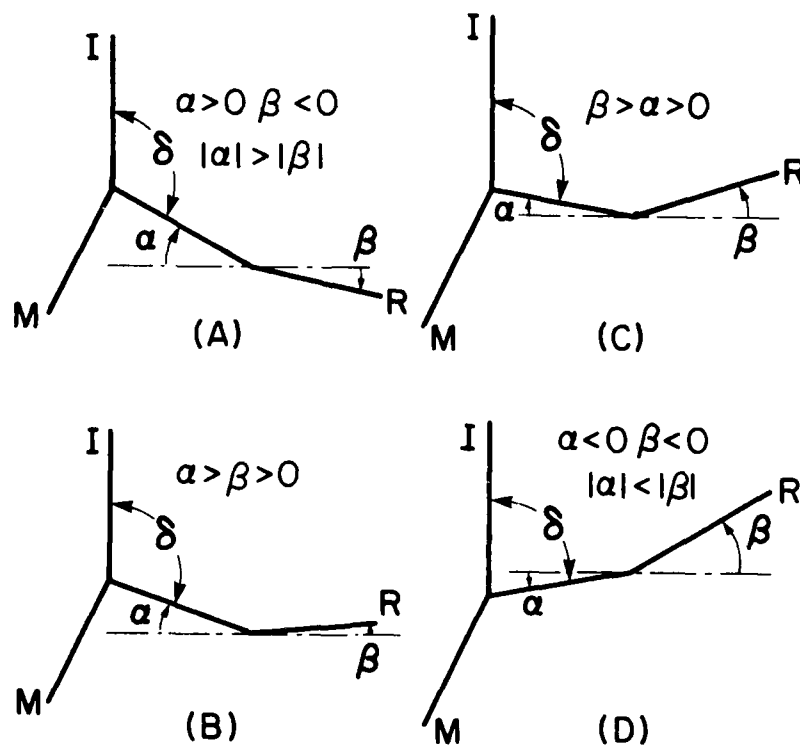


Fig. 9(c) Four possible geometric configurations of reflected shock wave.

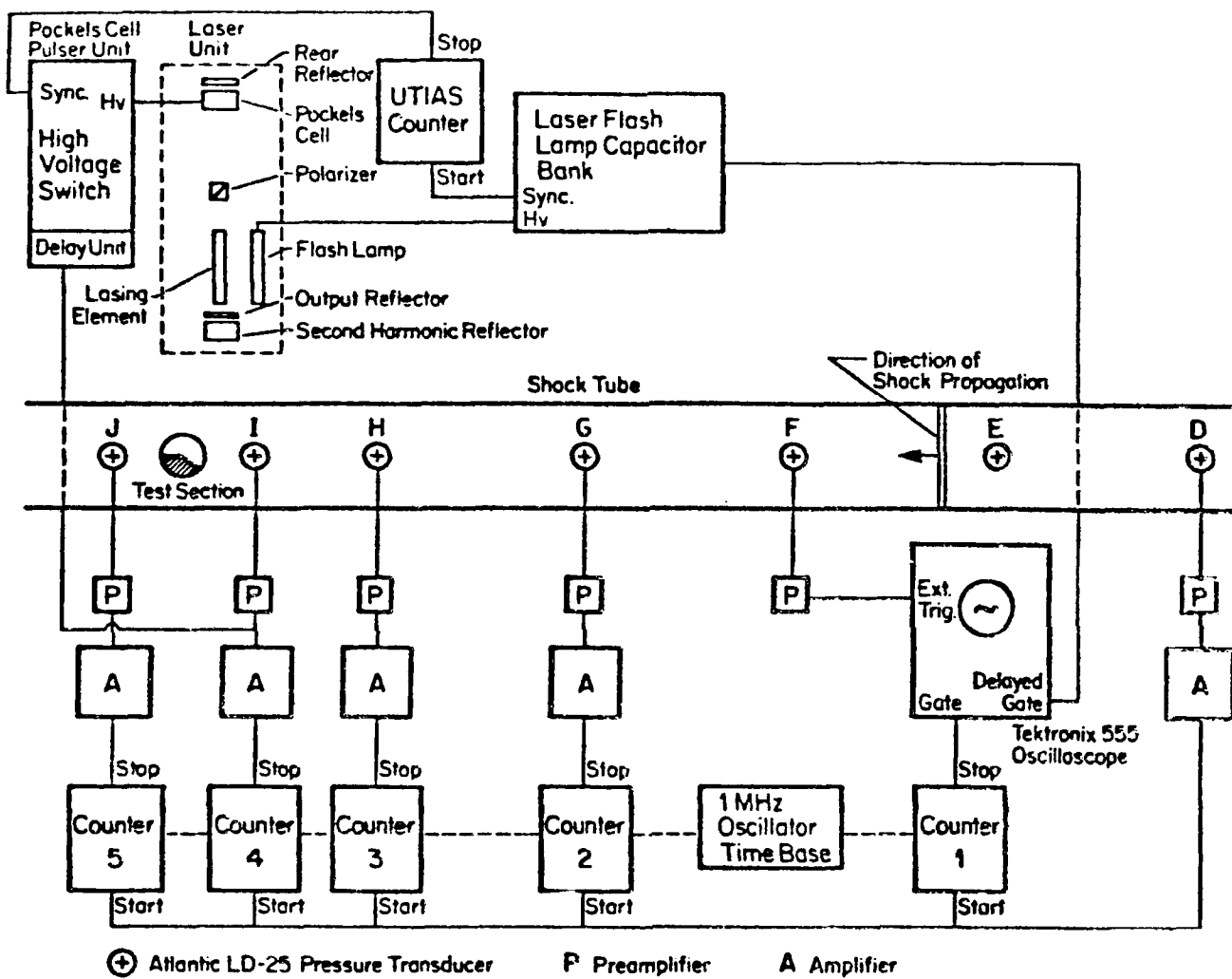


Fig. 10 Basic instrumentation setup for recording shock wave reflection process.

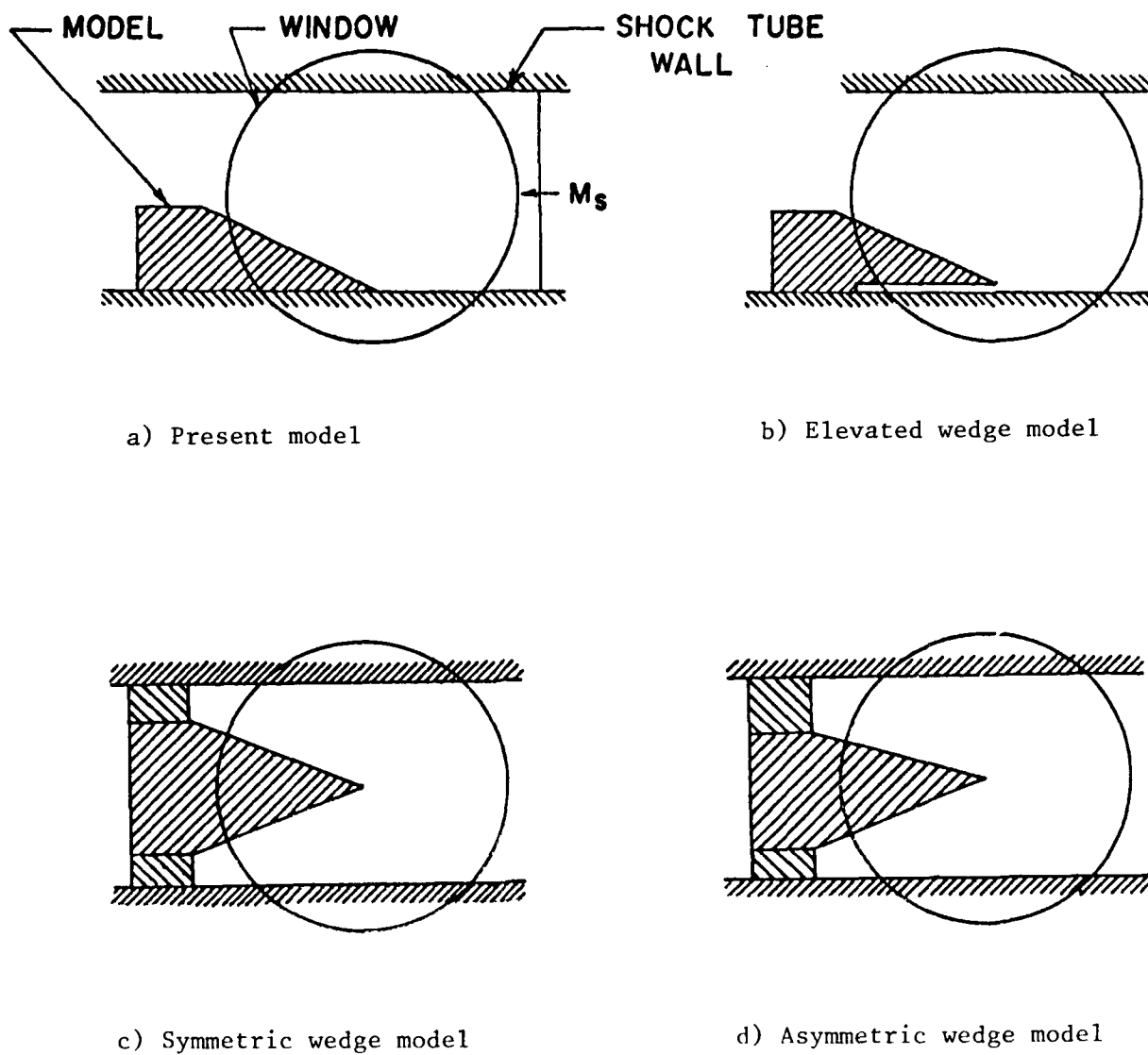


Fig. 11 Schematic diagram of possible models for studying shock wave reflection in a shock tube.



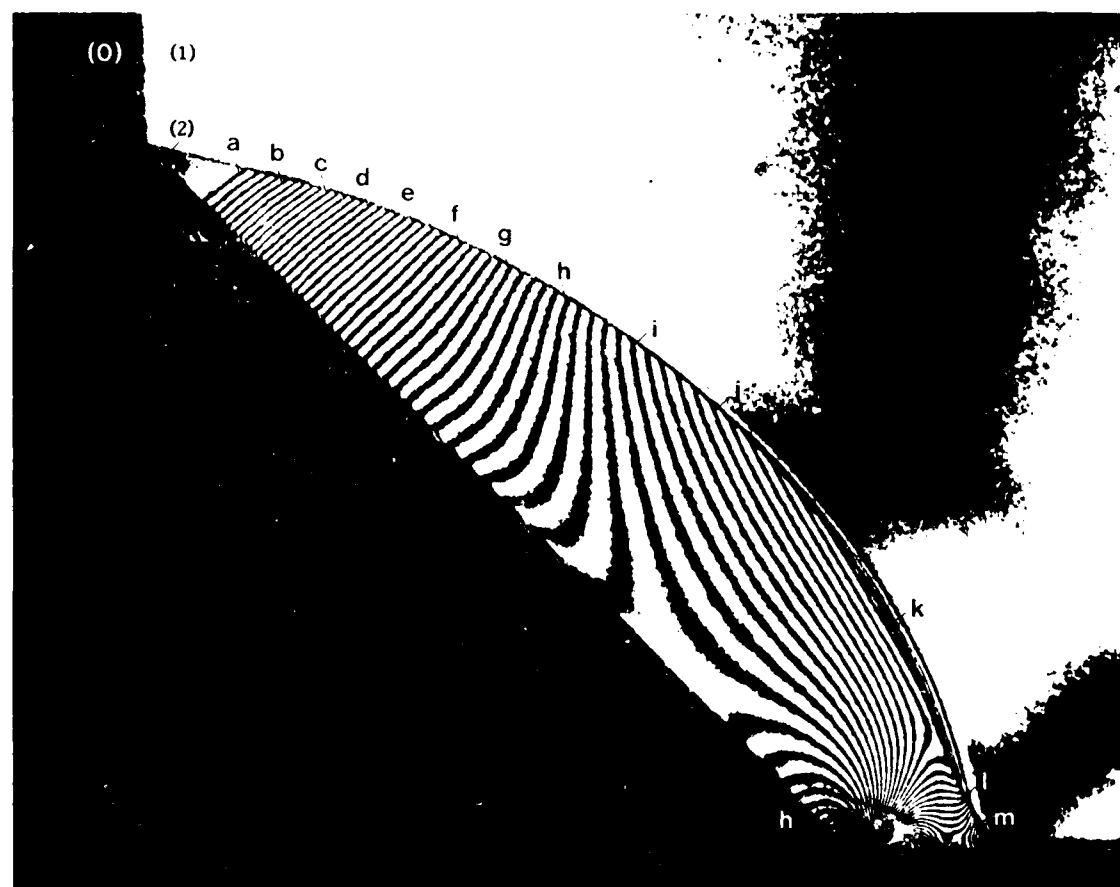
Fig. 12(a) Example of an infinite-fringe interferogram
for DMR taken with a light source of 6943 \AA
(first harmonic) in SF_6 .
 $M_s = 2.97$, $\theta_w = 20^\circ$, $P_0 = 10.7 \text{ torr}$,
 $T_0 = 297.0 \text{ K}$.



Fig. 12(b) Example of an infinite-fringe interferogram
for DMR taken with a light source of 3471.5 \AA
(second harmonic) in SF_6 .
 $M_L = 2.97$, $\theta_w = 20^\circ$, $P_s = 10.7 \text{ torr}$,
 $T_g = 297.0 \text{ K}$.



Fig. 12(c) Example of a shadowgraph of an unstable shock front in SF_6 driven by He.
 $M_S = 6.65$, $\theta_w = 4^\circ$, $P_0 = 15.1$ torr and
 $T_0 = 297.1$ K.



Region	ρ/ρ_0
(0)	1.000
(1)	3.016
(2)	7.676
a	7.627
b	7.430
c	7.185
d	6.939
e	6.694
f	6.448
g	6.202
h	5.957
i	5.711
j	5.465
k	5.220
l	4.974
m	4.729

$$\Delta\rho/\rho_0 = 0.0491$$

Region	P (torr)	T (K)	ρ (kg/m ³)
(0)	149.0	296.3	1.1775
(1)	509.6	335.9	3.5515
(2)	1421.8	368.3	9.0382

Fig. 13 Infinite-fringe interferogram of a detached regular reflection in SF₆.

$M_\infty = 1.82$, $\gamma_w = 47^\circ$, $P = 149.0$ torr,

$T = 296.3$ K, $\lambda = 6943$ Å.

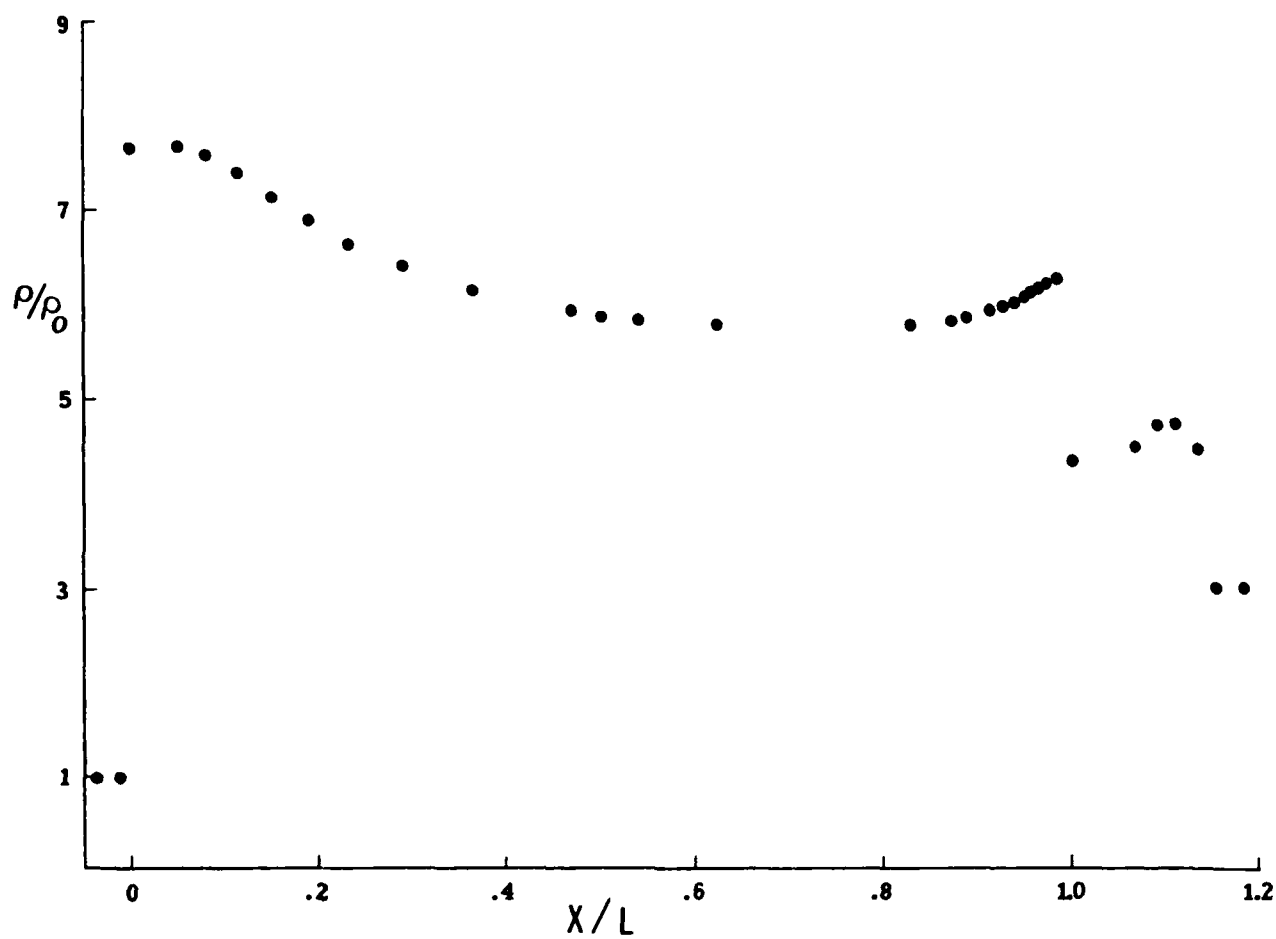
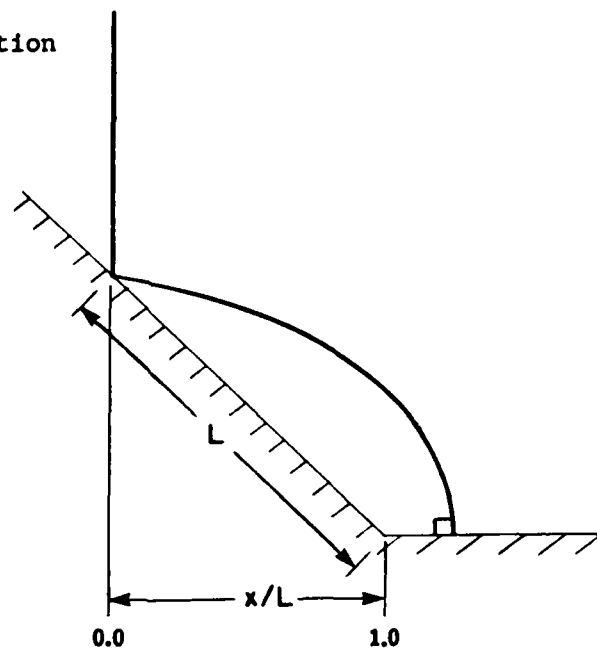


Fig. 14 Wall-density distribution for case 1 of a detached regular reflection in SF_6 .

a) Regular Reflection



b) Mach Reflection

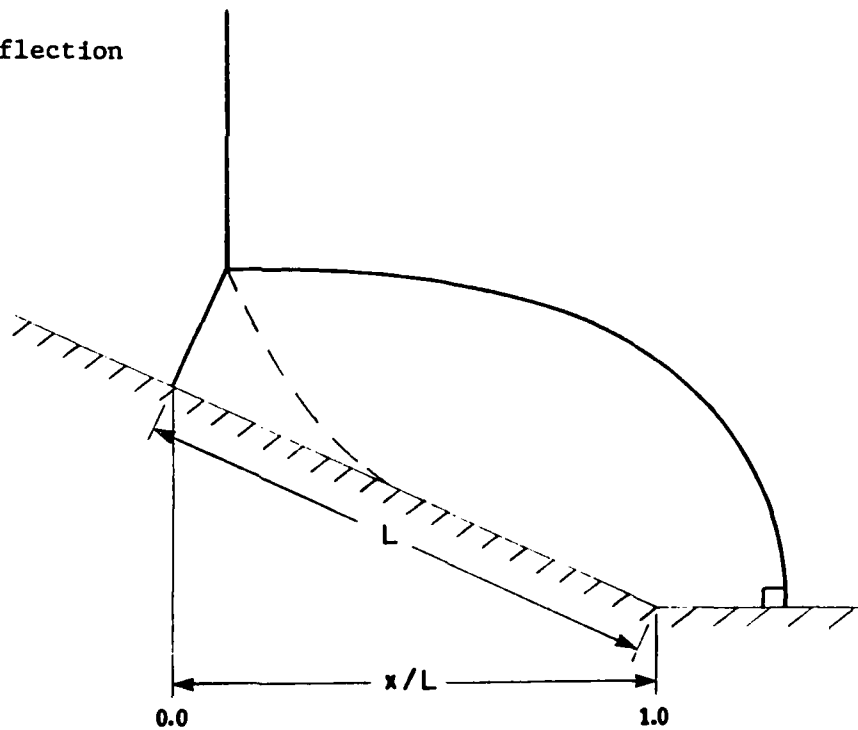


Fig. 15 Definition for the distance L .



Region	ρ/ρ_0
(0)	1.000
(1)	12.134
(2)	69.771
a	68.792
b	67.812
c	66.833
d	65.853
e	64.874
f	63.894
g	62.915
h	61.935
i	60.956
j	59.976

$$\Delta\rho/\rho_0 = 0.9795$$

Region	P (torr)	T (K)	ρ (kg/m ³)
(0)	7.5	297.4	0.0590
(1)	164.5	537.6	0.7165
(2)	1150.7	653.9	4.1200

Fig. 16 Infinite-fringe interferogram of an attached regular reflection in SF₆.

$M_S = 4.57$, $\theta_w = 40^\circ$, $P_0 = 7.5$ torr,

$T_0 = 297.4$ K, $\lambda = 6943$ Å.

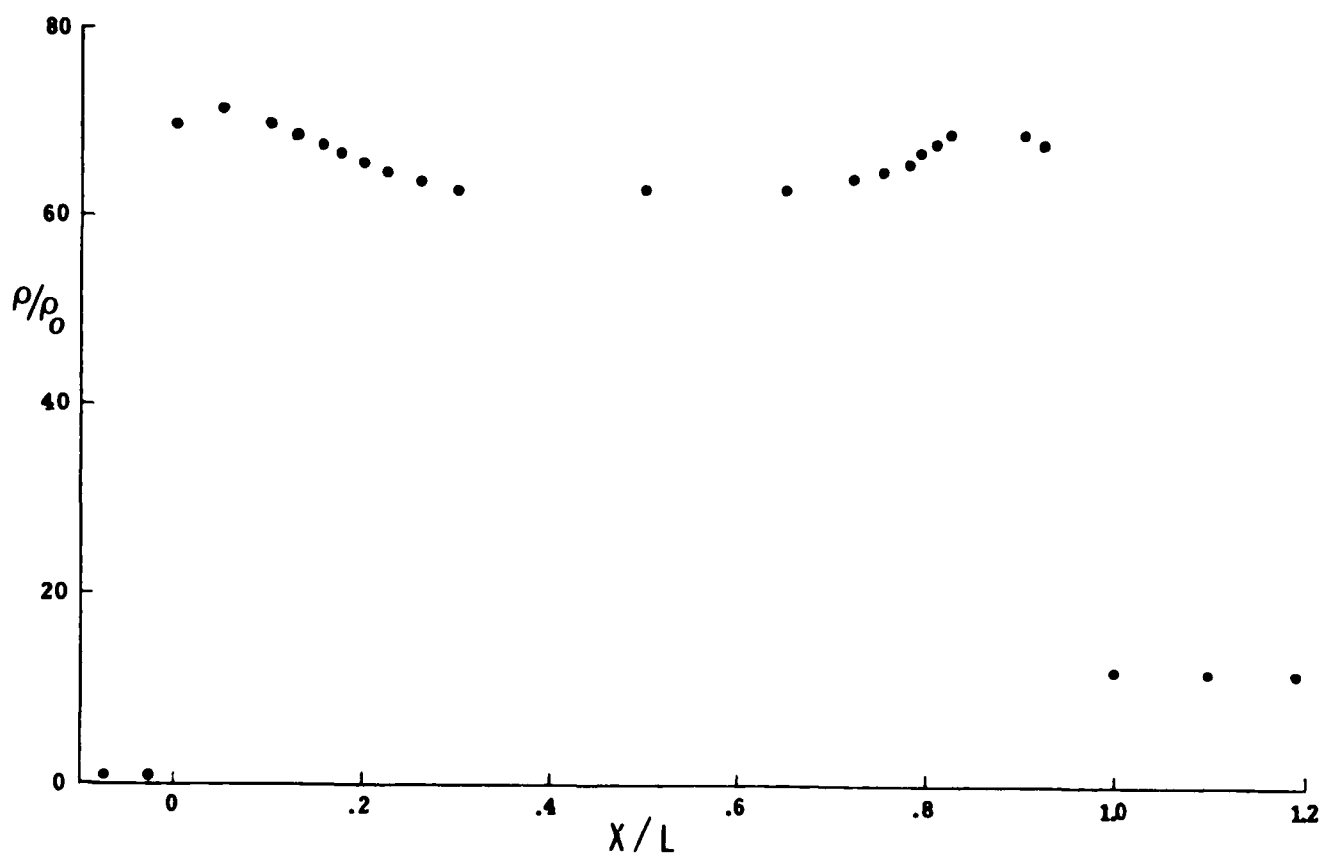
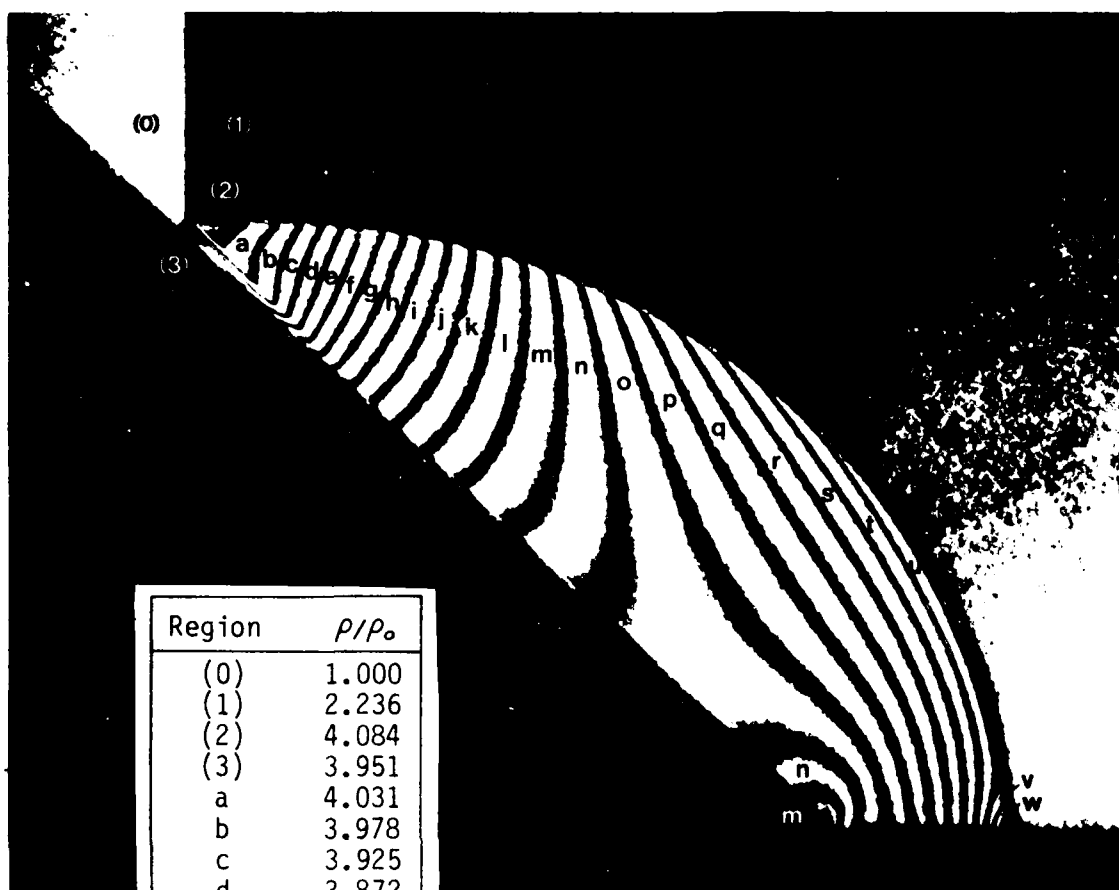


Fig. 17 Wall-density distribution for case 2 of an attached regular reflection in SF_6 .



Region	P/P_0
(0)	1.000
(1)	2.236
(2)	4.084
(3)	3.951
a	4.031
b	3.978
c	3.925
d	3.872
e	3.819
f	3.766
g	3.712
h	3.659
i	3.606
j	3.553
k	3.500
l	3.447
m	3.394
n	3.340
o	3.287
p	3.234
q	3.181
r	3.128
s	3.075
t	3.021
u	2.968
v	2.915
w	2.862

$$\Delta\rho/\rho_0 = 0.0532$$

Region	P (torr)	T (K)	ρ (kg/m ³)
(0)	138.0	296.9	1.0882
(1)	335.7	323.0	2.4334
(2)	648.6	341.7	4.4446
(3)	648.6	353.2	4.2997

Fig. 18 Infinite-fringe interferogram of a detached single-Mach reflection in SF_6 .
 $M_\infty = 1.54$, $\alpha_w = 42^\circ$, $P = 138.0$ torr,
 $T = 296.9$ K, $\lambda = 6943 \text{ \AA}$.

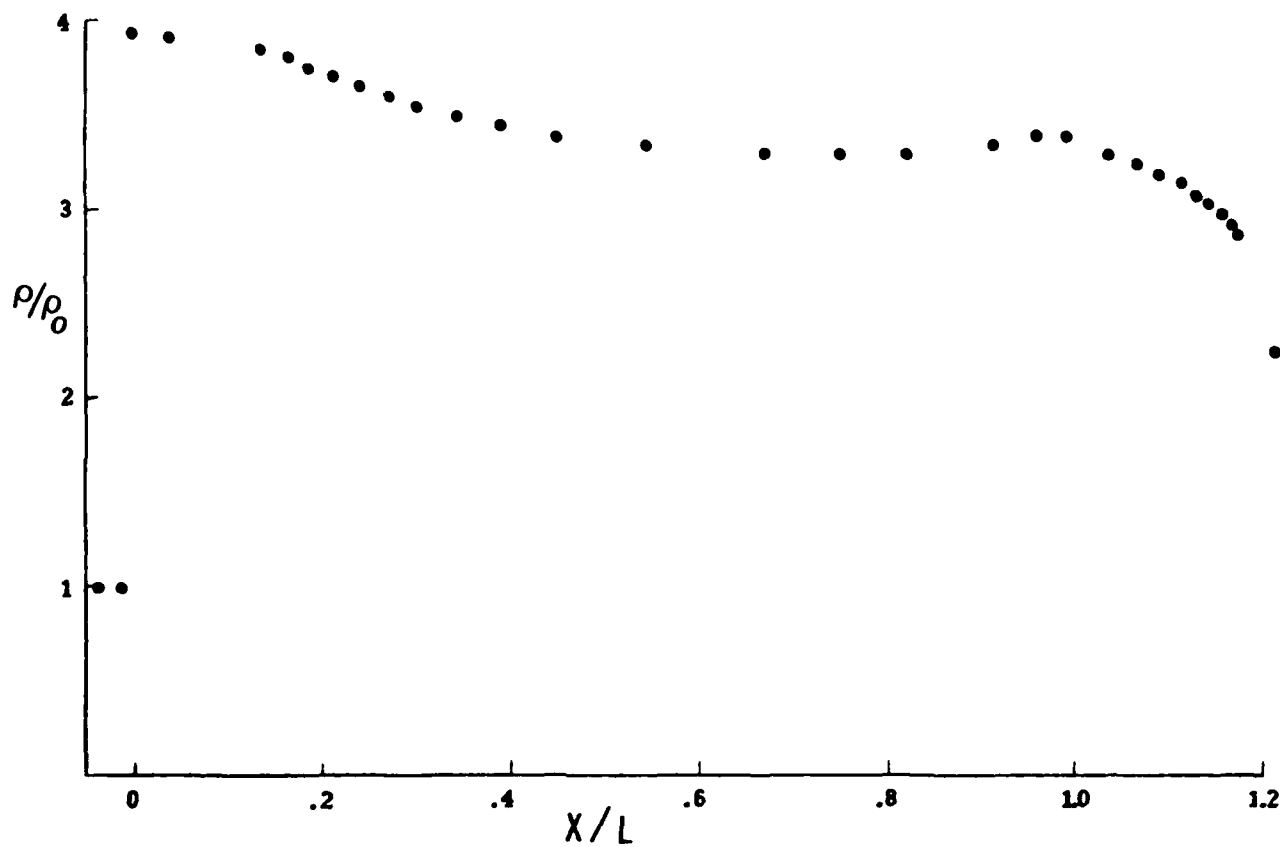


Fig. 19 Wall-density distribution for case 3 of a detached single-Mach reflection in SF_6 .



Region	ρ/ρ_0
(0)	1.000
(1)	3.888
(2)	4.949
(3)	4.820
a	4.949
b	5.199
c	5.448
d	5.698
e	5.947
f	6.197
g	6.446
h	6.696
i	6.945
j	7.195
k	7.444

$$\Delta\rho/\rho_0 = 0.2495$$

Region	P (torr)	T (K)	ρ (kg/m ³)
(0)	29.4	297.0	0.2318
(1)	135.5	351.9	0.9012
(2)	176.0	359.1	1.1471
(3)	176.0	368.7	1.1173

Fig. 20 Infinite-fringe interferogram of an attached single-Mach reflection in SF₆.

$M_0 = 2.11$, $\alpha = 20^\circ$, $P = 29.4$ torr,

$T = 297.0$ K, $\lambda = 6943$ Å.

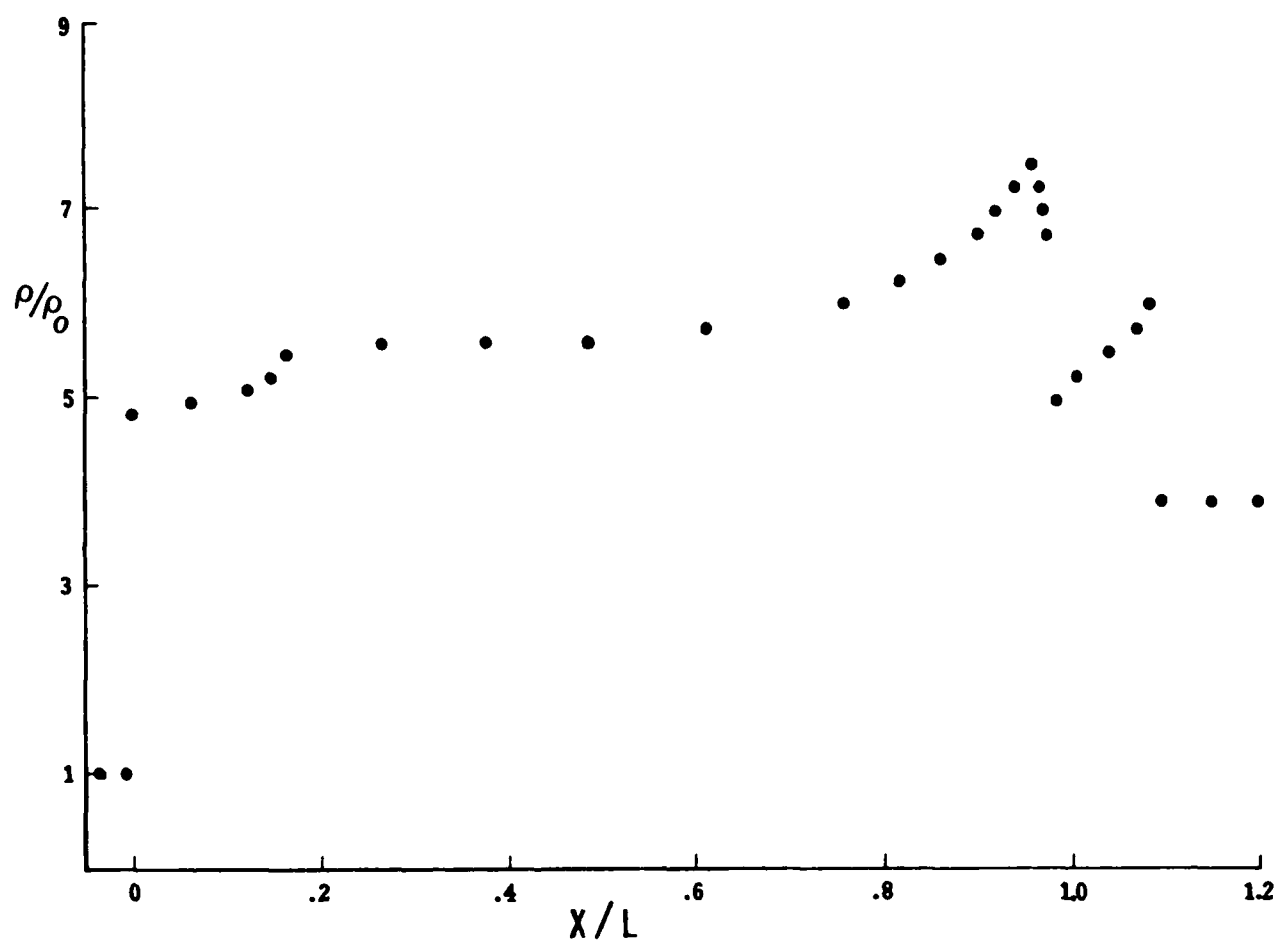


Fig. 21 Wall-density distribution for case 4 of an attached single-Mach reflection in SF_6 .



Region	ρ/ρ_0
(0)	1.000
(1)	2.736
(2)	4.841
(3)	4.632
a	3.961
b	4.092
c	4.254
d	4.417
e	4.483
f	4.539
g	4.743
h	4.906
i	5.069

$$\Delta\omega/\omega_0 = 0.0326$$

Region	P (torr)	T (K)	ρ (kg/m ³)
(0)	226.0	298.1	1.7752
(1)	690.4	332.8	4.8564
(2)	1286.7	350.6	8.5933
(3)	1286.7	366.4	8.2216

Fig. 2. Infinite-fringe interferogram of a detached complex-Mach reflection in SF₆.

$M_0 = 1.72$, $\omega_0 = 4.0^\circ$, $P = 226.0$ torr,

$T = 298.1$ K, $\lambda = 6943$ Å.

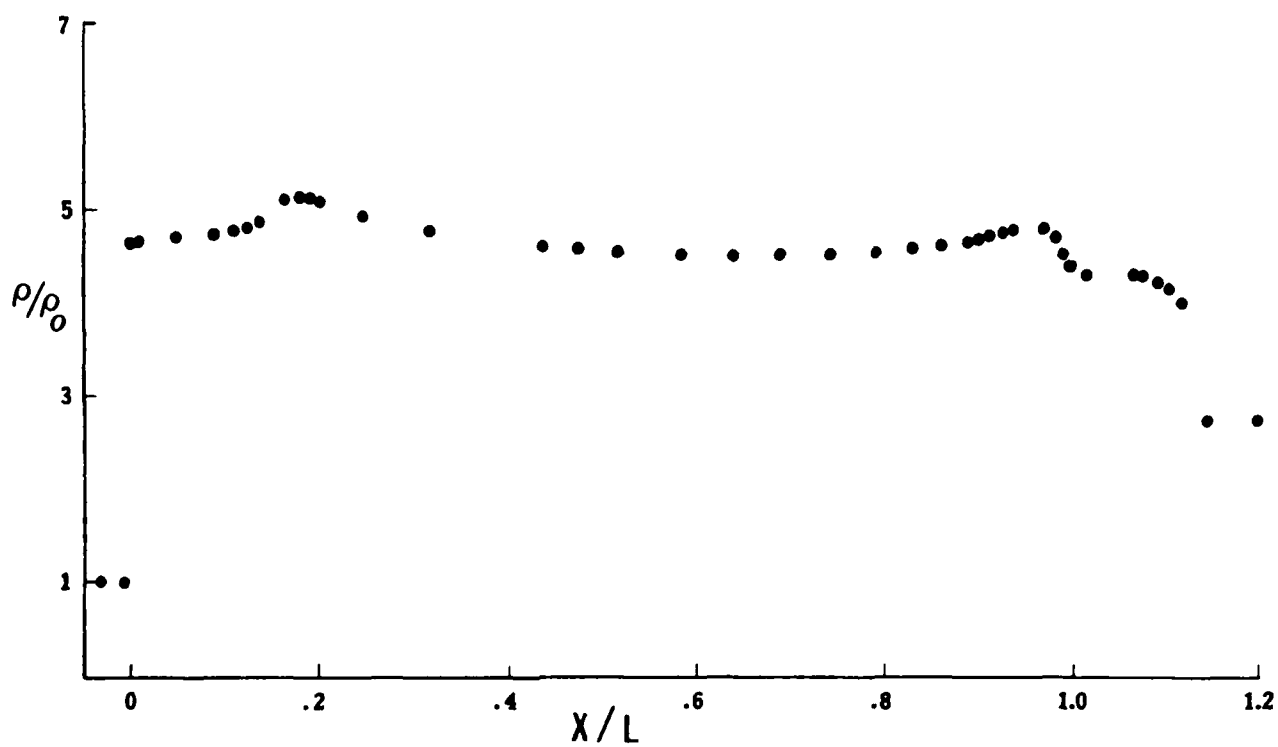


Fig. 23 Wall-density distribution for case 5 of a detached complex-Mach reflection in SF_6 .



Region	ρ/ρ_0
(0)	1.000
(1)	7.332
(2)	8.105
(3)	7.925
a	9.029
b	9.953
c	10.878

$$\Delta\rho/\rho_0 = 0.9244$$

Region	P (torr)	T (K)	ρ (kg/m ³)
(0)	7.9	297.5	0.0626
(1)	82.0	418.6	0.4588
(2)	91.4	421.7	0.5071
(3)	91.4	431.3	0.4959

Fig. 24(a) Infinite-fringe interferogram of an attached complex-Mach reflection in SF_6 .
 $M_0 = 3.14$, $\omega_0 = 10^\circ$, $P = 7.9$ torr,
 $T = 297.5$ K, $\lambda = 6943$ Å.



Region	P/P_0
(0)	1.000
(1)	7.332
(2)	8.105
(3)	7.925
a	8.567
b	9.029
c	9.491
d	9.953
e	10.416
f	10.878

$$\Delta\rho/\rho_0 = 0.4622$$

Region	P (torr)	T (K)	ρ (kg/m ³)
(0)	7.9	297.5	0.0626
(1)	82.0	418.6	0.4588
(2)	91.4	421.7	0.5071
(3)	91.4	431.3	0.4959

Fig. 24(b) Infinite-fringe interferogram of an attached complex-Mach reflection in SF_6 .
 $M_0 = 3.14$, $\theta_w = 10^\circ$, $P = 7.9$ torr,
 $T = 297.5$ K, $\lambda = 3472$ Å.

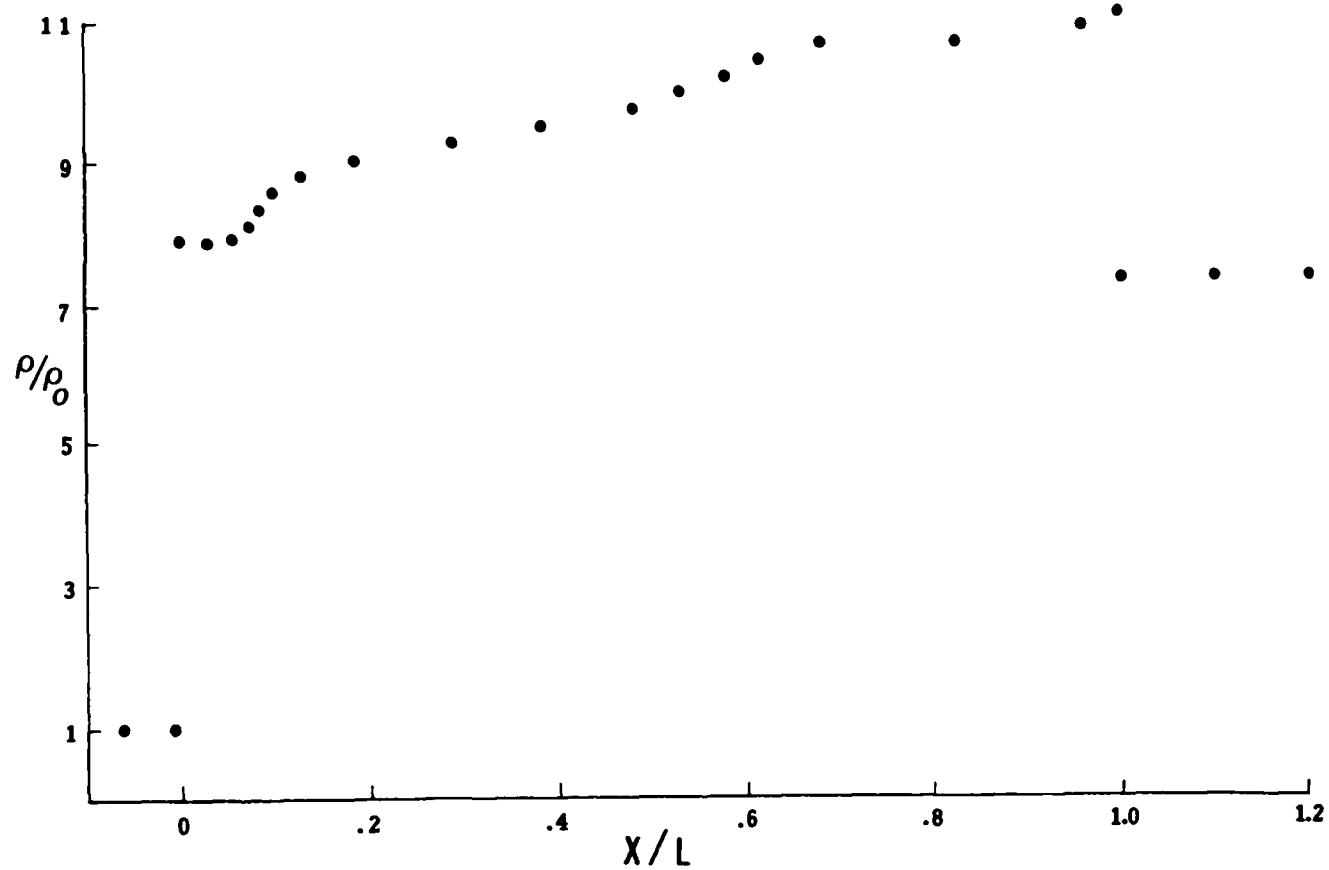


Fig. 25 Wall-density distribution for case 6 of an attached complex-Mach reflection in SF_6 .



Region	P/P_0
(0)	1.000
(1)	4.124
(2)	6.891
(3)	6.422
a	7.099
b	7.307
c	7.516
d	7.724
e	7.932
f	8.141
g	8.349
h	8.557
i	8.766
j	8.974
k	9.183
l	9.391
m	9.599
n	9.808
o	10.016

$$\Delta\rho/\rho_0 = 0.2084$$

Region	P (torr)	T (K)	ρ (kg/m ³)
(0)	35.2	296.9	0.2776
(1)	174.1	356.0	1.1449
(2)	304.0	372.1	1.9128
(3)	304.0	399.3	1.7829

Fig. 26 Infinite-fringe interferogram of an attached double-Mach reflection in SF₆.

$M_0 = 2.18$, $\theta_w = 37^\circ$, $P_0 = 35.2$ torr,

$T_0 = 296.9$ K, $\lambda = 6943$ Å.

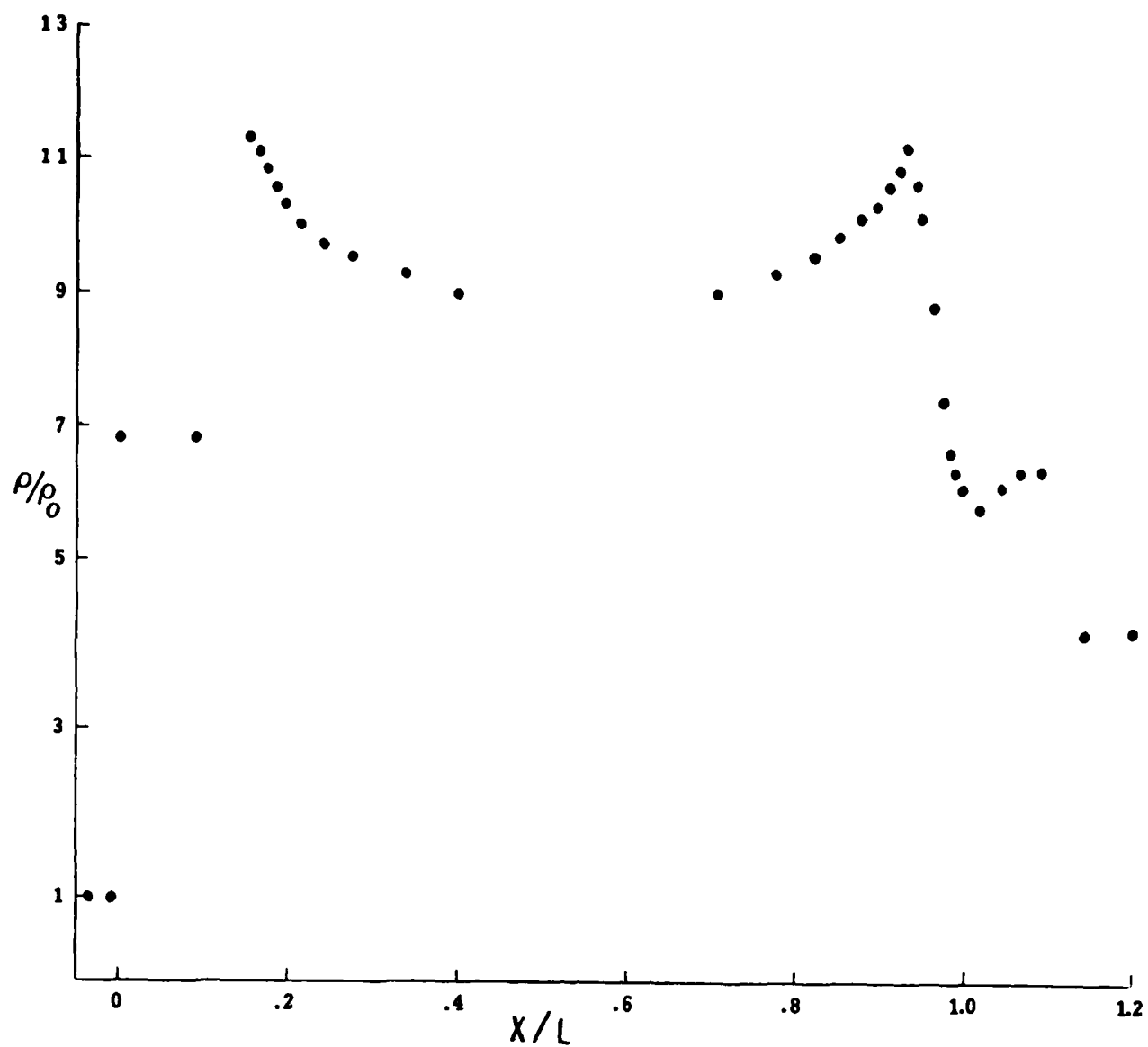
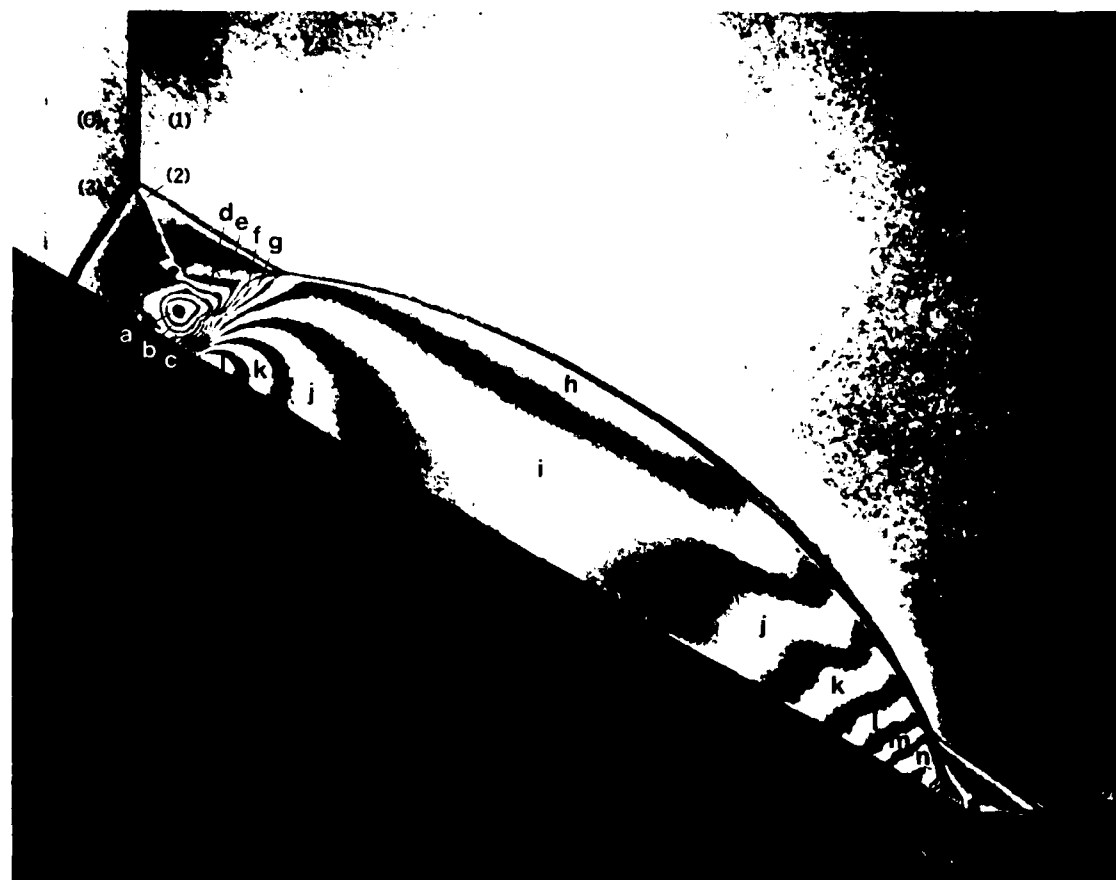


Fig. 27 Wall-density distribution for case 7 of an attached double-Mach reflection in SF_6 .



Region	P/P_0
(0)	1.000
(1)	5.472
(2)	7.947
(3)	7.428
a	5.974
b	6.632
c	7.290
d	7.947
e	8.605
f	9.263
g	9.921
h	10.578
i	11.236
j	11.894
k	12.551
l	13.209
m	13.867
n	14.524

$$\Delta\rho/\rho_0 = 0.6577$$

Region	P (torr)	T (K)	ρ (kg/m ³)
(0)	11.2	297.4	0.0879
(1)	78.4	381.3	0.4812
(2)	117.3	393.0	0.6989
(3)	117.3	420.5	0.6533

Fig. 28 Infinite-fringe interferogram of an attached double-Mach reflection in SF₆.
 $M_0 = 2.59$, $\theta_w = 30^\circ$, $P_0 = 11.2$ torr,
 $T_0 = 297.4$ K, $\lambda = 6943$ Å.

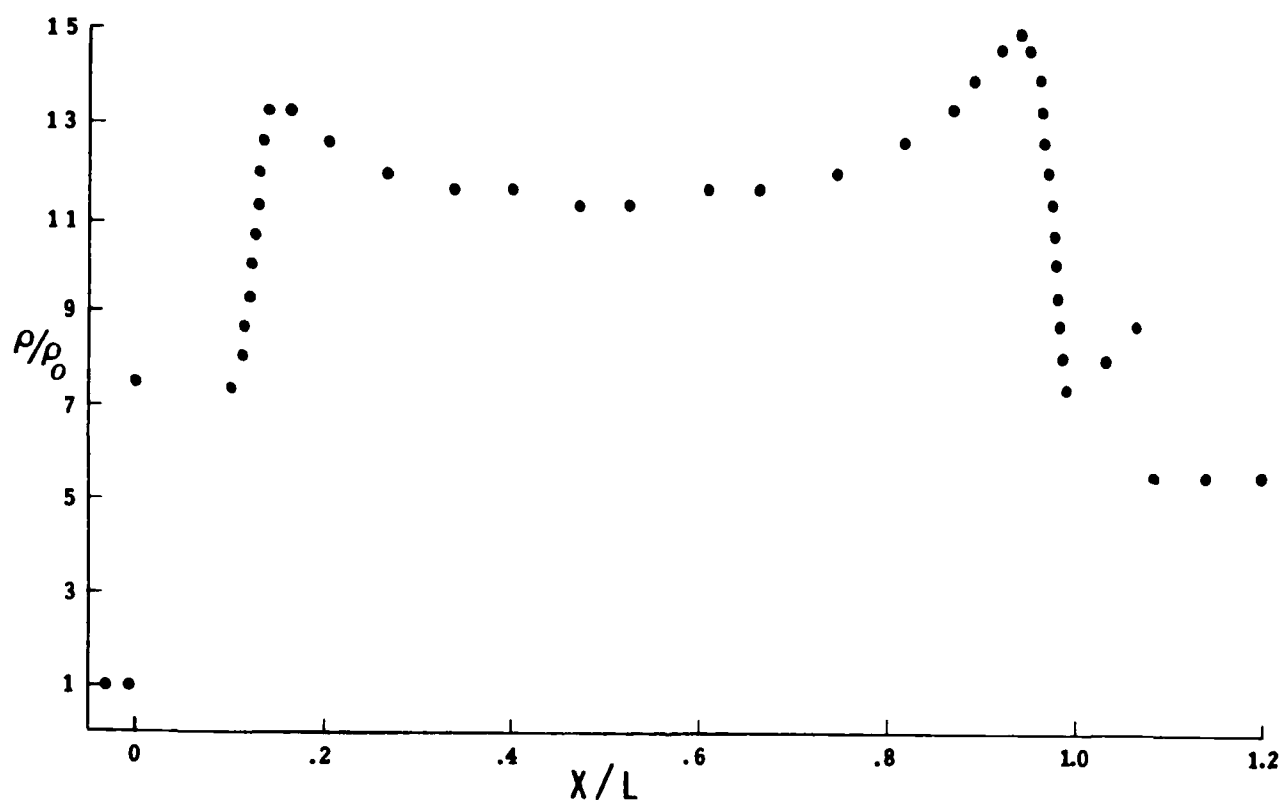
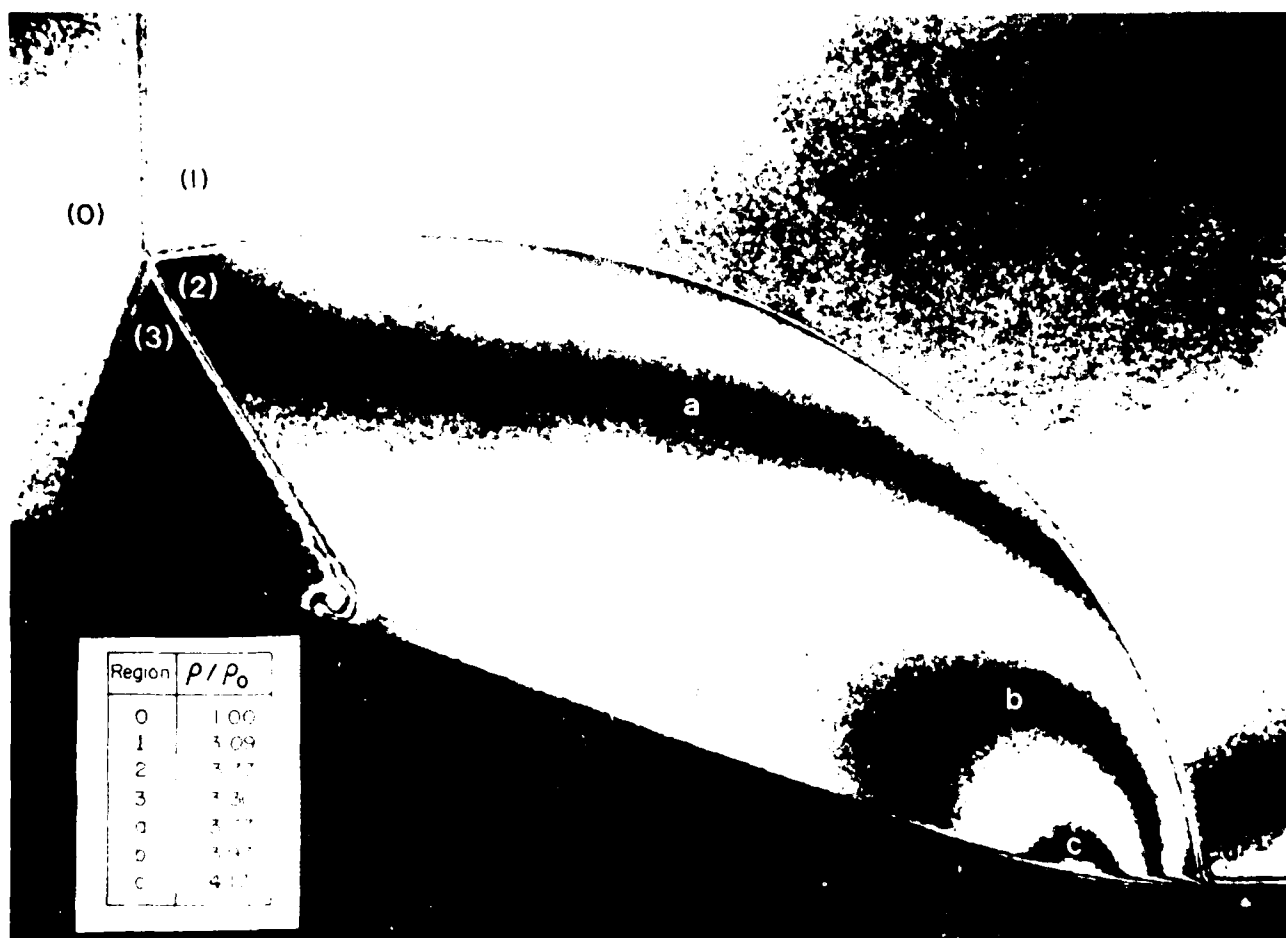
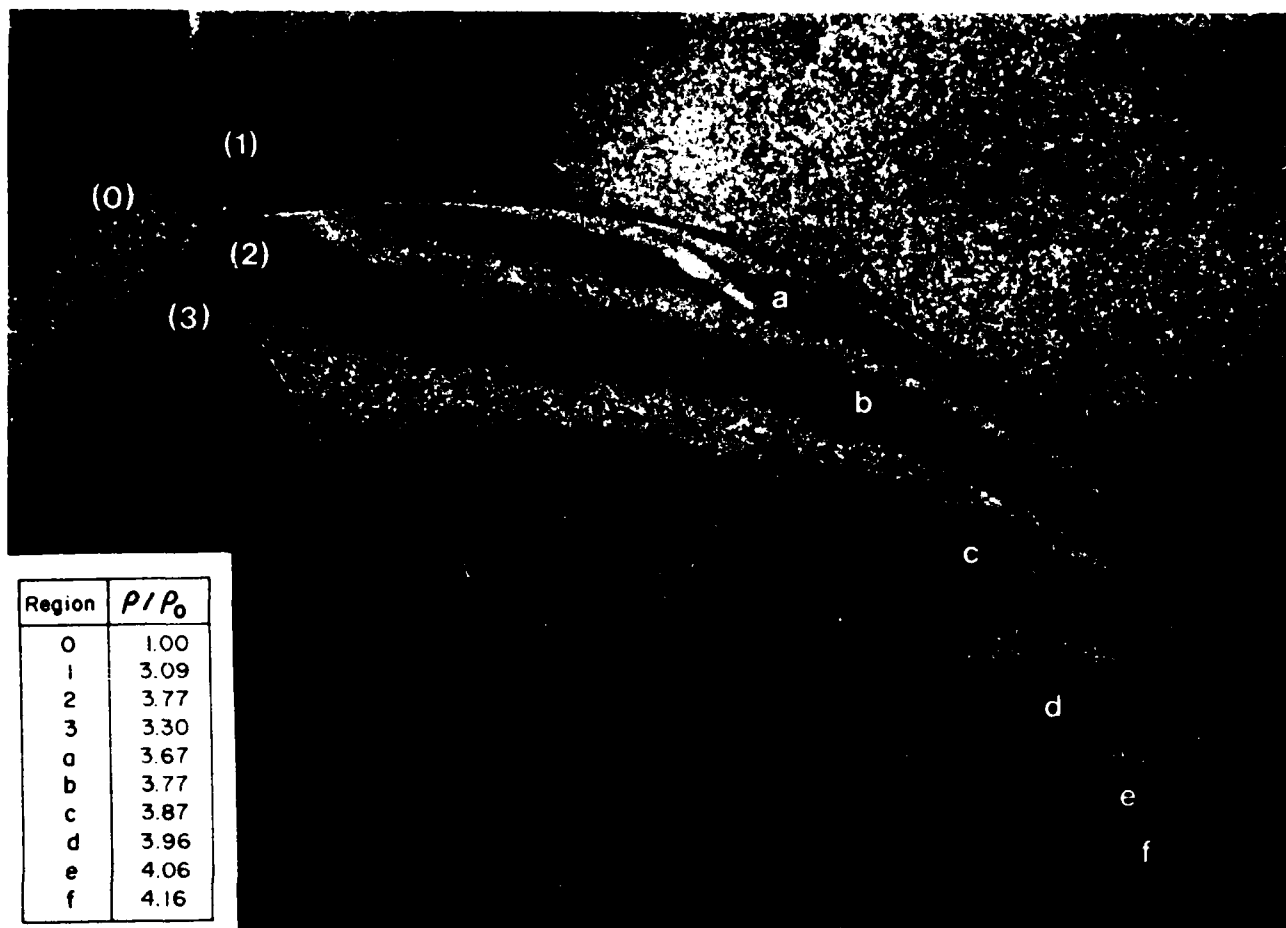


Fig. 29 Wall-density distribution for case 8 of an attached double-Mach reflection in SF_6 .





$$\Delta\sigma/\sigma = 0.10$$

Region	P (torr)	T (K)	ρ (kg/m ³)
(0)	100.0	247.7	0.22
(1)	1255.1	1208.1	0.67
(2)	1750.6	1381.7	0.81
(3)	1750.6	1578.6	0.71

Fig. 30(b) Infinite-fringe interferogram of a detached single-Mach reflection in Ar [32].
 $M_S = 3.20$, $\alpha_w = 20^\circ$, $P_0 = 100.0$ torr,
 $T_0 = 297.7$ K, $\lambda = 3471.5$ Å.



Position	λ/μ
(0)	1.96
(1)	2.03
(2)	3.31
(3)	2.05
a	2.26
b	2.42
c	2.58
d	2.75
e	2.91
f	3.07

$$\lambda/\mu = 0.47$$

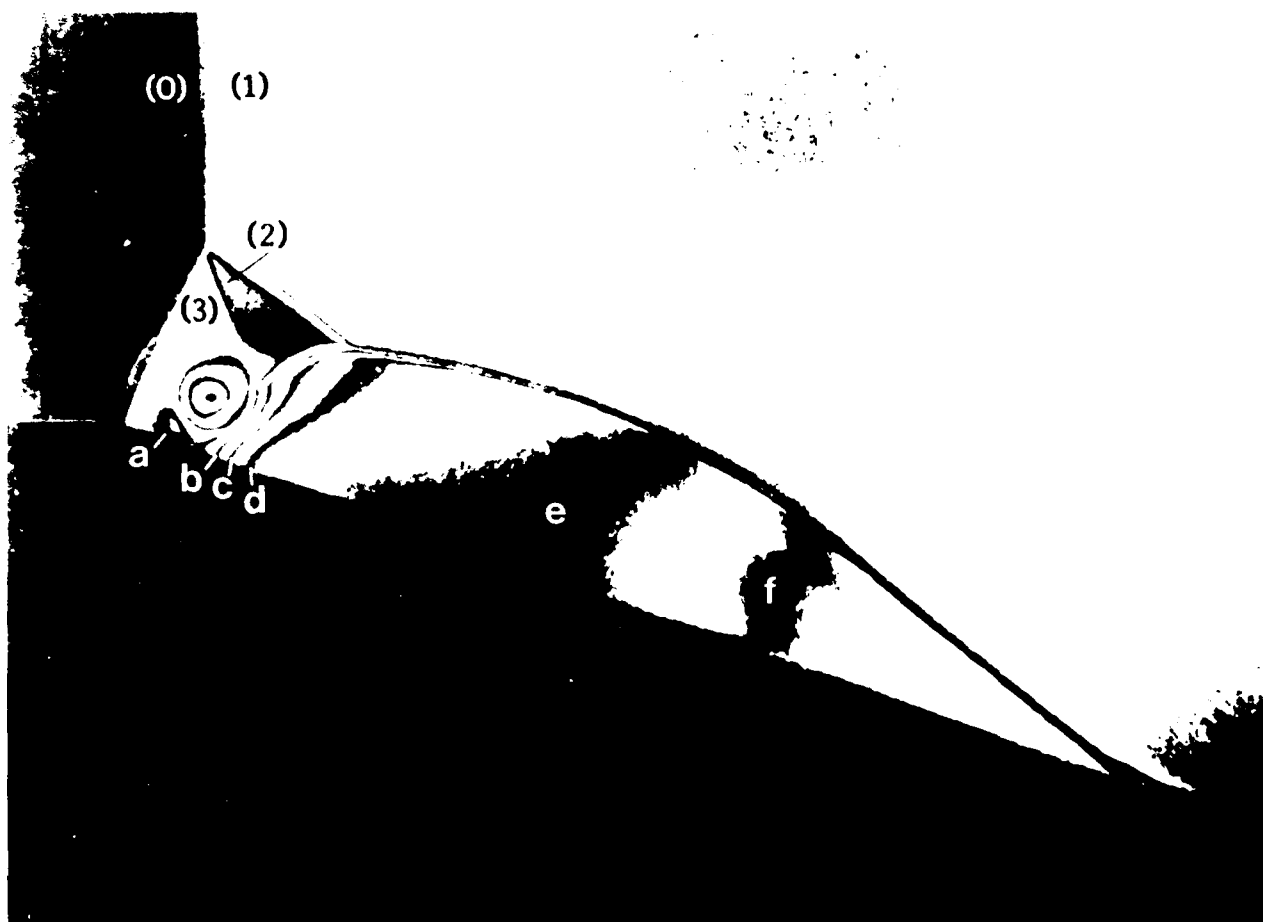
Position	P (torr)	λ/μ	λ/μ (calc)
(0)	60.0	1.957	1.960
(1)	807.2	1.971	2.030
(2)	1195.0	1.119	3.310
(3)	1195.0	1.782	2.050

Fig. 2. Interferogram of an attached drop, $\lambda/\mu = 0.47$, reflection in air. [20].
 $M_1 = 0.002$, $\mu = 20$, $P_2 = 60.0$ torr,
 $\lambda = 694.3 \mu$, $\mu = 694.3 \text{ \AA}$.



Region	P (torr)	T (K)	ρ (kg/m ³)
(0)	30.0	294.0	0.07
(1)	405.0	701.5	0.41
(2)	525.2	732.9	0.51
(3)	525.2	807.7	0.46

Fig. 30(d) Finite-fringe interferogram of an attached complex-Mach reflection in CO₂ [24].
 $M_S = 3.43$, $\theta_w = 20.3^\circ$, $P_0 = 30.0$ torr,
 $T_0 = 294.0$ K, $\lambda = 6943$ Å.

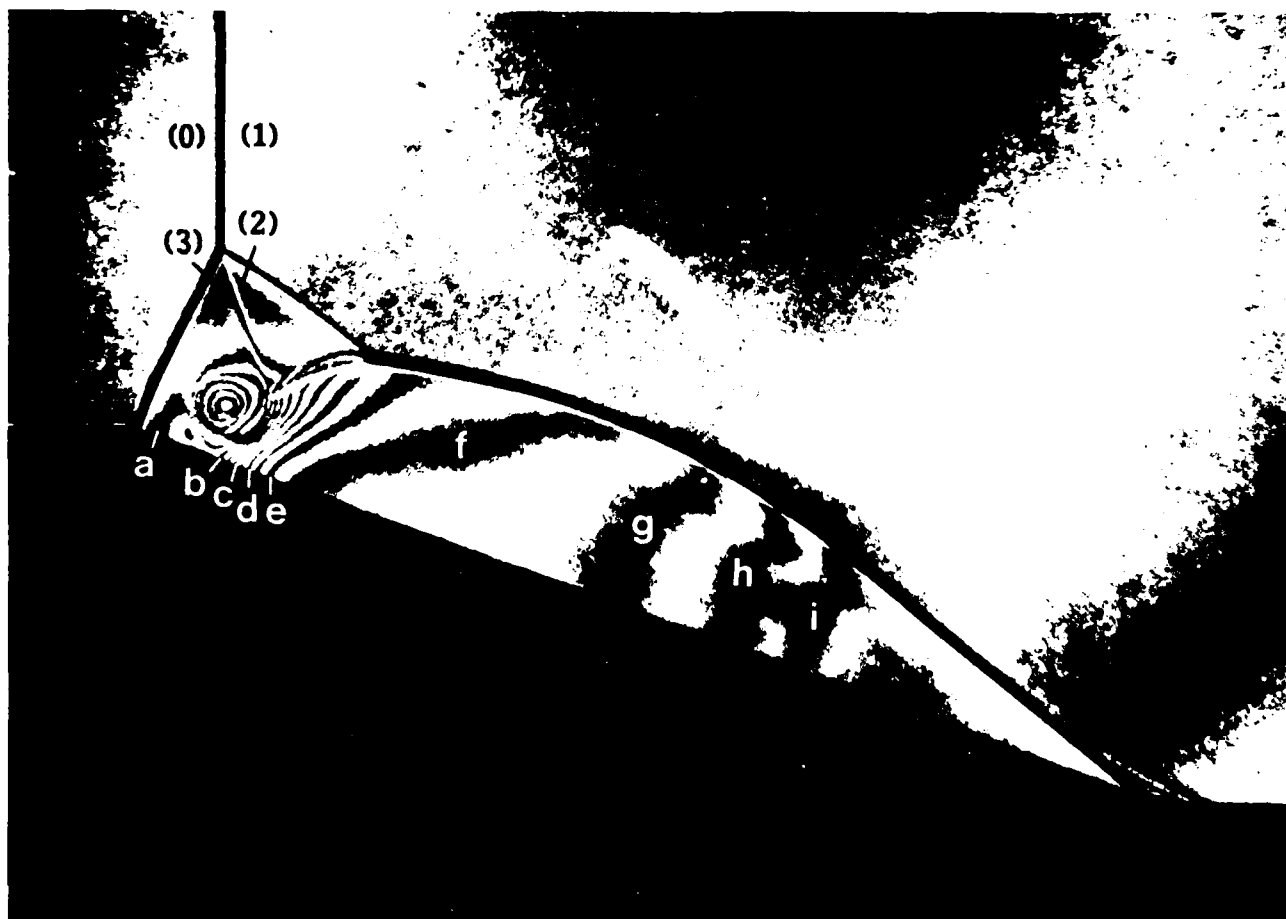


Скорость вращения, об/мин	Скорость течения, м/сек	Скорость течения, м/сек	Скорость течения, м/сек
1000	0,04	0,04	0,04
1500	0,04	0,04	0,04
2000	0,04	0,04	0,04
2500	0,04	0,04	0,04
3000	0,04	0,04	0,04
3500	0,04	0,04	0,04
4000	0,04	0,04	0,04
4500	0,04	0,04	0,04
5000	0,04	0,04	0,04
5500	0,04	0,04	0,04
6000	0,04	0,04	0,04
6500	0,04	0,04	0,04
7000	0,04	0,04	0,04
7500	0,04	0,04	0,04
8000	0,04	0,04	0,04
8500	0,04	0,04	0,04
9000	0,04	0,04	0,04
9500	0,04	0,04	0,04
10000	0,04	0,04	0,04

1,00

Скорость вращения, об/мин	Скорость течения, м/сек	Скорость течения, м/сек	Скорость течения, м/сек
1000	0,04	0,04	0,04
1500	0,04	0,04	0,04
2000	0,04	0,04	0,04
2500	0,04	0,04	0,04
3000	0,04	0,04	0,04
3500	0,04	0,04	0,04
4000	0,04	0,04	0,04
4500	0,04	0,04	0,04
5000	0,04	0,04	0,04
5500	0,04	0,04	0,04
6000	0,04	0,04	0,04
6500	0,04	0,04	0,04
7000	0,04	0,04	0,04
7500	0,04	0,04	0,04
8000	0,04	0,04	0,04
8500	0,04	0,04	0,04
9000	0,04	0,04	0,04
9500	0,04	0,04	0,04
10000	0,04	0,04	0,04

Скорость течения, м/сек, при скорости вращения, об/мин, 1000, 1500, 2000, 2500, 3000, 3500, 4000, 4500, 5000, 5500, 6000, 6500, 7000, 7500, 8000, 8500, 9000, 9500, 10000.



Region	x/λ
(0)	1.00
(1)	8.59
(2)	10.54
(3)	9.97
a	9.97
b	10.77
c	12.37
d	13.98
e	15.58
f	16.38
g	17.18
h	17.99
i	18.79

$$x/\lambda = 0.80$$

Region	P (torr)	T (K)	ρ (kg/m ³)
(0)	4.6	297.2	0.04
(1)	59.1	445.9	0.31
(2)	73.6	452.6	0.38
(3)	73.6	478.7	0.36

Fig. 30(f) Infinite-fringe interferogram of an attached double-Mach reflection in SF_6 .
 $M_0 = 3.51$, $\gamma_0 = 1.1$, $P_0 = 4.6$ torr,
 $T_0 = 297.2$ K, $\lambda = 671.5$ Å.

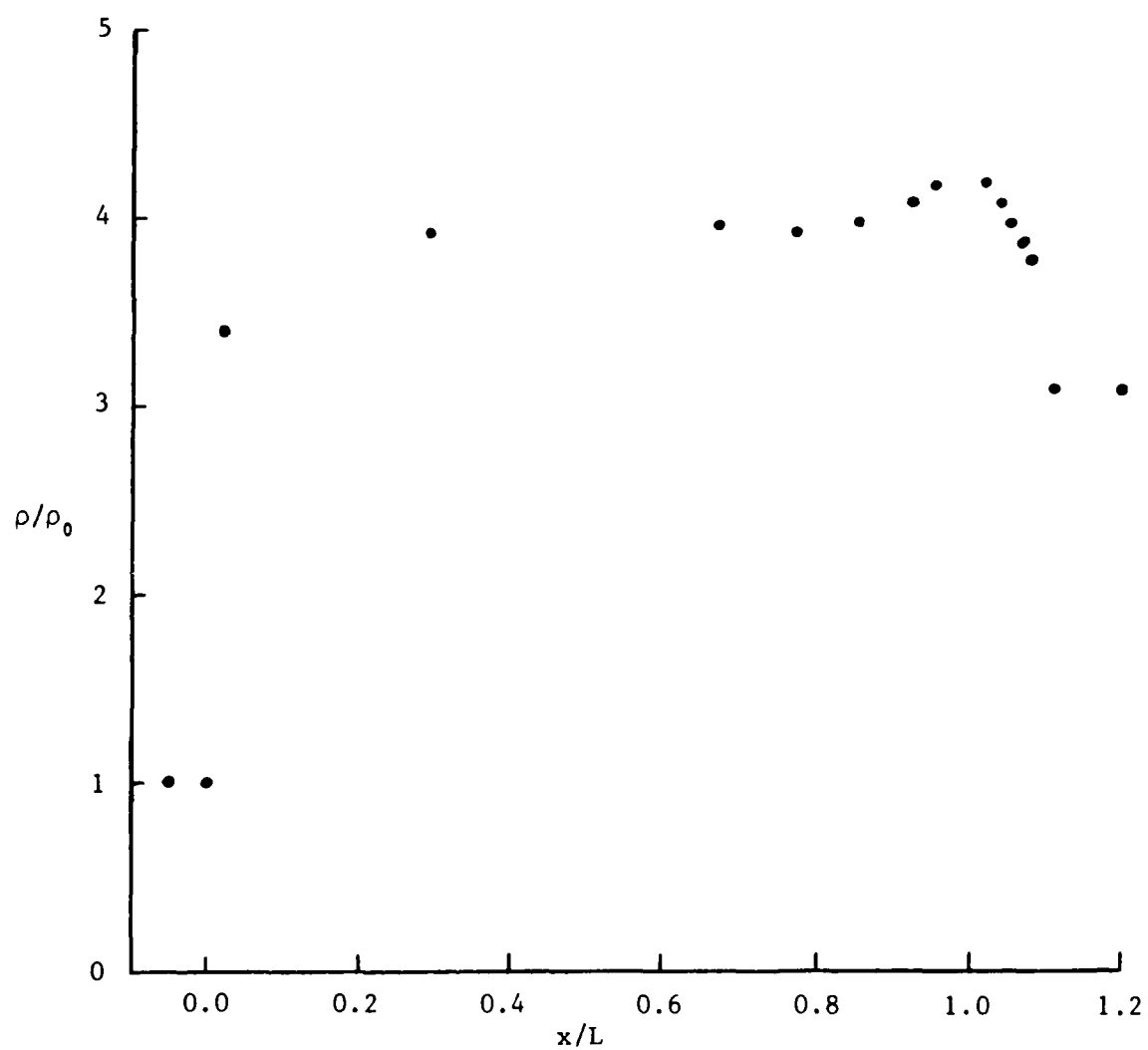


Fig. 31(a) Wall-density distribution for case 9 of a detached single-Mach reflection in Ar [32].

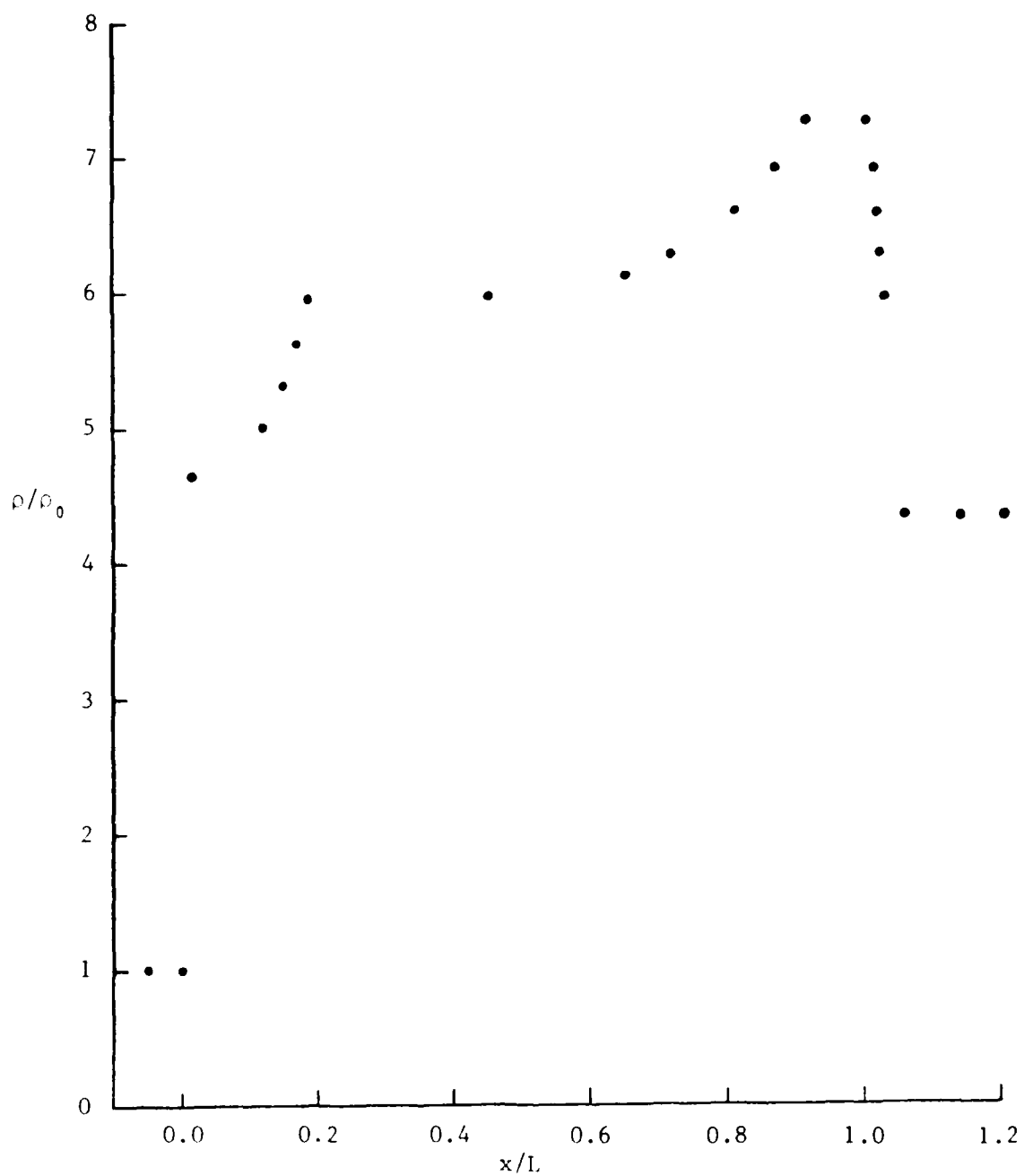


Fig. 31(b) Wall-density distribution for case 9 of an attached complex-Mach reflection in air [26].

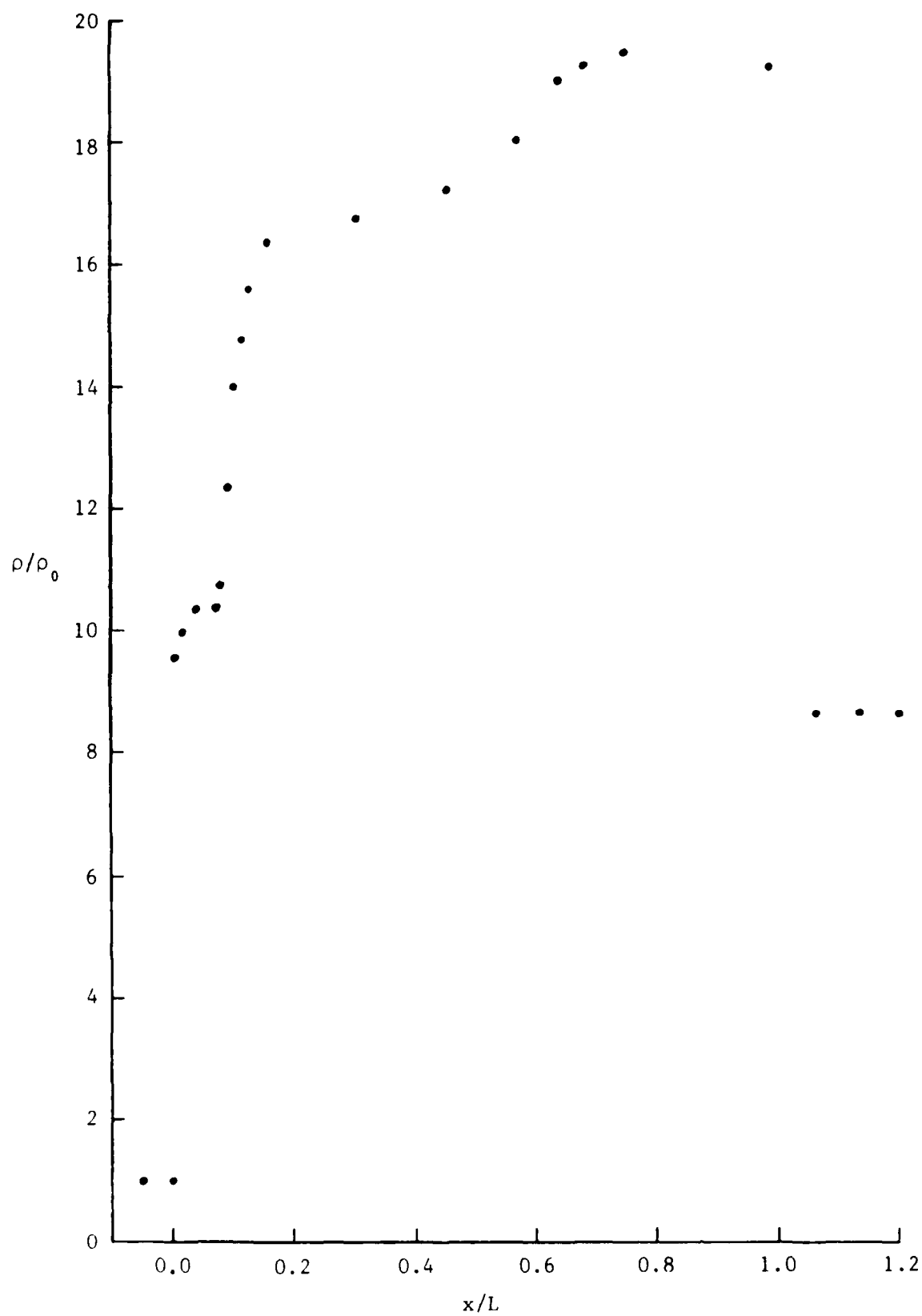


Fig. 31(c) Wall-density distribution for case 9 of an attached double-Mach reflection in SF_6 .

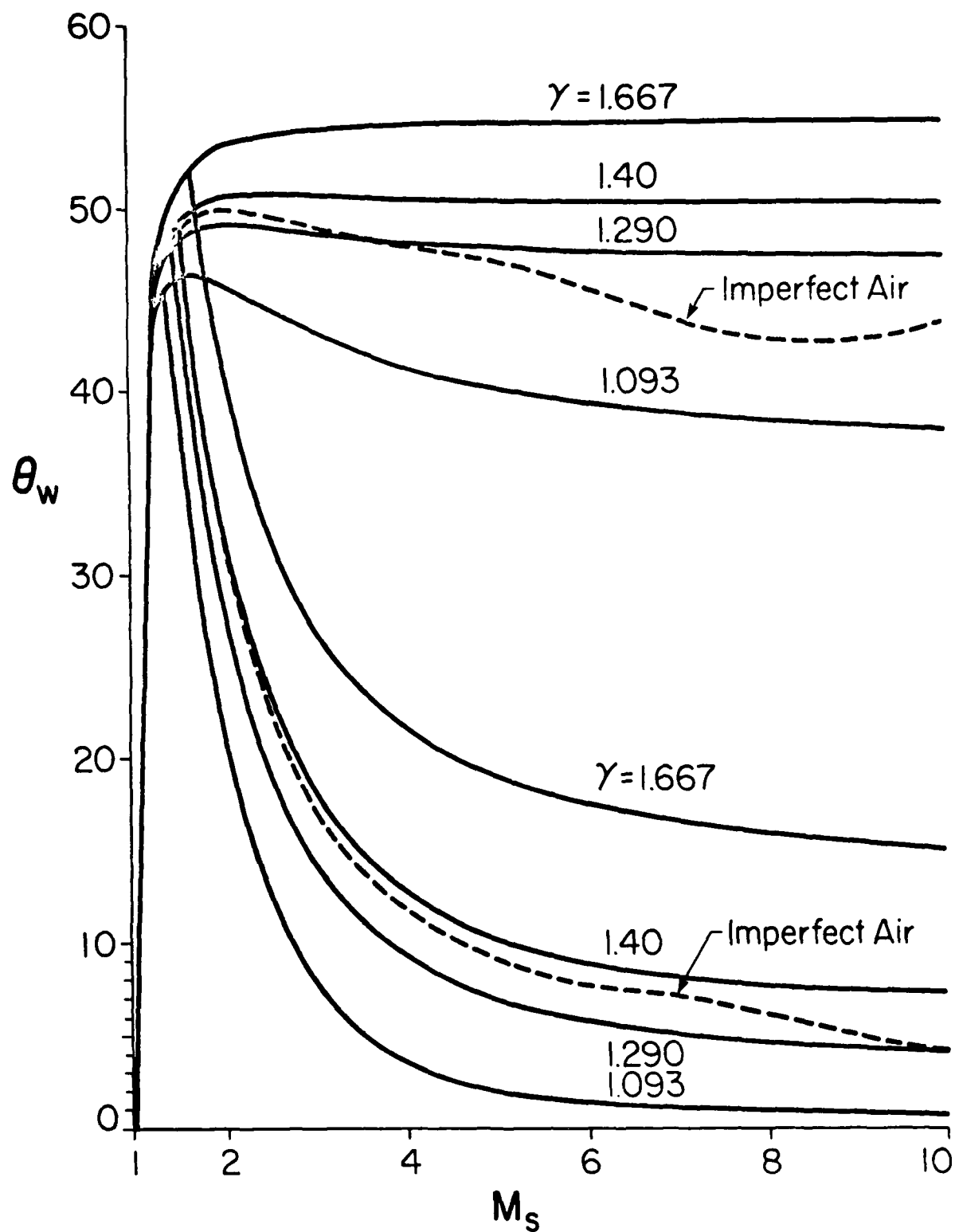


Fig. 31(d) Transition lines for RR \nleftrightarrow MR and SMR \nleftrightarrow CMR for perfect gases with different γ and imperfect air [25].

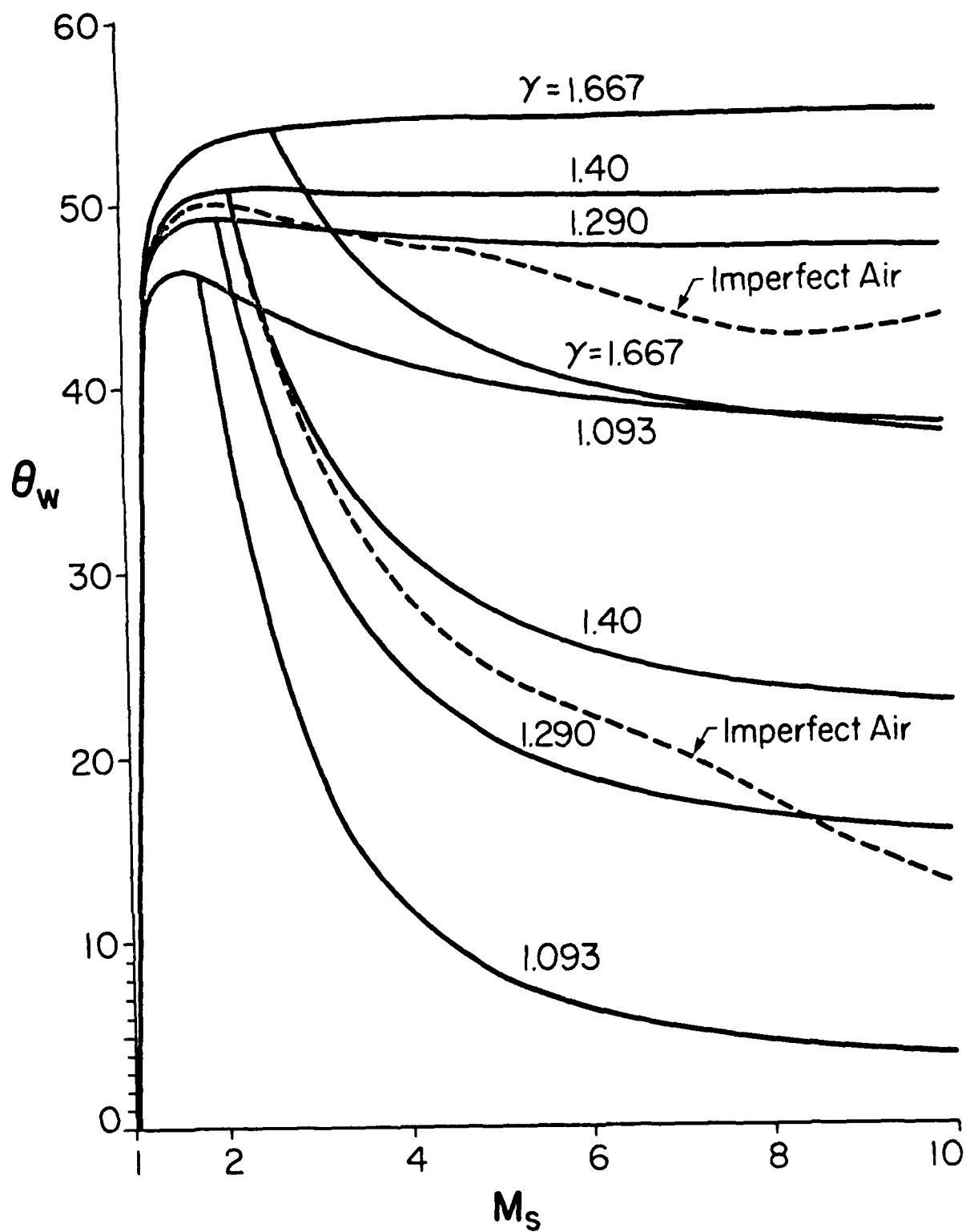


Fig. 31(e) Transition lines for $RR \rightleftharpoons MR$ and $CMR \rightleftharpoons DMR$ for perfect gases with different γ and imperfect air [25].

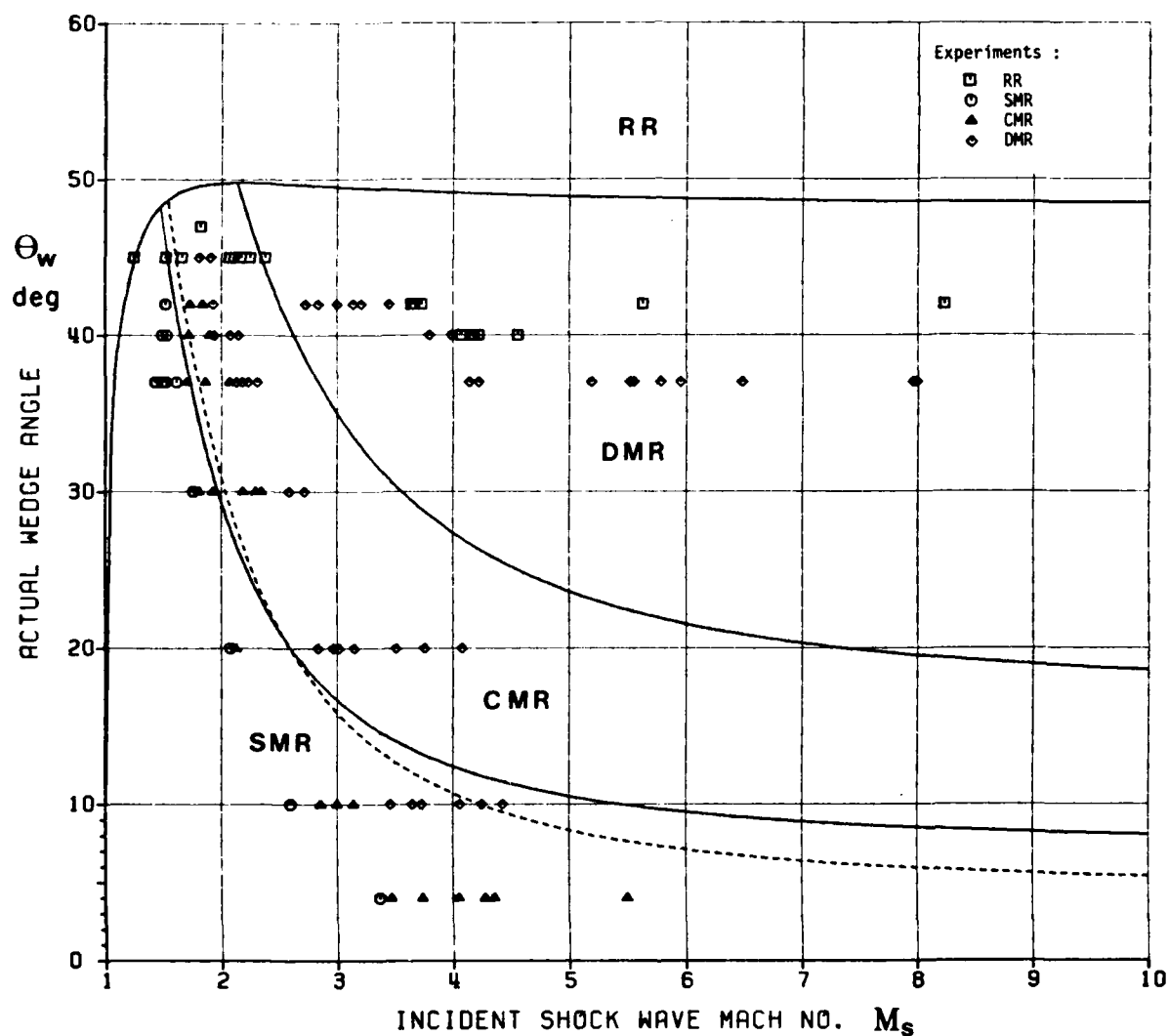


Fig. 32(a) Comparison of predicted domains of various types of reflection and experimental results in the $(M_s - \Theta_w)$ plane for frozen SF_6 with $\gamma = 4/3$.
 SMR \nearrow CMR transition boundaries :
 solid line is $\delta = 90^\circ$, dashed line is $M_{2T} = 1$.

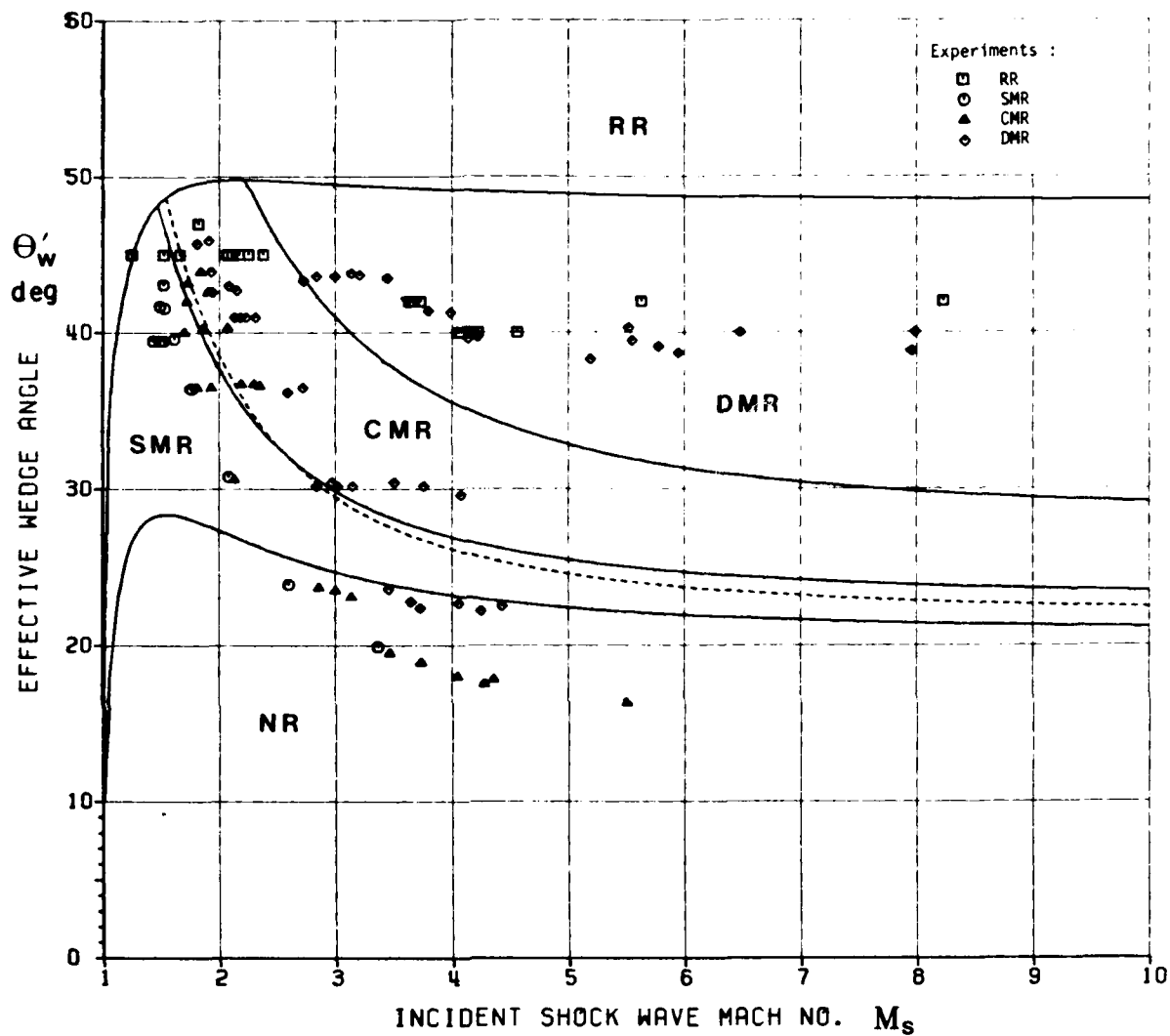


Fig. 32(b) Comparison of predicted domains of various types of reflection and experimental results in the $(M_s - \theta_w)$ plane for frozen SF_6 with $\gamma = 4/3$.
 SMR & CMR transition boundaries :
 solid line is $\delta = 90^\circ$, dashed line is $M_{2T} = 1$.

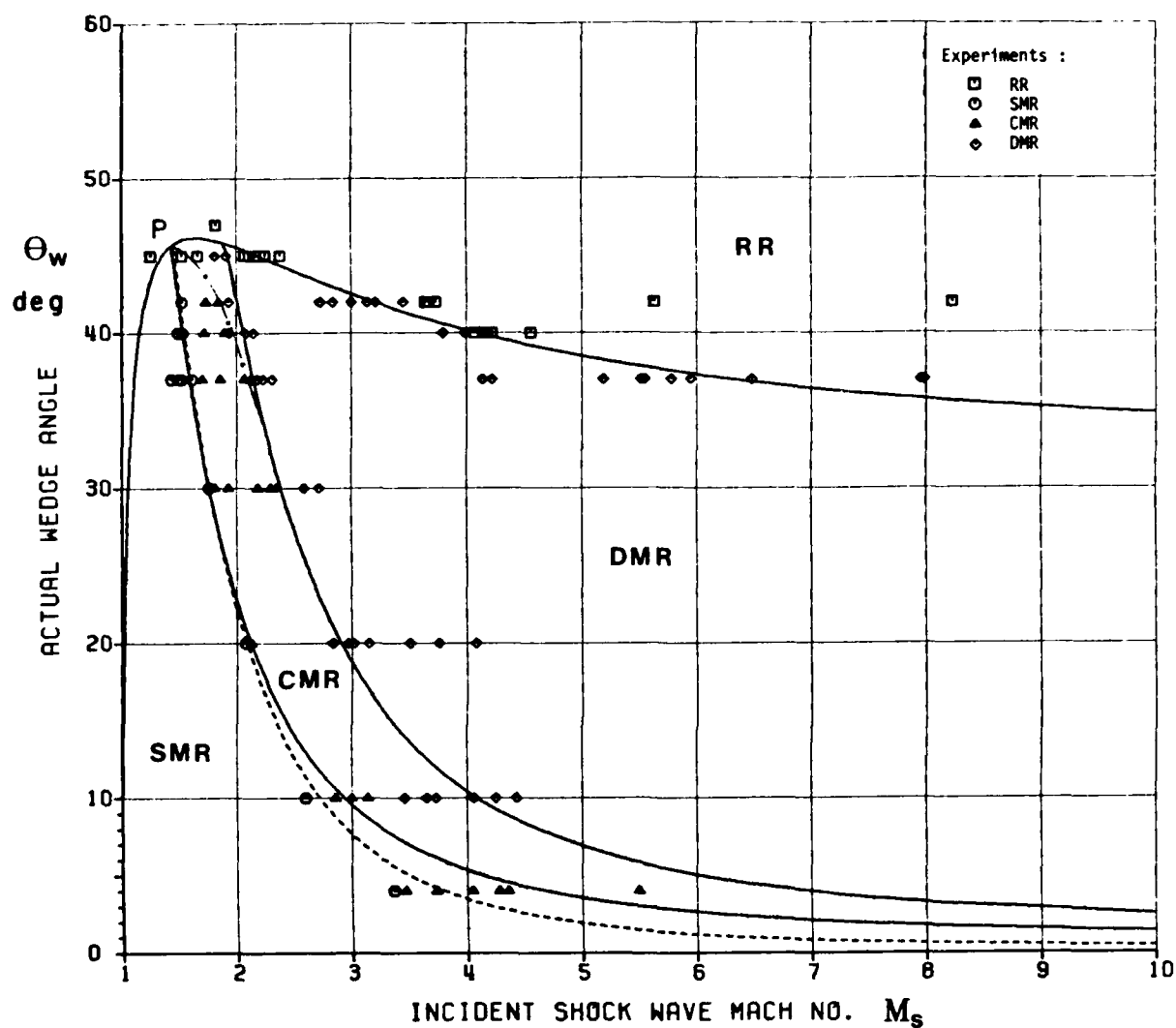


Fig. 33(a) Comparison of predicted domains of various types of reflection and experimental results in the $(M_s - \theta_w)$ plane for vibrational equilibrium SF_6 .
 SMR \nleftrightarrow CMR transition boundaries :
 solid line is $\delta = 90^\circ$, dashed line is $M_{2T} = 1$.

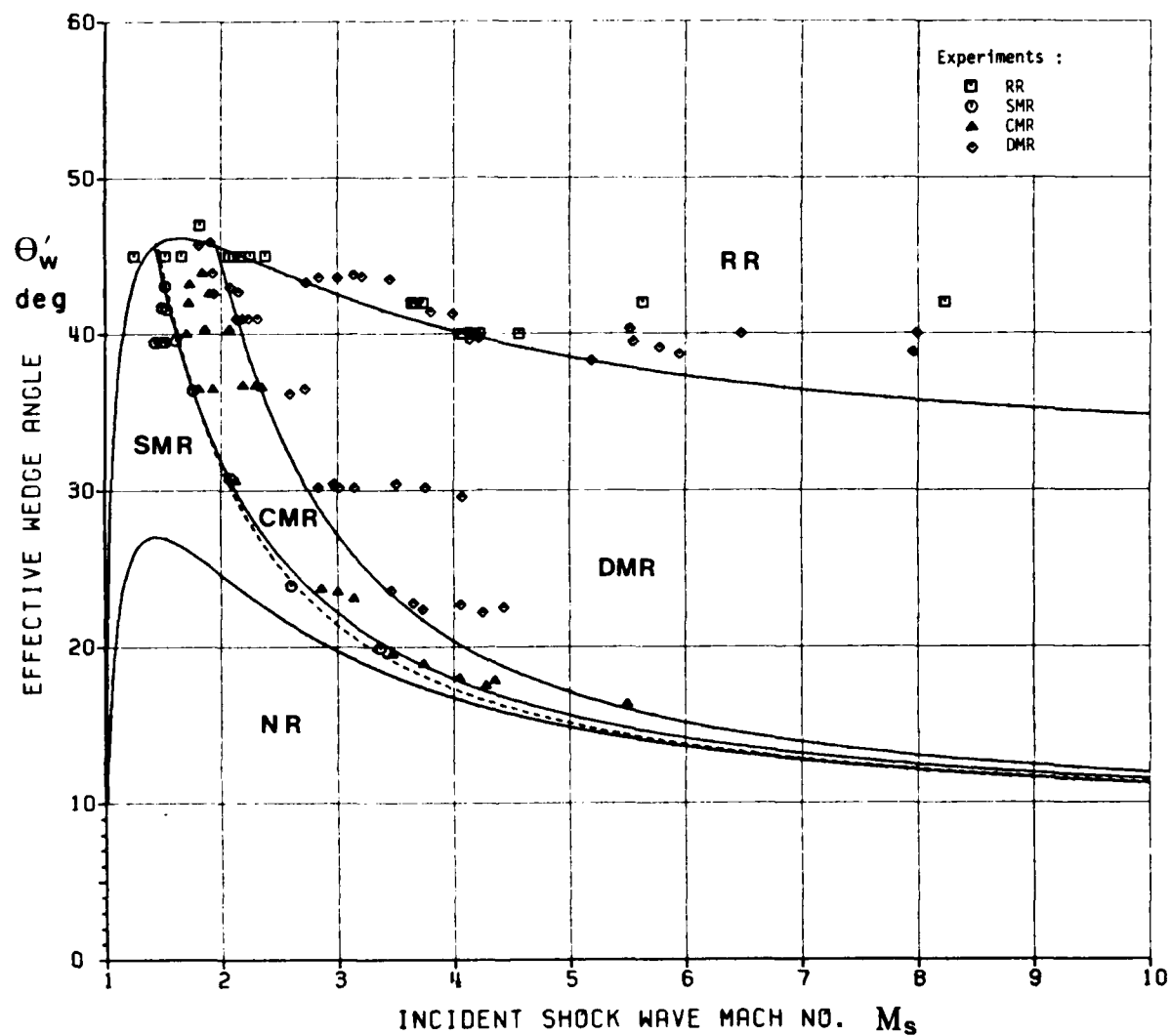


Fig. 33(b) Comparison of predicted domains of various types of reflection and experimental results in the $(M_s - \theta_w')$ plane for vibrational equilibrium SF_6 .
 SMR & CMR transition boundaries :
 solid line is $\delta = 90^\circ$, dashed line is $M_{2T} = 1$.

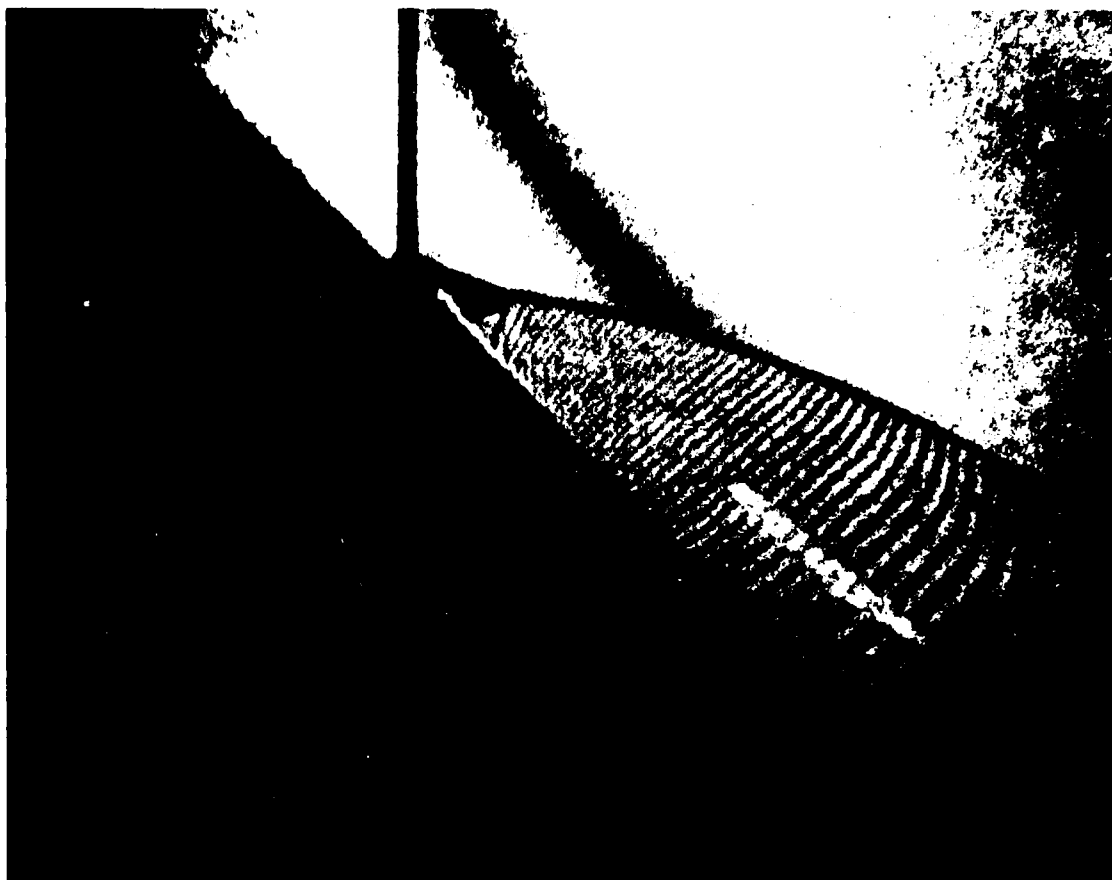


Fig. 34 Infinite-fringe interferogram of a double-Mach reflection with $\chi < 1^\circ$ in SF_6 .
 $M_s = 1.81$, $\theta_w = 45^\circ$, $P_0 = 101.2$ torr,
 $T_0 = 297.1$ K, $\lambda = 3471.5$ Å.

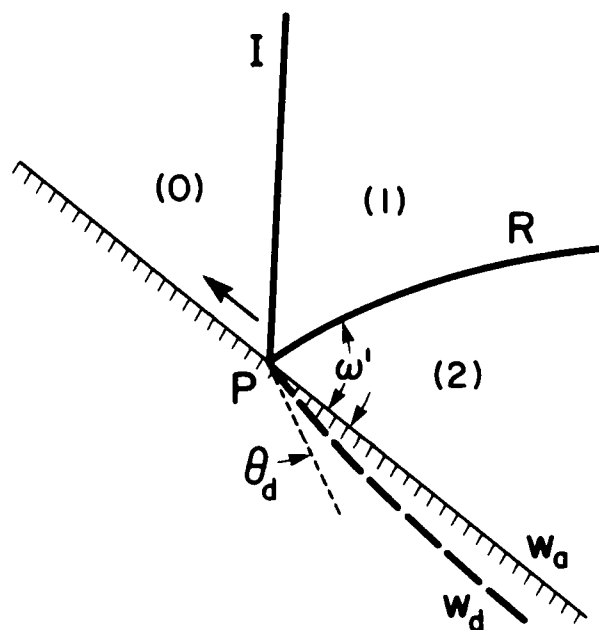
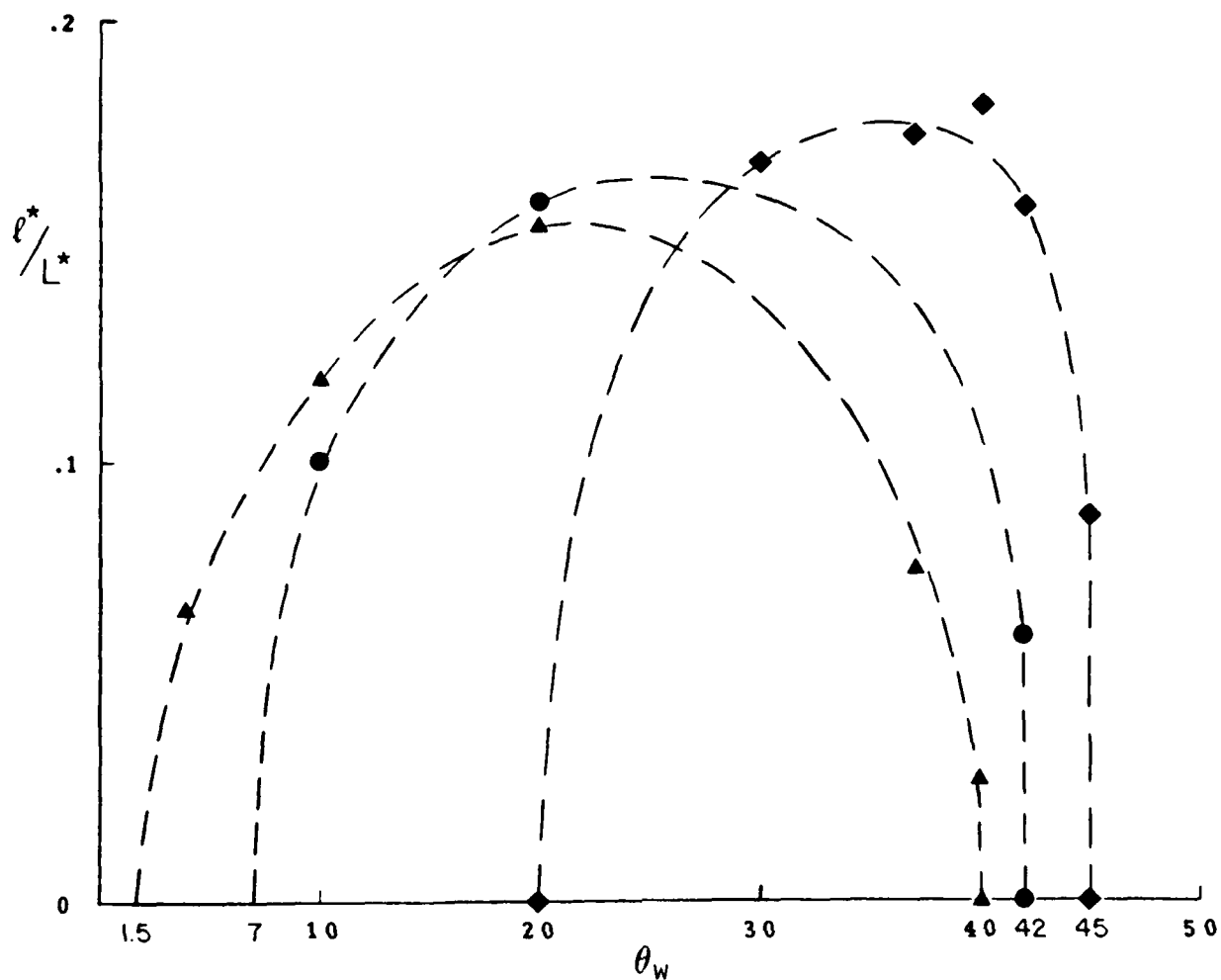


Fig. 35 Boundary-layer displacement effect behind reflection point P.

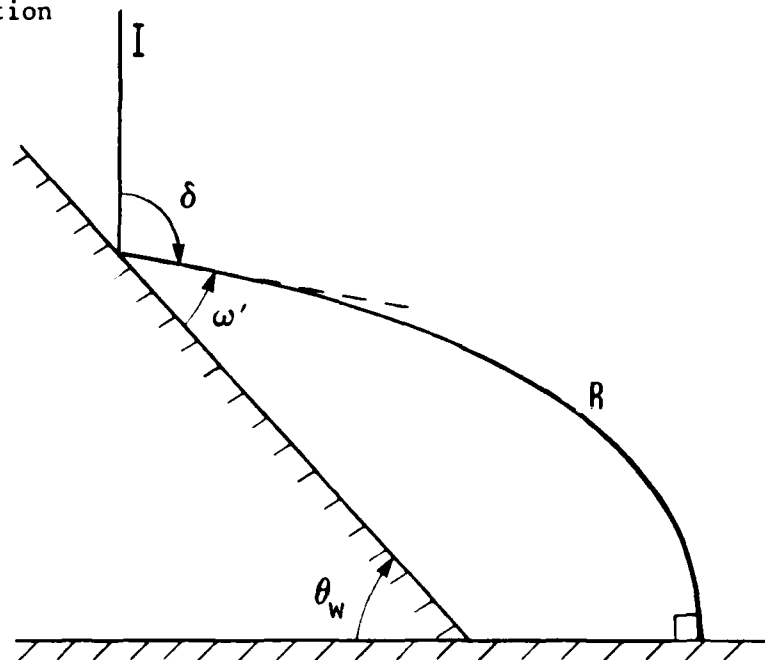
I - incident shock wave; R - reflected shock wave;
 θ_d - displacement angle; w_a - actual wedge surface;
 w_d - displaced wedge surface; ω' - reflection angle.



EXP	M_S	$\theta_w (^{\circ})$	ℓ^*/L^*
120	2.07	45	0.000
117	1.91	45	0.087
21	1.93	42	0.157
8	1.94	40	0.181
61	2.13	37	0.173
128	1.93	30	0.168
131	2.08	20	0.000
25	3.02	42	0.000
107	3.00	42	0.060
134	3.02	20	0.158
151	3.00	10	0.010
145	4.07	40	0.000
147	4.00	40	0.028
62	4.14	37	0.075
139	4.08	20	0.153
156	4.06	10	0.118
159	4.05	4	0.066

Fig. 36 Measured ratio ℓ^*/L^* vs. wedge angle for several Mach numbers in SF_6 . See Fig. 9(a) for the definition of ℓ^* and L^* .

a) Regular Reflection



b) Mach Reflection

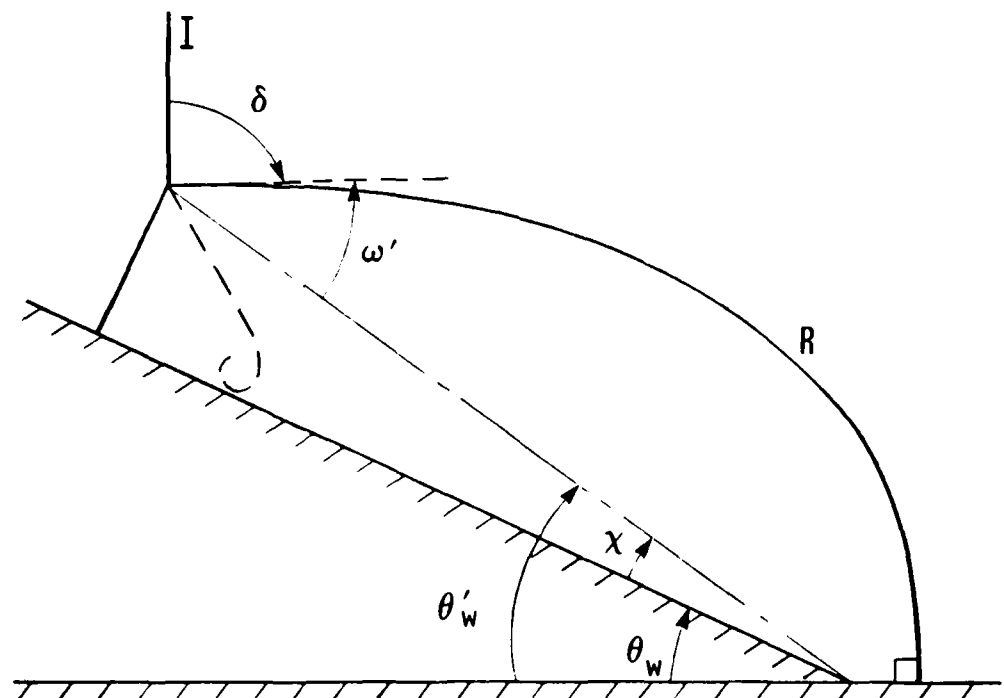


Fig. 37 Definition of the angles δ and ω' .

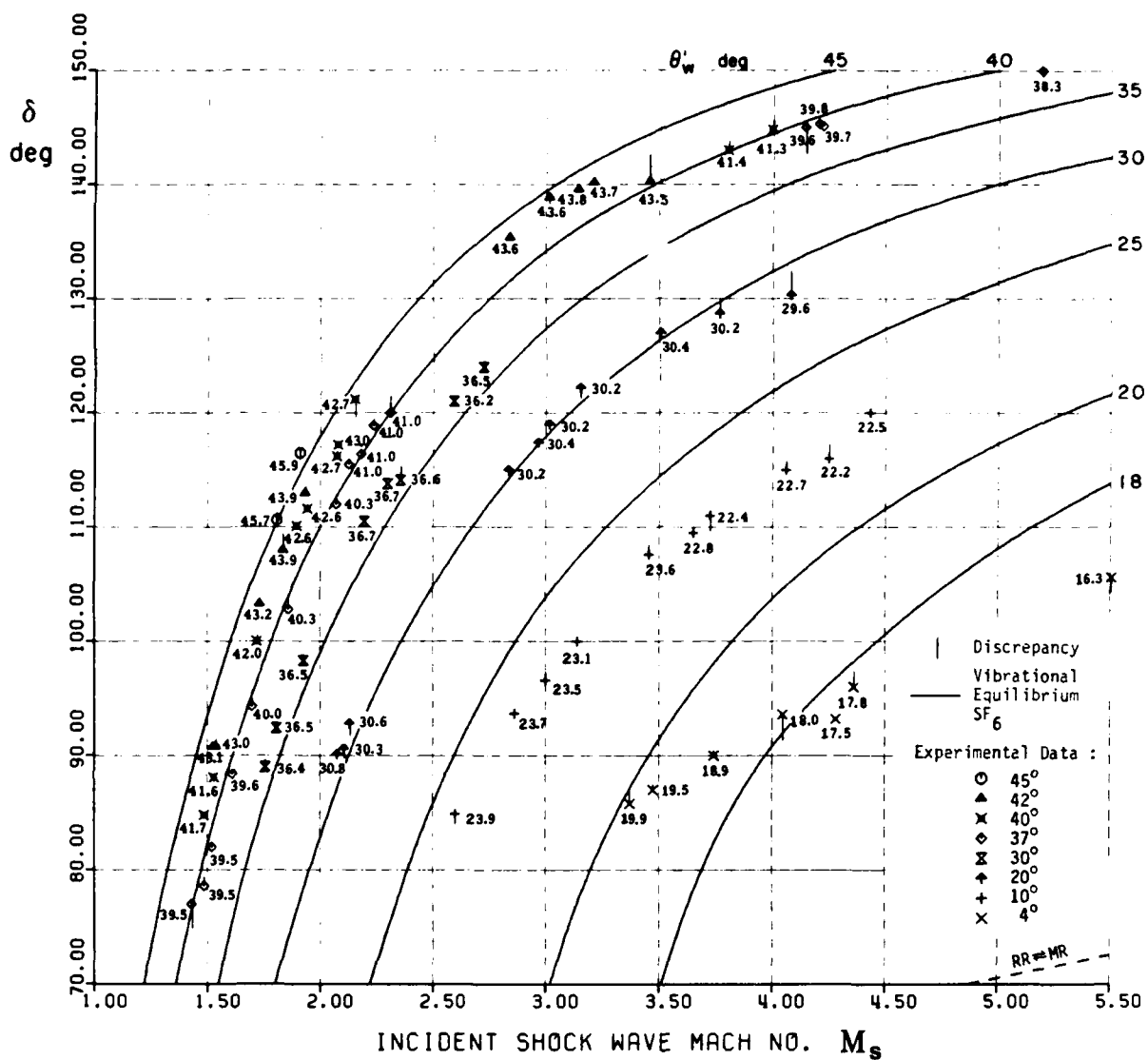


Fig. 38 Variation of δ vs M_s at fixed θ_w' for vibrational equilibrium SF_6 , $P_0 = 15$ torr, $T_0 = 300$ K.

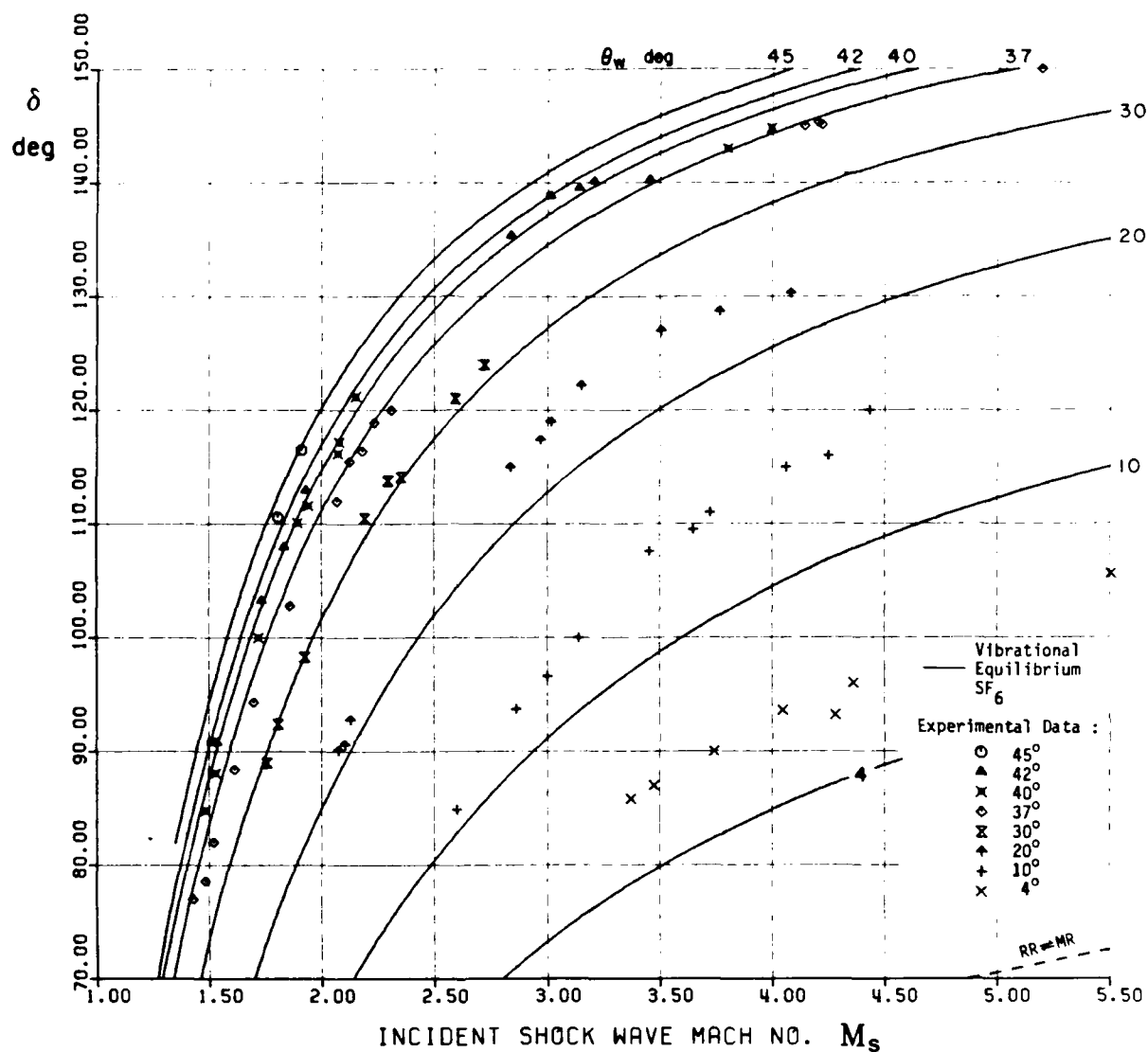


Fig. 39 Variation of δ vs M_s at fixed θ_w for vibrational equilibrium SF_6 , $P_0^s = 15$ torr, $T_0 = 300$ K.

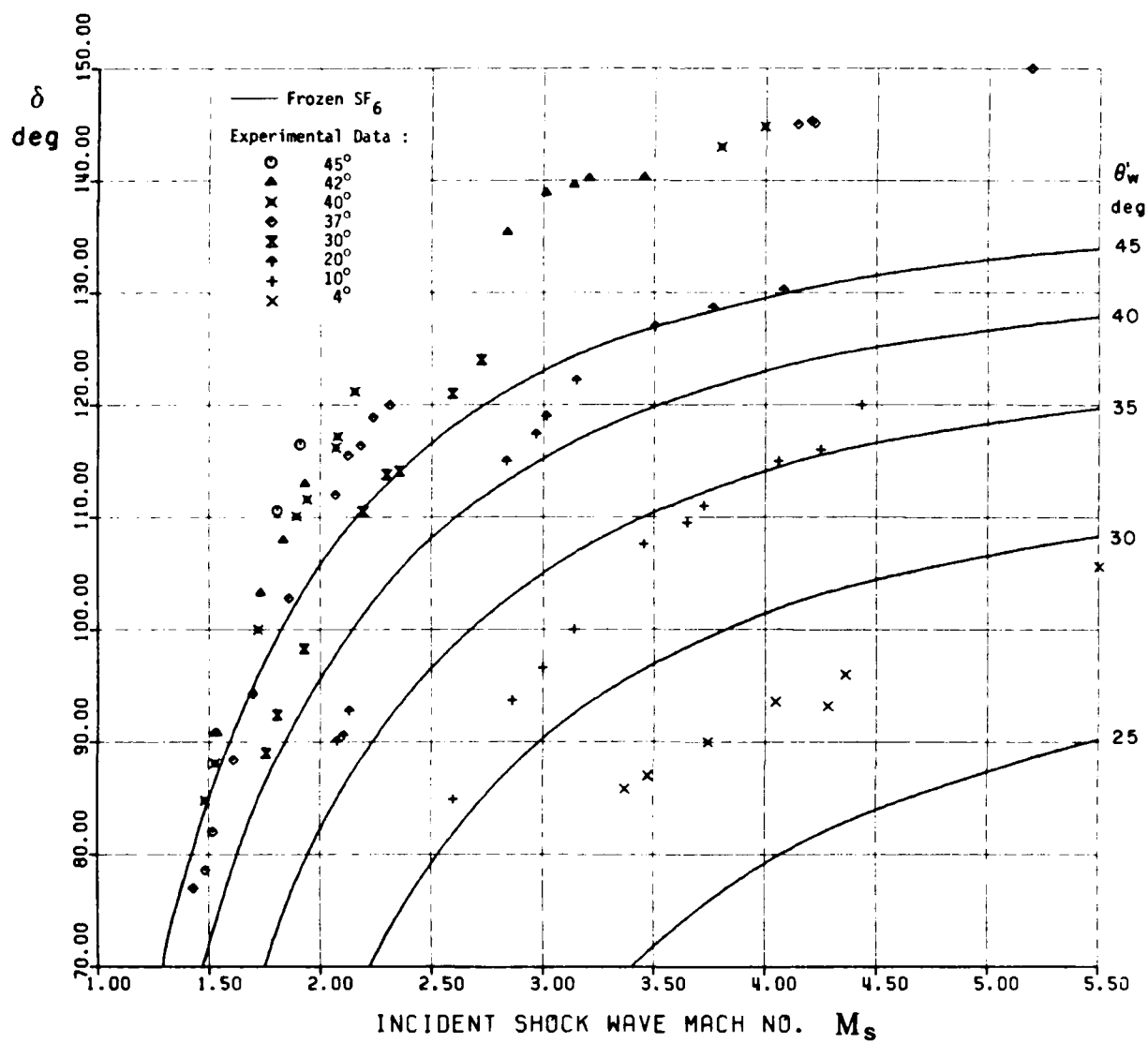


Fig. 40 Variation of δ vs M_s at fixed θ'_w for frozen SF_6 with $\gamma = 4/3$, $P_0 = 15$ torr, $T_0 = 300$ K.

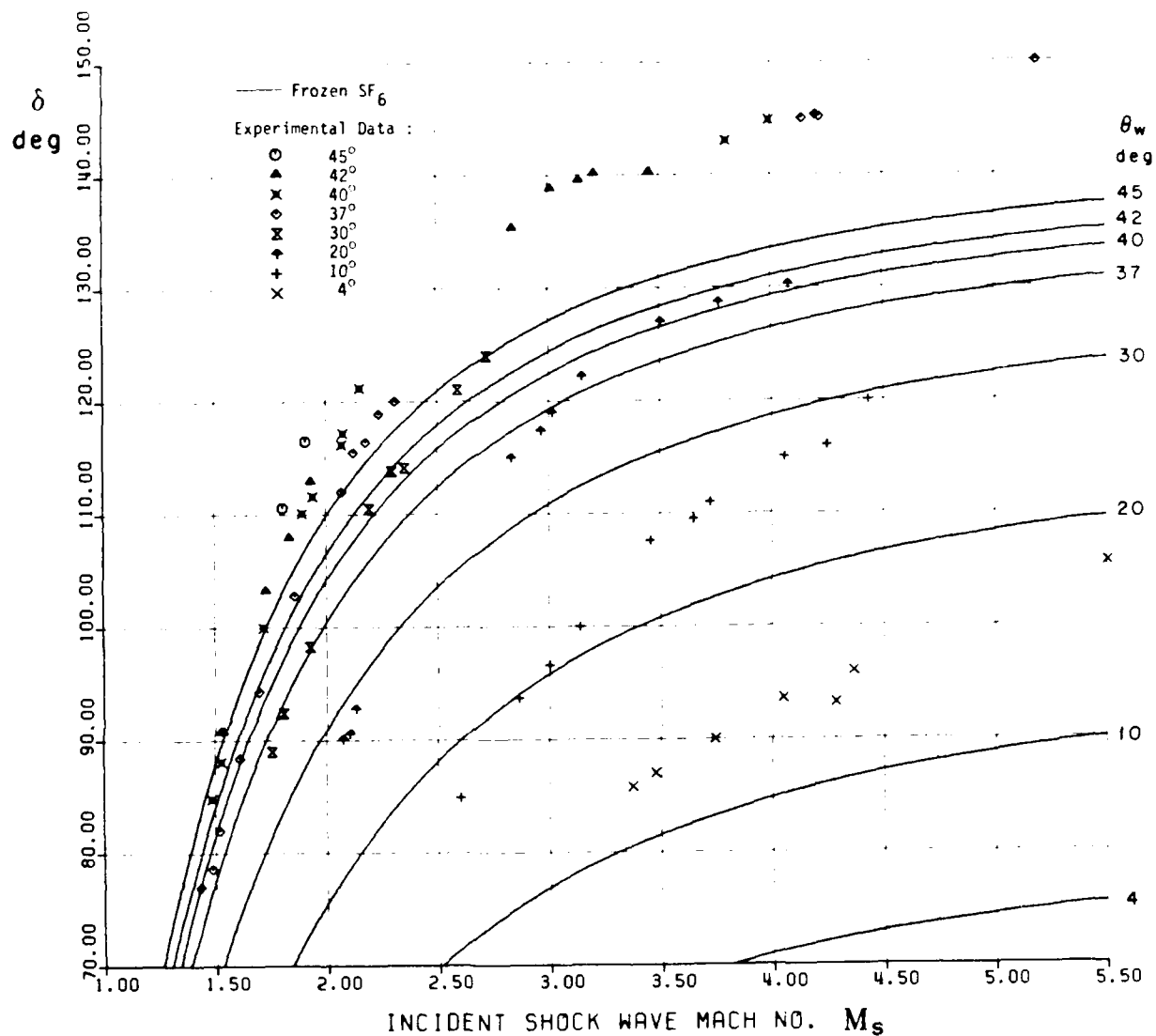


Fig. 41 Variation of δ vs M_s at fixed θ_w for frozen SF_6 with $\gamma = 4/3$, $P_0 = 15$ torr, $T_0 = 300$ K.

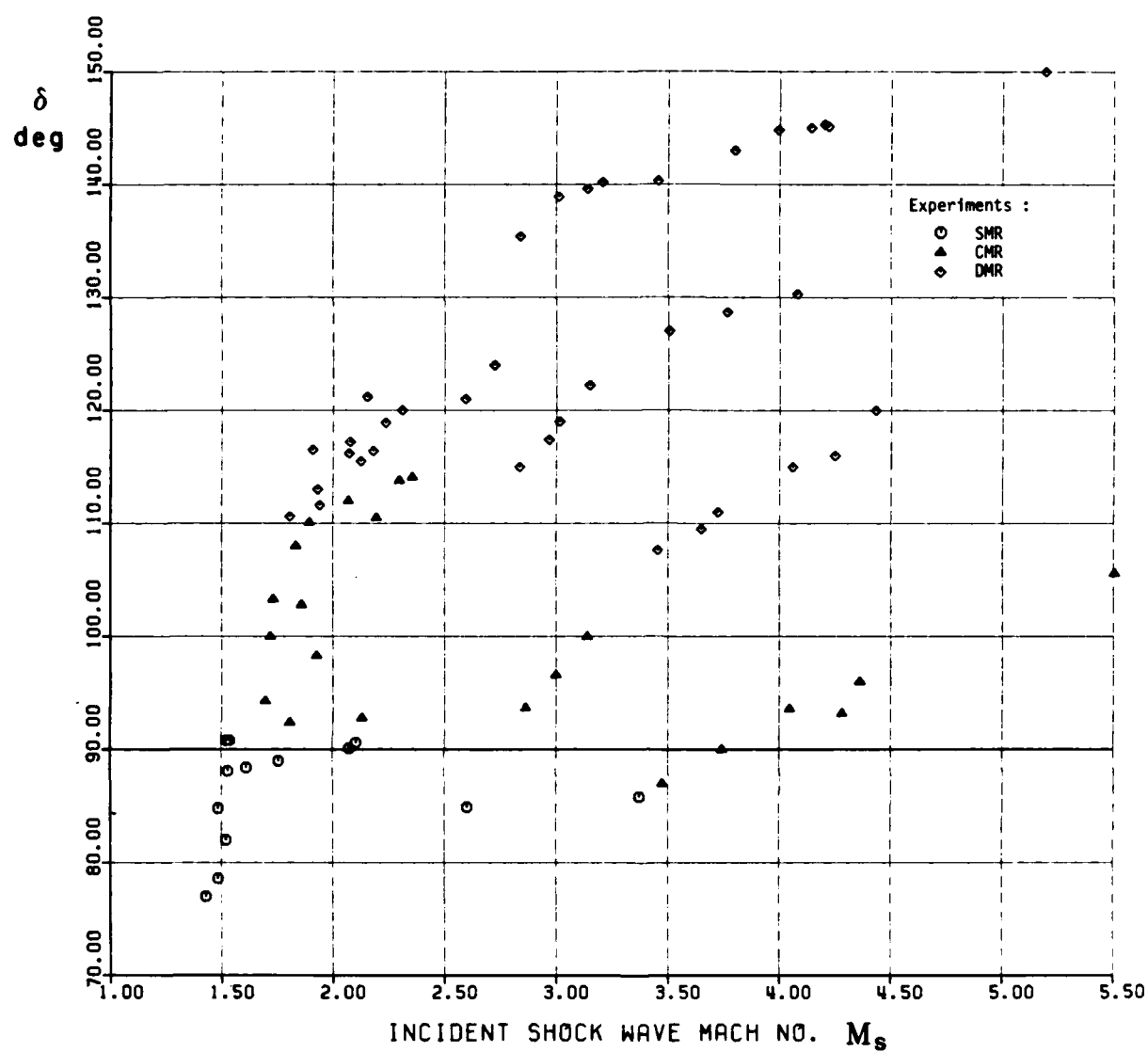


Fig. 42 Experimental relations between δ and type of reflection in SF_6 .

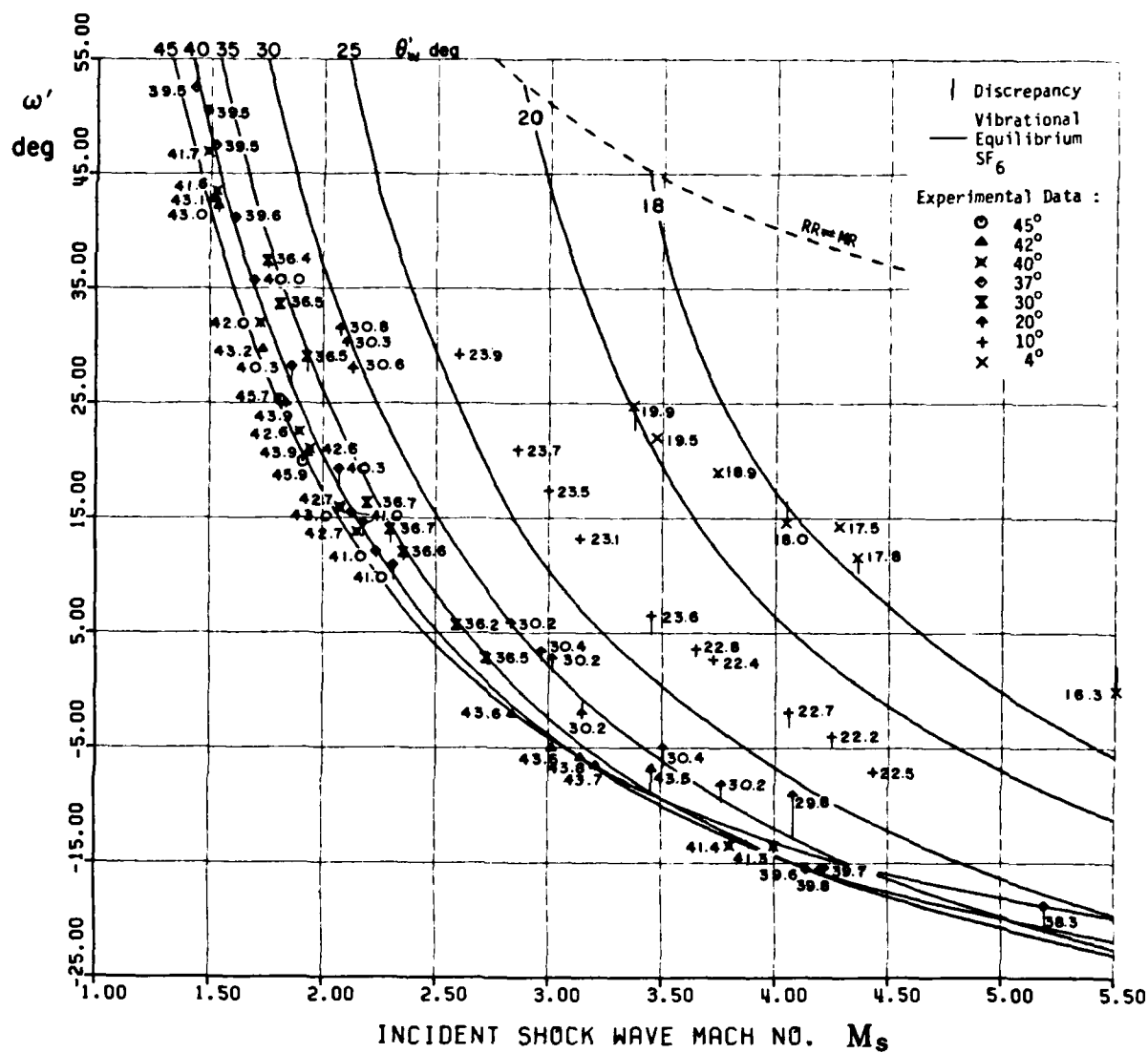


Fig. 43 Variation of ω' vs M_s at fixed θ_w' for vibrational equilibrium SF_6 , $P_0 = 15$ torr, $T_0 = 300$ K.

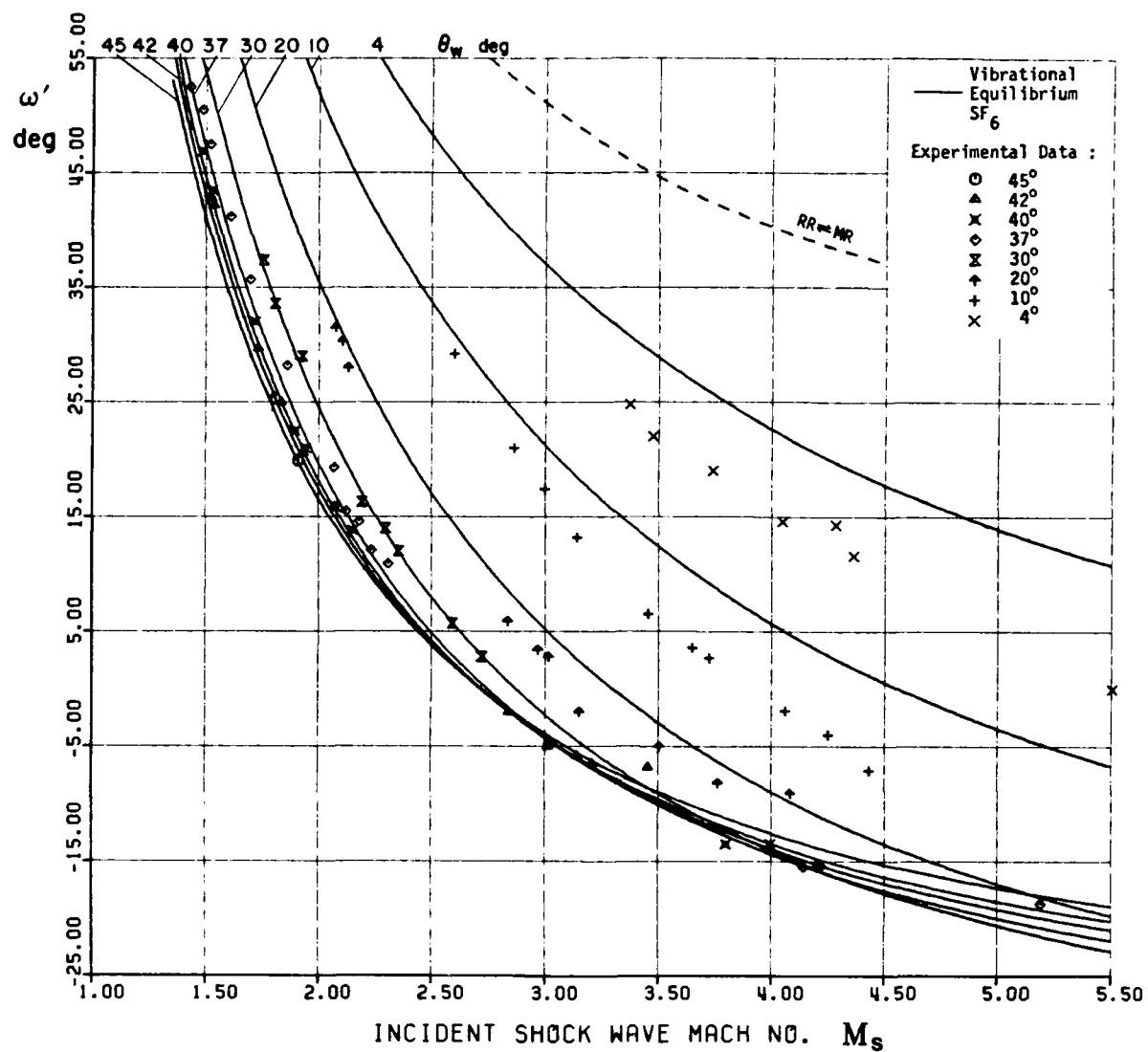


Fig. 44 Variation of ϵ' vs M_s at fixed θ_w for vibrational equilibrium SF_6 , $P_0 = 15$ torr, $T_0 = 300$ K.

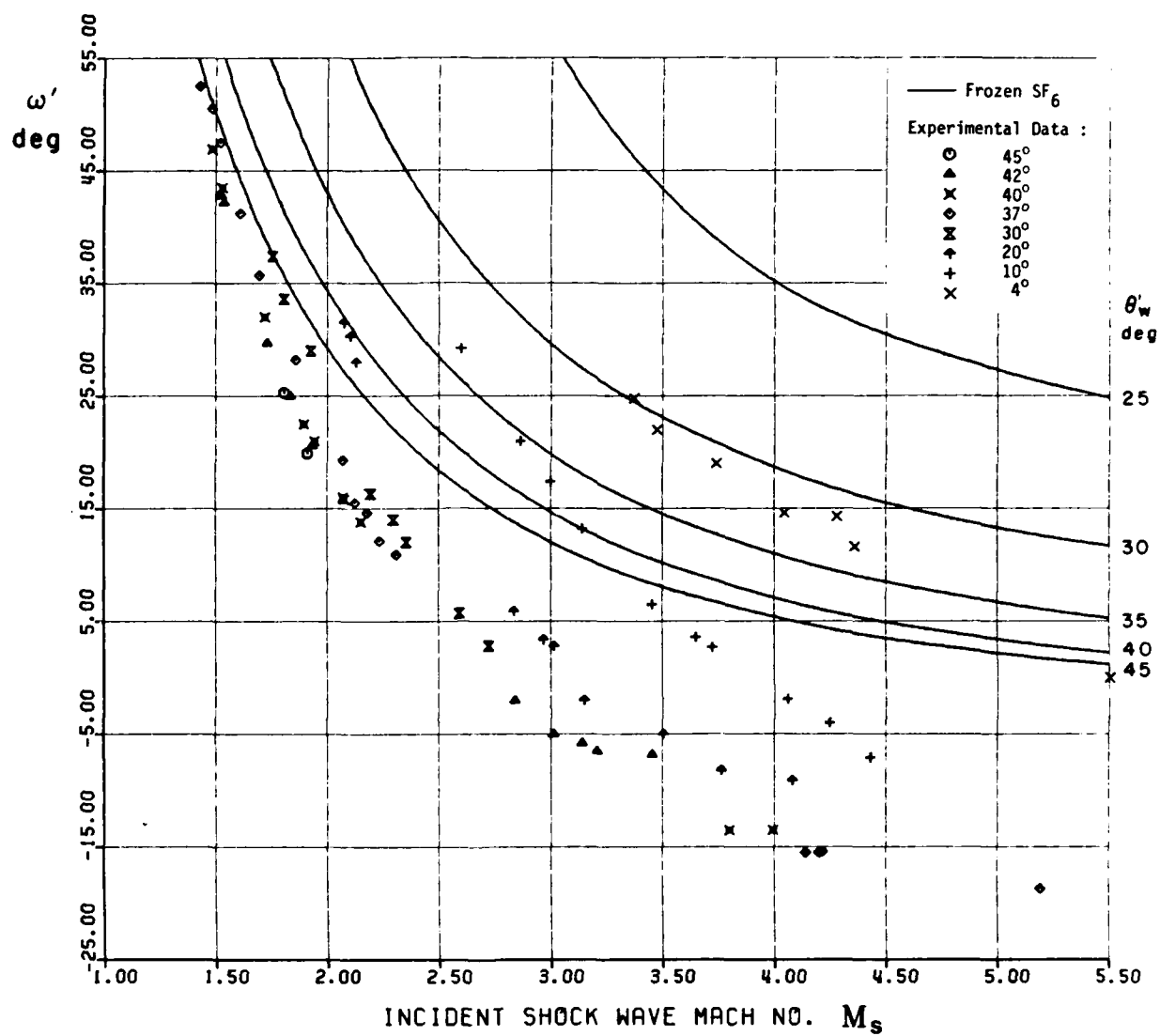


Fig. 45 Variation of ω' vs M_s at fixed θ_w' for frozen SF_6 with $\gamma = 4/3$, $P_0 = 15$ torr, $T_0 = 300$ K.

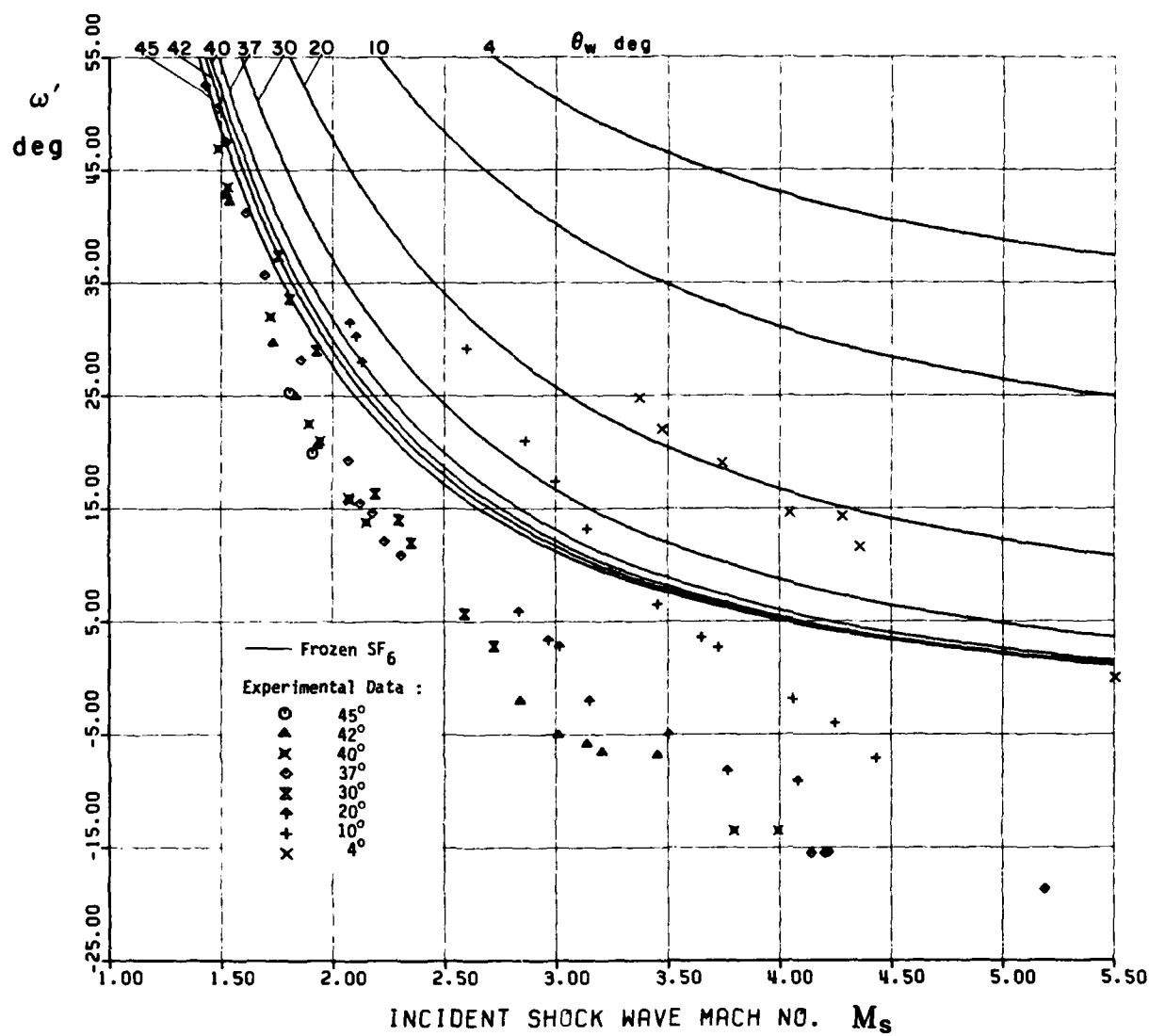


Fig. 46 Variation of ω' vs M_s at fixed θ_w for frozen SF_6 with $\gamma = 4/3$, $P_0 = 15$ torr, $T_0 = 300$ K.

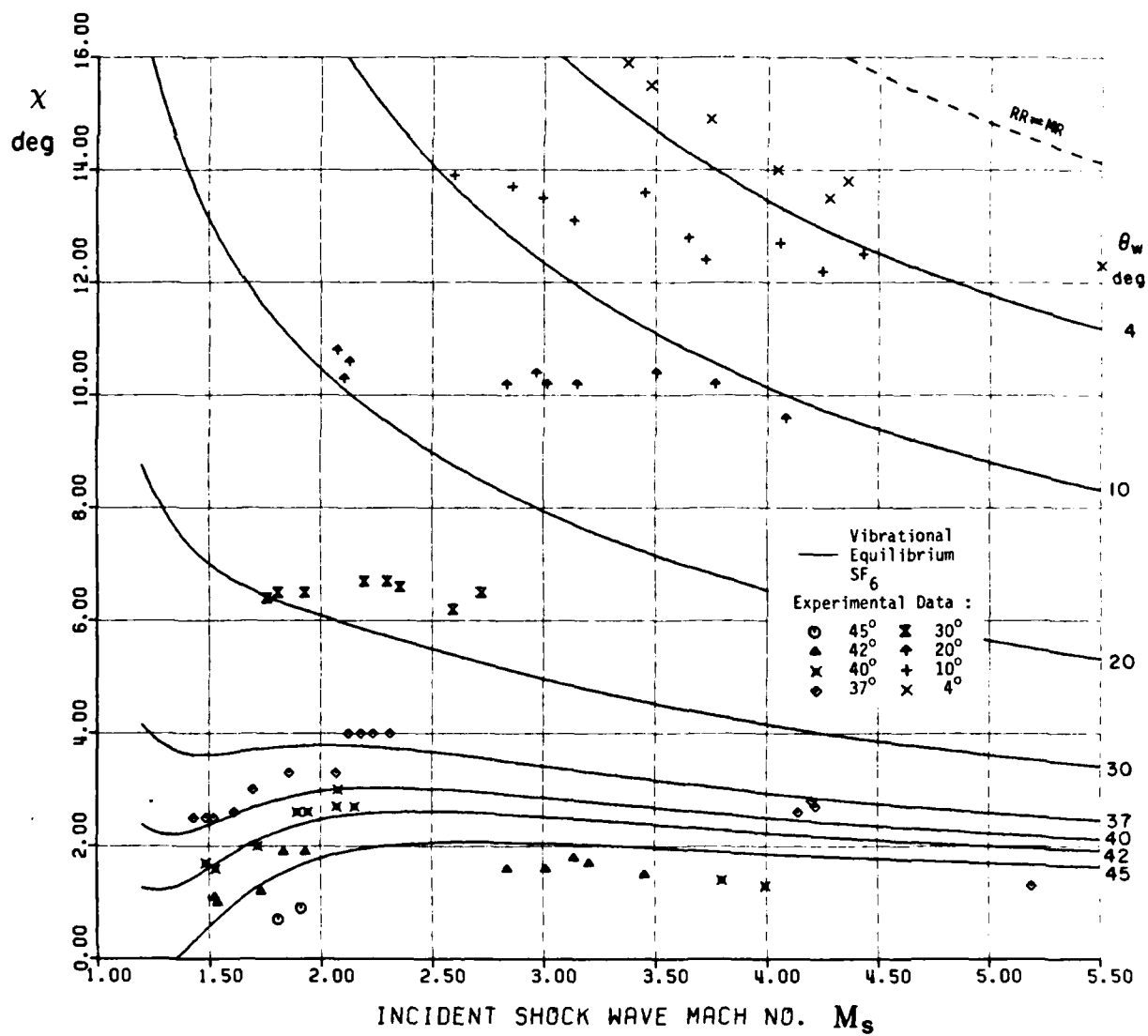


Fig. 47 Variation of χ vs M_s at fixed θ_w for vibrational equilibrium SF_6 , $P_0 = 15$ torr, $T_0 = 300$ K.

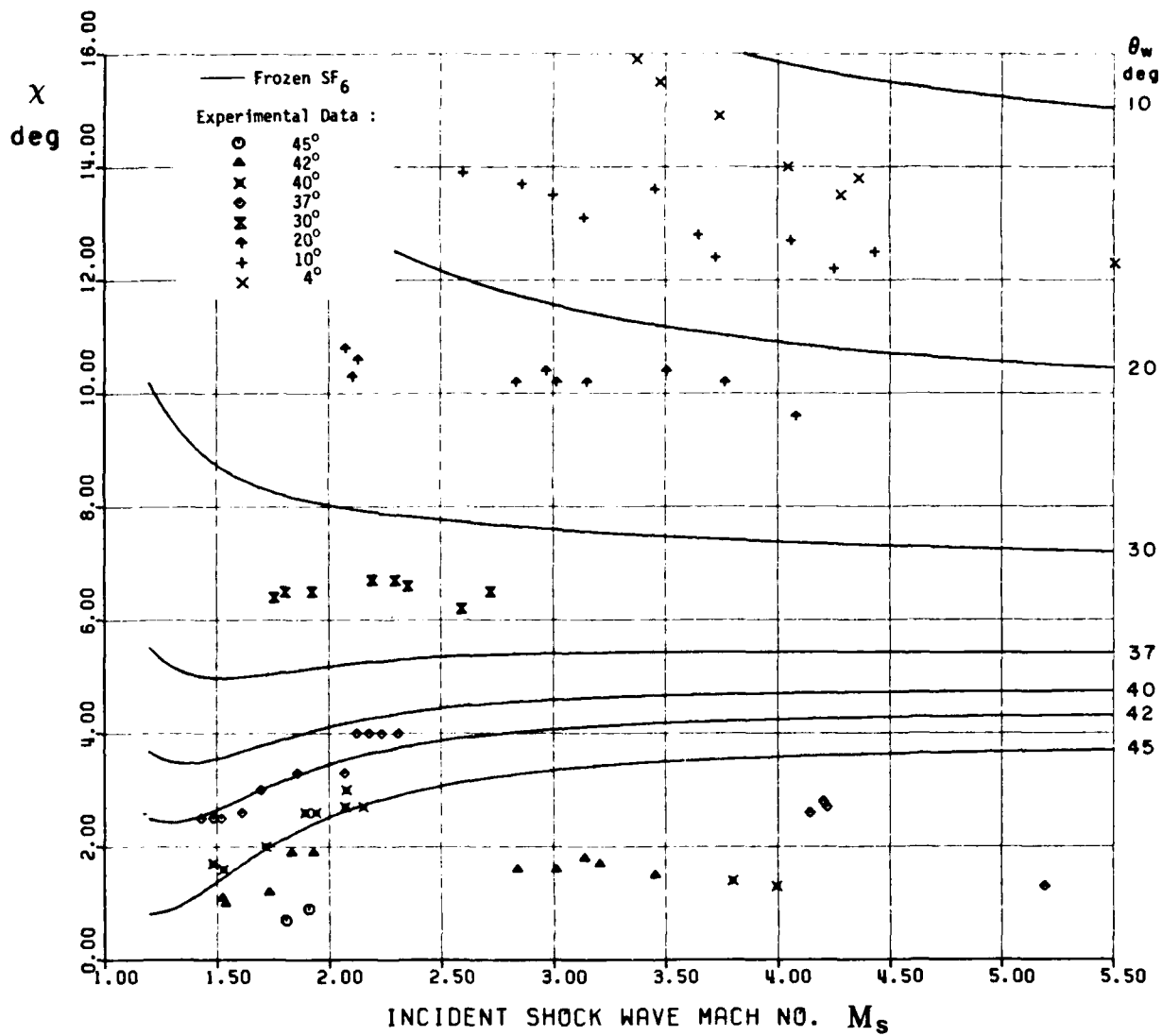


Fig. 48 Variation of χ vs M_s at fixed θ_w for frozen SF_6
 with $\gamma = 4/3$, $P_0 = 15$ torr, $T_0 = 300$ K.

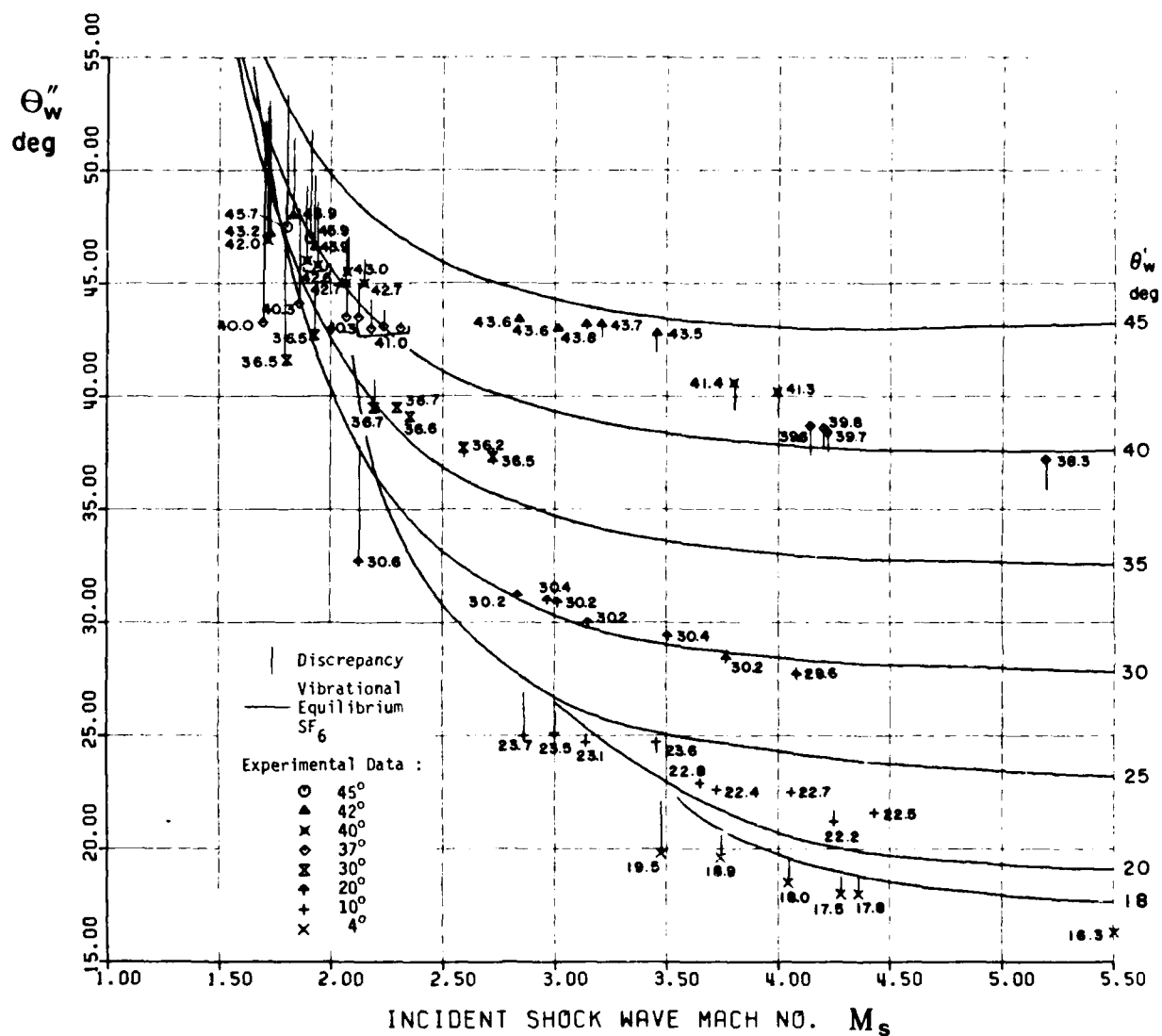


Fig. 49 Variation of θ_w'' vs M_s at fixed θ_w' for vibrational equilibrium SF_6 , $P_0 = 15$ torr, $T_0 = 300$ K.

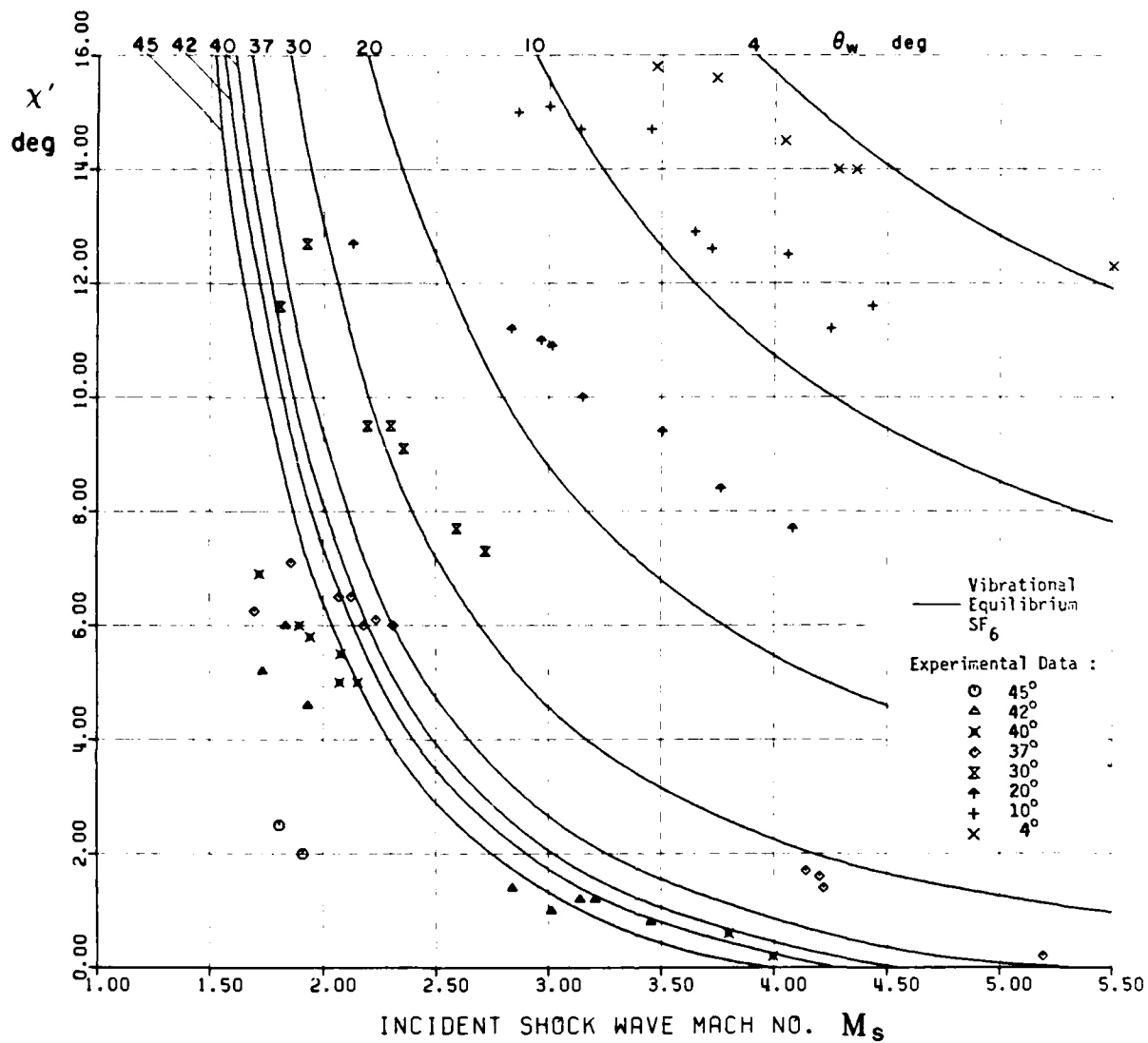


Fig. 50 Variation of χ' vs M_s at fixed θ_w for vibrational equilibrium SF_6 , $P_0 = 15$ torr, $T_0 = 300$ K.

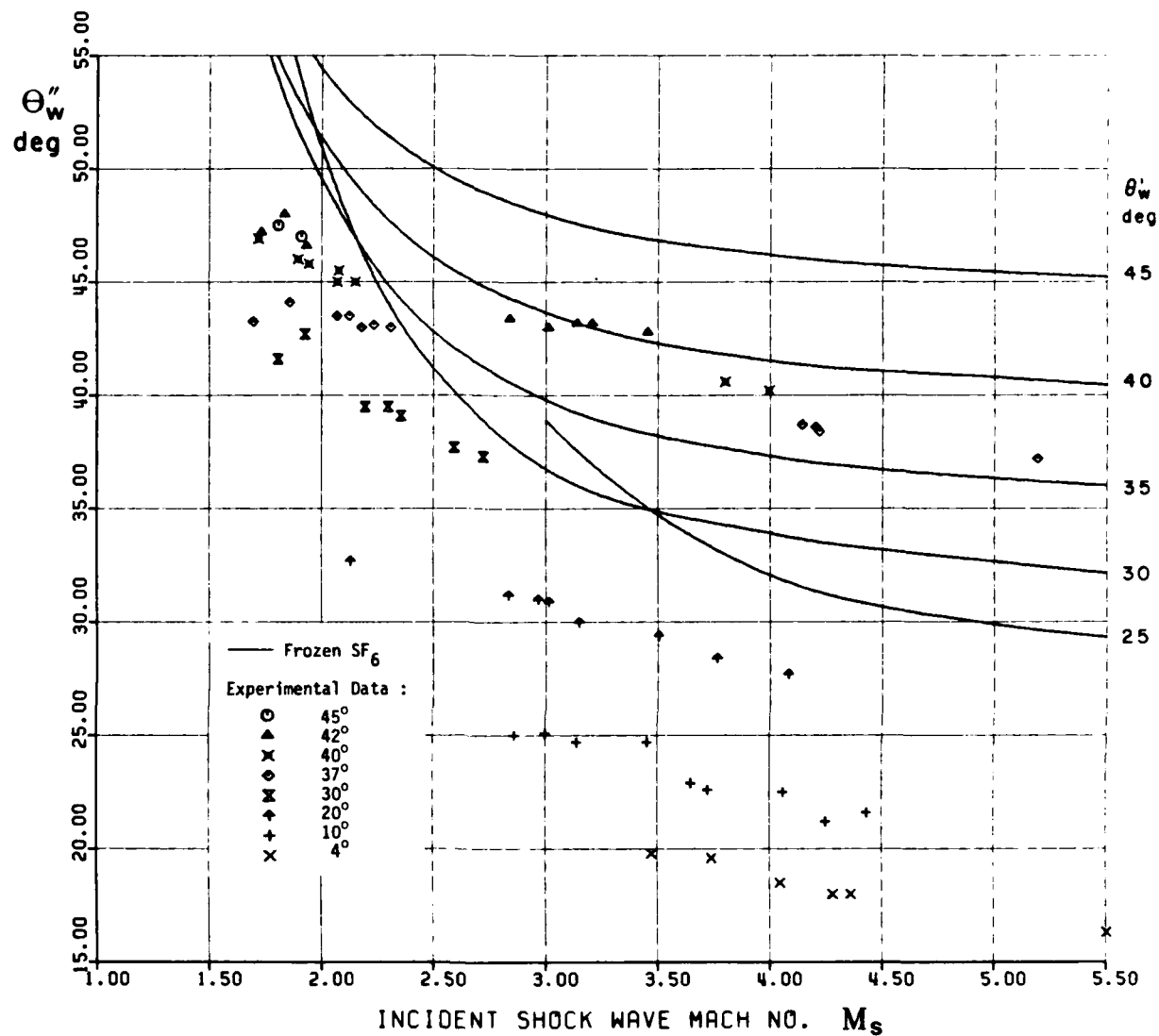


Fig. 51 Variation of Θ''_w vs M_s at fixed Θ'_w for frozen SF_6 with $\gamma = 4/3$, $P_0 = 15$ torr, $T_0 = 300$ K.

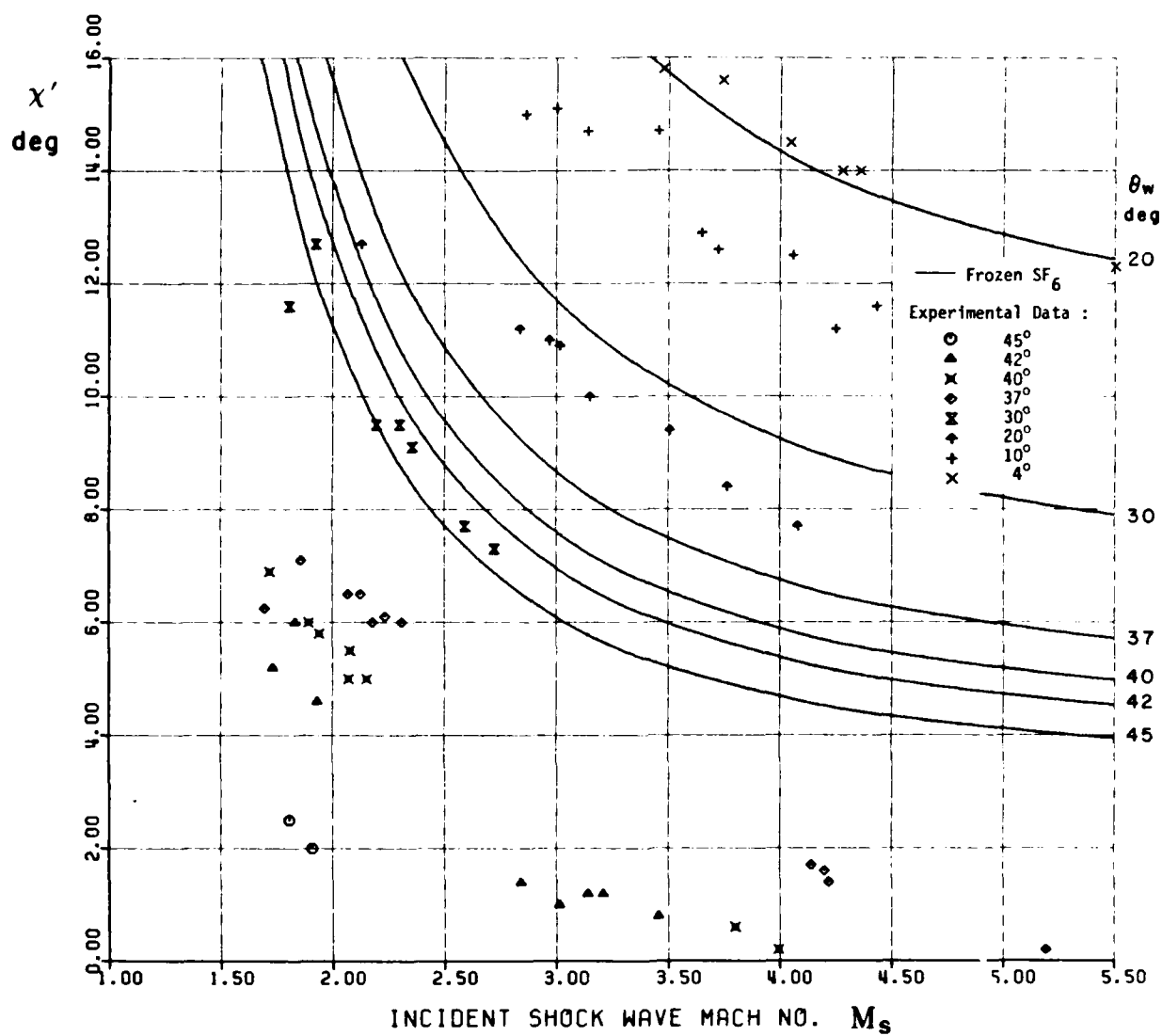


Fig. 52 Variation of χ' vs M_s at fixed θ_w for frozen SF_6 with $\gamma = 4/3$, $P_0 = 15$ torr, $T_0 = 300$ K.

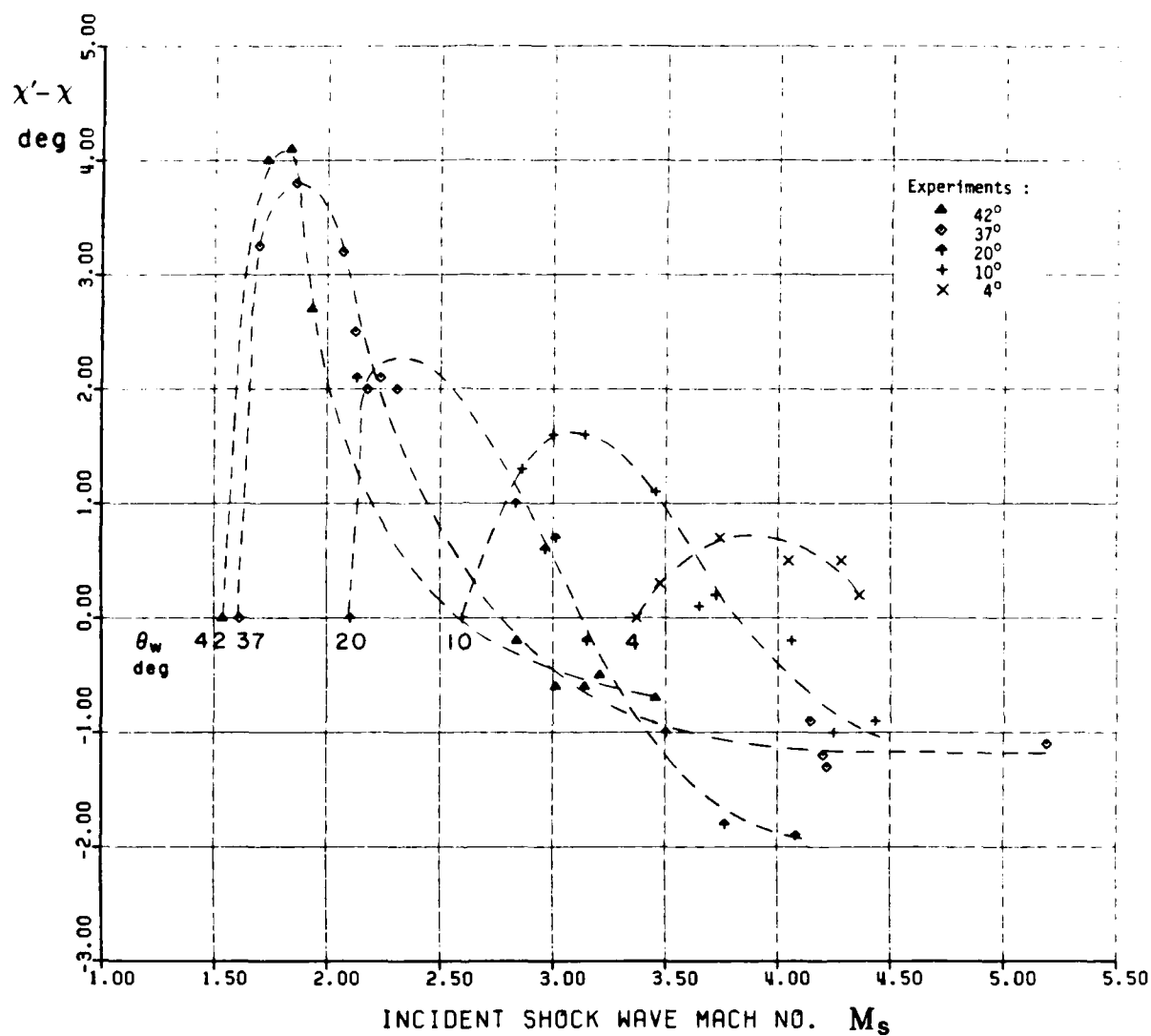
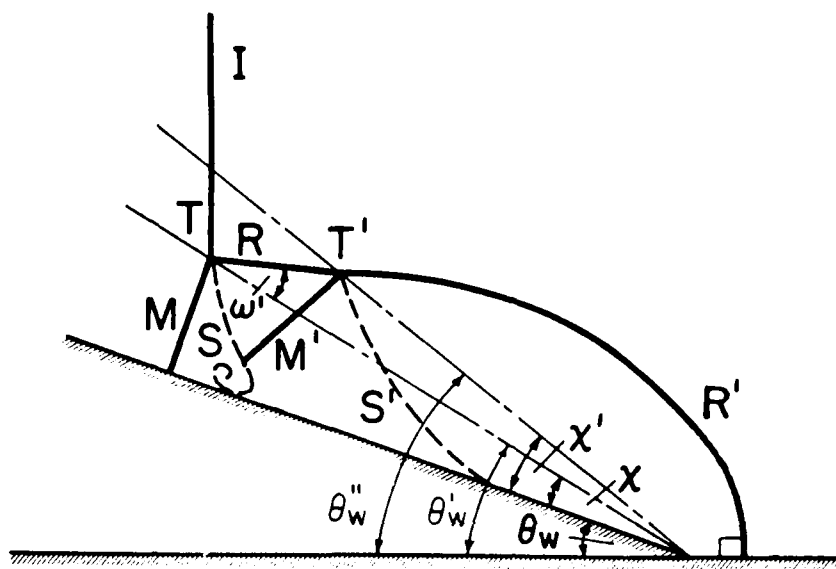
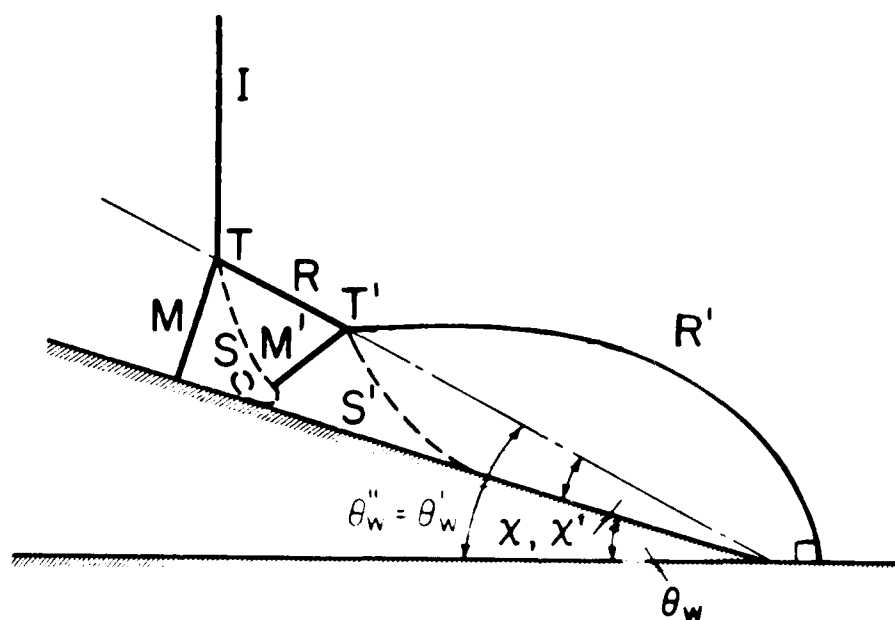


Fig. 53 Plot of the measured values for $(\chi' - \chi)$ vs M_s for several wedge angles in SF_6 .

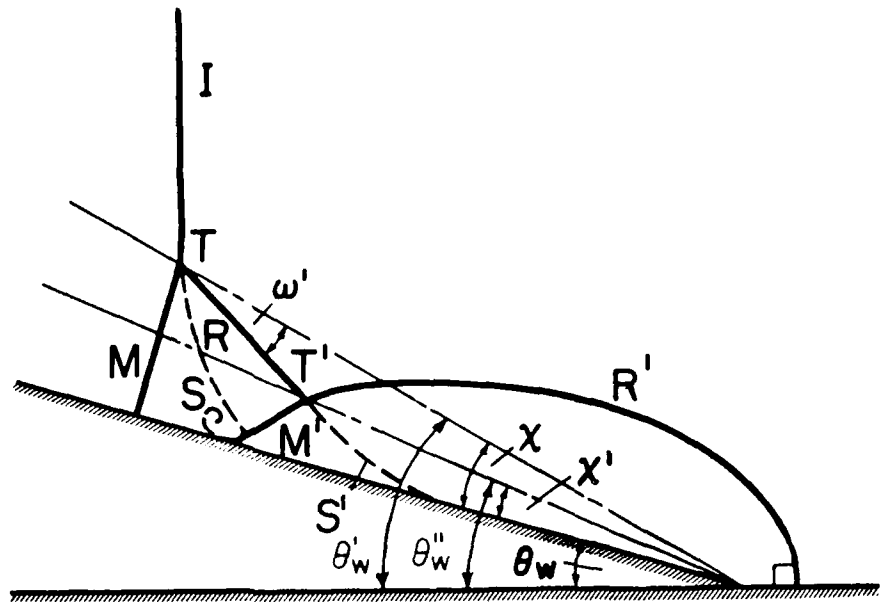


(a) $x' > x$, $\omega' > 0$, $\theta_w'' > \theta_w'$

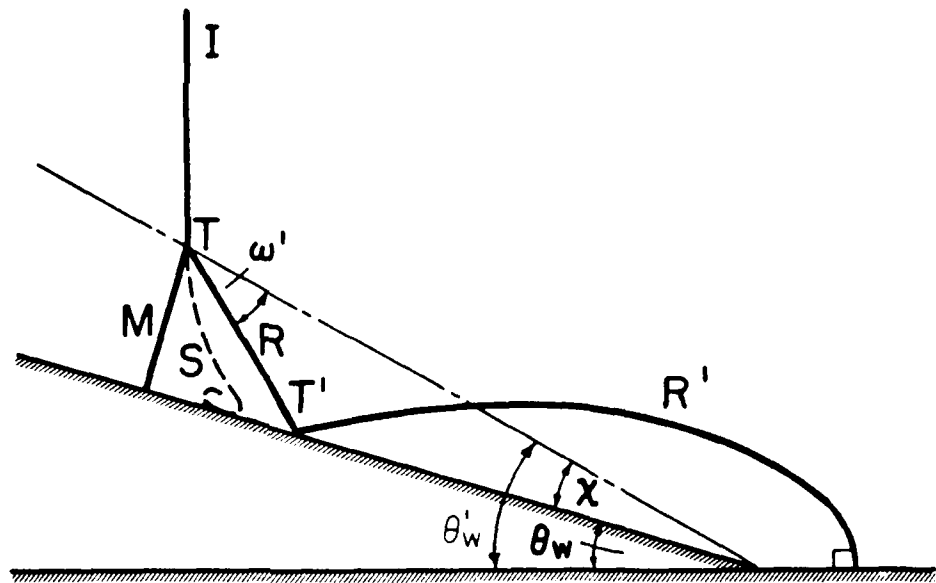


(b) $x' = x$, $\omega' = 0$, $\theta_w'' = \theta_w'$

Fig. 54 Schematic diagrams of four patterns of double-Mach reflection.



(c) $x' < x$, $\omega' < 0$, $\theta_w'' < \theta_w'$



(d) $x' = 0$, $\omega' < 0$, $\theta_w'' = \theta_w$

Fig. 54 (continued) Schematic diagrams of four patterns of double-Mach reflection.

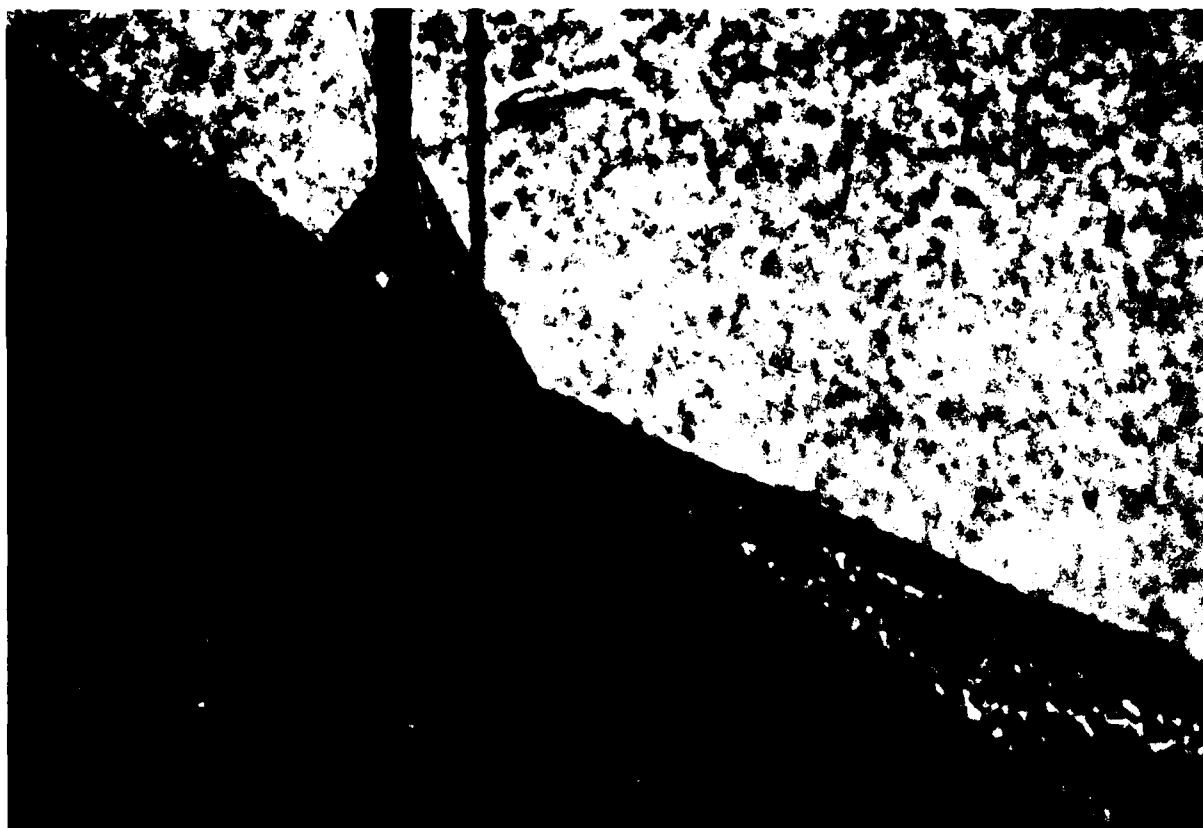


Fig. 55 Shadowgram showing a double-Mach reflection
with $\omega' < 0$ and $\chi' = 0$.
 $M_s = 7.96$, $\theta_w = 37^\circ$, $P_0 = 11.0$ torr,
 $T_0 = 296.6$ K in SF_6 .

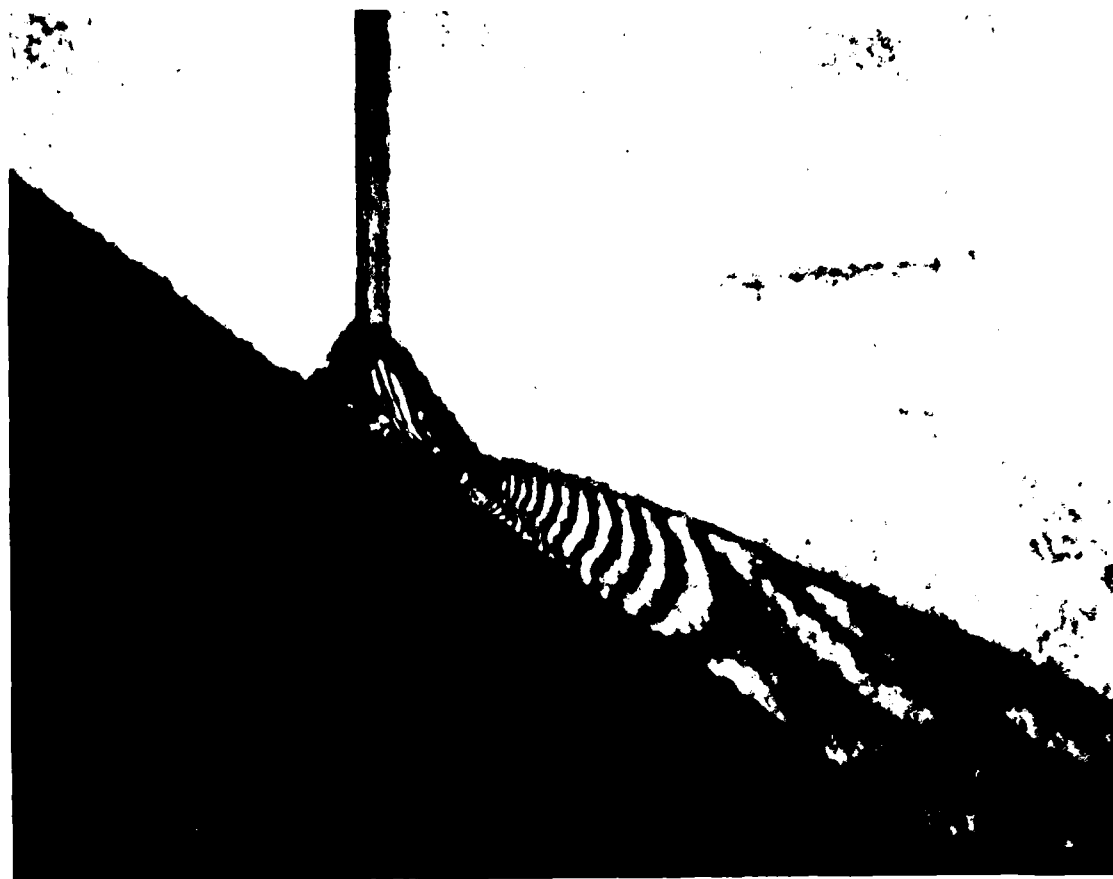


Fig. 56 Infinite-fringe interferogram showing a double-Mach reflection with $\omega' < 0$ and $X' < X$.
 $M_s = 4.20$, $\theta_w = 37^\circ$, $P_0 = 12.0$ torr,
 $T_0 = 296.9$ K in SF_6 .

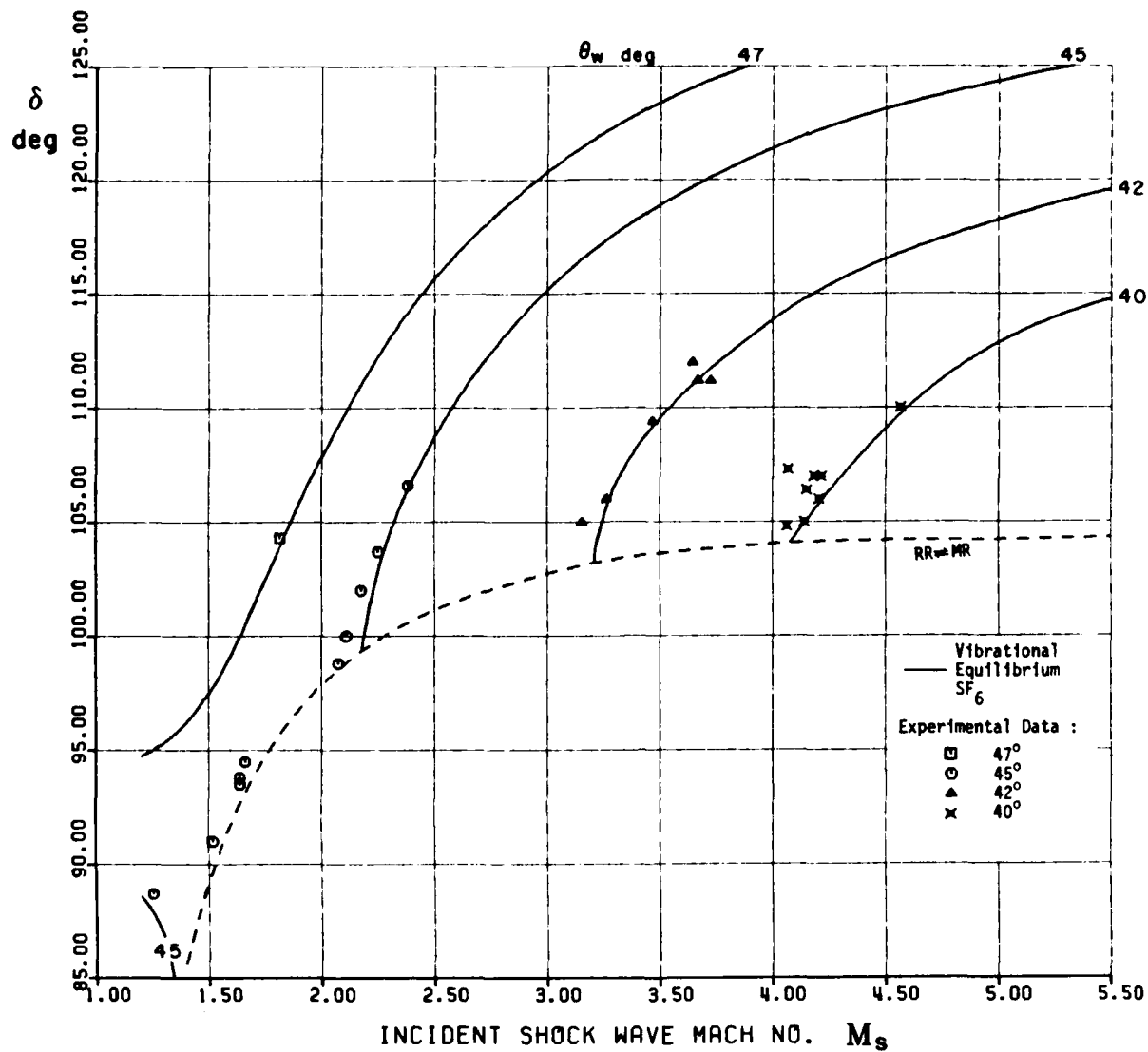


Fig. 57 Variation of δ vs M_s at fixed θ_w for vibrational equilibrium SF_6 in RR with $P_0 = 15$ torr, $T_0 = 300$ K.

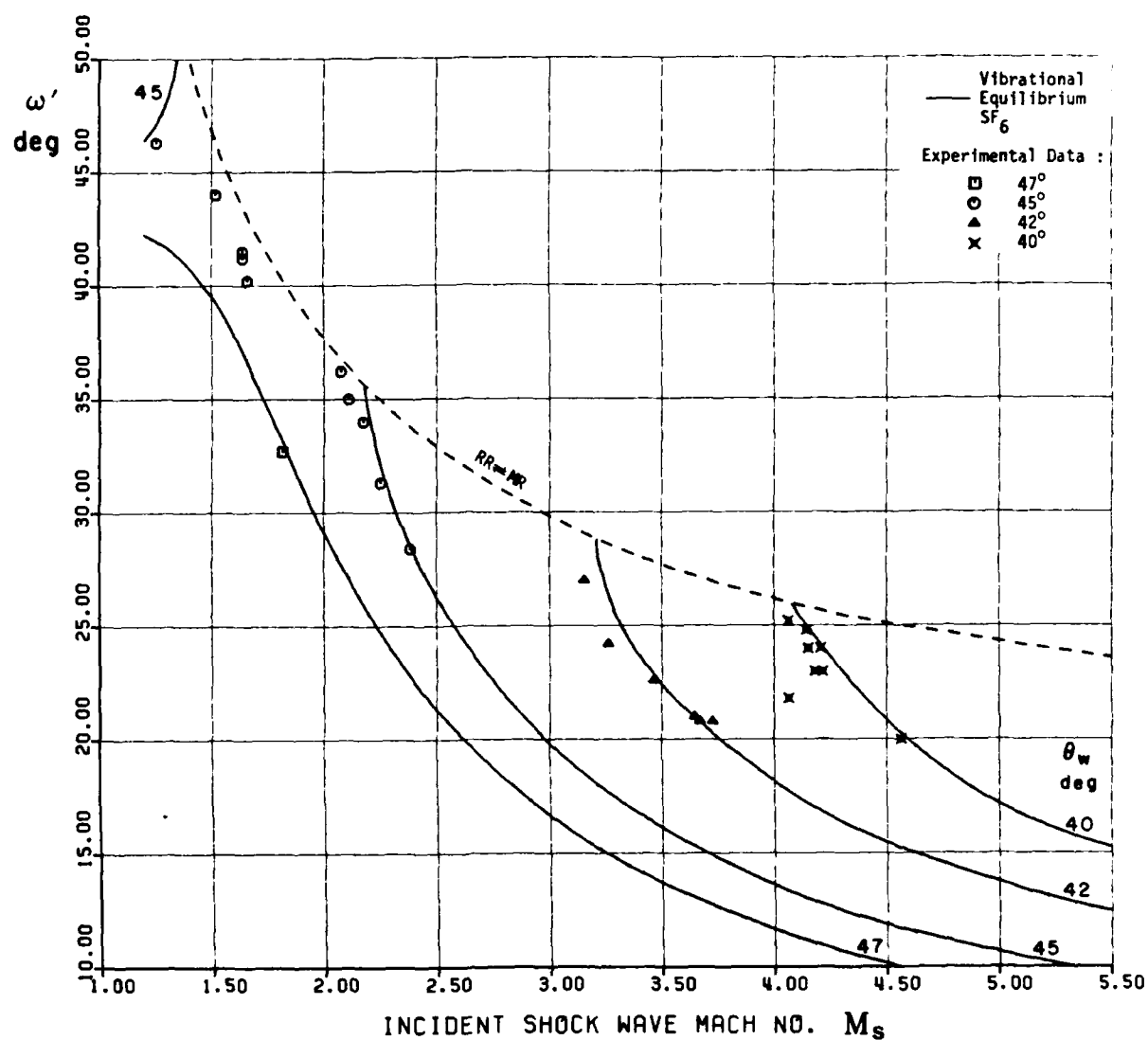
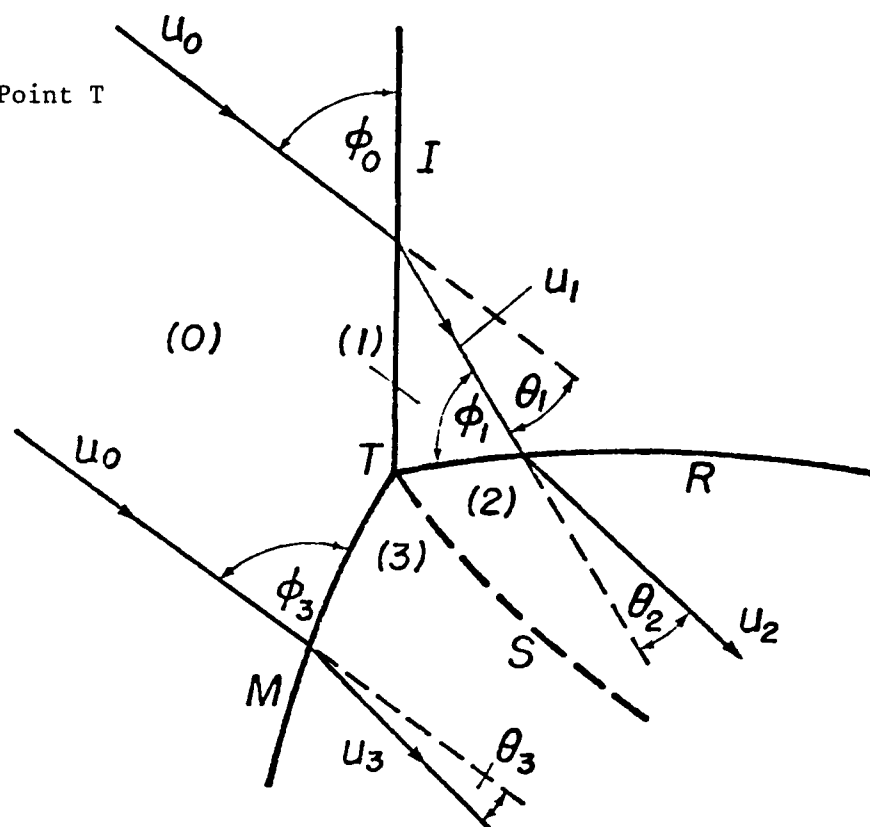


Fig. 58 Variation of ω' vs M_s at fixed θ_w for vibrational equilibrium SF_6 in RR with $P_0 = 15$ torr, $T_0 = 300$ K.

a) First Triple Point T



b) Second Triple Point T'

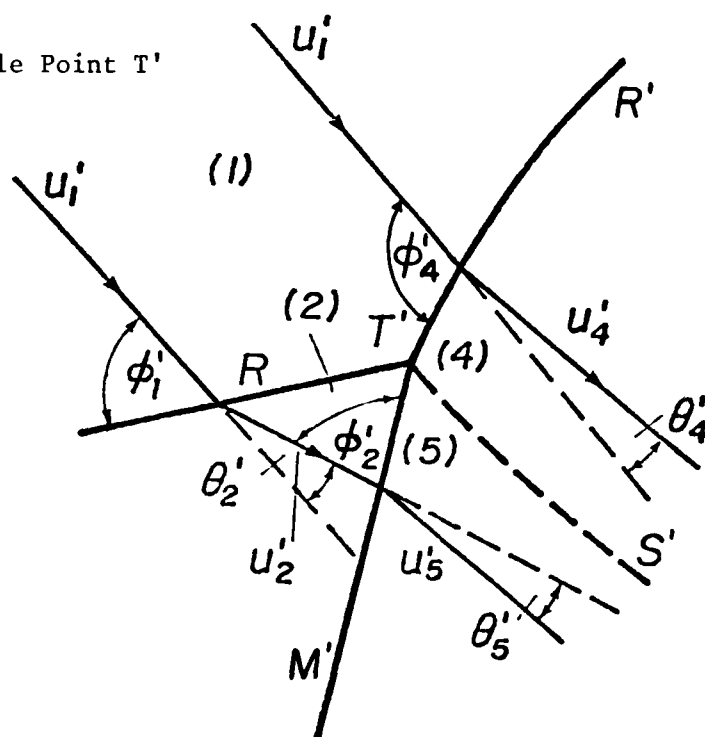
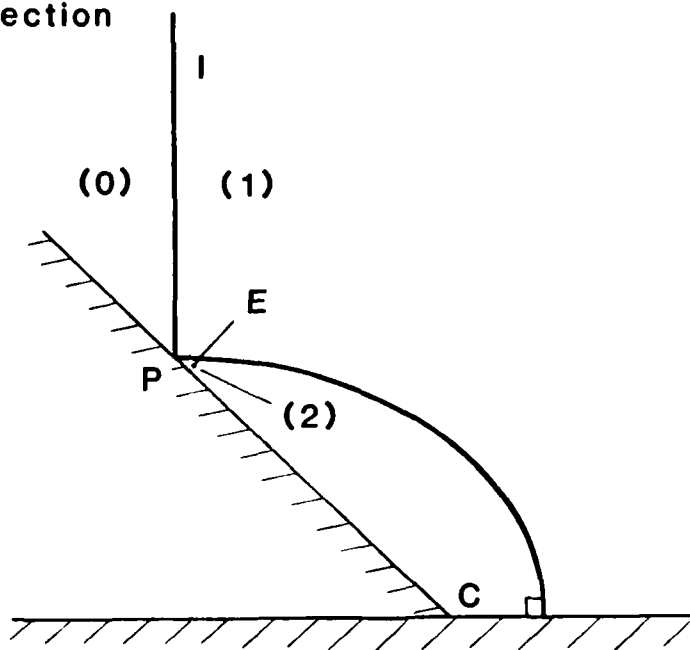


Fig. 59 The analogy between the two triple-point wave systems in a double-Mach reflection.

a) Regular Reflection



b) Double-Mach Reflection

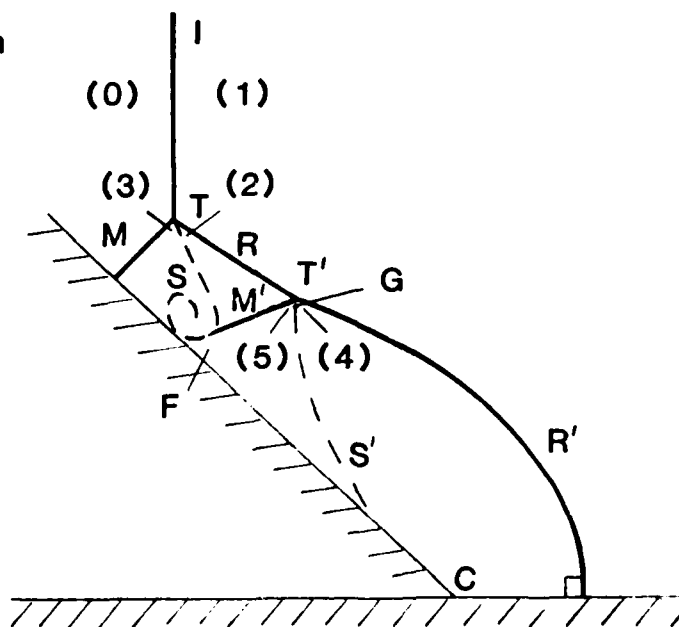


Fig. 60 Location of highest pressure in RR and DMR near the RR \nrightarrow DMR transition boundary.
 Point C - stagnation pressure at corner,
 Point E - highest pressure in RR,
 Region F - highest pressure in DMR,
 Point G - pressure behind second triple point T'.

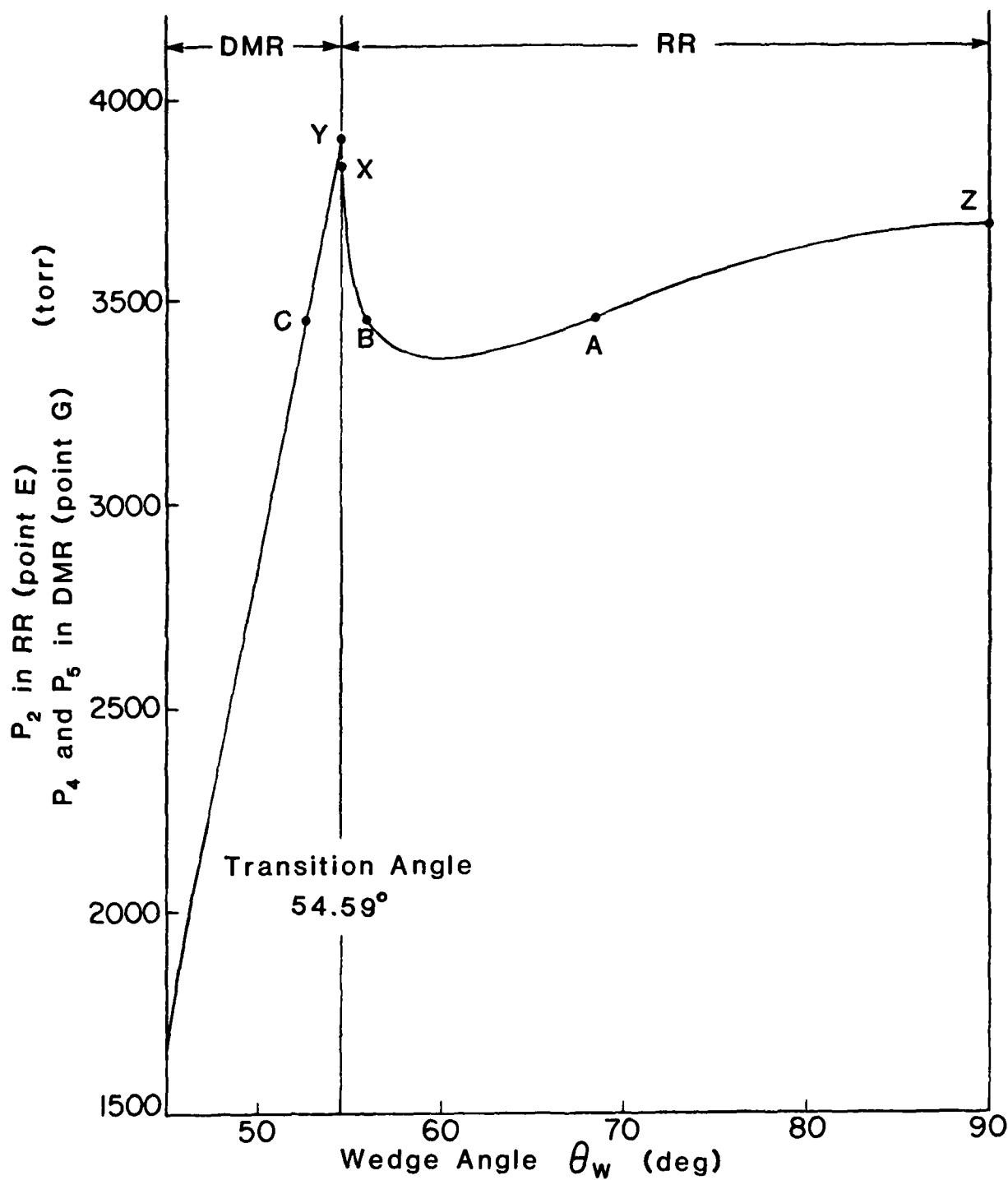
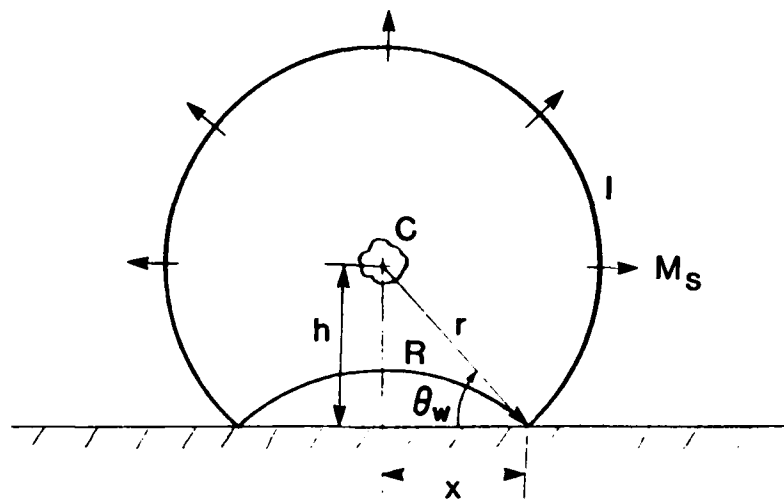


Fig. 61 Pressure behaviour at point E in RR and at point G in DMR as a function of wedge angle. $M_s = 6.0$, $P_0 = 15$ torr (2 kPa), and $T_0 = 300$ K in argon.

a) Regular Reflection



b) Mach Reflection

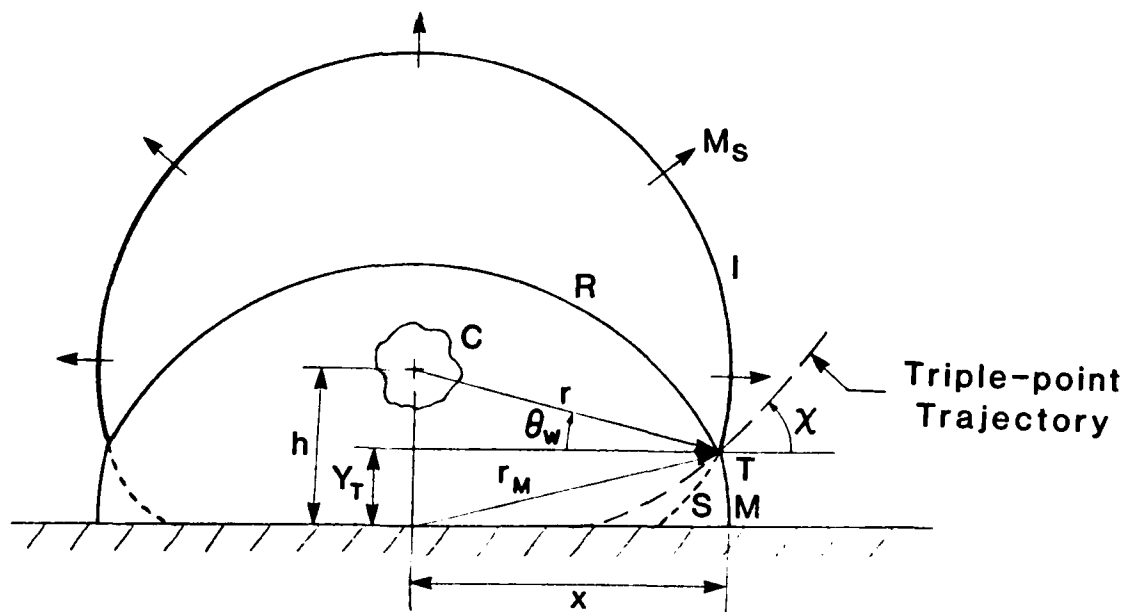


Fig. 62 Height-of-burst flow field of a spherical blast wave.

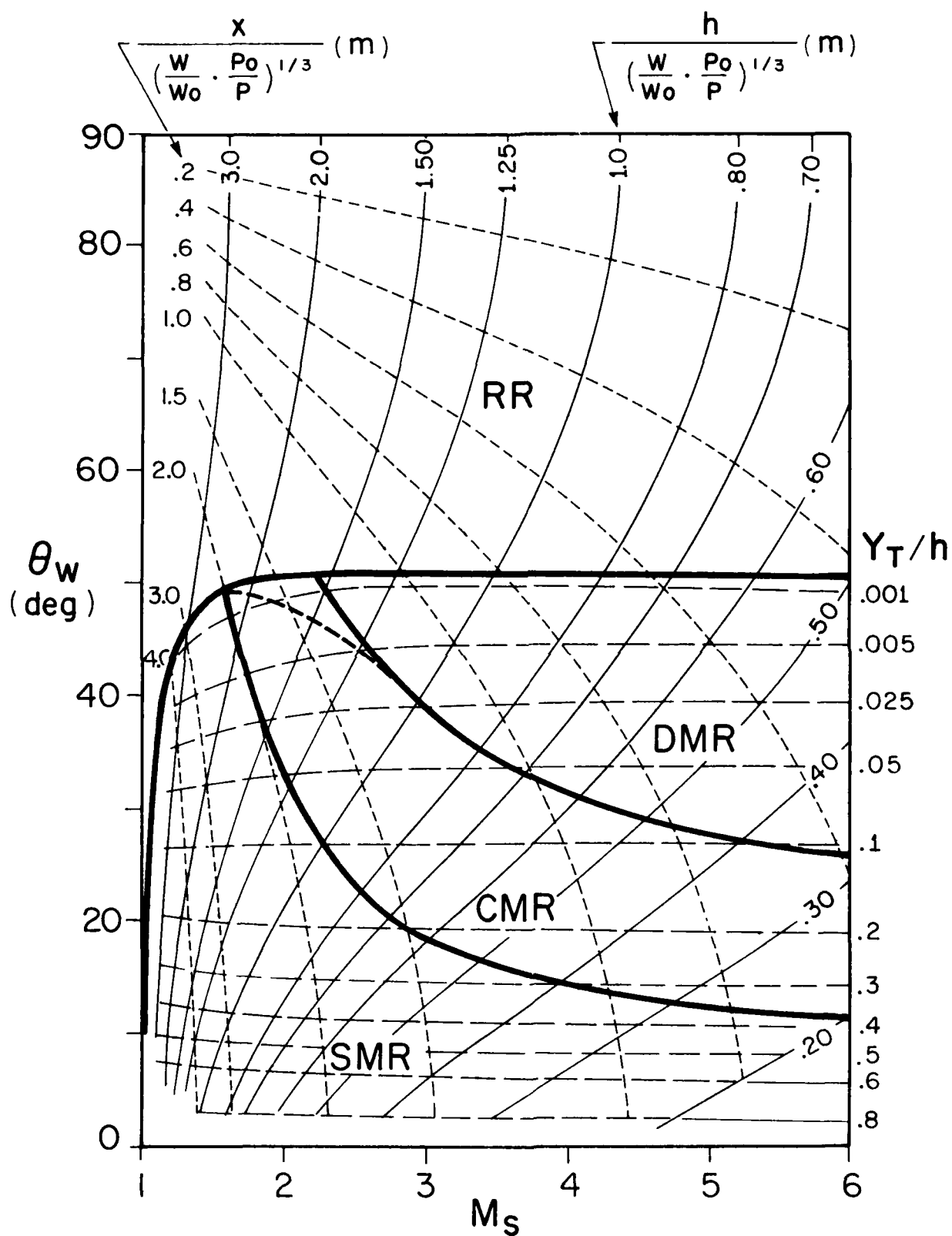


Fig. 63 Interaction of a spherical blast wave with a planar surface in perfect air at standard ambient conditions.

Appendix A

Method of Calculations

Reflections Inside a Shock Tube

Since the planar incident shock wave moves with constant velocity along the wedge surface, the entire reflection phenomenon can be considered as pseudo-stationary in a frame of reference attached to a point which moves with a constant velocity. Therefore, instead of three independent variables x , y and t , the phenomenon is described in terms of x/t and y/t and the flow is self-similar [19]. In a pseudo-stationary flow, the shock wave configuration remains self-similar and grows linearly with time from the moment the incident shock wave collides with the wedge corner. The phenomenon is also assumed to be a two-dimensional inviscid flow.

The calculations for obtaining the flow properties of each region in the angular vicinity of a shock confluence point require the formulation of the oblique-shock-wave relations for each shock wave. The reference point is the reflection point P in RR, and the triple point T in MR; the region which are divided by shock waves and a slipstream are designated by 0 to 3 as shown in Fig. 3a and 4. The details of the analytical formulations can be found in Law [47]. The physical quantities on both sides of each shock wave in the vicinity of the reference point satisfy the following equations of motion:

Conservation of tangential velocity

$$\rho_i \tan \phi_i = \rho_j \tan(\phi_i - \theta_j) \quad (\text{A.1})$$

Continuity

$$\rho_i U_i \sin \phi_i = \rho_j U_j \sin(\phi_i - \theta_j) \quad (\text{A.2})$$

Normal momentum

$$P_i + \rho_i U_i^2 \sin^2 \phi_i = P_j + \rho_j U_j^2 \sin^2(\phi_i - \theta_j) \quad (\text{A.3})$$

Energy

$$h_i + \frac{1}{2} U_i^2 \sin^2 \phi_i = h_j + \frac{1}{2} U_j^2 \sin^2(\phi_i - \theta_j) \quad (\text{A.4})$$

where i and j refer to the states ahead and behind the shock, respectively. The equations of state applied are

$$\rho = \rho(P, T), \quad h = h(P, T) \quad (\text{A.5})$$

In RR, or the two-shock theory, there are two sets of equations:

$$\text{For incident shock I:} \quad i = 0, j = 1 \quad (\text{A.6})$$

$$\text{For reflected shock R:} \quad i = 1, j = 2 \quad (\text{A.7})$$

These two sets of equations are solved under the boundary condition that the flow deflections across the incident and reflected shocks be equal and opposite with the direction of the flow behind the reflected shock wave being along the wedge surface, i.e.,

$$\theta_1 = \theta_2 \quad (\text{A.8})$$

The calculating procedures for the solution of equation (A.5) through (A.8) are as follows [11]:

1. The initial conditions of the pressure P_0 , the temperature T_0 , the Mach number M_5 and the wedge angle θ_w are given.
2. The first set of equations (A.6) is solved for P_1 , T_1 , U_1 , and θ_1 . Note that $U_0 = U_5 \sec \theta_w$ and $\phi_0 = 90^\circ - \theta_w$.
3. Some initial guess for ϕ_1 is made.
4. The second set of equations (A.7) is solved to obtain the values for P_2 , T_2 , U_2 and θ_2 .
5. The calculated results are checked against the boundary condition (A.8).
6. A new value of ϕ_1 is predicted.
7. The procedure is repeated until

$$|\theta_1 - \theta_2| < 10^{-4}$$

In the case of MR, or the three-shock theory, there are three sets of equations for the first triple-point system:

$$\text{For incident shock I:} \quad i = 0, j = 1 \quad (\text{A.9})$$

$$\text{For reflected shock R:} \quad i = 1, j = 2 \quad (\text{A.10})$$

$$\text{For Mach stem M:} \quad i = 0, j = 3, (\phi_i \text{ is referred to as } \phi_3) \quad (\text{A.11})$$

The above three sets of equations are solved under the boundary conditions that the flow deflection across the incident and reflected shocks be equal to the flow deflection across the Mach stem and the pressure on both sides of the slipstream be identical, i.e.,

$$\theta_3 = \theta_1 - \theta_2 \quad (\text{A.12})$$

$$P_2 = P_3 \quad (\text{A.13})$$

In MR, it is necessary to predict a value of the triple-point trajectory angle χ in order that the system of equations be closed. The Mach stem is assumed normal to the wedge surface based on experimental observations, and Law and Glass [15] introduced an additional geometrical relation

$$\phi_3 = 90^\circ - \chi \quad (\text{A.14})$$

The calculating procedures for the solution of equations (A.5) and (A.9) through (A.14) are as follows [11] :

1. The initial conditions of P_0 , T_0 , M_S and θ_w are given.
2. Some initial guesses for χ and ϕ_1 are made.
3. The first set of equations (A.9) is solved for P_1 , T_1 , U_1 and θ_1 . Note that $U_0 = U_S \operatorname{cosec} \phi_0$ and $\phi_0 = 90^\circ - (\theta_w + \chi)$.
4. The second set of equations (A.10) is solved for P_2 , T_2 , U_2 and θ_2 .
5. Using Eq. (A.14), the third set of equations (A.11) is solved for P_3 , T_3 , U_3 and θ_3 .
6. The calculated results are checked against the boundary conditions (A.12) and (A.13).
7. New values of χ and ϕ_1 are predicted.
8. The solutions are iterated until

$$\begin{aligned} &|\theta_3 - \theta_1 + \theta_2| < 10^{-4} \\ \text{and} \quad &|(P_3 - P_2)/P_2| < 10^{-4} \end{aligned}$$

Details of the analytical formulation of the second triple point T' is given by Ben-Dor [11]. The flow fields around T' are shown in Fig. 59 with the prime to denote that the properties are measured with respect to T' . The three set of equations for the system are :

$$\text{For reflected shock R:} \quad i = 1, j = 2 \quad (\text{A.15})$$

$$\begin{aligned} \text{For second reflected shock R':} \quad i &= 1, j = 4 \\ (\phi_i \text{ is referred to as } \phi_4) \end{aligned} \quad (\text{A.16})$$

$$\text{For second Mach stem M':} \quad i = 2, j = 5 \quad (\text{A.17})$$

The above three sets of equations are solved under the boundary conditions that the flow deflection across the reflected shock R and the second Mach stem M' be equal to the flow deflection across the second reflected shock R', and the pressure on both sides of the second slipstream S' be identical, i.e.,

$$\theta'_4 = \theta'_2 - \theta'_5 \quad (\text{A.18})$$

$$P_4 = P_5 \quad (\text{A.19})$$

The calculation involves a transformation of the already calculated values of U_1 and ϕ_1 from a frame of reference attached to T to a frame of reference attached to T' . Since thermodynamic properties do not depend on the frame of reference, the prime is omitted from the thermodynamic variables in the equations. The values of U'_1 and ϕ'_1 are given as

$$U_1' = U_1 \left[1 + \frac{\sin^2(\phi_0 - \theta_1)}{\sin^2(\phi_1 + \phi_0 - \theta_1)} - 2 \frac{\sin(\phi_0 - \theta_1)\cos\phi_1}{\sin(\phi_1 + \phi_0 - \theta_1)} \right]^{1/2} \quad (\text{A.20})$$

$$\phi_1' = \phi_1 + \phi_0 - \theta_1 \quad (\text{A.21})$$

The calculating procedures for the solution of equations (A.5) and (A.15) through (A.21) are as follows:

1. The initial conditions of P_1 , T_1 , M_1 , ϕ_0 , ϕ_1 and θ_1 are given.
2. Some initial guesses for ϕ_2' and ϕ_4' are made.
3. Using equations (A.20) and (A.21), the first set of equations (A.15) is solved for P_2 , T_2 , U_2 and θ_2 .
4. The second set of equations (A.16) is solved for P_4 , T_4 , U_4' and θ_4' .
5. The third set of equations (A.17) is solved for P_5 , T_5 , U_5' and θ_5' .
6. The calculated values are checked against the boundary conditions (A.18) and (A.19).
7. New values of ϕ_2' and ϕ_4' are predicted.
8. The solutions are iterated until

$$|\phi_4' - \theta_2' + \theta_5'| < 10^{-4}$$

and

$$|(P_4 - P_5)/P_5| < 10^{-4}$$

Ground Reflection of a Blast Wave

The curve fit that was reported by Sadek and Gottlieb [66] to represent the shock trajectory for a 1 kg TNT ground explosion in a standard atmosphere is

$$r_s = \frac{\alpha_1 \alpha_2 t_s}{1 + \alpha_2 t_s} + a_1 t_s + \alpha_3 [\ln(1 + \alpha_4 t_s)]^{1/2} \quad (\text{A.22})$$

where r_s is the shock radius, t_s is the shock arrival time, $\alpha_1 = 0.72$ m, $\alpha_2 = 1.872$ m/s, $\alpha_3 = 1.29$ m, $\alpha_4 = 0.3403$ m/s and $a_1 = 0.3403$ m/ms. Mach number of the blast front can be obtained by differentiating the above equation and then dividing it by the speed of sound.

In the calculation of the blast-front-trajectory path on the ($M_s - \theta_w$) transition map, an incident shock wave Mach number M_s is first chosen. The time of arrival t_s is then determined and substituted into equation (A.22) to obtain the shock radius r_s . To obtain an equivalent shock radius r for the case of HUB explosion above a perfect planar surface, r_s is multiplied by the factor $2^{1/3}$.

For RR, at a given HOB h and M_s , the radius of the blast front r can be calculated as mentioned above. Ground range x and the corresponding wedge angle θ_w , as shown in Fig. A-1(a), can be determined from the relations

$$x^2 = r^2 - h^2 \quad (A.23)$$

$$\sin \theta_w = h/r \quad (A.24)$$

For MR, at a given HOB h and M_s , the radius of the blast front r is calculated the same way as for RR. To find the ground range x and the wedge angle θ_w , it is essential to know the height of the first triple point Y_T . As illustrated in Fig. A-1(b), x , h , Y_T and θ_w are related by

$$r^2 = x^2 + (h - Y_T)^2 \quad (A.25)$$

$$\tan \theta_w = (h - Y_T)/x \quad (A.26)$$

and the slope of the first-triple-point trajectory is given by

$$\frac{dY_T}{dx} = \tan \chi \quad (A.27)$$

If equation (A.26) is first differentiated, then substituted into equation (A.27) and finally the result is integrated, the following two relations are obtained [67]:

$$\frac{Y_T}{h} = 0 \quad \text{for } \theta_w > \theta_d \quad (A.28)$$

$$\frac{Y_T}{h} = 1 - \exp \int_{\theta_d}^{\theta_w} \frac{\tan \chi \, d\theta_w}{\sin^2 \theta_w (1 + \tan \chi / \tan \theta_w)} \quad \text{for } \theta_w < \theta_d \quad (A.29)$$

where θ_d is the RR \leftrightarrow MR transition angle according to the detachment criterion. Equation (A.28) is applicable to RR which states that no triple point exists if θ_w is above θ_d . Equation (A.29) is applicable to MR and can be integrated if the relation between θ_w and χ in a two-dimensional shock tube flow is assumed valid here.

The following fix point iterative scheme is used to determine the value of Y_T :

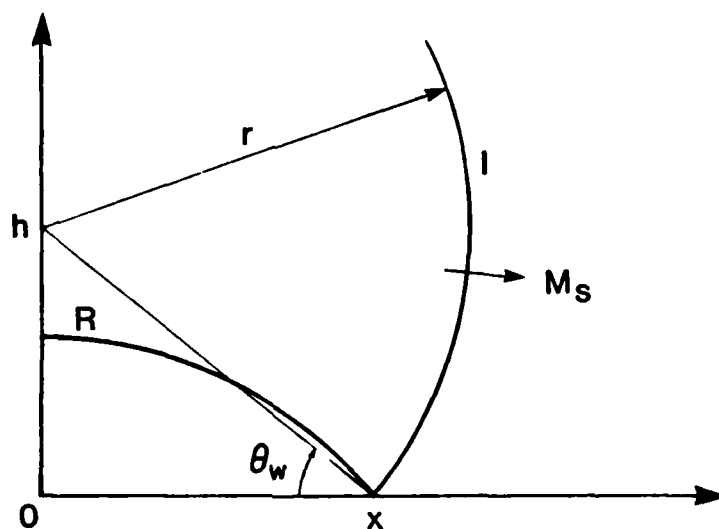
1. The HOB h and the incident shock Mach number M_s are given.
2. Calculate the shock radius r with the given M_s .
3. Some initial guess of Y_T is made.
4. Calculate wedge angle θ_w from the relation obtained by substituting equation (A.25) into (A.26)

$$\theta_w = \tan^{-1} \left\{ \left[\frac{r^2}{(h - Y_T)^2} - 1 \right]^{-1/2} \right\} \quad (A.30)$$

5. With θ_w calculate Y_T using equation (A.29).
6. Check if the difference of the new Y_T and the last Y_T is within the tolerance of 10^{-4} .
7. Steps 4 and 5 are repeated until the tolerance in step 6 is achieved.

Once Y_T is determined, x and θ_w can be calculated using equation (A.25) and (A.26). In real explosions, the Mach stem M is not entirely straight from the first triple point to the ground, but curved as shown in Fig. A-1(b). Such bulging effect of the Mach stem is simply simulated by assuming that the Mach stem M is an arc cutting the first triple point at T and the ground at x' with its radius being r_M . The ground range x in MR then takes the value of x' .

a) Regular Reflection



b) Mach Reflection

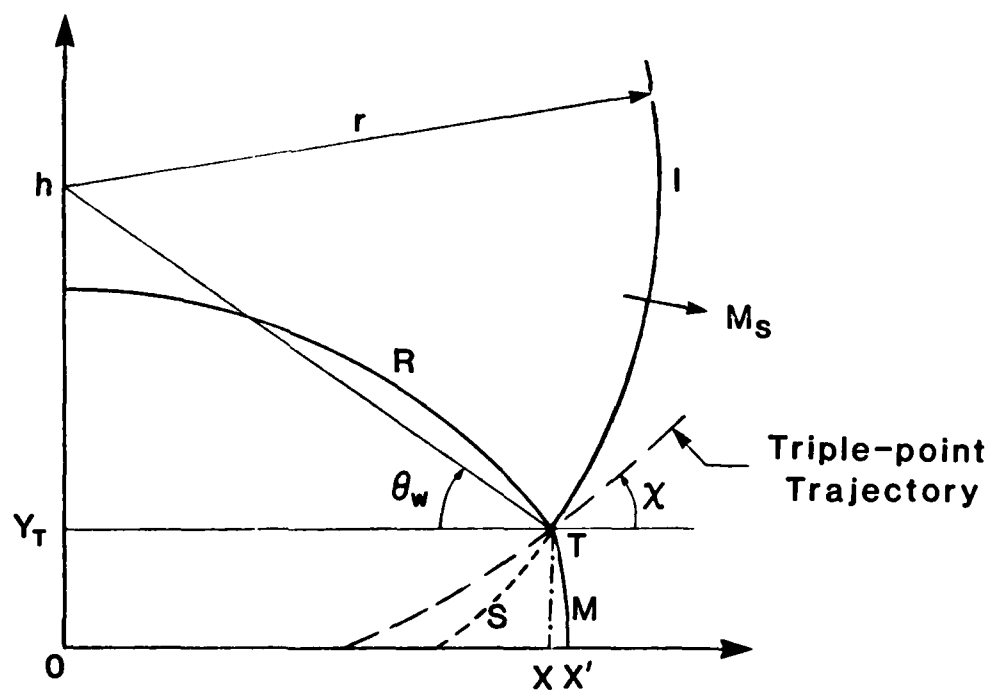


Fig. A-1 Flow field of a free-air explosion.

Appendix B

Thermodynamic Properties of Sulfur Hexafluoride

Sulfur hexafluoride is a gaseous dielectric of great importance in the electrical and communications industries as an insulating and quenching medium in circuit breakers [48]. It alone or in a mixture with other gases has the possibilities as a refrigerant. Its symmetric shape and the presence of the six fluorine atoms make it of theoretical interest in the study of intermolecular forces. Plasma environment studies of a body during atmospheric reentry have created an interest in the effect of electrophilic gases on high temperature plasmas. In particular, when SF_6 is injected into a supersonic plasma stream, a large electron density reduction is observed [49]. Recently, in the course of finding a method of simulating blast-intercept loadings on full scale reentry vehicle models, the heavy gas SF_6 was used since it would produce high flow Mach numbers and high dynamic pressures [50].

The polyatomic SF_6 molecule has one sulfur atom surrounded by six fluorine atoms in the form of a regular octahedron with 15 vibrational degrees of freedom (see Appendix C). The characteristic modes of vibration of SF_6 with corresponding degeneracy factors and wave numbers [51] are shown in Fig. B1.

The thermodynamic quantities are given by

$$P = \rho \frac{R}{m} T, \quad a = \sqrt{\gamma P / \rho}, \quad U = Ma$$

In the frozen-gas model, only translational and rotational degrees of freedom are excited to the new equilibrium state and the other degrees are frozen at the initial state, thus

$$h = \frac{\gamma_0}{\gamma_0 - 1} \frac{R}{m} T$$

where

$$\gamma_0 = 4/3$$

and

$$\gamma = \gamma_0$$

In the equilibrium-gas model, all vibrational, translational and rotational modes are excited to the new equilibrium state immediately behind the shock wave. The enthalpy and specific heats ratio are given by

$$h = \frac{\gamma_0}{\gamma_0 - 1} \frac{R}{m} T + \sum_k n_k \frac{T_k}{\exp(T_k/T - 1)} \frac{R}{m}$$

$$\gamma = \frac{\gamma/(\gamma_0 - 1) + V}{1/(\gamma_0 - 1) + V}$$

where

$$V = \sum_k n_k \exp(T_k/T) \left[\frac{T_k/T}{\exp(T_k/T) - 1} \right]^2$$

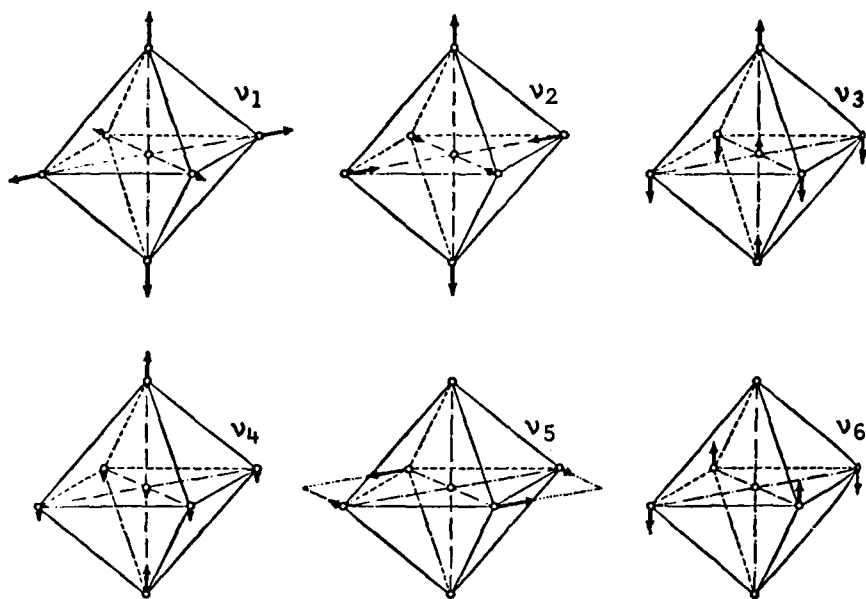
and

$$T_k = h\nu_k/K$$

with h being the Planck constant and K the Boltzmann constant.

The composition of SF_6 has been computed by Frie [52] at atmospheric pressure, including the chemical species of SF_6 , SF_4 , SF_2 , S_2 , F_2 , S , F , S^+ , S^{++} , F^+ , F^- and e^- . The variation of particle density with temperature for SF_6 is shown in Fig. B2. Minute amounts of SF_4 and F begin to occur around a temperature of 1000 K and the SF_6 line drops from the total number of particles ($\sum n_i$) line at a temperature about 1400 K, with the dissociation reaching a peak slightly below 2000 K. The ionization of sulfur and fluorine peaks at 12000 K and 17000 K, respectively. Frost and Liebermann [48] have extended the computation of the composition of SF_6 up to a pressure of 16 atm and a temperature of 45000 K. Their results agree well with the earlier calculation of Frie [52] at 1 atm. The compressibility factor Z , which is an indicator of the number of moles of gas formed due to dissociation and/or ionization from one mole of gas at room temperature, of SF_6 at various pressures and temperatures is reproduced from reference [48] in Table B1. The value of Z in the temperature range from 1000 K to 2300 K for several pressures is plotted in Fig. B3. It is seen in this figure that the dissociation process is intensified with increasing temperature and decreasing pressure as expected.

Using Table B1 and Fig. B3, the range of Mach number in which no dissociation of SF_6 occurs can be determined. In the discussions which follow, larger than 5% of dissociation of the gas is considered significant. According to the vibrational equilibrium-gas analysis at $M_s = 11$ with an initial pressure and temperature $P_0 = 15$ torr (2 kPa) and $T_0 = 300$ K, the pressure $P_1 = 2.53$ atm, the temperature $T_1 = 1470$ K with $Z \approx 1.055$ in region (1) behind the incident shock front. Thus the vibrational equilibrium-gas analysis predicts that dissociation will become significant at $M_s > 11$. Since the comparison of the analytical and experimental results is done for cases with $M_s < 5.5$, it is necessary to check if dissociation occurs behind the reflected shock wave as well. As discussed in Sec. 4.6, for a given M_s , the highest pressure obtained from reflection occurs at the RR \leftrightarrow DMR transition boundary. For $M_s = 5.5$, just before RR terminates, $P_2 = 5.11$ atm and $T_2 = 790$ K in region (2). However, this T_2 is not high enough to cause significant dissociation to occur. Hence, in the range of Mach number $M_s < 5.5$, no dissociation of the gas comes into play and only vibrational excitation needs to be taken into account in the analysis.



Mode k	ν_k (cm^{-1})	T_k (K)	n_k
1	775	1114.5	1
2	644	954.8	2
3	960	1380.5	3
4	615	884.4	3
5	524	753.5	3
6	363	522.0	3

Fig. B1 Characteristic modes of vibration of sulfur hexafluoride with corresponding degeneracy numbers, wave numbers and characteristic vibrational temperatures.

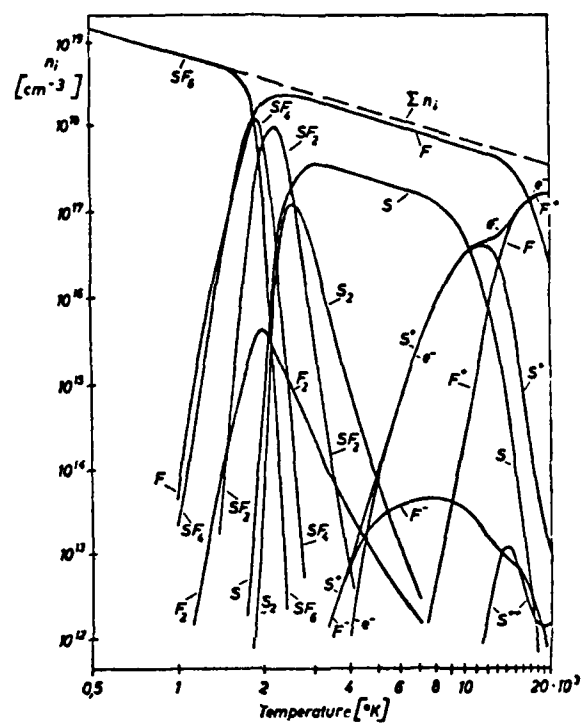


Fig. B2 Composition of SF_6 as a function of temperature at 1 atm [52].

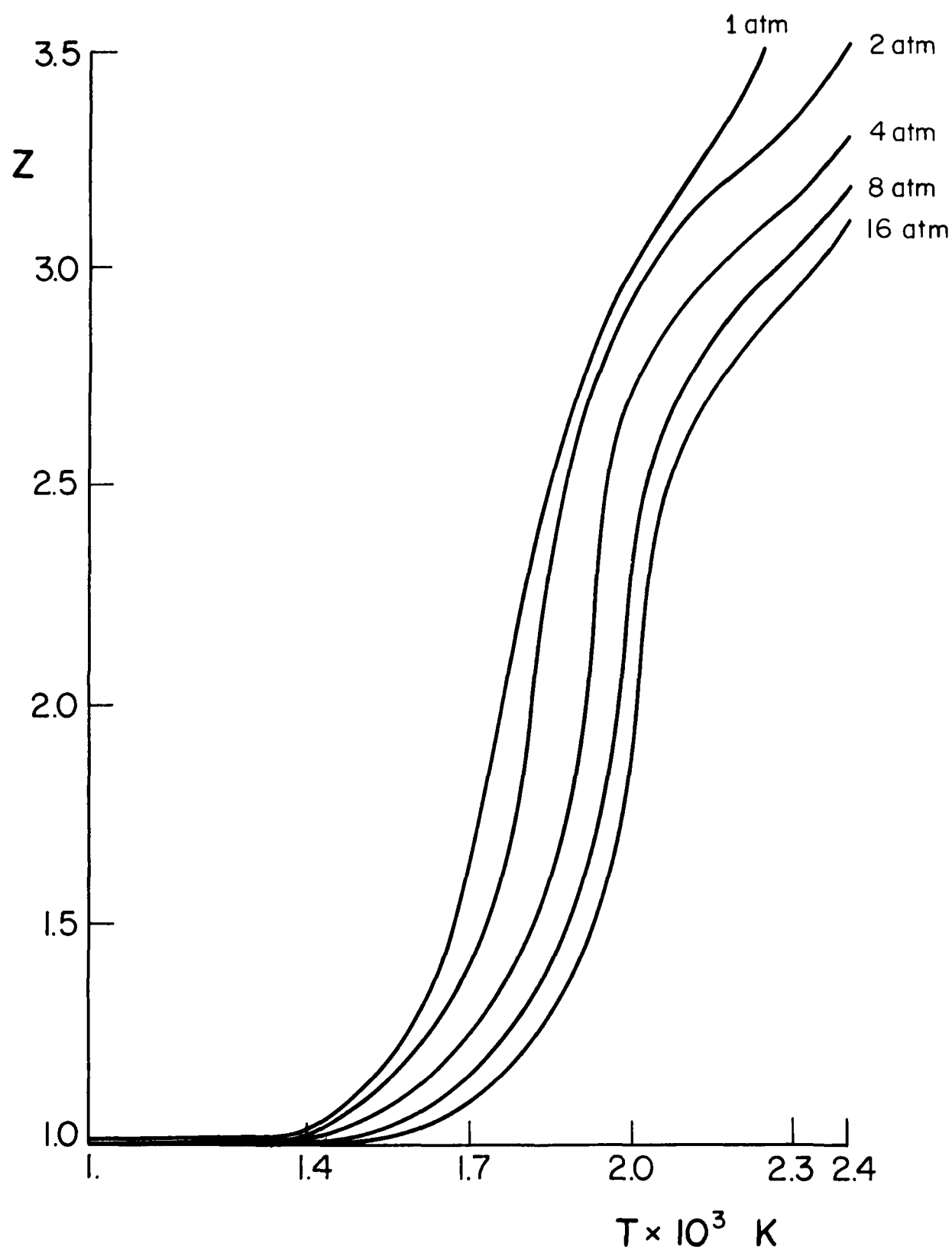


Fig. B3 Compressibility factor Z for SF_6 as a function of temperature at different pressures [48].

Table B1

Compressibility Factor of Sulfur Hexafluoride [48]

T (10^3 K)	Z				
	1 atm	2 atm	4 atm	8 atm	16 atm
1.0	1.001	1.0001	1.0000	1.0000	1.0000
1.4	1.031	1.020	1.0133	1.0088	1.0059
1.7	1.669	1.4070	1.2490	1.1550	1.098
2.0	3.005	2.9050	2.6920	2.3040	1.8660
2.3	3.668	3.3340	3.1500	3.0410	2.9400
2.6	5.490	4.8100	4.1500	3.6280	3.3010
3.0	6.480	6.3000	5.9900	5.4810	4.8140
3.5	6.830	6.7360	6.6200	6.4720	6.2530
4	6.960	6.9220	6.8640	6.7790	6.6650
5	6.996	6.9920	6.9850	6.9700	6.9430
6	7.004	7.0020	6.9990	6.9950	6.9890
7	7.019	7.0130	7.0090	7.0050	7.0005
8	7.064	7.0450	7.0320	7.0230	7.0150
9	7.164	7.1190	7.0850	7.0610	7.0430
10	7.335	7.2500	7.1840	7.1340	7.0960
11	7.555	7.4370	7.3340	7.2500	7.1830
12	7.780	7.6500	7.5200	7.4040	7.3060
13	8.020	7.8700	7.7200	7.5850	7.4590
14	8.380	8.1400	7.9500	7.78400	7.6340
15	8.950	8.5500	8.2550	8.0250	7.8340
16	9.750	9.1600	8.7000	8.3500	8.0860
18	11.710	10.8600	10.0700	9.4000	8.8660

Table B1 (continued)

Compressibility Factor of Sulfur Hexafluoride [48]

T (10^3 K)	Z				
	1 atm	2 atm	4 atm	8 atm	16 atm
20	13.150	12.5000	11.7100	10.8600	10.0650
22	13.940	13.5100	12.9500	12.2400	11.4200
26	14.770	14.5300	14.2200	13.8200	13.3100
30	15.780	15.3000	14.9400	14.6100	14.2600
35	19.010	17.8600	16.8000	15.9500	15.3000
40	21.230	20.5700	19.6600	18.5500	17.4000

Appendix C

Vibrational Relaxation in Sulfur Hexafluoride

When a shock wave propagates through a gas, the translational and rotational degrees of freedom of the gas molecules are excited to the new equilibrium state in a few mean-free-path lengths. The other internal degrees of freedom, on the other hand, require a much longer length to reach their equilibria. Relaxation lengths play an important role in the analysis of gasdynamic phenomena. In the case that the internal degree of freedom whose relaxation length is much longer than a characteristic length of the phenomenon, the internal degrees of freedom can be treated as frozen at the initial state. However, if the relaxation length of the internal degrees of freedom is shorter than a characteristic length of the phenomenon, it can be assumed to be in equilibrium behind the shock wave. If the relaxation length and the characteristic length lie between the extreme cases of frozen and equilibrium flow, the gas is in nonequilibrium. In the problem of shock-wave reflection, a characteristic length of 1 mm is chosen [16].

Vibrational relaxation of the polyatomic molecule SF_6 has been extensively studied by ultrasonic methods [53, 54, 55] in the temperature range of 200 K to 400 K. Vibrational relaxation times were determined by time-resolved measurements of the post-shock density gradient using a laser beam deflection technique over the temperature range of 450 K to 1050 K by Breshears and Blair [56]. The vibrational relaxation time of SF_6 attributable to $\text{SF}_6 - \text{SF}_6$ collisions is expressed as

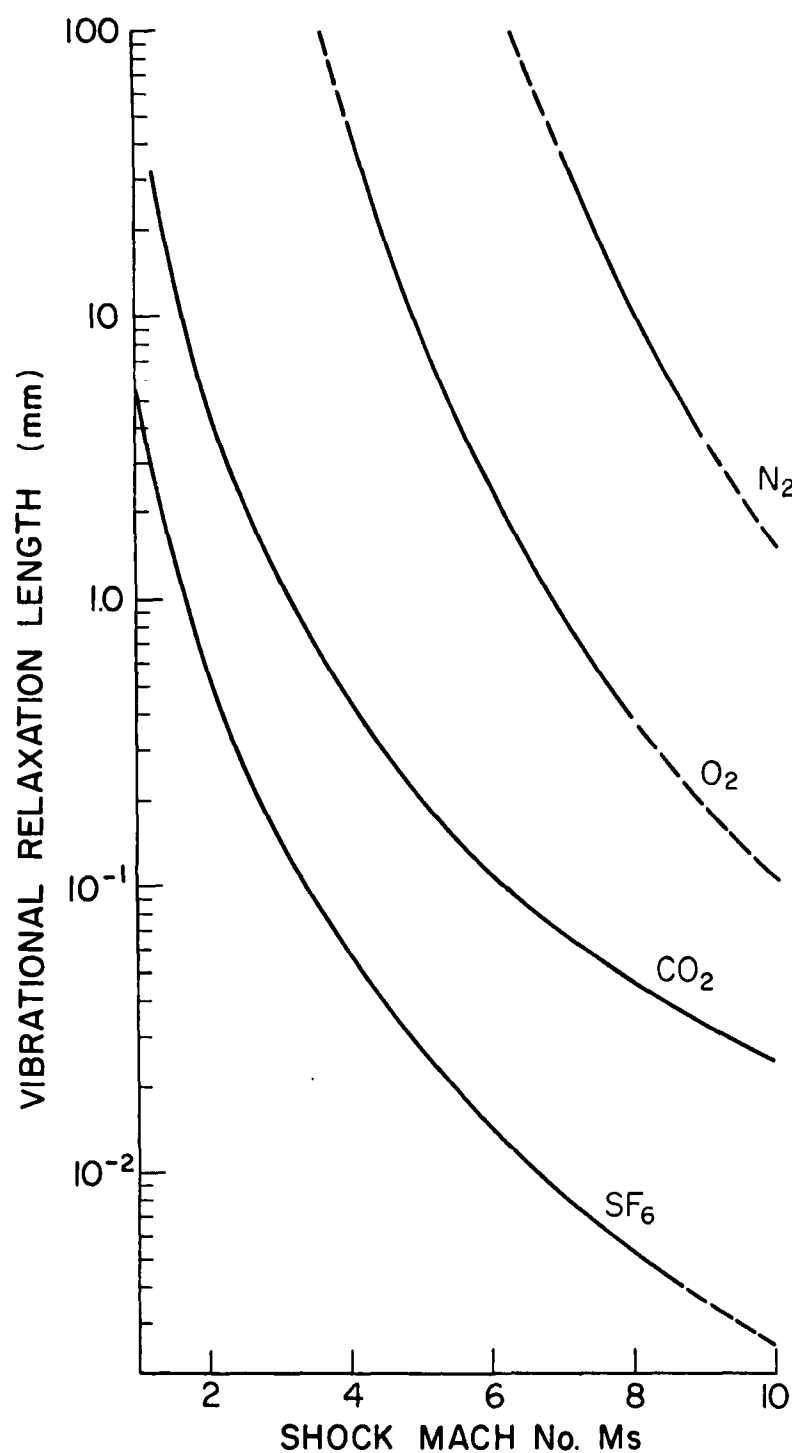
$$P\tau = 2.92 \times 10^{-3} \exp(38.0 T^{-1/3}) \mu\text{sec-atm}$$

where P is the pressure in atm and T is the temperature in degree Kelvin. Breshears and Blair also indicated that the ultrasonic data in the low temperature range of 200 K to 400 K are in good agreement with their relaxation time equation.

Using flow properties behind a shock wave and the vibrational relaxation time equation, a vibrational relaxation length can be obtained. The vibrational relaxation lengths behind a normal shock wave versus Mach number are plotted in Fig. C1 for the diatomic gases N_2 and O_2 , triatomic gas CO_2 and polyatomic gas SF_6 . These curves are for the initial conditions of $P_0 = 15$ torr (2 kPa) and $T_0 = 300$ K, and were obtained on the basis of the theoretical and empirical analyses [56, 57, 58, 59]. It is clear from Fig. C1 that for a given M_s , N_2 has the longest vibrational relaxation length, which is then followed by O_2 , CO_2 and SF_6 . Among the four gases, SF_6 has the shortest vibrational relaxation length. This ordering can be explained in terms of the type of molecule (no. of vibrational degree of freedom) and the vibrational characteristic temperature. To describe the motion of N nuclei in a molecule, it needs $3N$ coordinates; there are $3N$ degrees of freedom. For a diatomic and a linear triatomic molecule, there are three translational and two rotational degrees of freedom. The number of vibrational degrees of freedom becomes $3N-5$. For a polyatomic molecule, there are three rotational degrees of freedom instead of two, and thus there are $3N-6$ vibrational degree of freedom. Consequently, diatomic gases N_2 and O_2 have each one degree, linear triatomic gas CO_2 has four degrees and polyatomic SF_6 has 15 degrees of freedom in vibration. The vibrational

characteristic temperatures T_k of these four gases are listed also in Fig. C1. N_2 has a much higher T_k than O_2 , therefore it needs a very high temperature to get its vibrational mode excited. O_2 can be excited at a lower temperature, and it reaches equilibrium sooner than N_2 , thus for a given M_s , its vibrational relaxation length is shorter than N_2 . CO_2 does not only have more vibrational modes than O_2 , but also three of its four T_k 's are much smaller than that of O_2 . This implies that the first three vibrational modes of CO_2 are excited earlier, reaching equilibrium sooner and have a shorter relaxation length than O_2 . Moreover, the last mode has a T_k that is higher than that of N_2 . It is expected that vibrational excitation in CO_2 will reach complete equilibrium at a temperature higher than the other four gases.

The average T_k for SF_6 is lower than for the other four gases and it reaches vibrational equilibrium much faster than the others. Raising the pressure at a given temperature enhances particle collisions and vibrational equilibrium is reached more quickly. From Fig. A4, it is expected that vibrational relaxation in SF_6 at $M_s < 1.7$ with an initial pressure of 15 torr (2 kPa) and a temperature of 300 K will take place in less than 1 mm. However, at such a low Mach number, a relatively higher initial pressure is required for the experiment. Increasing the pressure will shift the vibrational relaxation length curve down, therefore no vibrational relaxation length will be observed. Since the vibrational relaxation length is less than 1 mm over the entire range of Mach number studied in this work, it can be safely assumed that SF_6 is in vibrational equilibrium.



Gas	T_k	n_k
N_2	3340.0	1
O_2	2230.0	1
CO_2	960.2	2
	1932.2	1
	3380.3	1
SF_6	522.0	3
	753.5	3
	884.4	3
	954.8	2
	1114.5	1
	1380.5	3

Fig. C1 Vibrational relaxation length behind shock wave vs M_s at initial conditions of $P_0 = 15$ torr, $T_0 = 300$ K for various gases (after Refs. [56, 57, 58, 59]). The characteristic vibrational temperatures and degeneracy numbers for the different gases are given in the table.

<div>UTIAS Technical Note No. 253</div> <div>Institute for Aerospace Studies, University of Toronto (UTIAS) 4925 Dufferin Street, Downsview, Ontario, Canada, M3H 5T6</div> <div>PSEUDO-STATIONARY OBLIQUE-SHOCK-WAVE REFLECTIONS IN A POLYATOMIC GAS - SULFUR HEXAFLUORIDE</div> <div>Hu, John Tin Cheung</div> <div><div>1. Pseudo-stationary oblique-shock-wave reflections</div><div>2. Shock-tube flows</div><div>3. Interferometry</div><div>4. Frozen and real-gas effects</div><div>5. Numerical analysis</div></div> <div><div>1. Hu, John Tin Cheung</div><div>11. UTIAS Technical Note No. 253</div></div> <div><p>The pseudo-stationary oblique-shock-wave reflections in sulfur hexafluoride, SF_6, were investigated experimentally and numerically. Experiments were conducted in the UTIAS 10x18 cm Hypervelocity Shock Tube at 1.25 < M_0 < 8.0 and $4^\circ < \theta < 47^\circ$ with $4 < P_0 < 267$ torr and to near 300 K. The four major types of shock-wave reflection, i.e., regular reflection (RR), single-Mach reflection (SMR), complex-Mach reflection (CMR) and double-Mach reflection (DMR), were observed. These were studied with infinite-fringe interferograms using a 23-cm dia field of view Mach-Zehnder interferometer. The isopycnics obtained and the density distributions along the wedge surface were presented for the various reflection processes.</p><p>The analytical transition boundaries between the four types of reflection were established up to $M_0 = 10.0$ for frozen and vibrational equilibrium. In general, the equilibrium-gas analytical transition boundaries agreed with the experiments. However, RR persisted beyond the RR termination boundary determined by the detachment criterion, and several Mach reflections (MR) lie outside their analytically predicted domains. Experiments substantiated that the CMR to DMR transition line approached the SMR to CMR transition line and would merge at a single point on the RR termination line. The analytical results were compared with the experimental data for the reflection angles θ and ϕ, and the triple-point trajectory angles χ and ψ, and it was verified that the shock-wave reflection systems were in vibrational equilibrium. It was found that negative values for the angle ψ were possible under certain conditions of Mach reflection and the pattern of DMR with $\chi' = 0$ was obtained experimentally. The numerical results of the second triple-point system show that for a given Mach number, the highest pressure is achievable by an RR instead of a DMR. It has been shown analytically that when the transition of RR \neq MR occurs, no significant amount of pressure changes behind the bow shock wave is obtained.</p></div> <div>Available copies of this report are limited. Return this card to UTIAS, if you require a copy.</div>	<div>UTIAS Technical Note No. 253</div> <div>Institute for Aerospace Studies, University of Toronto (UTIAS) 4925 Dufferin Street, Downsview, Ontario, Canada, M3H 5T6</div> <div>PSEUDO-STATIONARY OBLIQUE-SHOCK-WAVE REFLECTIONS IN A POLYATOMIC GAS - SULFUR HEXAFLUORIDE</div> <div>Hu, John Tin Cheung</div> <div><div>1. Pseudo-stationary oblique-shock-wave reflections</div><div>2. Shock-tube flows</div><div>3. Interferometry</div><div>4. Frozen and real-gas effects</div><div>5. Numerical analysis</div></div> <div><div>1. Hu, John Tin Cheung</div><div>11. UTIAS Technical Note No. 253</div></div> <div><p>The pseudo-stationary oblique-shock-wave reflections in sulfur hexafluoride, SF_6, were investigated experimentally and numerically. Experiments were conducted in the UTIAS 10x18 cm Hypervelocity Shock Tube at 1.25 < M_0 < 8.0 and $4^\circ < \theta < 47^\circ$ with $4 < P_0 < 267$ torr and to near 300 K. The four major types of shock-wave reflection, i.e., regular reflection (RR), single-Mach reflection (SMR), complex-Mach reflection (CMR) and double-Mach reflection (DMR), were observed. These were studied with infinite-fringe interferograms using a 23-cm dia field of view Mach-Zehnder interferometer. The isopycnics obtained and the density distributions along the wedge surface were presented for the various reflection processes.</p><p>The analytical transition boundaries between the four types of reflection were established up to $M_0 = 10.0$ for frozen and vibrational equilibrium. In general, the equilibrium-gas analytical transition boundaries agreed with the experiments. However, RR persisted beyond the RR termination boundary determined by the detachment criterion, and several Mach reflections (MR) lie outside their analytically predicted domains. Experiments substantiated that the CMR to DMR transition line approached the SMR to CMR transition line and would merge at a single point on the RR termination line. The analytical results were compared with the experimental data for the reflection angles θ and ϕ, and the triple-point trajectory angles χ and ψ, and it was verified that the shock-wave reflection systems were in vibrational equilibrium. It was found that negative values for the angle ψ were possible under certain conditions of Mach reflection and the pattern of DMR with $\chi' = 0$ was obtained experimentally. The numerical results of the second triple-point system show that for a given Mach number, the highest pressure is achievable by an RR instead of a DMR. It has been shown analytically that when the transition of RR \neq MR occurs, no significant amount of pressure changes behind the bow shock wave is obtained.</p></div> <div>Available copies of this report are limited. Return this card to UTIAS, if you require a copy.</div>
---	---